

Investigating axonal transport in Charcot-Marie-Tooth disease Type 2A using a human embryonic stem cell model

By:

Lydia Helen Jestice

A thesis submitted in partial fulfilment of the requirements for the degree of Doctor of Philosophy

The University of Sheffield

Faculty of Science

School of Bioscience

2025

Acknowledgements

It feels incredibly surreal to be writing the acknowledgements of my PhD thesis and I'm struggling to find the right words to sum up the last three and half years. This PhD has been filled with highs and lows and has taught me many many things beyond how to be a good scientist. It's an experience I am incredibly grateful to have, but I am even more grateful to the people who made it possible for me. My friends, my family, and my colleagues have been a constant source of support, joy, hugs, and laughter – I really could not have done it without you.

I'd like to start by thanking my supervisor Prof. Ivana Barbarić for her constant words of encouragement, support, and wisdom, and for helping me believe that I could do this. I'd also like to thank my secondary supervisor Prof. Kurt De Vos for his vast neuroscience expertise and insightful suggestions that have kept me fascinated by neurodegeneration throughout this project. A big thank you to my scientific advisor Dr Anestis Tsakiridis for his help in this project. You always bought a sense of optimism to our meetings which was invaluable. I would also like to say thank you to Dr Alison Twelvetrees, without you I would not have a lot of the data, skills, or determination needed to finish this project. I'm incredibly grateful for the time you gave me and the motivational pep talks.

An enormous amount of thanks needs to go to the past and present members of the Barbarić, Tsakiridis, and De Vos groups who have given me constant support and been some of the loveliest people I've ever met. Please know that so grateful to each of you for giving me your time and wisdom and a special shout-out to Gabi and Beth for your friendship and constant emotional support. A huge thank you is needed for my friends and housemates Louise and Joe for all the reciprocal love and support - I could not have asked to two better people to do this with. Additionally, I'd like to thank my all my friends and family for all their support and love throughout my PhD and for allowing me to enjoy some much-needed time away from the lab. You've all made me feel like the smartest in the room for doing this.

I'd like to acknowledge the MRC DiMeN DTP who funded this work - thank you very much for giving me this opportunity. The DiMeN student experience is unparalleled and I've loved all the training experiences and people I've met along the way. DiMeN

has provided me with friends and a sense of community during one of the loneliest academic pursuits, and for that I'm very grateful.

Finally, I would like to thank me. There were many points where I considered giving up, when life continuously threw curveballs at me, and I'm really glad I didn't. This experience has taught me that I am incredibly capable and smart and kind and resilient and generous, and it probably shouldn't have taken doing an entire PhD to figure that out but oh well! I'm really proud of myself, and I hope I've made everyone else proud too. I will be forever changed by this experience and for the better.

Enjoy the thesis xx

Abstract

Charcot-Marie-Tooth (CMT) disease is one of the most common forms of inherited peripheral neuropathy and has many different subtypes. One such subtype is sensory and motor neuropathy CMT Type 2A (CMT2A), for which no treatments currently exist. CMT2A is caused by mutations in Mitofusin 2 (MFN2), and it is unknown how these mutations drive disease. Hence, I set out to create the first human embryonic stem cell (hESC) model of CMT2A to investigate the impact of a CMT2A-causing mutation in a disease-relevant cell type.

I generated a panel of CMT2A hESC clones by introducing the disease-causing heterozygous R94Q mutation into Mitofusin 2 via CRISPR-Cas9 editing. The clone panel was subsequently differentiated into a disease-relevant cell type: limb-innervating motor neurons. The introduction of the CMT2A-causing mutation had no effect on differentiation. Limb-innervating motor neurons containing the disease-causing mutation displayed a mitochondrial trafficking defect characterised by a reduction in the number of motile mitochondria and the motile dynamics. The reduction in motile mitochondria could be rescued via small molecule inhibition of the deacetylase HDAC6. Furthermore, using protein over-expression and co-immunoprecipitation, I also show that MFN2 containing the R94Q mutation interacts more strongly with the trafficking cargo adapter protein TRAK1, leading to TRAK1 having a reduced interaction with the axonal motor protein kinesin.

Overall, I have successfully created hESCs containing a CMT2A-causing mutation that can be differentiated into limb-innervating neurons, providing a new *in vitro* platform for CMT2A research. Additionally, results here contribute to evidence that axonal transport deficits are a common CMT2 hallmark. This work provides a new hypothesis for CMT2A pathophysiology and is a foundation for the further study of axonal transport machinery and its functionality in CMT2A.

Table of Contents

Acknowledgements....ii
Abstract....iv
Table of Contents.... v
List of figures x
List of tables....xiv
List of abbreviations....xv
Chapter 1 - Introduction: 1
Neurodegeneration.... 1
Axonal transport 1
Microtubules 1
Microtubule post-translational modifications 3
Axonal transport motors.... 4
Axonal transport in neurodegeneration 5
Charcot-Marie-Tooth disease.... 6
Charcot-Marie-Tooth disease Type 2A.... 10
Mitofusin 2.... 12
CMT2A modelling.... 18
Human Pluripotent stem cells.... 21
Thesis aims 25
1. **Generation of a panel of hESCs for CMT2A modelling**.... 26
2. **Characterisation of mitochondrial trafficking in a CMT2A hESC model** 26
3. **Compare functions of wild-type and mutated MFN2 linked to axonal transport**.... 26
Chapter 2 - Methods and materials:.... 27
2.1 hPSC culture 27
2.1.1 Cell Lines.... 27
2.1.2 Preparation of culture vessels.... 28
2.1.3 S8 Media recipe.... 28
2.1.4 S8 Media preparation 29
2.1.5 Passaging hPSCs 29
2.1.6 Freezing hPSCs 30
2.1.7 Thawing hPSCs.... 30

2.1.8 Single cell dissociation of hPSCs 30
2.2 Immortalised cell culture 30
2.3 Karyotyping and SNP array 31
2.4 Motor neuron differentiation of hPSCs 31
2.4.1 N2B27 media 31
2.4.2 Motor neuron differentiation protocol 31
2.5 qPCR gene expression analysis 32
2.5.1 RNA extraction 32
2.5.2 cDNA generation 33
2.5.3 qPCR 33
2.5.4 qPCR analysis 33
2.5.5 Primer validation 33
2.5.6 Primer sequences 34
2.6 Immunofluorescence 35
2.6.1 Immunocytochemistry 35
Proximity Ligation Assay (PLA) 35
2.7 DNA extraction 36
2.8 Transmission Electron Microscopy 36
2.8.1 Fixation 36
2.8.2 TEM 37
2.9 Mitochondrial trafficking 37
2.9.1 Transfection 37
2.9.2 Imaging 37
2.9.3 Analysis 38
2.10 CRISPR gene editing of cells 38
2.10.1 On and off-target primer design 38
2.10.2 Transfection of Cas9 and guides 39
2.10.3 Single cell sort and cloning 40
2.10.4 DNA extraction from 96-well plates 41
2.10.5 PCR and Restriction digest screen 42
2.10.6 Sanger sequencing 43
2.10.7 Low-pass whole genome sequencing 44
2.10.8 Surveyor Nuclease assay 45
2.11 Western Blotting and co-immunoprecipitation 45
2.11.1 Protein extraction 45

2.11.2 Protein quantification 45
2.11.3 SDS-PAGE 45
2.11.4 Protein transfer 46
2.11.5 Protein detection 47
2.11.6 Western blotting buffer recipes 47
2.11.7 Plasmid mutagenesis 48
2.11.8 Plasmid production 48
2.11.9 Transfection, lysis, and co-immunoprecipitation 49
2.12 Antibodies 49
2.12.1 Primary antibodies for immunofluorescence 49
2.12.2 Primary antibodies for Western blotting 50
2.12.3 Secondary antibodies for Western blotting 51
2.12.4 Secondary antibodies for Immunofluorescence 51
2.13 Solutions and buffers 52
2.13.1 PBS 52
2.13.2 4% PFA 52
2.13.3 TBE 52
2.14 Statistical analysis 52
Chapter 3 - Generation of hESC lines containing CMT2A-causing mutations via CRISPR-Cas9 gene editing: 54
3.1 Introduction: 54
3.1.1 Aims 55
3.2 Generating and characterisation of CMT2A hESC sub-clones using CRISPR editing: 56
3.2.1 Generation and identification of CRISPR edited hESCs containing MFN2$^{R94Q/+}$ 56
3.2.2 Characterisation of pluripotency of MFN2$^{R94Q/+}$ hESCs 61
3.2.3 MFN1/MFN2 expression in MFN2$^{R94Q/+}$ hESCs 66
3.2.4 Generation and identification of CRISPR edited hESCs containing MFN2$^{T105M/+}$ 67
3.3 Generation of spinal motor neurons (sMNs) from MFN2$^{R94Q/+}$ hESCs: 72
3.3.1 Motor neuron differentiation protocol: 72
3.3.2 Expression of key sMN markers in neurons generated by the optimised sMN differentiation protocol 75
3.3.3 Additional assessment of sMN markers by RT-qPCR 81
3.3.4 Additional assessment of sMN function 85

3.4 Discussion ... 88
Chapter 4: Characterisation of mitochondrial transport in an hESC model of CMT2A ... 93
4.1 Introduction: ... 93
4.2 Results: ... 97
Establishing a mitochondrial trafficking assay and analysis pipeline ... 97
CMT2A motor neurons have reduced mitochondrial size in axons ... 99
CMT2A motor neurons have a mitochondrial trafficking deficit ... 112
Mitochondrial size in CMT2A axons is rescued by HDAC6 inhibition ... 126
CMT2A mitochondrial trafficking deficit is rescued by HDAC6 inhibition 133
4.3 Discussion ... 145
4.3.1 MFN2$^{R94Q/+}$ mitochondria are smaller and display an axonal transport defect ... 145
4.3.2 HDAC6 inhibition alleviates MFN2$^{R94Q/+}$ mitochondrial transport defect ... 148
4.3.3 HDAC6 inhibition as a potential therapeutic for CMT2A ... 150
Chapter 5: Linking MFN2 to mitochondrial transport ... 151
5.1 Introduction: ... 151
5.2 Results: ... 153
5.2.1 Assessing α-tubulin acetylation is MFN2$^{R94Q/+}$ motor neurons ... 153
5.2.2 ER-mitochondrial contacts are unaffected by R94Q ... 155
5.2.3 MFN2 interactions with TRAK1 are altered by R94Q ... 162
5.3 Discussion ... 174
5.3.1 α-tubulin acetylation ratios are unaffected in MFN2$^{R94Q/+}$ motor neurons ... 174
5.3.2 MERCS number and contact size is unaffected in MFN2$^{R94Q/+}$ motor neurons ... 175
5.3.3 The R94Q mutation alters MFN2-TRAK1-KIF5B interactions ... 176
Chapter 6: General discussion and concluding remarks ... 179
6.1 A novel hESC model of CMT2A ... 179
6.2 Characterising mitochondrial trafficking in hESC-based MFN2$^{R94Q/+}$ neurons ... 181
6.3 Molecular mechanisms driving axonal transport defects in an *in vitro* CMT2A model ... 183
6.4 Future therapies for CMT2A ... 185
6.5 Closing remarks ... 186
Appendix 1 ... 188

Appendix 2..... 198
Bibliography 201

List of figures

Figure number	Page number
1.1 Microtubules formed from tubulin dimers are dynamic	2
1.2 Dynein and kinesin govern retrograde and anterograde axonal transport	5
1.3 Subtypes of Charcot-Marie-Tooth disease	8
1.4 Structure of Mitofusin-2	14
1.5 STRING analysis of MFN2	16
1.6 Derivation of hPSCs	23
3.1 Generation of MFN2$^{R94Q/+}$ clones from MasterSheff11 hESCs using CRISPR-cas9 with no detected off-target editing	59
3.2 Sub-cloning of 2 putative MFN2$^{R94Q/+}$ clones	60
3.3 Screen for off-target mutations in MFN2$^{R94Q/+}$ sub-clones	61
3.4 CMT2A pluripotency marker expression	64
3.5 Trilineage differentiation of the CMT2A hESC clone panel	65
3.6 Expression of Mfn1 and Mfn2 in MFN2$^{R94Q/+}$ clone panel	67
3.7 CRISPR-cas9 editing using previously generated guides for MFN2$^{T105M/+}$	70
3.8 Generation of a new gRNA for MFN2$^{T105M/+}$	71
3.9 Optimised spinal motor neuron differentiation protocol	73
3.10 Organisation of the motor columns	74
3.11 ISL1/2 expression in sMNs	76
3.12 ChAT expression in sMNs	77
3.13 Foxp1 expression in sMNs	79
3.14 HB9 expression in sMNs	80
3.15 Expression of additional sMN markers across differentiation	82
3.16 HOX gene expression across sMN differentiation	84
3.17 Electrophysiological characterisation of hESC-derived sMNs	86

3.18 Characterisation of the axon initial segment in hESC-derived sMNs	88
4.1 Mitochondrial shape descriptors	95
4.2 Low-efficiency transfection isolates neurons in dense cultures	97
4.3 ImageJ processing and KymoButler analysis	99
4.4 Mitochondrial spacing along the axon worsened by $MFN2^{R94Q/+}$	100
4.5 Reduction in $MFN2^{R94Q/+}$mitochondrial area is most pronounced in the distal axon	102
4.6 Mitochondrial length is reduced in $MFN2^{R94Q/+}$ sMNs	104
4.7 Mitochondrial aspect ratio is not altered in $MFN2^{R94Q/+}$ sMN axons	107
4.8 Mitochondrial circularity is not altered in $MFN2^{R94Q/+}$ sMN axons	109
4.9 Mitochondrial form factor is not altered in $MFN2^{R94Q/+}$ sMN axons	111
4.10 $MFN2^{R94Q/+}$ sMNs have fewer motile mitochondria across the length of the axon	114
4.11 $MFN2^{R94Q/+}$ sMNs have fewer motile mitochondria moving in the anterograde direction across the length of the axon	116
4.12 $MFN2^{R94Q/+}$ sMNs have fewer motile mitochondria moving in the retrograde direction across the length of the axon	118
4.13 Mitochondrial velocity varies with direction and MFN2 status	120
4.14 Pausing of motile mitochondria in CMT2A sMN axons	122
4.15 Velocity variation in motile mitochondria in $MFN2^{+/+}$ and $MFN2^{R94Q/+}$ sMNs	124
4.16 Motile track length in $MFN2^{+/+}$ and $MFN2^{R94Q/+}$ sMNs	125
4.17 HDAC6 inhibition increases mitochondrial area in $MFN2^{R94Q/+}$ in the distal axon	128

4.18 HDAC6 inhibition increases mitochondrial length in MFN2$^{R94Q/+}$ in the distal axon	130
4.19 HDAC6 inhibition does not alter mitochondrial shape descriptors	132
4.20 HDAC6i rescues trafficking defect in MFN2$^{R94Q/+}$ sMNs	135
4.21 HDAC6i increases anterograde transport in MFN2$^{R94Q/+}$ sMNs	137
4.22 HDAC6i increase retrograde transport in MFN2$^{R94Q/+}$ sMN axons	139
4.23 HDAC6 inhibition alters the velocity of motile mitochondria in sMN axons	141
4.24 Pausing of motile mitochondria in sMNs treated with ACY-738.	143
4.25 HDAC6i does not alter motile track length	144
5.1 Tubulin acetylation is increased by HDAC6 inhibition but not altered by MFN2$^{R94Q/+}$	154
5.2 Proximity ligation assay	155
5.3 PLA between VAPB and PTPIP51 to visualise MERCS in MFN2$^{+/+}$ and MFN2$^{R94Q/+}$ hESCs	156
5.4 Manual analysis of PLA images in CMT2A hESCs	158
5.5 PLA quantification using establish ImageJ macro	159
5.6 TEM images of Day 34 hESC-derived limb innervating motor neurons	161
5.7 Analysis of mitochondrial morphology from TEM images	162
5.8 Generation of R94Q MFN2 encoding plasmid	163
5.9 Myc-MFN2 interacts with HA-TRAK1 and a CMT2A-causing mutation increases this interaction	164
5.10 Less KIF5B is pulled down by TRAK1 in the presence of R94Q MFN2	165
5.11 KIF5B is not precipitated by Myc-Mfn2	166
5.12 Neither endogenous cytoplasmic dynein nor endogenous MIRO are pulled down by HA-TRAK1.	168

5.13 MFN2 R94Q overexpression in HEK293 cells does not reduce α-tubulin acetylation.	169
5.14 Western blot analysis of α-tubulin acetylation in HEK293 cells treated with increasing ACY-738 concentrations.	170
5.15 ACY-738 treatment has a modest effect on TRAK1-MFN2 interactions.	171
5.16 ACY-738 treatment does not increase TRAK1-KIF5B interactions in the presence of R94Q MFN2.	173
5.17 Proposed model for MFN2/TRAK1/KIF5B interactions in CMT2A	178

List of tables

Table number	Page number
1.1 Overview of in vivo models of CMT2A	19
2.1 50x S8 supplement components	28
2.2 Components of N2B27 media	31
2.3 SYBRgreen RT-qPCR instrument settings	33
2.4 List of RT-qPCR primer sequence	34
2.5 List of PCR primers for on- and off-target sequencing of $MFN2^{R94Q/+}$ cells	39
2.6 List of PCR primers for on-target editing of $MFN2^{T105M/+}$ cells	39
2.7 Components for gDNA lysis buffer	41
2.8 Components for a single PCR reaction	42
2.9 Thermal cycler settings for PCR	42
2.10 Components for a singular restriction digest reaction using BseMII	43
2.11 Components for a singular restriction digest reaction using FokI	43
2.12 Components for a singular PCR reaction using Platinum II taq	44
2.13 Thermocycler settings for PCR using Platinum II taq	44
2.14 Components for 4% and 6% stacking gels for SDS-PAGE gels	46
2.15 Components for 7.5%, 10%. 12% and 14% resolving gels for SDS-PAGE gels	46
2.16 List of primary antibodies used for immunocytochemistry analysis	49
2.17 List of primary antibodies used for Western blotting	50
2.18 List of secondary antibodies used for Western blotting	51
2.19 List of secondary antibodies used for immunocytochemistry analysis	51

List of abbreviations

ALS	Amyotrophic Lateral Sclerosis
ANOVA	One-way analysis of variance
ATP	Adenosine triphosphate
cMN	Cranial motor neuron
CMT	Charcot-Marie-Tooth disease
CMT2A	CMT Type 2A
CRISPR	Clustered regularly interspaced short palindromic repeats
crRNA	CRISPR RNA
DNA	Deoxyribonucleic acid
DSB	Double-stranded break
DSD	Dejernie-Sottas Disease
DRG	Dorsal root ganglion cells
EB	Embryoid body
ER	Endoplasmic reticulum
GFP	Green fluorescent protein
gRNA	Guide RNA
GTP	Guanosine triphosphate
HDAC6	Histone Deacetylase 6
HDR	Homology directed repair
hESC	Human embryonic stem cell
HMSN	Hereditary motor and sensory neuropathy
hPSC	Human pluripotent stem cell
iPSC	Induced pluripotent stem cell
MEF	Mouse embryonic fibroblasts
MERCS	Mitochondria endoplasmic reticulum contact sites
MFN1	Mitofusin 1
MFN2	Mitofusin 2
mRNA	messenger RNA
NHEJ	Non-homologous end joining
NHS	National Health Service
PCR	Polymerase chain reaction
PLA	Proximity ligation assay

RD	Restriction digest
RNA	Ribonucleic acid
RLS	Roussy-Levy syndrome
RT-qPCR	Quantitative reverse transcription PCR
SD	Standard deviation
SEM	Standard error of the mean
sMN	Spinal motor neuron
ssODN	Single-stranded oligodeoxynucleotides
TEM	Transmission electron microscopy
tracrRNA	Trans-activating CRISPR RNA
TRAK1	Trafficking kinesin-binding protein 1

Chapter 1 - Introduction:

Neurodegeneration

Neurodegenerative diseases are one the largest conundrums facing the scientific community and one of the largest burdens on global healthcare. As a group, neurodegenerative diseases are typically age-related and are characterised by the progressive and irreversible loss of neurons from the central or peripheral nervous systems. With ageing populations, the number of global deaths caused by these neurological disorders is predicted to increase by 237% by 2040 (Foreman et al., 2018). There are multiple shared hallmarks of neurodegeneration including toxic protein aggregation, mitochondrial dysfunction, disturbed axonal transport, and dysregulated calcium handling but the precise cellular mechanisms underlying each neurodegenerative disease varies greatly and are experimentally difficult to pin down. As a consequence, the current state of therapeutics for neurodegenerative diseases is insufficient to cope with present incidence rates; there exists no efficacious drug that can halt disease progression.

Axonal transport

As previously stated, impaired axonal transport is a common hallmark of neurodegeneration. Axonal transport is the process by which neurons ferry intracellular cargo from the cell body to the axon terminal and back to the soma (Guedes-Dias and Holzbaur, 2019). The majority of synthesis occurs in the soma, and macromolecules and organelles required in synapses must be targeted correctly. Reciprocally, matter from the synapses must be removed and re-delivered to the soma for degradation or recycling. Due to the polarity and size of neurons, particularly in the periphery of the human body, it is essential that axonal transport is as efficient as possible to ensure neuronal survival, function, and homeostasis.

Microtubules

To move such intracellular cargo large distances in a timely manner, ATPase motor proteins kinesin and dynein couple to cargo via organelle-specific adaptor proteins, and move along microtubule highways, using the polarity of microtubules to determine direction (Shelley, 2016). Microtubules are comprised of α- and β-tubulin

GTP-bound heterodimer subunits that form protofilaments which go on to form hollow microtubules which average a diameter of ~ 25 nm (Figure 1.1A) (Shelley, 2016).

Microtubules are typically dynamic structures that are constantly growing and shrinking due to GTP hydrolysis, creating a cytoskeleton that is responsive to stress or damage. This dynamic instability mainly occurs at the plus end of microtubules, with GTP-bound tubulin subunits being incorporated leading to growth, and GTP hydrolysis occurring during the polymerisation (Nogales et al., 1998a). Microtubule catastrophe occurs when GDP-tubulin is lost from the end of the microtubule, shortening the length of the polymer. Tubulin exchange can also occur within the main shaft of the microtubule, with free tubulin dimers being incorporated into small breaks within the lattice (Gazzola et al., 2023). Neuronal microtubules however are mostly very stable to support the extreme length and life-span of neurons, as well as facilitating long-range axonal transport (Baas et al., 2016). It is thought that greater stability in microtubules confers preferential binding of axonal transport motors and their cargo; a subtype of the anterograde motor kinesin (kinesin 1) preferentially interacts with acetylated microtubules, a post-translational modification of α-tubulin that stabilises microtubules (Reed et al., 2006),

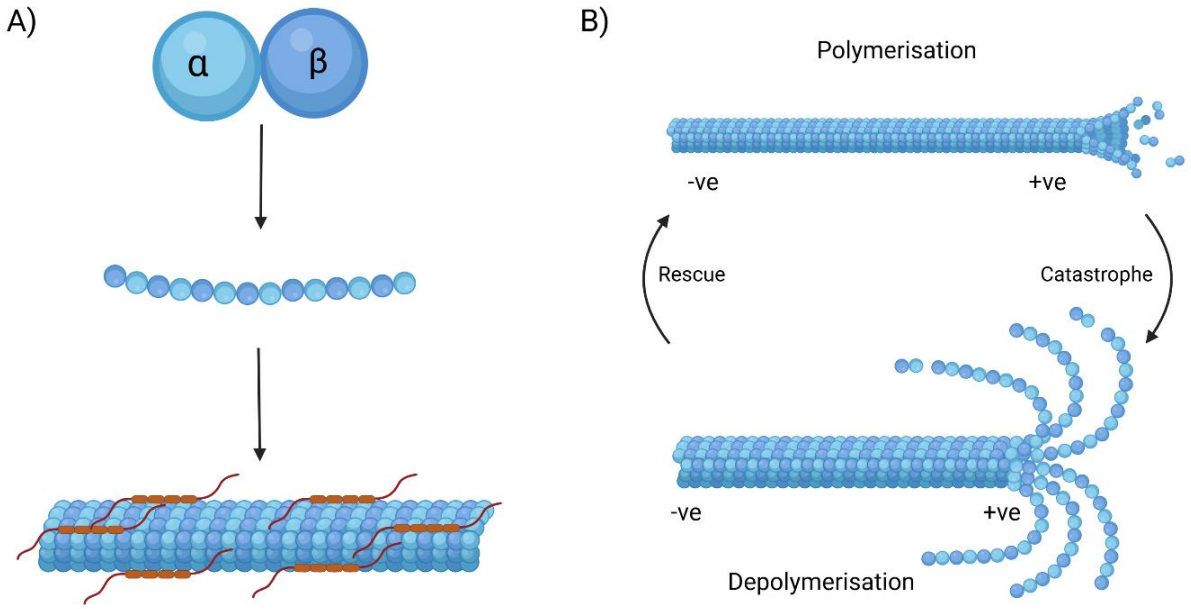


Figure 1.1: Microtubules formed from tubulin dimers are typically dynamic. *(A) α-tubulin and β-tubulin form dimers that polymerise to form protofilaments. Protofilaments organise into a cylindrical structure – the microtubule. Microtubule associated proteins (MAPs) such as Tau (shown in orange) decorate the microtubule providing additional stability. (B) Microtubules polymerise by incorporating*

tubulin heterodimers into the plus end. Destabilisation leads to catastrophe, where tubulin is lost from the growing end of the microtubule. Schematic made using Biorender.com

The stability of axonal microtubules is supported by structural microtubule-associated proteins such as Tau, microtubule associated protein 2 (MAP2), and doublecortin (DCX) which are incorporated into the tubule, minimising microtubule dynamics and supporting microtubule rescue (Papasozomenos et al., 1985, Gordon-Weeks and Fischer, 2000, Cario and Berger, 2023) (Figure 1.1 A, B). Microtubule-associated proteins can also modulate motor protein binding and consequently axonal transport efficiency (Chaudhary et al., 2019, Hooikaas et al., 2019).

Microtubule post-translational modifications

Microtubules are also subjected to post-translational modifications, including acetylation, sumoylation, phosphorylation, and detryosination (Wloga and Gaertig, 2010). These chemical modifications are proposed to influence the interactions between microtubules and motor proteins (Hammond et al., 2009, Sirajuddin et al., 2014) and both stabilise and destabilise tubulin dynamics (Bär et al., 2022, Chen and Roll-Mecak, 2023, Sanyal et al., 2023). The acetylation of axonal microtubules is one of the most well-studied post-translational modifications thanks to its implications in neurodevelopmental and neurodegenerative disorders. α-tubulin is acetylated at lysine 40 (K40). The acetylation/deacetylation cycle of α-tubulin in axons is governed by the deacetylase histone deacetylase 6 (HDAC6) and the acetylase α-tubulin acetyltransferase (α-TAT1) within the microtubule lumen (Soppina et al., 2012).

The histone deacetylase superfamily (HDACs) comprises of 4 HDAC classes (Classes I, IIa, IIb, III, IV), defined by sequence homology and required cofactors. HDACs are epigenetic modulators, primarily responsible for the deacetylation of histones which consequently influences chromatin folding and gene transcription, with each HDAC having a different tissue and subcellular distribution (Simões-Pires et al., 2013). HDAC6 is a class IIb HDAC that almost exclusively resides in the cytoplasm and specifically deacetylates lysine residues on α-tubulin, as well as deacetylating and interacting with other cytoplasmic proteins (Kalveram et al., 2008, Parmigiani et al., 2008, Chen et al., 2010, Li et al., 2011).

Axonal transport motors

Kinesin is the anterograde motor that moves towards the plus ends of microtubules, transporting cargo from the soma to the axonal terminal (Figure 1.2A). The kinesin superfamily is comprised of 14 subfamilies with 44 different genes (Miki et al., 2001). Kinesin 1 (KIF5A-5C) and kinesin 3 are the most well characterised kinesins with regard to axonal transport (Guedes-Dias and Holzbaur, 2019, Zahavi et al., 2021). Kinesin is a heterotetramer, comprised of two heavy chains and two light chains (Marx et al., 2009). A central hinge region within the heavy chains allows for kinesin to auto-inhibit, which serves as a level of control for transport (Chiba et al., 2022). Motor proteins like kinesin are only capable of moving multiple intracellular cargos thanks to cargo adaptors, proteins or complexes that interact directly with motor proteins and cargos to bridge the two. Many organelle-specific anterograde adaptor proteins and regulators have been identified which help to orchestrate correct organelle localisation (Maday et al., 2014).

Dynein is the retrograde minus end-directed motor than moves cargo from distal regions of the axon back to the soma (Figure 1.2B). In contrast to the extended kinesin family, there is only one form of cytoplasmic dynein that is required for retrograde transport. Dynein is a 1.4 MDa motor complex comprised of: two heavy chains, two intermediate chains, two light intermediate chains, and three dynein light chain families (Reck-Peterson et al., 2018). Dynein associates with dynactin, another large (1.1MDa) multiprotein complex, and an activating adaptor protein to establish a motor complex that can transport cargo long distances (Gill et al., 1991, Mckenney et al., 2014). Eight adaptor proteins have been identified for dynein (Reck-Peterson et al., 2018), with many more putative adaptor proteins suggested (Merdes et al., 2000, Fumoto et al., 2006, Caviston et al., 2007, Spronsen et al., 2013).

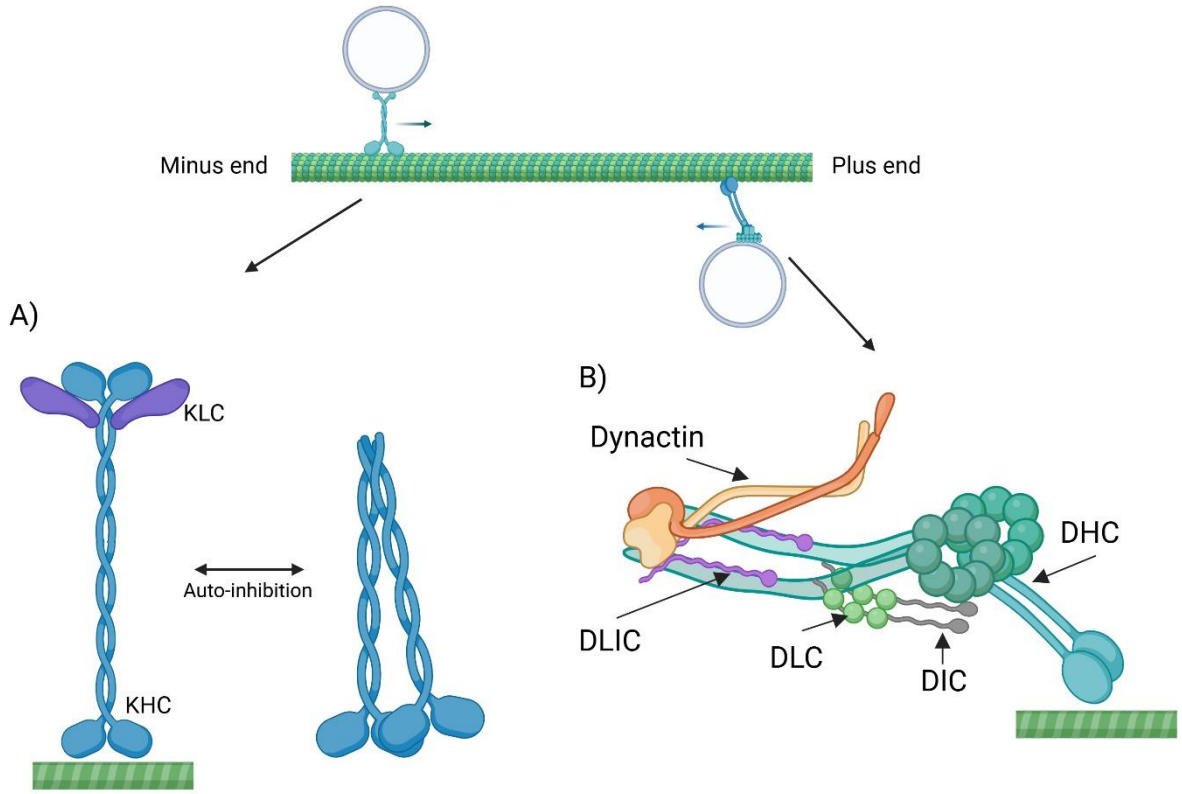


Figure 1.2: Dynein and kinesin govern retrograde and anterograde axonal transport. *(A) Kinesin heavy chains (KHC) form a dimer that interacts with microtubules and hydrolyses ATP at the N-terminal motor domains. Kinesin light chains (KLC) associate with the C-terminal tails of KHCs, which interacts with cargo adaptor proteins. Kinesin autoinhibits via a conformational change in the stalk. (B) Cytoplasmic dynein interacts with microtubules via dynein heavy chain (DHC). The dynein complex is formed of DHC, dynein intermediate chains (DIC), dynein light intermediate chains (DLIC), and dynein light chains (DLC). In order for dynein for motile, dynactin must associate with the complex to facilitate ATP hydrolysis and bind cargos. Schematic made using Biorender.com*

The spatial and temporal control of axonal transport is governed beyond microtubules and cargo adaptor protein by additional factors like post-translational modifications of motor proteins (Fan and Lai, 2022, Kubo and Bui, 2023) and intracellular calcium levels (Wang and Schwarz, 2009).

Axonal transport in neurodegeneration

Disturbed axonal transport has become a hallmark for many neurodegenerative diseases, with perturbations being noted in multiple in vitro and in vivo models of Alzheimer's disease (AD), Parkinson's disease (PD), Huntington's Disease (HD), Amyotrophic Lateral Sclerosis (ALS), and Charcot-Marie-Tooth disease (CMT). For example, mutations in kinesins and dynein have been identified in ALS, CMT Type 2O, and hereditary spastic paraplegia (HSP) (Reid et al., 2002, Weedon et al., 2011, Nicolas et al., 2018, Baron et al., 2022, Mentis et al., 2022). Mutations in cargo adaptor proteins that impair axonal transport have been identified in HD, lower motor

neuron disease, and Perry syndrome (Puls et al., 2003, Caviston et al., 2007, Konno et al., 2017).

Alterations to microtubules via altered post-translational modifications, dynamics, and stability have also been noted in models of AD (Zhang et al., 2015), PD (Godena et al., 2014, Toba et al., 2017), HD (Dompierre et al., 2007), HSP (Lopes et al., 2020), CMT Type 2D (Tischfield et al., 2010, Hong et al., 2015), and ALS (Gal et al., 2013, Guo et al., 2017, Fumagalli et al., 2021). Specifically, reductions in α-tubulin acetylation have been identified in models of AD, PD, and CMT2A (Esteves et al., 2019, Picci et al., 2020). HDAC6 has been subject to pharmacological inhibition to increase α-tubulin acetylation which rescues the deficits in axonal transport seen in models of Rett syndrome (Xu et al., 2014), CMT2A (Picci et al., 2020), CMT2D (Mo et al., 2018), CMT2F (D'Ydewalle et al., 2011), and HD (Dompierre et al., 2007). HDAC6 has also been implicated in protein aggregate formation, and HDAC6 inhibitors are also being investigated for neurodegenerative disease that display aberrant aggregate formation such as AD (Li et al., 2021) and PD (Francelle et al., 2020, Li et al., 2022b).Whether perturbed axonal transport is a downstream byproduct of axonal degeneration and synaptic dysfunction or an initiating event in disease is yet to determined and the answer may vary between diseases. One neurodegenerative disease for which this is being investigated is the peripheral neuropathy Charcot-Marie-Tooth disease.

Charcot-Marie-Tooth disease

Charcot-Marie-Tooth disease (CMT) is the most common inherited peripheral neuropathy in the world, affecting every ~1 in 2500 people (Martyn and Hughes, 1997). CMT was named after Dr Jean-Marie Charcot, Dr Pierre Marie, and Dr Henry Tooth, who described the disease in 1866 (Charcot and Marie, 1886, Tooth, 1886). Both publications described a “progressive muscular atrophy” in patients presenting with pes cavus (abnormally high foot arches), hammer toes, impaired gait, and atrophy of the leg muscles. Here, Tooth was the first to correctly hypothesise that these patients were suffering from peripheral nerve dysfunction (Tooth, 1886).

Even with these two independent descriptions of this peripheral neuropathy, much confusion remained amongst clinicians due to the significant overlap of symptoms between multiple syndromes. Dejerine and Sottas described a hypertrophic

neuropathy that presented more severely than the patients described by Charcot, Marie, and Tooth, naming it Dejerine Sottas disease (DSS) in 1893 (Dejerine and Sottas, 1893). Roussy and Levy described Roussy Levy syndrome (RLS) as an early onset syndrome with ataxia, tremors, and lower limb wastage (Roussy and Levy, 1923). Dawidenkow was the first to attempt a formal classification of inherited neuropathies, but today's classification of CMT is based on the work of Dyck and Lambert who incorporated mode of inheritance and electrophysiology into their analysis of CMT (Dawidenkow, 1927, Dyck, 1968, Dyck and Lambert, 1968).

Today, CMT and the clinically-related hereditary motor and sensory neuropathies (HMSN) (including DSS and RSL) are grouped together into six subtypes: hereditary motor neuropathy, hereditary sensory neuropathy, CMT Type 1, intermediate CMT, CMT Type 2, and X-linked CMT (Figure 1.3A). This categorisation is based on causal mutation, inheritance pattern, electrophysiological symptoms, and clinical presentation. CMT naming remains a debated topic thanks to advances in DNA sequencing technology, with new naming systems being suggested (Magy et al., 2018) but not widely adopted.

There are two main subtypes of CMT: CMT Type 1 and CMT Type 2. CMT Type 1 is referred to as demyelinating CMT, characterised by the loss of the myelin sheath around peripheral neurons resulting in a decreased nerve conductance velocity along the length of the axon (Figure 1.3B). CMT1 is the most common form of CMT, accounting for ~60% of all CMT patients (Verhoeven, 2006). CMT Type 2 is referred to as axonal CMT and is responsible for ~18% of all CMT cases (Verhoeven, 2006). Here, peripheral nerves maintain their conductance velocity, but compound muscle action potential amplitudes are reduced (Figure 1B) (Bergamin et al., 2014). Subtypes are further characterised by their causal genetic mutation and mode of inheritance.

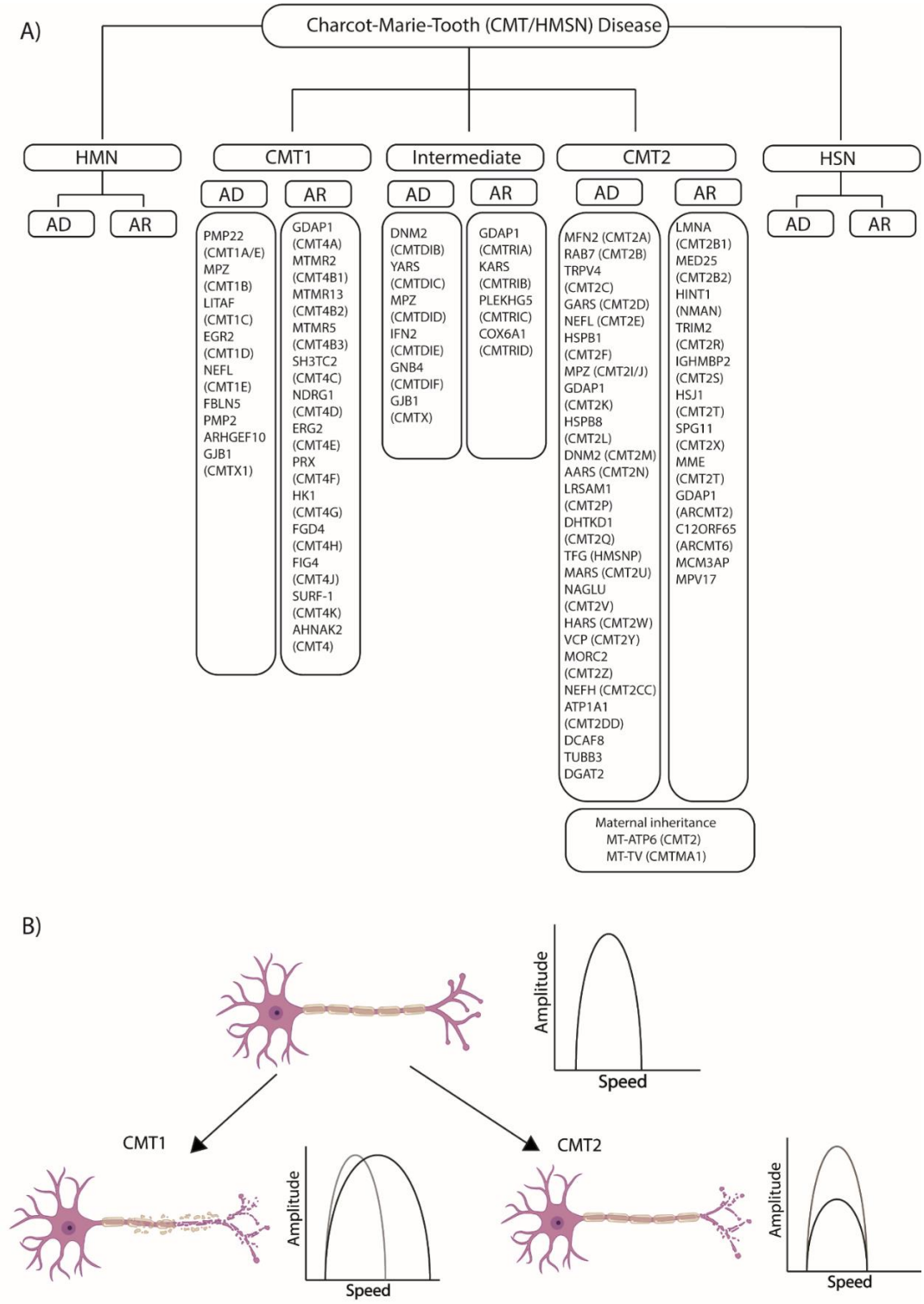


Figure 1.3: Subtypes of Charcot-Marie-Tooth disease. *(A) Charcot-Marie-Tooth disease (CMT) and Hereditary Motor and Sensory neuropathies (HMSN) are group together due to overlapping symptoms. Hereditary Motor neuropathies (HMN) are categorised into autosomal dominant (AD) and autosomal recessive (AR) HMN. Hereditary Sensory neuropathies (HSN) are also categorised into AD and AR. CMT is split into three groups: Type 1 (CMT1), intermediate, and type 2 (CMT2). Each group has AD and AR forms. X-linked forms of CMT from maternal inheritance are often grouped with CMT2 due to clinical presentations. Figure adjusted from (Candayan et al., 2022). Boxes show identified causal mutations and the corresponding CMT subtype. (B) Action potentials in CMT1 have a reduced conductance due to a loss of myelin and saltatory conductance. Action potentials in CMT2 tend to maintain conductance speeds but have a reduced amplitude due to axonal degeneration. Schematic made using Biorender.com.*

Diagnosis of CMT requires electrophysiological tests, genetic tests, radiography, family history, and an evaluation of other bodily systems that can be impacted by CMT. Once diagnosed, treatment for CMT is limited and mainly symptomatic with no approved pharmacological treatments. Physiotherapy and occupational therapy are recommended to allow patients who are experiencing muscle wastage to carry out daily activities. Additional mobility aids may be required depending on the severity of symptoms. In the most severe cases, surgical intervention may be needed to correct significant deformities (NHS England, 2022). At present, the only pharmacological treatments available to CMT patients are targeted at reducing pain and include non-steroidal anti-inflammatory drugs for joint and muscle pain or tricyclic antidepressants for long-term neuropathic pain.

Clinical trials relating to CMT and HMSN have predominantly focused on procedural interventions, but registered clinical trials testing pharmacological interventions have risen steadily over the past 20 years with some promising candidates for approval (Nair et al., 2023). PXT3003 is a combination therapy containing baclofen (GABA derivative), naltrexone (opioid receptor antagonist), and sorbitol (non-stimulant laxative) (Chumakov et al., 2014). All three components are approved for other indication and in combination showed positive results in a Phase III trial for patients with mild to moderate CMT1A (Attarian et al., 2021). NMD Pharma have developed NMD670 which entered Phase IIa trials for CMT1 and CMT2 patients in September 2024 (NCT06482437). NMD670 aims to reduce skeletal muscle weakness and is also in Phase II trials for Myasthenia Gravis (Skov et al., 2024). NMD670 was awarded Orphan Drug Designation by the FDA for CMT1 and CMT2 in January 2025. Govorestat is a selective Aldose Reductase inhibitor that was developed for the treatment of Galactosemia and CMT-SORD (CMT caused by mutations in sorbitol dehydrogenase). Govorestat received Orphan Medicinal Product Designation from the European Medicines Agency (EMA) and Orphan Drug designation from the Food and Drug Administration (FDA) in 2023. However, the FDA rejected the company’s (Applied Therapeutics) application for a New Drug Application, and Govorestat’s application for marketing authorisation was withdrawn from the EMA in late 2024. At present, a different aldose reductase inhibitor Epalrestat is in Phase II trials for CMT-SORD (NCT05777226).

Cell and gene therapy is considered to be the next frontier in human medicine, and Schwann cells have been the focus of this endeavour for CMT1A, 1B, and X-linked CMT (Wei et al., 2024). A Phase I trial for intramuscular injections of CLZ-2002 for CMT1 patients has recently been completed (NCT05947578). CLZ-2002 contains allogeneic mesenchymal stem cells that were able to remyelinate the sciatic nerve of a CMT1A mouse model (Park et al., 2018). Pharmacological developments have mainly focused on CMT1 and CMT-SORD, but endeavours to treat CMT2 are in motion. In February 2025, a Phase I clinical trial for a TRPV4 inhibitor for the treatment of CMT2C commenced. Ultimately, no pharmacological interventions for CMT have been approved despite advances in the understanding of the underlying genetic causes and disease pathologies of CMT.

Charcot-Marie-Tooth disease Type 2A

CMT Type 2A (CMT2A) is caused by mutations in Mitofusin 2 (MFN2), a GTPase primarily located on the outer mitochondrial membrane (Züchner et al., 2004). Initially, the genetic cause of CMT2A was thought to be mutations in KIF1B as a Japanese family diagnosed with CMT2 all carried KIF1B mutations (Zhao et al., 2001). Unable to identify KIF1B mutations in other CMT2 patients with similar symptoms, researchers continued to search for the genetic cause of CMT2A. It was in this continued search where MFN2 mutations were identified, as MFN2 and KIF1B both reside on Chromosome 1, 1p36.22 (Züchner et al., 2004). For a while, both KIF1B-CMT and MFN2-CMT were referred to as CMT2A in published literature. To reduce confusion, KIF1B mutations were then designated CMT2A1 and MFN2 mutations were designated CMT2A2. The KIF1B association to CMT2A was officially retracted in 2020 (Clinical Genome Resource, 2020) and in 2025, CMT2A1/CMT2A2/CMT2A2A all refer to CMT2A caused by autosomal dominant mutations in MFN2 (Züchner et al., 2004). Autosomal recessive mutations in MFN2 are sometimes referred to as CMT2A2B. For clarity, in this thesis, CMT2A refers to *MFN2* mutations.

CMT2A has an estimated prevalence of 1 in 60,000 and is the most common form of axonal CMT, accounting for 30 – 40% of axonal CMT and ~4% of all CMT cases. At present, over 150 mutations have been identified across the entirety of *MFN2* in patients displaying CMT2A symptoms (Appendix 1; adapted from Butler, 2021). The

majority of mutations are point mutations, but insertions (Engelfried et al., 2006, Park et al., 2012, Kotruchow et al., 2013, Bergamin et al., 2014), deletions (Verhoeven, 2006, Lin et al., 2011, Mccorquodale et al., 2011, Bergamin et al., 2014, Antoniadi et al., 2015), nonsense mutations (Verhoeven, 2006, Züchner et al., 2006, Brožková et al., 2013), compound mutations (Verhoeven, 2006, Vallat et al., 2008, Park et al., 2012), and splicing mutations (Brockmann et al., 2008, Chung et al., 2010, Kotruchow et al., 2013) have been identified in patients. An autosomal dominant inheritance pattern is the most common mode of inheritance but recessive mutations in *MFN2* have also been noted in patients (Hikiami et al., 2017, Masingue et al., 2017, Iapadre et al., 2018). Mutations appear to cluster in the GTPase domain of MFN2 (Brockmann et al., 2008, Choi et al., 2015, Ando et al., 2017) but have also been identified in the HR1 domain (You et al., 2018, Sharma et al., 2022), HR2 domain (Ando et al., 2017, Lin et al., 2020), and transmembrane domain (Hikiami et al., 2017). This range of mutations paired with a spectrum of clinical presentations adds a layer of complexity for the molecular determination of CMT2A.

CMT2A is associated with having a more clinically severe phenotype that is motor dominant compared to other CMT subtypes. Distal limb weakness and wastage is the most common symptom in patients as a consequence of axonal degeneration (Verhoeven, 2006, Pipis et al., 2020). CMT2A is not typically associated with a reduced life expectancy however this has not been extensively explored; only one study has investigated mortality rates in CMT patients in Denmark and whilst a higher standardised mortality rate was found in CMT patients, CMT subtype was not factored in to this analysis (Vaeth et al., 2017).

CMT2A is also associated with an earlier disease onset, typically within the first and second decade of life that is often referred to as early-onset severe CMT2A. This typically presents as difficulties with balance or walking first, progressing to a variety of classical peripheral neuropathy symptoms which can include weakness and sensory loss of the limb extremities, decreased deep tendon reflexes, dexterity difficulties, tremors, and chronic pain. Foot deformities are particularly common in CMT2A patients, with most requiring orthoses, walking aids, or wheelchair use. The symptoms of severe CMT2A can affect more bodily functions compared to other subtypes, with clinicians noting optic atrophy (Verhoeven, 2006, Züchner et al., 2006), vocal cord impairment (Chung et al., 2010, Kanemaru et al., 2019), white

matter lesions (Chung et al., 2010, Lee et al., 2017), upper motor neuron involvement (Chung, 2006, Ajroud-Driss et al., 2009, Luigetti et al., 2016), and learning difficulties in some patients (Brockmann et al., 2008, Tufano et al., 2015, Tomaselli et al., 2018). A cohort of CMT2A patients present with late-onset mild CMT2A, which displays a later age of onset, typically in the fourth or fifth decade of lif, and slower disease progression. The lines between early- and late-onset CMT2A are blurred by shared mutations in MFN2, shared symptoms and symptom severity, further highlighting the heterogeneity of CMT2A (Kotruchow et al., 2015, Pipis et al., 2020).

No CMT2A-specific circulating biomarkers have been identified for the purpose of diagnosis or monitoring disease progression but some less specific CMT1 and CMT2 biomarkers have. Neurofilament light (NfL) plasma concentrations have been proposed as a CMT biomarker, with elevated levels identified in CMT2A patients alongside other CMT1 and CMT2 subtypes (Sandelius et al., 2018, Rossor et al., 2022). GDF15 has also been identified as raised in a small cohort CMT1 and CMT2 patients, although it is yet to be determined if all subtypes, including CMT2A, display elevated GDF15 levels in patient sera (Jennings et al., 2022).

Very few histopathological investigations have been conducted on CMT2 and more specifically CMT2A patients. Consistent with peripheral nerve degeneration, sural nerve biopsies of patients with confirmed MFN2 mutations display a reduction in myelinated fibers and myelinated fiber diameter (Wu et al., 2021). Furthermore, CMT2A sural tissue contain onion bulbs - concentrically layered Schwann-cell processes around nerve fibers - and regeneration clusters of myelinated fibers – disorganised groups of newly formed, small-diameter nerve fibers (Benedetti et al., 2010, Wu et al., 2021, Abati et al., 2022).

Mitofusin 2

Mitofusin 2 (MFN2) is a ubiquitously dynamin-related GTPase of 757 amino acids located on the outer mitochondrial membrane. MFN2 consists of a large N-terminal GTPase domain, two coiled-coil heptad-repeat domains (HR1 and HR2), a proline-rich domain (PR), and a transmembrane domain (TMD) (Figure 1.4). MFN2 is considered to have two splice variants, Isoform 1 and Isoform 2. Isoform 1 produces the 757 amino acid protein and is considered the canonical isoform. Isoform 2 is

predicted to generate a 436 amino acid protein via alternative splicing. MFN2's paralogue, Mitofusin 1 (MFN1), shares 80% homology with MFN2 and contains the same domains but lacks the proline-rich domain. Full crystal structures of MFN1 have been elucidated (Qi et al., 2016, Cao et al., 2017, Yan et al., 2018), but only the crystal structure of truncated MFN2 has been identified (Li et al., 2019). Predictions of MFN2 crystal structures in opened and closed positions have been modelled with confidence thanks to the high homology between MFN1 and MFN2 (Figure 1.4C) (Samanas et al., 2020). MFN2 is considered to be active in its open conformation, with HR2 domains exposed and able to dimerise with mitofusins on opposing mitochondria (Franco et al., 2016).

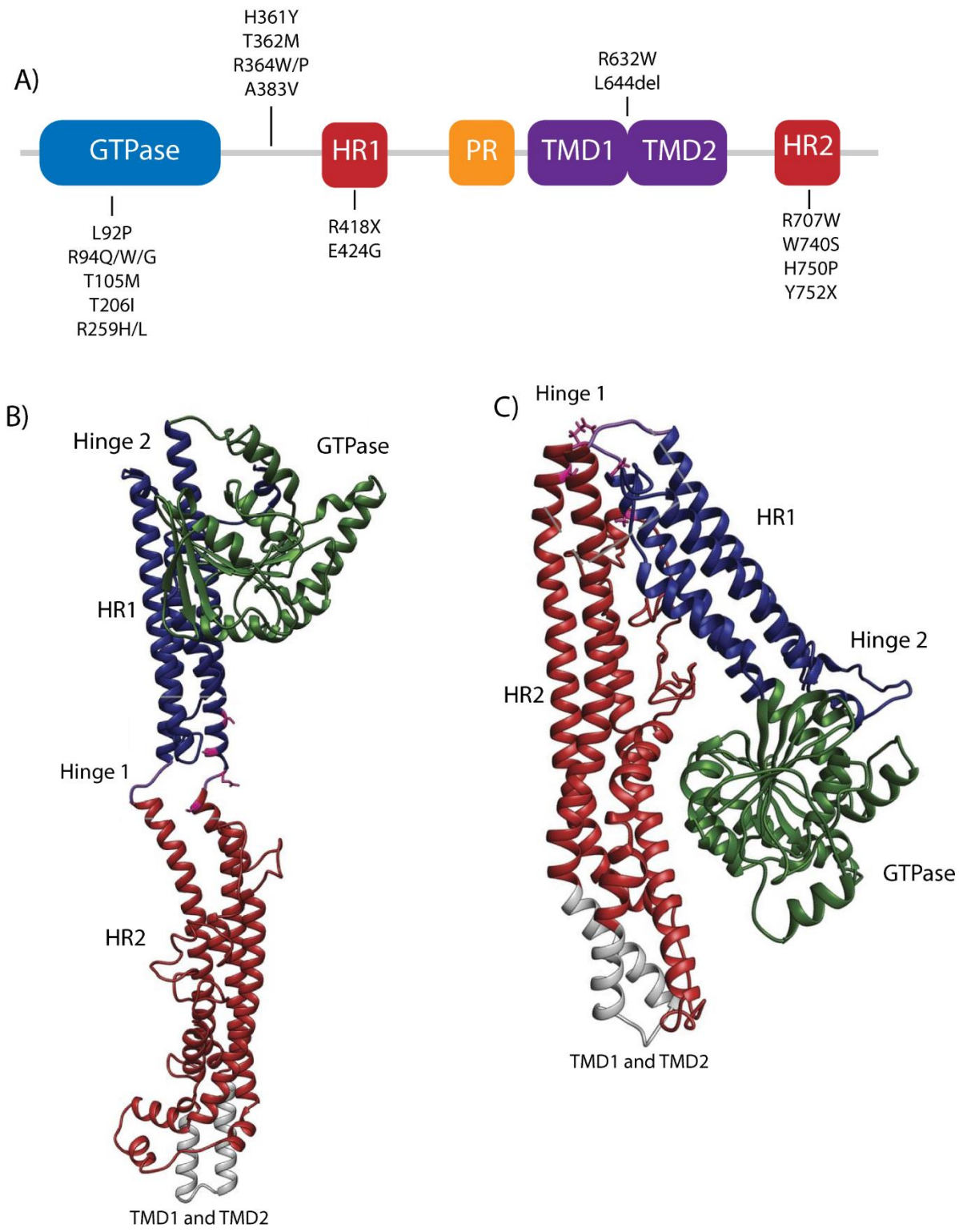


Figure 1.4: Structure of Mitofusin-2. (A) *Schematic of MFN2 gene showing the GTPase domain, coiled-coil heptad repeats 1 and 2 (HR1 and HR2 respectively), a proline rich domain (PR), and two transmembrane domains (TMD1 and TMD2). Common MFN2 mutations associated with a more severe motor phenotype in CMT2A are shown in their respective domains.* ***(B)*** *Predicted crystal structure of MFN2 in the open conformation, adapted from Samanas et al., 2020.* ***(C)*** *Predicted crystal structure of MFN2 in the closed conformation, adapted from Samanas et al., 2020.*

MFN2 is lowly expressed in every cell in the human body, with high RNA expression in the tongue, heart and skeletal muscle, and high protein expression in the central nervous system, heart, and gastrointestinal tract (Human Protein Atlas, 2025).

The canonical role of the mitofusins is to drive the fusion of the outer mitochondrial membrane during mitochondrial fusion. MFN1 and MFN2 can form hetero- and homodimers between opposing mitochondria via HR2 interactions, and through GTP hydrolysis pull the negatively-charged outer mitochondrial membrane together (Gao and Hu, 2021). MFN2 GTPase activity is in part regulated by Smad2 and Ras and Rab Interactor 1 (RIN1) which acts as a guanine nucleotide exchange factor (GEF) (Kumar et al., 2016). The inner mitochondrial membrane is fused by another dynamin-related GTPase named optic atrophy 1 (OPA1), named so as mutation in OPA1 result in Optic atrophy Type 1 (Eiberg et al., 1994, Alavi and Fuhrmann, 2013). The fusion of mitochondria, as well as its reverse action, mitochondrial fission, are constant processes that maintain a dynamic mitochondrial network. Fusion is necessary for mitochondrial communication and exchange of mitochondrial DNA (Chen et al., 2007) whereas fission is required for redistributing mitochondria and isolating defective mitochondria in preparation for degradation (Twig et al., 2008). Fission is mediated by dynamin-related protein 1 (DRP1), which forms a contractile ring around mitochondria and results in symmetric or asymmetric cleavage of a mitochondria (Hinge et al., 2020, Liu et al., 2020).

MFN1, MFN2, OPA1, and DRP1 knockouts are embryonically lethal in mice (Chen et al., 2003, Davies et al., 2007, Ishihara et al., 2009). Loss of MFN2 in cultured cells results in a fragmented mitochondrial network with reduced respiratory capacity (Chen et al., 2005). Furthermore, reductions in either fission or fusion within cells results in a perturbation of ATP production and incorrect mitochondrial distribution, which can have lethal consequences for cells (Detmer and Chan, 2007).

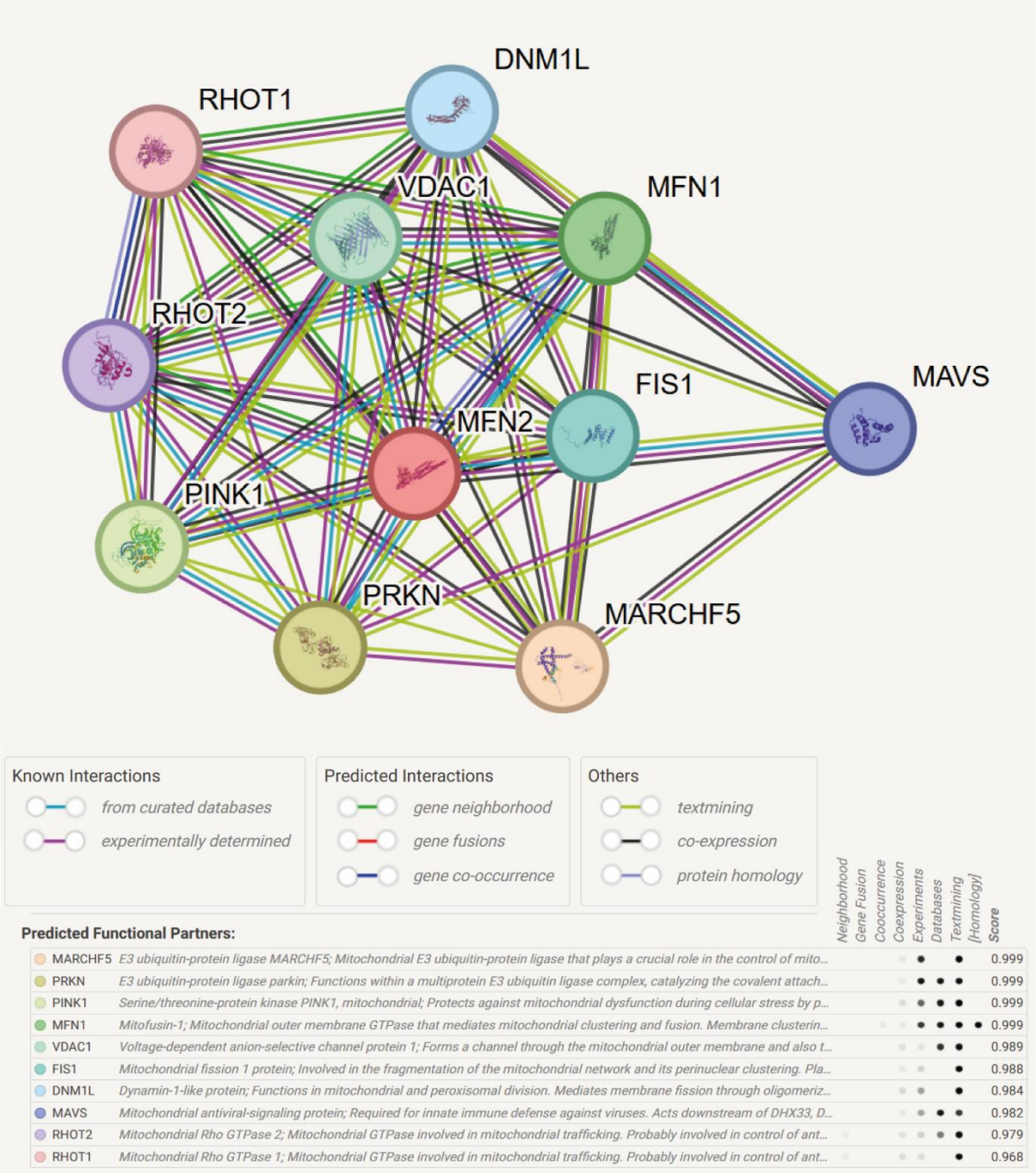


Figure 1.5: STRING analysis of MFN2. *STRING analysis of MFN2 shows predicted and validated protein interactors. Shell proteins are connected to MFN2 with coloured lines corresponding to the origin of association. Predicted functional protein interactors are ranked based on the cumulative score of all available evidence to the software.*

Beyond mitochondrial fusion, MFN2 has been implicated in a variety of intracellular pathways as evidenced by multiple *in vitro* and *in vivo* experiments, and predictive STRING (string-db.org) analysis (Figure 1.5). . MFN2 is necessary for PINK1/Parkin-dependent mitophagy, the process by which mitochondria are selectively degraded (Gegg et al., 2010); MFN2 is subjected to phosphorylation by PINK1 and

ubiquitination by Parkin to tag mitochondria for removal (Chen and Dorn, 2013, Li et al., 2022a).

MFN2 has been tied to the unfolded protein response (UPR) (Hetz et al., 2020) with a loss of MFN2 upregulating ER stress (Ngoh et al., 2012, Sebastián et al., 2012). This was credited to MFN2 interacting with, and regulating the activity of PERK, a kinase effector of one of the branches of the UPR (Muñoz et al., 2013).

MFN2 also plays a role in lipid metabolism. MFN2 has been shown to interact with perilipin in the outer shell of lipid droplets, promoting mitochondria-lipid droplet interactions and regulating lipid metabolism (Boutant et al., 2017, Cai et al., 2024). MFN2 is reported to mediate other mitochondria-organelle contacts including peroxisome-mitochondrial contacts, known as PerMit contacts (Huo et al., 2022). These contacts facilitate citrate shuttling from the peroxisomes to mitochondria for the tricarboxylic acid cycle, helping to maintain mitochondrial fusion and mitochondrial membrane potential (Alsayyah et al., 2024). Furthermore, MFN2 has been implicated in mitochondria-ER contact sites (MERCS) (Voeltz et al., 2024) but the exact nature of MFN2's role in MERCS has been controversial but appears to be context-specific. Some groups have proposed that MFN2 acts as a tether (De Brito and Scorrano, 2008, Chen et al., 2012, Casellas-Díaz et al., 2021) and others have presented evidence that MFN2 is a regulator (Cosson et al., 2012, Filadi et al., 2015). More recently, Naón et al identified two short splice variants of MFN2 that reside in the ER and facilitate MERCS (Naón et al., 2023). MERCS are responsible for calcium exchange between the ER and mitochondria, allowing mitochondria to buffer intracellular calcium concentrations (Lim et al., 2021). MFN2 has been stipulated to regulate calcium handling beyond direct involvement in MERCS, purportedly through an interaction with NCLX (Samanta et al., 2018, Kolitsida et al., 2024).

In addition, MFN2 has been linked to axonal transport of mitochondria through interactions with the adaptor protein Miro and the *Drosophila* orthologue of TRAK1 – Milton (Misko et al., 2010).

Considering the number of roles MFN2 plays in cell physiology, very little is known about how different MFN2 domains contribute to its different functions and consequently how disease-causing mutations affect the function of different

domains. Li et al. recently began to characterise the effect of CMT2A-causing mutations on GTP turnover by truncated MFN2 (Li et al., 2019). Whilst most mutations were not predicted to disrupt protein folding, several mutations were able to increase MFN2 GTPase activity despite a lack of proximity to the catalytic site (Li et al., 2019). Whether the functions of other domains are affected in this model is yet to be elucidated.The above evidence demonstrates the pivotal roles that mitochondria and MFN2 play in a variety of cell types, but raises the question: why are peripheral nerves predominantly affected by mutations in MFN2, when other tissues required MFN2 to function? The role of MFN2 may be context-specific, with the GTPase being implicated differentially in different tissues.

CMT2A modelling

As previously mentioned, there are currently no approved treatments for CMT2A and with MFN2 having such a varied role within the cell, elucidating the exact mechanism by which mutated MFN2 generates CMT2A has not yet been achieved. Consequently, there is a need for *in vitro* and *in vivo* models that can recapitulate pathology as accurately as possible to further understanding of CMT2A disease mechanisms and provide a platform for pharmacological testing.

Some of the first modelling of CMT2A was conducted using *in vivo* models, with the majority focussing on the most common mutations seen in the clinic: R94Q, T105M, and R364W (Table 1). All *in vivo* models display an impaired motor phenotype in the presence of mutated MFN2. Mouse models of CMT2A are the most numerous within the literature, most likely due to the high homology between murine and human MFN2 sequence and structure. As previously mentioned, complete loss of MFN2 is embryonically lethal due to its role in placental development (Chen et al., 2003) and furthermore, conditional MFN2 knockouts that avoid cells forming the placenta allow for live births of severely impaired pups that do not survive past P17 (Chen et al., 2007). This problem led the field to develop mouse models that conditionally overexpress MFN2 containing CMT2A-associated mutations in all mature neurons (known as the MitoCharc1 and MitoCharc2 mice) (Cartoni et al., 2010, Bernard-Marissal et al., 2019), peripheral motor neurons (Detmer et al., 2007), early neural tissues (Zhou et al., 2019), and all neurons with some non-neuronal tissue (Bannerman et al., 2016).

These classic CMT2A mouse models alongside newer models with rarer MFN2 mutations have been used to demonstrate mitochondrial abnormalities including changes in morphology (Zhang et al., 2024) and axonal distribution (Cartoni et al., 2010, Stavropoulos et al., 2021). Mouse models of CMT2A have also proven useful for pharmacological testing with the motor deficits of T105M knock-in mice being rescued by the use of mitofusin activators (Franco et al., 2020, Weigele et al., 2024).

Table 1: Overview of in vivo models of CMT2A. *In vivo models of CMT2A include zebrafish, drosophila, rat, and mouse models which all display a motor deficit to some extent, mimicking some of the symptoms seen in patients. Different mutations in MFN2 have been used in different models, and each model sees impacted mitochondria to some degree*

Organism	MFN2 mutation	Motor deficit	Mitochondria	Paper
Zebrafish	L285X, L76P, R94Q	Yes	Axonal transport deficit	(Chapman et al., 2013, Bergamin et al., 2016)
Drosophila	L76P, R94Q, T105M, R364W	Yes	Clustering, reduced fusion	(El Fissi et al., 2018)
Rat	H361Y, R364W	Yes	Reduced number at synapses, mitochondrial swelling	(De Gioia et al., 2020, Sato-Yamada et al., 2022)
Mouse	R94Q	Yes	Clustering, fragmentation, increased number in distal sciatic nerve	(Cartoni et al., 2010, Zhou et al., 2019, Shen et al., 2021, Rizzo et al., 2023, Shahin et al., 2023)
Mouse	T105M	Yes	Reduced number in peripheral axons	(Detmer et al., 2007, Bannerman et al., 2016, Franco et al., 2020, Franco et al., 2022, Zhang et al., 2022a, Weigele et al., 2024)
Mouse	H165R, G176S, K357T, R364W, R400Q, L643P	Yes	Clustering in sciatic nerve	(Stavropoulos et al., 2021, Franco et al., 2023, Hines et al., 2023, Zhang et al., 2024)

.

Dorsal root ganglion cells (DRGs) can be isolated from mice as an *in vitro* neuronal model to further explore mitochondrial morphology and transport. Primary DRGs expressing human MFN2 containing a CMT2A-associated mutation displayed a reduction in mitochondrial motility in the axon compared to DRGs expressing wild-type human MFN2 (Baloh et al., 2007, Franco et al., 2022). Additionally, this reduced motility led to axonal degeneration due to correct distribution of mitochondria in the axon (Misko et al., 2012).

Whilst *in vivo* mouse models can offer an integrated physiology, they are somewhat hindered by the potential differences in the role of MFN2 between rodents and humans. Homozygous mutations in MFN2 are required to generate the severe progressive motor and sensory phenotype associated with CMT2A in rodents, whereas the majority of CMT2A-causing mutations in humans are heterozygous. Furthermore, most of the rodent models overexpress an MFN2 transgene, either ubiquitously or solely within the CNS, which alters the levels of MFN2 beyond what is physiological.

To complement *in vivo* models, the focus on human modelling of CMT2A has grown over the past twenty years. Immortalised cell lines isolated from human tumours have long been a popular *in vitro* model of human biology thanks to their fast growth rate and amenability to genetic manipulation. CMT2A modelling using immortalised cell lines may be useful for drug screening purposes as some phenotypic differences have been noted in cells containing CMT2A-associated mutations. U2OS cells overexpressing mutant MFN2 displayed altered mitochondrial morphology and an impairment of the respiratory chain (Yenkin et al., 2022). Similarly, HeLa cells exogenously expressing T206I-MFN2 had mitochondrial hyperfusion (Das et al., 2024).

The use of patient fibroblasts has also been a popular CMT2A model as these cells are easy to obtain from patients, culture long-term, and can capture the complex genetic landscape of patients (Loiseau et al., 2007, Amiott et al., 2008, Guillet et al., 2010). Loiseau et al. (2007) and Guillet et al. (2010) reported a reduction in oxidative phosphorylation efficiency that was compensated for by increased oxygen consumption resulting in a normal mitochondrial network. Amoitt et al. (2008)

showed that mitochondrial fusion and respiration was unaffected in the fibroblasts they studied. This lack of phenotype is probably due to the fact that fibroblasts are unable to recapitulate the specific vulnerability that sensory and motor neurons experience in CMT2A.

The key determinate of the selective vulnerability of peripheral neurons in CMT2A patients has not been elucidated. Absolute size of the neurons may be a factor in determining the selective vulnerability of motor and sensory neurons, with peripheral neurons being some of, if not the largest in the body (Stifani, 2014). This size renders the neurons particularly reliant on efficient axonal transport. To examine this hypothesis *in vitro*, fibroblasts can be reprogrammed into induced pluripotent stem cells (iPSCs) that can then be differentiated into motor and sensory neurons (Van Lent et al., 2024). Van Lent et al. showed that these cell types display a mitochondrial and lysosomal trafficking deficit in the presence of $MFN2^{R94Q/+}$ (Van Lent et al., 2021), and mitochondrial clustering associated with reduced movement was seen in iPSC-derived motor neurons containing $MFN2^{A383V/+}$ (Rizzo et al., 2016). Altered electrophysiological profiles of CMT2A motor neurons has also been reported (Saporta et al., 2015).

The discordant data reported across *in vivo* models and non-neuronal *in vitro* models of CMT2A highlight the need for context-specific models of disease like iPSC-derived peripheral neurons. In vitro stem cell modelling of CMT2A would further benefit from human embryonic stem cell models, which are yet to be seen in the literature.

Human Pluripotent stem cells

Human pluripotent stem cells (hPSCs) are a unique subset of human cells that can self-renew indefinitely *in vitro* whilst retaining the ability to differentiate into any cell type found within the human body. HPSC is an umbrella term and two of the most common cell types covered by this term are human embryonic stem cells (hESCs) (Thomson et al., 1998) (Figure 1.6A) and induced pluripotent stem cells (iPSCs) (Takahashi et al., 2007) (Figure 1.6B). HPSCs have been an increasingly useful tool within basic scientific research and regenerative medicine thanks to their inherent properties, allowing for a scalable and flexible source of biomaterials. Human disease modelling has benefited greatly from the use of hPSCs, as the widely available array of differentiation protocols paired with genetic editing tools has

allowed for the generation of disease-relevant human cell types with disease-causing mutations.

Embryonic stem cells were first derived from mice following the identification of cells that had developmental potential from mouse blastocysts (Evans and Kaufman, 1981, Martin, 1981). Using the same immunosurgery techniques, Thomson et al. derived the first hESCs by extracting the inner cell mass from human blastocysts (Thomson et al., 1998) (Figure 1.6A). These cells were cultured on mouse embryonic fibroblast (MEFs) to provide the necessary extracellular support and consequently the cells were able to be kept in an undifferentiated state for over four month continuously, as well as being able to give rise to the three germ layers (Thomson et al., 1998). Since this seminal discovery, hundreds of hESC lines have been derived with over 1000 hESC lines registered on hPSCreg (https://hpscreg.eu) thanks to advances in derivation methods (Vazin and Freed, 2010). HESC applications have been expanded with advances in culture methods, with the field moving away from MEF-based co-cultures and favouring feeder-free culturing that utilises extracellular matrices and medium containing chemically-derived growth factors. The transition to feeder-free cultures reduced the need for animal-derived products but moral ethical concerns still remain around the use of hESCs, particularly for clinical applications (Wert, 2003).

In 2006, Takahashi and Yamanaka introduced retroviral vectors containing Oct3/4, Klf4, c-Myc, and SOX2 into mouse embryonic fibroblast and successfully reprogrammed the adult cells into embryonic stem cells, creating induced pluripotent stem cells (iPSCs) (Takahashi and Yamanaka, 2006). This finding was then replicated in human cells, generating the first human iPSCs (hiPSCs) (Takahashi et al., 2007). With the advent of this discovery, thousands of wild-type and patient-specific iPSC lines have been generated using a variety of viral vector approaches, with over 1400 hiPSC lines registered with WiCell (wicell.org) (Cerneckis et al., 2024). HiPSCs are now routinely used for disease modelling, drug discovery, and regenerative medicine (Wu and Hochedlinger, 2011, Jin et al., 2023).

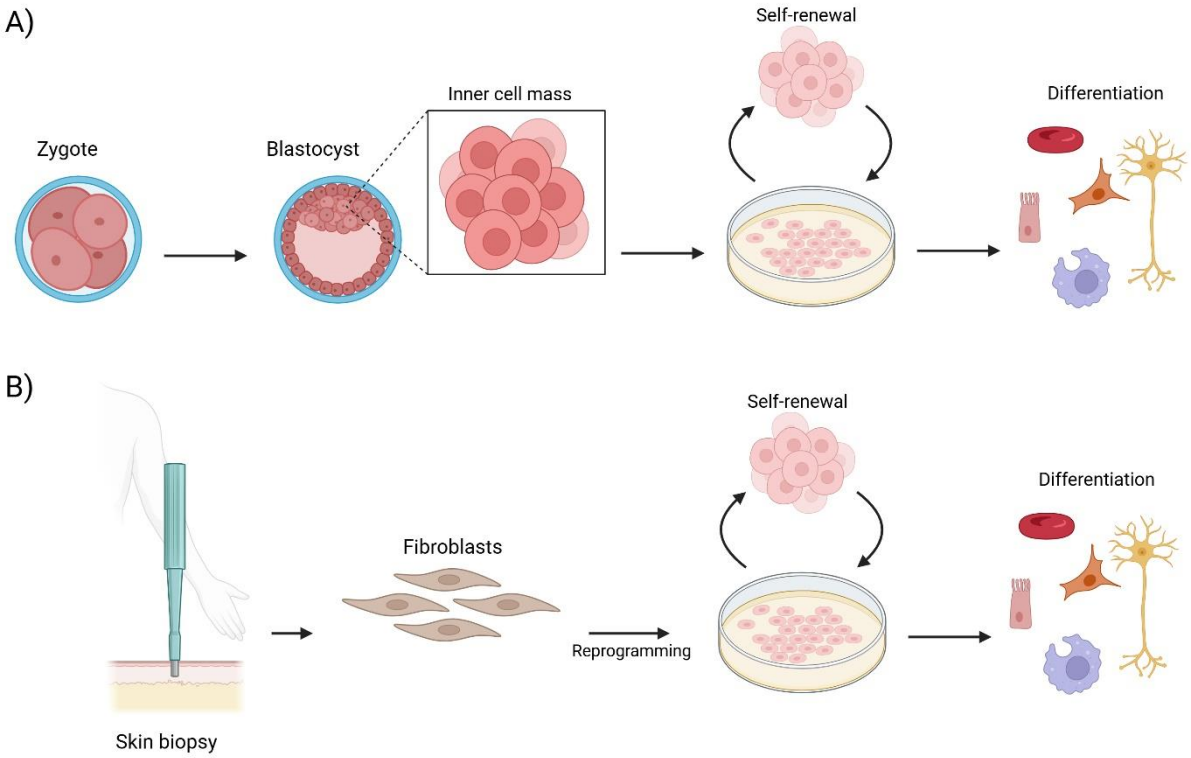


Figure 1.6: Derivation of hPSCs. *(A) A fertilised zygote begins to divide and developments into the blastocyst. The inner cell mass is extracted and cultured to give rise to hESCs. HESCs can be cultured as stem cells indefinitely or differentiated into other human cell types. (B) Skin punch biopsies are taken from patients or healthy controls and fibroblasts are cultured from the biopsy. Somatic cells, such as fibroblasts, are reprogrammed into iPSCs which can be cultured as stem cells indefinitely or differentiated into other human cell types. Schematic made using Biorender.com.*

HESCs and hiPSCs are considered similar populations of cells, thanks to their ability to self-renew indefinitely and to differentiate into cell types from the three germ layers. HESCs and hiPSCs also share comparable expression of pluripotency-association markers like SSEA3 and NANOG (Andrews and Gokhale, 2024), morphology, and minimal variation in global chromatin structure (Guenther et al., 2010). However, some key differences have been identified between ESCs and iPSCs. These include greater variability in differentiation efficiency (Hu et al., 2010, Narsinh et al., 2011), and the ability of iPSCs to retain an epigenetic memory from the cell type of origin which translates to different gene expression profiles in hiPSCs depending on which cell type they were derived from (Ghosh et al., 2010, Kim et al., 2010, Scesa et al., 2021).

Thanks to the ability of hPSCs to differentiate into other cell types in the human body, a new world of human physiological modelling is available to researchers. With

hPSC technology, cell types that can't be biopsied from patients can be generated *in vitro* as well as early cell types of human development. This has proved revolutionary for the field of neuroscience, whereby the lack of translatability of classic *in vitro* models that utilise immortalised cell culture has hindered the development of efficacious treatments (Williams and Hong, 2011, Kumar et al., 2022). The rise of directed differentiation protocols that utilise small molecules to manipulate signalling pathways has given rise to a plethora of 2D and 3D protocols that can generate different populations of neurons belonging to the central and peripheral nervous system (Slanzi et al., 2020). With this increased specificity in *in vitro* models, neuron-specific pathways implicated in neurodegeneration, such as synapse dysfunction (Hu et al., 2018, Meijer et al., 2019) or axonal transport (Alami et al., 2014, Boecker et al., 2021) can be studied. Complex 3D models have evolved from these protocols including organoid co-culture and organs-on-a-chip; these models incorporate a complex microenvironment, cell-cell interactions, and exhibit an extended lifespan (Zhuang et al., 2018). These 3D models bridge the gap between the cost- and time-efficient 2D hPSC models and predictive but resource-intensive *ex vivo*/*in vivo* models (Whitehouse et al., 2023). Ultimately, all these hPSC-derived models of neurodegeneration are more capable of recapitulating pathogenesis compared to previously used models and thus will facilitate greater understanding of disease mechanisms and successful drug development.

Being able to generate neurons *in vitro* that closely recapitulate the *in vivo* template allows for research to be conducted in the most translatable context possible. This is particularly advantageous for the study of diseases that specifically target certain cell types, such as Charcot-Marie-Tooth disease, because there are clear differences in the biology between cell types that are influencing pathogenesis and this needs to be accounted for in order to detangle disease mechanisms and develop efficacious treatments.

A small number of CMT2A patient-derived fibroblasts and iPSCs already exist within the literature and commercial cell banks and these comprise of the R94Q, C217F, S249T, P251L, H361Y, R364W, and A383V mutations (Saporta et al., 2015, Rizzo et al., 2016, Xu et al., 2019, Van Lent et al., 2021, Giovenale et al., 2025). These patient fibroblasts can be reprogrammed into iPSCs as previously mentioned or directly differentiated into post-mitotic cell types. Whilst iPSC generation and consequent

differentiation into motor neurons has been employed into CMT2A modelling (Saporta et al., 2015, Rizzo et al., 2016, Van Lent et al., 2021), trans-differentiation of fibroblasts has not yet been attempted for CMT2A modelling. Directly induced neurons (iNs) via trans-differentiation of fibroblasts retain aged-related disease phenotype that aren't maintained when neurons are generated from iPSCs (Mertens et al., 2015, Tang et al., 2017). CMT2A can present as early- or late-onset with no correlation to causative mutation and at present no investigations have been made into the cellular and molecular differences between early- and late-onset CMT2A. The use of iNs alongside iPSC-derived neurons would provide an experimental platform to investigate the role of age and ageing in the development of CMT2A.

HESCs, like iNs, have not been utilised to model CMT2A. In order for hESCs to a useful *in vitro* model, a MFN2 mutation identified in patients needs to be introduced via gene editing. Over 150 MFN2 mutations have been identified in CMT2A patients (Appendix 1) and hESC editing provides a suitable platform to model multiple mutations in different MFN2 protein domains which patient fibroblast availability is not currently able to do. HESCs also boast a greater differentiation efficiency compared to iNs (Schaukowitch et al., 2023). At present, a hESC-based model of CMT2A is best posited to investigate the cellular and molecular consequences of multiple CMT2A-causing or -associated mutations in human neurons.

Thesis aims

The overarching aim of this thesis is to generate an *in vitro* human model of CMT2A and use this to investigate possible molecular mechanisms of CMT2A. This will be done using a physiologically relevant cell type as previous use of human cell types that are not affected in patients has yielded conflicting results (Saporta et al., 2015, Larrea et al., 2019). To this effect, human spinal motor neurons will be generated from hESCs after they have had a CMT2A-causing mutation introduced by CRISPR-Cas9 editing. Mitochondrial transport has been postulated to a key feature of CMT2A disease models (Misko et al., 2010, Mou et al., 2021, Van Lent et al., 2021) thus mitochondrial transport in wild-type and CMT2A hESC-derived motor neurons will be extensively characterised and compared to identify any impacts exerted by the CMT2A-causing mutation. If a mitochondrial trafficking deficit is found, then pharmacological inhibition will be tested in an attempt to rescue this phenotype.

Finally, work will look to link molecular function of MFN2 to axonal transport in CMT2A. To address this, the following experimental aims have been outlined:

1. Generation of a panel of hESCs for CMT2A modelling

In this first aim, hESCs will undergo CRSIPR-Cas9 editing to introduce a heterozygous CMT2A-causing mutation. These edited cells will be extensively characterised in the stem cell state to examine the impact of the CMT2A mutation on stem cells. These CMT2A hESCs will then be differentiated into limb-innervating spinal motor neurons and again, wild-type and CMT2A cells will be characterised and compared to identify any impacts of the CMT2A-causing mutation on differentiation.

2. Characterisation of mitochondrial trafficking in a CMT2A hESC model

Here, mitochondrial transport and morphology in human spinal motor neurons will be compared between wild-type and CMT2A cells, as preliminary data suggests that CMT2A motor neurons display a mitochondrial trafficking defect. Inhibition of HDAC6, which has proved effective in other CMT2A disease models, will be used to try and rescue any defects seen in CMT2A neurons.

3. Compare functions of wild-type and mutated MFN2 linked to axonal transport

Finally, different aspects of MFN2 function will be investigated to try and link axonal transport defects to CMT2A pathology. This will include post-translational modifications of the cytoskeleton, endoplasmic reticulum-mitochondrial contacts, and protein-protein interactions between MFN2 and motor protein adaptors.

Chapter 2 - Methods and materials:

2.1 hPSC culture

2.1.1 Cell Lines

Human embryonic stem cell lines in this work were used with approval from The University of Sheffield Stem Cell Steering Committee.

MasterSheff11, male human embryonic stem cell line derived at the University of Sheffield, Centre for Stem Cell Biology under GMP-like conditions as described in Thompson et al., 2020 (Thompson et al., 2020). In brief, MasterShef11 was derived by trophectoderm removal of the embryo by dissection laser and explanted whole onto Laminin-511 in Nutristem medium, with manual passaging every seven days at a ratio of 1:2. MasterShef11 was subjected to karyotyping by G-Banding and whole genome sequencing. Further detail on derivation and characterisation can be found on hPSCreg. hPSCreg name: UOSe015-A (https://hpscreg.eu/cell-line/UOSe015-A). RRID: CVCL_BW83

WT2, male human embryonic stem cell line generated by CRISPR-cas9 editing of MasterSheff11 by Larissa Butler at the University of Sheffield Centre for Stem Cell Biology (Butler, 2021). RRID: CVCL_E3QK

Het1, male human embryonic stem cell line generated by CRISPR-cas9 editing of MsterSheff11 to contain $MFN2^{R94Q/+}$ by Larissa Butler at the University of Sheffield Centre for Stem Cell Biology (Butler, 2021). RRID: CVCL_E3QL

HEK293T, a female immortalised cell line derived from embryonic kidney tissue, supplied by ATCC. RRID: CVCL_0045

Master cell banks were made for all human embryonic stem cell lines, and these banks were subjected to karyotyping via G-banding, SNP-array, and DNA fingerprinting. A personal working bank was prepared from the master bank for routine culture and all experiments shown in this body of work. Working banks were also subjected to karyotyping via G-banding, SNP-array, and DNA fingerprinting. Banks were prepared as detailed in 2.1.6. One parental line was chosen for this

body of work (MasterShef11) to control the genetic background and minimise any confounding effects from interindividual genetic or epigenetic heterogeneity.

A corrected MFN2$^{+/+}$ was not generated from one of the MFN2$^{R94Q/+}$ isogenic lines as the MFN2$^{+/+}$ isogenic line that had undergone CRSIPR-cas9 editing (WT2) was deemed a strong enough control line alongside the parental line (MasterShef11). Furthermore, risk of introducing genetic aberrations (from single-nucleotide polymorphisms to whole chromosome changes) increases with each culture bottleneck (electroporation to introduce CRISPR-cas9 components and multiple rounds of single-cell cloning).

2.1.2 Preparation of culture vessels

GelTrex (GTX) (Thermofisher, A1413202) was thawed at 4 °C and aliquoted for storage at -20 °C. Aliquots were thawed on ice and diluted 1:100 in ice-cold DMEM/F12 (Sigma, D6425). Tissue culture-treated flasks were coated with an appropriate volume of GTX (for example 2 ml for a T12.5 flask) and incubated at 37 °C for at least 1 hour. Coated vessels were either used the same day as coating or stored at 4 °C for future use. GTX was removed from culture vessels immediately before plating cells and kept for re-use. GTX was re-used no more than twice.

2.1.3 S8 Media recipe

Table 2.1: 50x S8 supplement components.

Component	Stock concentration	50x concentration	Final concentration	Supplier	Catalogue number
DMEM/F12		348 ml		Sigma	D6425
L-ascorbic acid	Powder	3200 mg	64 mg/L	Sigma	A8960
Sodium selenite	14 mg/ml	50 µl	14 µg/L	Sigma	S5261-10G

Insulin	10 mg/ml	97 ml	19.4 mg/L	Thermofisher	A113821J
$NaHCO_3$	powder	69.15 g	1383 mg/L	Sigma	S5761
Transferrin	10 mg/ml	53.5 ml	10.7 mg/L	Sigma	T0665-500
Glutamax	100x	500 ml	10 ml/L	Gibco	35050-038
bFGF	500 µg/ml	4 ml	40 µg/L	QKine	QK053
TGFβ	100 µg/ml	1 ml	2 µg/L	QKine	QK010

2.1.4 S8 Media preparation

Stable Essential 8 media (S8) was prepared in-house using a recipe adapted from (Chen et al., 2011). This recipe was adapted by increasing the $NaHCO_3$ concentration and replacing FGF-2 with heat stable recombinant human bFGF. Batches of 50x S8 supplement were prepared and stored as 10 mL aliquots at -20 °C. To prepare 1x S8 medium, one aliquot of 50x S8 supplement was defrosted overnight at 4 °C and added to 490 mL of DMEM/F12. This was then sterile filtered through a 0.22 µM filter bottle (VWR, 514-0332) and kept at 4 °C for up to two weeks.

2.1.5 Passaging hPSCs

hPSCs were passaged used ReLeSR (Stem Cell Technologies, 05873), an enzyme-free passaging reagent. To passage the cells, media was removed from the culture vessel and cells were then incubated with 100 µl/cm^2 ReLeSR at room temperature for 30 seconds. ReLeSR was aspirated and the cells were further incubated at room temperature for 3-6 minutes, depending on colony density. Following the addition of fresh S8 media, the culture vessel was tapped gently to ensure proper detachment of cells from the culture flask. The cell suspension was pipetted up and down gently using a 10 ml stripette to break colonies into small clumps. Colonies were seeded into new flasks at various split ratios from 1:6-1:16 depending on the desired confluence.

2.1.6 Freezing hPSCs

hPSC cultures of approximately 70% confluence were harvested using the method described in 2.1.4). At the final step, instead of resuspending in culture media cells were resuspended in Stem-Cell Banker (Amsbio, 11924). Aliquots of 0.5 ml cells in freezing media were pipetted into cryovials using a 10 ml stripette and placed into CoolCell (Corning, 432000) at -80 °C overnight. The following day, cryovials were transferred to liquid nitrogen for long term storage.

2.1.7 Thawing hPSCs

Cryovials were removed from liquid nitrogen and placed into a 37 °C water bath until thawed. The cells were transferred to a 15 ml falcon tube containing 4 ml DMEM-F12 pre-warmed to 37 °C. The cells were then centrifuged at 240 g for 4 minutes. The supernatant was aspirated, and the cell pellets were gently resuspended in S8 containing 10 μM of the Rho-associated, coiled-coil containing protein kinase (ROCK) inhibitor Y-27632 (Generon, 1596-1).

2.1.8 Single cell dissociation of hPSCs

To dissociate hPSC colonies into single cells, media was removed from the culture vessel and cells were incubated with 40 μl/cm^2 TrypLE (Gibco, 12604021) at 37 °C for 4 minutes. Flasks were then gently tapped to ensure proper detachment of the cells from the culture flask. TrypLE was diluted by the addition of fresh DMEM-F12 at a ratio of 9:1 into the culture vessel. Cells were transferred to an appropriate size falcon tube and centrifuged at 240 g for 4 minutes. Cell pellets were resuspended in the appropriate medium, counted using a haematocytometer and diluted to desired cell number per millilitre.

2.2 Immortalised cell culture

HEK293 cells were maintained in high glucose DMEM (VWR, 392-0414) supplemented with 10% FBS (Sigma, F7524). Cells were passaged using split ratios between 1:5 and 1:20 using 1x trypsin (Santa Cruz Biotechnology, sc-363354). Cells were not cultured past 25 passages. Cells were frozen down in DMEM/10% FBS media supplemented with 10% DMSO with > 3 million cells per cryovial.

2.3 Karyotyping and SNP array

Karyotyping was performed by a Genetic Technologist and checked by a Clinical Scientist at the Sheffield Diagnostic Genetics Service. Typically, 20-30 metaphases were analysed by G-banding per sample (as described in (Price et al., 2021). Genotyping was also carried out via a qPCR analysis (Baker et al., 2016, Laing et al., 2019). SNP arrays were also performed by the Sheffield Diagnostic Genetics Service.

2.4 Motor neuron differentiation of hPSCs

2.4.1 N2B27 media

Table 2.2: Components of N2B27 media

Component	Stock concentration	Final concentration	Supplier	Catalogue number
DMEM/F12	1x	1:1 with Neurobasal	Sigma	D9785
Neurobasal medium	1x	1:1 with DMEM/F12	Gibco	21103049
N2	100x	1x	Gibco	17502-001
B27	50x	1x	Gibco	17504-001
Glutamax	100x	1x	Gibco	35050038
Non-essential amino acids	100x	1x	Gibco	11140050
β-mercaptoethanol	50 mM	50 nM	Gibco	31350010
Pen/Strep	100x	1x	Merck	P0781

2.4.2 Motor neuron differentiation protocol

On Day 0, 3000 hPSCs were plated per well in 96 well U-bottomed low attachment plates (Greiner, 650185) in 150 µl N2B27 media containing: 20 ng/ml FGF-2 (R&D Systems, 3718-FB), 10 µM Y-27632 (Adooq Bioscience, A11001), 0.2 µM LDN193189 (Tocris, 6053), 4 µM Chir99021 (Tocris, 4423), 40 µM SB431542 (Tocris, 1614) and 0.05% PVA (Sigma, P8136). Plates were spun at 400 g for 4 minutes to ensure that cells were at the bottom of the well to form embryoid bodies (EBs). All medium changes within this plate were done by replacing 50% of the media to ensure the EB was not disturbed, and media was changed every two days unless otherwise stated.

On Day 2, medium was changed to contain 20 ng/ml FGF-2, 0.2 μM LDN193189, 4 μM Chir99021, 40 μM SB431542, 1 μM retinoic acid (Merck, R2625) and 0.5 μM SAG (Tocris, 4366). On Day 4 and Day 6, the medium added to the EBs contained 1 μM retinoic acid and 0.5 μM SAG. On Day 7, medium contained 1 μM retinoic acid, 0.5 μM SAG, 10 ng/ml BDNF (PeproTech, 450-02) and 10 ng/ml GDNF (PeproTech, 460-10). On Day 9 and Day 11, the medium added contained 10 μM DAPT (Tocris, 2634), 10 ng/ml BDNF, 10 ng/ml GDNF, 1 μM retinoic acid and 0.5 μM SAG.
On Day 13, EBs were pooled together in a 1.5 ml Eppendorf, washed once with DMEM/F12, and dissociated using 1 mL Accutase (Merck,) and an Eppendorf shaker (Eppendorf,) set at 37°C at increasing speeds from 800rpm to 1400rpm for 30 minutes or until the EBs dissociated. Speeds increased by 100 rpm every 5 minutes, with EBs being manually pipetted up and down between speed changes. Once at single cells, they were re-plated at 70,000 cells/cm^2 in media containing which 10 μM DAPT, 10 ng/ml BDNF, 10 ng/ml GDNF, 0.1 μM retinoic acid, 0.5 μM SAG, and 10 μM Y-27632. Plates were prepared with Poly-L-Ornithine (Sigma, P4957) for 30 minutes at 37°C, followed by washing three times with PBS and then coated with GelTrex (1:100 in ice-cold DMEM) for 1 hour at 37 °C. Media changes were now 50% every three days, with media added gently to the side of the well.
Day 14 medium contained 10 ng/ml BDNF, 10 ng/ml GDNF, and 20 μM DAPT. Day 16 medium contained 10 ng/ml CNTF (PeproTech, 450-13), 10 ng/ml BDNF, 10 ng/ml GDNF, and 20 μM DAPT
Day 17 medium contained 10 ng/ml BDNF, 10 ng/ml GDNF, 10 ng/ml CNTF, and 200 μM L-ascorbic acid (Sigma, A4403). This Day 17 medium was used for the rest of the differentiation as a maintenance medium until the cells were ready to be used.

2.5 qPCR gene expression analysis

2.5.1 RNA extraction

Cells of interest were pelleted as described in section 2.1.8 before storage at -80°C. RNA was extracted from these pellets using the Norgen Total RNA Purification Plus Kit (Norgen, 48300) according to the manufacturer's instructions. RNA was eluted in the appropriate buffer and quantified using a Nanodrop Lite (Thermofisher).

2.5.2 cDNA generation

RNA was reverse transcribed into cDNA using High-Capacity Reverse Transcriptase (Applied Biosystems, 4368813) according to the manufacturer's instructions. In brief, each 20 µl cDNA reaction contained; 1X RT buffer, 1x dNTP mix, 1X RT random primers, 1-unit Reverse Transcriptase, nuclease-free water and 1000 ng of RNA.

2.5.3 qPCR

Each 10 µl qPCR reaction contained 8.9 µl of SYBR green MasterMix (0.4 µl of 10 µM forward and reverse primers, 5 µl SYBRgreen mix (ThermoFisher, A25777) and 3.5 µl nuclease-free water) and 1 µl of cDNA at 5 ng/µl. This was run on QuantStudio 12K Flex Thermocycler (ThermoFisher) with the following parameters:

Table 2.3 SYBRgreen RT-qPCR instrument settings

Step	Temperature (°C)	Duration	Cycles
Enzyme activation	95	2 mins	1
Denature	95	15 seconds	40
Anneal/extend	60	60 seconds	
Hold	4	Up to 24 hours	1

2.5.4 qPCR analysis

qPCR analysis was carried out according to the ΔΔCt method (Livak and Schmittgen, 2001). Housekeeping Ct was subtracted from the gene of interest Ct to generate ΔCt. The ΔCt of Day 0 or control samples were subtracted from the ΔCt of Day 13/34 or treated samples to generate ΔΔCt. Fold expression was calculated as 2^-(ΔΔCt) and this value was plotted.

2.5.5 Primer validation

Primer sequences were sourced either from previously established laboratory protocols or designed using PrimerBLAST (NCBI) and ordered as DNA oligos from Integrated DNA Technologies. RT-qPCR primer efficiency was validated by generating a standard curve. Firstly, a 5-fold serial dilution of cDNA that was positive for the gene of interest was generated in a five-step series. Primer sets and serial dilutions of cDNA were run as detailed in section 2.5.3. Primer efficiency was calculated from a relative standard curve and primer pairs with an efficiency between

90% - 110% passed. A melt curve analysis was also performed to identify any primer-dimers or contamination.

2.5.6 Primer sequences

Table 2.4: List of RT-qPCR primer sequence

Gene Name	Forward sequence	Reverse sequence
GAPDH	agccacatcgctcagacac	gcccaatacgaccaaatcc
LHX1	atgcaacctgaccgagaagt	caggtcgctaggggagatg
BRACHYURY (TBXT)	tgacaaacaaccagctcttca	tgagggctcagcacttgtt
OLIG2	aggtacccaaccctgagga	gcaggtgagttgtcagaataggt
ISLET1	agctcctcaaatcgcatcc	atagtcgtcgcagctttcg
HB9	gcagcccaatgacaaaactaa	ccgtcgtgtctctctggact
HOXA4	ttacctgacttatgaaacttgaaacc	cccagagacgtaagcataaacc
HOXB5	gttgccacccaagagagaac	ccaagtagtccttctcaggtatcc
HOXB6	aagcttcacatcagccatga	cggttgaagtggaactccttt
HOXB7	tggaagctgaagaagaaactgaa	gccgggtttatgatttgttg
HOXC8	ctacccctggatgcgaag	caggtagcgattgtagtgaaattct
HOXC9	tcctagcgtccaggtttcc	gctacagtccggcaccaa
FOXA2	tcctagcgtccaggtttcc	gctacagtccggcaccaa
PAX6	cgagatttcagagccccata	aagacaccaccgagctgatt
ChAT	cgaggagagcaggtccaca	ctgctgggagttttgctgc
PHOX2B	ctaccccgacatctacactcg	ctcctgcttgcgaaacttg
NANOG	aactctccaacatcctgaacc	ccttctgcgtcacaccatt
SIRT2	ggtcggtgacagcctcaag	cgcaggaagtccatgtctgc
ACOT2	tgctggagtatcgggctagt	tcctggacctttacctcggg
TXRDN2	ctggctgaaggaatcccctg	tggaggacatttgctggtcg

2.6 Immunofluorescence

2.6.1 Immunocytochemistry

Live cells were fixed using 4% PFA for 15 minutes, followed by washing three times with PBS. Cells were incubated with 50 mM NH_4Cl for 10 minutes to quench autofluorescence. Cells were permeabilised using 0.2% Triton X-100 in PBS for 10 minutes and washed three times with PBS. Cells were then incubated for one hour with blocking buffer (10% FCS/0.1% BSA in PBS). Primary antibodies were diluted to the appropriate concentration in blocking buffer and applied to the cells for two hours at room temperature or overnight at 4°C. Cells were then washed three times with blocking buffer. Secondary antibodies were diluted 1:1000 in blocking buffer supplemented with 1:10,000 Hoechst 33342 (Thermofisher, H3570) and applied to the cells for 30 minutes at room temperature whilst protected from light. Cells were washed three times with blocking buffer the once with PBS. Cells were imaged using an InCell Imager 2200 or an Olympus BX61 microscope.

Proximity Ligation Assay (PLA)

Cells plated on glass coverslips were fixed at 70% confluency (mitotically active) or at the relevant differentiation time point using 4% PFA for 15 minutes before being washed three time with PBS. Cells were incubated with 50 mM NH_4Cl for 10 minutes then permeabilised with 0.2% Triton X-100 in PBS for 15 minutes. Cells were washed three times with PBS and glass coverslips were incubated with 50 µl of DuoLink blocking solution in a humidity chamber at 37°C for 30 minutes. Primary antibodies were diluted in DuoLink antibody diluent and applied to glass coverslips for one hour at room temperature. Coverslips were then washed twice with DuoLink Wash Buffer A and incubated with PLUS and MINUS probes, which had been diluted 1:5 in antibody diluent, in a humidity chamber for one hour at 37°C. Coverslips were washed 2x in Wash Buffer A and ligation buffer was diluted 1:5 in high purity water with ligase added at 1:40. Ligation solution was applied for 30 minutes at 37 °C in a humidity chamber. Coverslips were washed 2x in Wash Buffer A. 5x Amplification buffer was diluted 1:5 in high purity water and Polymerase was added 1:80. This was applied to coverslips in a humidity chamber at 37 °C for 100 minutes. After, coverslips were washed 3x in Wash Buffer B then incubated for 10 minutes with 1:10,000 Hoechst (Thermofisher, H3570) diluted in 0.01% Wash Buffer B. Coverslips

were then washed 3x with 0.01% Wash Buffer B and mounted onto slides with a minimal volume of mounting medium. Coverslips were then imaged within 72 hours of mounting using an Olympus BX61 fluorescent microscope.

2.7 DNA extraction

Live cells were dissociated according to 2.1.8. and pelleted at 240 g for 5 minutes. DNA was then extracted using the DNEasy Blood and Tissue kit (Qiagen, 69506), with some alterations to the manufacturer's instructions. Pellets were resuspended in 200 µl PBS with 20 µl Proteinase K. 200 µl of Buffer AL was added to this and mixed by gently pipetting with a P1000. 200 µl of 100% ethanol was then added and mixed by gentle pipetting. This lysate was placed on a spin column and centrifuged at 6000g for 1.5 minutes. The column was washed twice with 500 µl of Wash Buffer 1 and 2, respectively, at 6000 g and 14000 g, respectively. DNA was eluted from the column in 50 µl of Elution buffer that had been pre-heated to ≥ 50°C. DNA quantity and purity was quantified using a Nanodrop Lite (ThermoFisher, ND-LITE-PR).

2.8 Transmission Electron Microscopy

2.8.1 Fixation

Neurons were grown on 35-mm Ibidi u-dish (50 grid, glass bottomed) culture dishes and fixed using 2% glutaraldehyde buffered with 0.1 M sodium cacodylate at pH 7.4 for 1 hour at room temperature. Samples were left in fixing solution overnight at 4°C and placed in PBS the next day. Samples were then transferred to the University of Sheffield Electron Microscopy facility. Samples were then washed three times in 0.1 M sodium cacodylate at pH 7.4 and post-fixed in 2% aqueous OsO4 at room temperature for 1 hour, washed again three times in distilled water before staining in 1% aqueous tannic acid 4 °C, again for 1 hour.

After washing free of unbound Tannic Acid, the pellets were dehydrated in graded steps of ethanol (50, 75, 95, and 100%), twice with 100% dried ethanol, cleared of ethanol in Propylene Oxide and embedded into Epon resin (Agar Scientific). Sections (80 nm thick) were cut on a Reichart Ultacut E ultramicrotome and post stained with 2% aqueous Uranyl Acetate for 10 minutes, followed by Reynold's Lead Citrate for 5 minutes.

2.8.2 TEM

Sections were viewed with a Fei Tecnai T-20 BioTwin Spirit transmission electron microscope with a Gatan Orius 1000B, and Gatan Digital Micrograph software. Imaging was performed by the University of Sheffield Electron Microscope Facility.

2.9 Mitochondrial trafficking

2.9.1 Transfection

Motor neuron progenitors were plated at 70,000 cells/cm^2 in 3.2 cm ibidi dishes and cultured according to the protocol outlined in 2.3.2. On Day 34, cells were co-transfected with pCAG-GFP (Addgene, 11150**)** and MitoDsRed (TanakaBio, 632421) using Lipofectamine LTX with Plus Reagent (ThermoFisher, 15338100) and Opti-MeM (Gibco, 31986062) as indicated in the manufacturer's instructions. Plasmids pCAG GFP and ds-RedMito plasmid (red fluorophore with mitochondrial targeting sequence, under CMV promotor) were used in a 1:1 ratio with 1 µg DNA delivered to each ibidi dish. Transfection components were incubated with cells for 6 hours before media was replaced with fresh motor neuron maintenance media. Neurons were used for trafficking experiments 48 hours after transfection. If neurons were to be dosed with compound, they were fed motor neuron maintenance media after the transfection end the exposed to the compound for the 24 hours prior to imaging.

2.9.2 Imaging

Mitochondrial trafficking in motor neurons was imaged using a custom built TIRF/FRAP microscope with widefield capabilities. Videos were captured with the corresponding excitation laser and a TIRF Quad cube with the TRF89901-EMv2 filter set from Chroma: Excitation, ZET405/488/561/640x-V2; Dichroic, ZT405/488/561/640rpc-UF2-V2 and Emission filter ZET405/488/561/640m-V2. Additional emission clean-up was provided by a Cairn Optospin filter wheel with ET445/58m, ET525/50m, ET595/44m or ET706/95m filters for 405, 488, 561 and 638 laser lines respectively.

One hour prior to imaging, the microscope and its enclosed environment were heated to 37.5 °C with a small open source of water to humidify the environment. Imaging commenced once the temperature has been stable for 15 minutes.

The custom microscope has the following specification:

- Fully automated Nikon Ti2-E inverted microscope with Perfect Focus System
- Nikon CFI Plan Apochromat Lambda 60x Oil objective
- ASI automated XY stage and piezo-Z
- iLas2 scanning TIRF/FRAP unit with Cairn dual-collimation optics
- Cairn multiline laserbank with 405 (FRAP), 488, 532, 561 & 637 (TIRF) lasers
- Chroma sputter coated filters
- Cairn Optospin
- Photometrics Prime 95B sCMOS camera
- MetaMorph acquisition software
- OKO-Labs enclosure & temperature controller
- Quad TIRF/Widefield settings : TIRF and Widefield imaging were performed with the corresponding excitation laser and a TIRF Quad cube with the TRF89901-EMv2 filter set from Chroma: Excitation, ZET405/488/561/640x-V2; Dichroic, ZT405/488/561/640rpc-UF2-V2 and Emission filter ZET405/488/561/640m-V2. Additional emission clean-up was provided by a Cairn Optospin filter wheel with ET445/58m, ET525/50m, ET595/44m or ET706/95m filters for 405, 488, 561 and 638 laser lines respectively.

2.9.3 Analysis

A semi-automated pipeline was created to analyse the videos of mitochondrial movement acquired in 2.9.2. ImageJ macros were created for pre-processing: isolating the axon, generating kymographs, and measuring size and shape parameters of the mitochondria in the first frames of the videos. The ImageJ PlugIn ‘KymoButler’ was used to identify tracks on the kymographs. An R script was written to process and measure the tracks generated by KymoButler.

2.10 CRISPR gene editing of cells

2.10.1 On and off-target primer design

Previously designed primers were used for the identification of on- and off-target editing for the generation of MFN2$^{R94Q/+}$ cells (Butler, 2021).

Table 2.5: List of PCR primers for on- and off-target sequencing of MFN2$^{R94Q/+}$ cells

Target	Forward primer	Reverse primer
MFN2 R94Q	tgaggccacagagctagaaag	cctgcctggaacgttctgt
Off-target site 1	aggttcttttgcttgaggcca	Tcagctttgtcagtgcttgc
Off-target site 2	gctgtgaaatgatgcgtgga	cagctctggagagagatgtc
Off-target site 3	tccttatactcccttgcgcc	gggcctgggatctagcagta
Off-target site 4	ccagggcatctgtgggatc	tagagagtggaatccccatg
Off-target site 5	tcatgacacggaggaactgg	tgccggagagactaacctcc

To generate on- and off-target primers for the generation of MFN2$^{T105M/+}$ cells, DNA sequences for the desired sites from GRCh38 were run through PrimerBlast (https://www.ncbi.nlm.nih.gov/tools/primer-blast/) and three pairs were selected based on having a G/C content between 40% to 60%, a melting temperature between 57 and 60 °C, and a final product size of ~500 base pairs.

Table 2.6: List of PCR primers for on-target editing of MFN2$^{T105M/+}$ cells.

Target	Forward primer	Reverse primer
MFN2 T105M	atgaaccaggggcatgtcag	ggtctcccattcacctccac

2.10.2 Transfection of Cas9 and guides

Upon purchase, crRNA and ALT-R® CRISPR-Cas9 tracrRNA (IDT, 1072532) were diluted to 100 µM in Nuclease-Free Duplex Buffer (IDT, 11-01-03-01), aliquoted and stored at -20 °C. Aliquots of cRNA and tracRNA were mixed in equimolar concentrations in a sterile tube and heated at 95 °C for 5 minutes to form the crRNA:tracrRNA duplex (this is the sgRNA) before being allowed to cool to room temperature. The ALT-R® S.p. HiFi Cas9 Nuclease V3 (IDT, 1081060) was diluted in Resuspension Buffer R (part of kit 10µl electroporation kit, Invitrogen, MPK1025) to 36 µM and incubated at room temperature in a 50:50 mix with the crRNA:tracrRNA duplex to form the ribonucleoprotein (RNP) complex. The repair template was resuspended to 100 µM in Nuclease-Free Duplex Buffer, aliquoted and stored at -

20 °C. For use in experiments, 100 µM stock was diluted to 10.8 µM in Resuspension Buffer R.

To introduce the CRISPR components into cells, cells were dissociated to a single cell suspension, as described in 2.1.8, and pelleted. The cell pellet was resuspended in the Resuspension Buffer R at 2.2x107 cells/ml. For each electroporation, 1 µl of RNP complex, 9 µl cell suspension and 2 µl of repair template (replaced with R buffer if not used) was mixed and pipetted into a 10 µl Neon electroporation tip (Invitrogen, MPK1025). Electroporation was carried out on DigitalBio Microporator (ThermoFisher) with the following settings: 1400 V, 20 ms, 1 pulse.

Cells were transferred to one well of a 12-well plate that was prewarmed, coated with GelTrex, and contained MTesR Plus supplemented with 1:10 CloneR2 (100-0691, StemCell Technologies) and 10 µM Y-27632. Cells were fed with fresh media containing the same supplements 24 hours later.

2.10.3 Single cell sort and cloning

48 hours post-transfection, cells were dissociated according to 2.1.8 and resuspended in MTesR Plus with 1:10 CloneR2 and 10 µM Y-27632. Cells were single cell sorted into 96-well plates coated with GelTrex containing 50 µl mTeSR Plus with 1:10 CloneR2, 10 µM Y-27632 and 1:500 Normacin (ant-nr-05, InvivoGen) using a FACS Jazz (BD Biosciences). Immediately after sorting, plates were centrifuged at 252 g for 15 seconds to facilitate cell attachment to the GelTrex and placed in a cell culture incubator to grow. 48 hours post-sorting, all wells had 50 µl of warm media (mTeSR Plus, 1:500 Normacin, 10 µM Y-27632) gently added. Cells were fed every 48 hours by 80% media changes. Media was slowly transitioned from mTeSR Plus to S8 but always contained 1:500 Normacin. Colony formation was monitored from 48 hours after sorting, with notes being made on which wells contained colonies, the speed at which these colonies grew, and their morphology to avoid selecting colonies that behaved like variant cultures. Once a colony had grown to cover ~70% of its well, it was passaged using ReLeSR into one well of a new GelTrex-coated 96-well plate and one well of a GelTrex-coated 12-well plate. The new 96-well plates were for DNA extraction and the 12-well plates were for cryopreservation. Cells were cryopreserved according to 2.1.6 when the well was ~80% confluent.

2.10.4 DNA extraction from 96-well plates

Once clones had been passaged into a fresh well of a 96-well plate, cells were allowed to become >100% confluent to maximise material for DNA extraction. A DNA lysis buffer was made consisting of:

Table 2.7: Components for gDNA lysis buffer.

	Catalogue number	**Company**
100 mM Tris Base	T1503	Sigma
5 mM EDTA	E9884	Sigma
200 mM NaCl		Sigma
0.2% SDS		Sigma

The buffer was pH adjusted to 8.0 with HCl (Sigma) and supplemented with 100 µg/ml Proteinase K just before use.

Media was removed from cells manually and 50 µl lysis buffer supplemented with Proteinase K was added to each well. The plate was incubated at 37°C for 24 hours in a cell culture incubator. Following incubation, the contents of each well was transferred to a V-bottom 96-well plate and 50 µl ice-cold isopropanol was added to each well and the plate was shaken for 30 minutes at a speed greater than 1000 rpm. The plate was then centrifuged for 5 minutes at 2500 rpm to pellet the DNA. The plate was turned upside down over a waste bucket to discard the isopropanol, and whilst keeping the plate upside down, was dropped gently onto a paper towel from a height of ~2 cm to remove any remaining liquid. 100 µl of 70% ice-cold ethanol was added to each well, and the plate was centrifuged at 2500 rpm for 5 minutes. Again, the plate was inverted to remove the ethanol and dropped onto a paper towel. This wash step was repeated once more. After the second centrifugation, the plate was inverted to remove the ethanol and the plate was dropped onto a paper towel three time, keeping the plate inverted at all times. The plate was returned to the right way up and any excess ethanol was removed from the top of the plate with a paper towel. 45 µl TE buffer (pH 8, 11-05-01-05, IDT) was added to each well immediately and the plate was sealed with adhesive film, ensuring that each well was completely isolated from its neighbours. The plate was shaken for 3 hours at 400 rpm at 55°C. This was extended to overnight if the DNA

pellet had not resuspended. DNA quantity of each sample was then determined using a Nanodrop Lite (Thermofisher).

2.10.5 PCR and Restriction digest screen

To screen clones for potential on-target edits, DNA was amplified by PCR and digested using a restriction enzyme to see if an additional cut site had been introduced by CRISPR-cas9 editing. DNA from each clone, extracted as detailed in 2.10.4, was amplified in the following 25 µl PCR reaction:

Table 2.8: Components for a single PCR reaction.

Component	Volume	Catalogue number	Company
2x Optima PCR HotStart ReadyMix with dye	12.5 µl	LS29	Geneflow
Forward primer (10 µM)	1.25 µl	-	-
Reverse primer (10 µM)	1.25 µl	-	-
DNA	100 ng	-	-
Water	Up to final 25 µl volume	-	-

The PCR reaction was performed with the following cycling protocol:

Table 2.9: Thermal cycler settings for PCR

Step	Temperature	Duration	Cycles
Initial denaturation	95 °C	3 min	1
Denaturation	95 °C	15 sec	35 cycles
Annealing	56 °C	20 sec	
Extension	72 °C	30 sec	
Final extension	72°C	30 sec	1
Store	4°C	hold	1

Once completed, the PCR reaction was split into two equal volumes. One half was stored at 4 °C to be run on an agarose gel later. The other half was digested using BseMII (ThermoFisher, ER1401) for $MFN2^{R94Q/+}$ CRISPR-Cas9 experiments or FokI

(ThermoFisher, FD2144) for $MFN2^{T105M/+}$ CRISPR-Cas9 experiments. The restriction digest using BseMII was performed according to the following:

Table 2.10: Components for a singular restriction digest reaction using BseMII.

Component	Volume	Catalogue number	Company
BseMII	1 µl	ER1401	ThermoFisher
SAM	0.4 µl	ER1401	ThermoFisher
Tango	2 µl	ER1401	ThermoFisher
Water	6.6 µl	-	-
PCR product	10 µl	-	-

The reaction was mixed by pipetting gently and spun down, then incubated at 55°C for two hours.

The restriction digest using FokI was performed according to the following:

Table 2.11: Components for a singular restriction digest reaction using FokI.

Component	Volume	Catalogue number	Company
FokI	1 µl	FD2144	ThermoFisher
10X FastDigest buffer	2 µl	FD2144	ThermoFisher
Water	7 µl	-	-
PCR product	10 µl	-	-

The reaction was mixed by pipetting gently and spun down, then incubated at 37 °C for 5 minutes.

Once all PCR and restriction digests had been performed, samples were run on a 2% agarose gel made with TBE. The uncut and cut PCR product of each colony was run side by side to compare.

2.10.6 Sanger sequencing

DNA extracted by 2.7 and desired DNA sites were PCR amplified according to the following reaction:

Table 2.12: Components for a singular PCR reaction using Platinum II taq.

Component	Volume	Catalogue number	Company
Platinum II Hot-start PCR MasterMix (2x)	25 µl	14000012	ThermoFisher
Forward primer (10 µM)	0.4 µl		
Reverse primer (10 µM)	0.4 µl		
DNA	500 ng		
Water	To 50 µl		

The PCR reaction was performed with the following cycling protocol:

Table 2.13: Thermocycler settings for PCR using Platinum II taq.

Step	Temperature	Duration	Cycles
Initial denaturation	94°C	3 min	1
Denaturation	94°C	15 sec	33 cycles
Annealing	60°C	15 sec	
Extension	68°C	10 sec	
Store	4°C	hold	1

A sample of each PCR reaction was run on a 2% agarose gel made with TBE to confirm that only one DNA band was present. The rest of the PCR product was cleaned using the NucleoSpin™ PCR and Gel Clean-Up kit (Macherey-Nagel, 12303368) according to the manufacturer's instructions. The clean PCR product was quantified using the Qubit Broad Range DNA kit (Q32853, ThermoFisher) according to the manufacturer's instructions. Samples were sent to Source Bioscience at room temperature for Sanger sequencing. Ab1 files received from Source Bioscience were accessed using ApE (Davis and Jorgensen, 2022).

2.10.7 Low-pass whole genome sequencing

Genomic DNA of samples was extracted according 2.7 and quantified using the Qubit Broad Range DNA kit (ThermoFisher, Q32853) according to the manufacturer's instructions. Samples were sent to Azenta GeneWiz on dry ice for

low-pass whole genome sequencing. Data was analysed in-house to generate Manhattan plots to compare chromosome copy number.

2.10.8 Surveyor Nuclease assay

Cells were electroporated with guides to be tested according to 2.10.2 and DNA was extracted according to 2.7 48 hours later. The DNA region of interest was amplified by PCR according to 2.10.5. The PCR product that contained the putative edit was hybridised with control DNA before incubation with the Surveyor nuclease for 30 minutes at 42 °C. Samples were run on a 2% agarose gel made with TBE alongside provided controls within the Surveyor Nuclease kit to identify any new cuts that signalled gRNA activity (IDT, 706025).

2.11 Western Blotting and co-immunoprecipitation

2.11.1 Protein extraction

Cells were dissociated with TrypLE (12604021, ThermoFisher) or Accutase (A6964, Sigma) according to 2.1.8. and suspended in ice-cold DMEM/F12. Cells were pelleted at 1000 rpm at 4 °C for 5 minutes. The supernatant was discarded, 100 µL RIPA lysis buffer was added to the pellet and vortexed to resuspend the pellet. Samples were kept on ice for 20 minutes, with samples being vortexed every 5 minutes. Samples were then spun at 13200 rpm at 4 °C for 15 minutes. The supernatant containing the protein was transferred to a clean Eppendorf to be snap frozen at -80 °C and stored at -80 °C if not being immediately used in SDS-PAGE.

2.11.2 Protein quantification

The concentration of extracted protein was quantified using a BCA assay (Pierce, 10741395), a colorimetric assay based on the reduction and chelation of copper ions.. Protein concentration was determined by reading the corresponding concentration off the linear graph.

2.11.3 SDS-PAGE

Samples were prepared using 5x protein loading buffer and 5-20 µg of protein was loaded per lane alongside a pre-stained protein ladder (BioRad, 1610373). SDS-PAGE gels were made with 4% stacking gel if the resolving gel was <10% or 6%

stacking gel if the resolving gel was ≥10%. Lower percentage gels were made to resolve higher molecular weight proteins. Gels were run at 120 mV for 90 minutes.

Table 2.14: Components for 4% and 6% stacking gels for SDS-PAGE gels.

Stack Gel	**4%**	**6%**
Acrylamide (30%)	666 µl	1.00 ml
0.5M Tris-HCl pH 6.8	1.25 ml	1.25 ml
SDS (10%)	50 µl	50 µl
H_2O	3 ml	3 ml
APS (10%)	30 µl	30 µl
TEMED	15 µl	15 µl

Table 2.15: Components for 7.5%, 10%. 12% and 14% resolving gels for SDS-PAGE gels.

Resolving Gel	**7.5%**	**10%**	**12%**	**14%**
Acrylamide (30%)	6.25 ml	8.33 ml	10.00 ml	11.67 ml
1.5M Tris-HCl pH 8.8	6.25 ml	6.25 ml	6.25 ml	6.25 ml
SDS (10%)	250 µl	250 µl	250 µl	250 µl
H_2O	12 ml	10 ml	8.2 ml	6.6 ml
APS (10%)	250 µl	250 µl	250 µl	250 µl
TEMED	25 µl	25 µl	25 µl	25 µl

2.11.4 Protein transfer

SDS-PAGE gels were transferred onto nitrocellulose membranes (Amersham, 15259794) using a wet transfer method. The nitrocellulose membrane was equilibrated in transfer buffer for 5 minutes. Transfer stacks were made up of 2 pieces of 3 mm filter paper soaked in transfer buffer (anode end), nitrocellulose membrane, SDS-PAGE gel, then 2 pieces of 3 mm filter paper soaked in transfer buffer (cathode end). Transfers were run at 100 mV for 30 minutes.

2.11.5 Protein detection

After transfer, membranes were blocked in 5% dried milk in TBS-T for 1 hour at room temperature. Membranes were then probed with the appropriate primary antibodies diluted in 5% milk in TBS-T at 4°C overnight with constant agitation. Membranes were washed for 10 minutes three times with sufficient TBS-T and constant agitation and then incubated with the appropriate secondary antibodies diluted in TBS-T at room temperature for 1 hour with constant agitation and protected from light if using fluorescent secondaries. Membranes were again washed for 10 minutes three times with TBS-T. Fluorescent detection of bands was performed using a Licor Odyssey Imager.

2.11.6 Western blotting buffer recipes

2.11.6.1 RIPA

50 mM Tris HCl, pH 7.4, 150 mM NaCl, 1% Triton X-100, 0.5% sodium deoxycholate, 0.1% SDS, 1mM EDTA, and 10 mM NaF was combined and made up to 100 ml with distilled water.

2.11.6.2 BRB80 lysis buffer

Base buffer was made using 80 mM PIPES pH 6.8, 1 mM EDTA, 1 mM $MgCL_2$, 1% NP40 and 150 mM NaCl with distilled water. Prior to use, 50 ml of base buffer was supplemented with 10 mM NaF, 10 mM Na_2VO_4, 10 mM $Na_4P_2O_7$, and 50 mM beta-glycerophosphate. 1:100 Halt protease inhibitor (ThermoFisher, 1861279) and 1:10 PhosSTOP tablet (Roche, 04906837001) was added immediately before use.

2.11.6.3 Protein Loading Buffer

5x protein loading buffer consisted of 1 M DTT, 2% SDS, 20% glycerol, 62.5 mM Tris HCl, 200 µL 0.02% Bromophenol Blue, one protease inhibitor cocktail tablet (Roche, 04906837001), made up to 10 mL with deionised water. This was aliquoted and frozen for future use.

2.11.6.4 1.5M Tris HCl pH 8.8 buffer

18.15 g Tris base was dissolved in 80 ml distilled water and pH was adjusted to 8.8 using HCl. Volume was then adjusted to 100 ml with distilled water.

2.11.6.5 0.5M Tris HCl pH 6.8 buffer

6 g Tris base was dissolved in 80 ml distilled water and pH was adjusted to 6.8 using HCl. Volume was then adjusted to 100 ml with distilled water.

2.11.6.6 Transfer buffer

3.03 Tris Base and 14.4 g Glycine were dissolved in 500 ml of deionised water. 200 mL methanol was added, giving a final concentration of 20%. The volume was made up to 1 L and was mixed thoroughly until all components were dissolved.

2.11.6.7 SDS-PAGE running buffer

A Tris-Glycine-SDS (TGS) running buffer was used for SDS-PAGE gels. TGS buffer comprised of 25 mM Tris Base, 250 mM Glycine, and 0.1% SDS. This was made at 10x concentration (pH 8.3) and diluted when required.

2.11.7 Plasmid mutagenesis

Plasmid sequences were provided by Kurt De Vos (unpublished) and validated by cross-checking the translated sequence with human protein sequences available on NCBI. Point mutations were introduced into plasmids by site-directed mutagenesis. Site-specific primers used to introduce substitutions were designed using https://www.agilent.com/store/primerDesignProgram.jsp . Substitutions were introduced into plasmids using QuikChange Lightning (Aligent, 210518-5) according to the manufacturer's instructions.

2.11.8 Plasmid production

Plasmids were transformed into XL10 gold bacteria (Aligent, 200315). Briefly, XL10 cells were thawed on ice and 1 µl β-mercaptoethanol was added to each sample and mixed by gentle swirling. 2 µl of ligation mixture (plasmid generated in 2.11.7) was added to thawed XL10 cells and the cells were incubated on ice for 30 minutes. Cells were then heat shocked at 42 °C for 30 seconds, then immediately moved back to ice for 2 minutes. In sterile conditions, 250 µl of LB broth containing the appropriate antibiotic was added to the transformed cells and put in a shaker at 37 °C horizontally for 1 hour. 50 µl of mixture was spread onto pre-warmed agar plates with the appropriate antibiotic and plates were incubated overnight at 37 °C. Colonies were picked the next day and expanded for sequencing. Plasmid was grown up and extracted using the NucleoSpin Miniprep kit (Macherey-Nagel, 740490.50,)

according to the manufacturer's instructions. Plasmids were sent for sequencing with Plasmidsaurus for confirmation of successful plasmid mutagenesis. Once this was confirmed, plasmid was grown up and extracted using the NucleoSpin Maxiprep kit (Macherey-Nagel, 12748412). DNA quality and quantity was confirmed using a Nanodrop.

2.11.9 Transfection, lysis, and co-immunoprecipitation

Purified plasmids (pcDNA3.1_MFN2_10xMyc (Wild-type or R94Q) and pRK5_TRAK1_HA) were transfected into HEK293 cells using Lipofectamine 2000 (Thermo Fisher Scientific, 11668019) and left for 24 hours before harvesting. Transfected HEK293 cells were washed in PBS, harvested into modified BRB80 buffer (80 mM PIPES pH 6.8, 150 mM NaCl, 1 mM $MgCl_2$, 1 mM EDTA, 1% w/v NP-40, 1 × Halt™ Protease Inhibitor Cocktail (Thermo Fisher Scientific)) and lysed at 4 °C for 30 min. Lysates were cleared by centrifugation at 15,000 g for 20 min at 4 °C, protein concentration measured by Bradford protein assay (Bio-Rad) and 0.5–1 mg protein was incubated with primary antibody overnight at 4 °C. 15 µl Protein G Mag Sepharose beads (GE Healthcare) or 8 µl Myc-Trap beads (ChromoTek) were added to the samples and incubated for 2 hours at 4°C. Beads were washed with buffer and eluted into Laemmli. Magnetic beads were harvested using an Extractman device (Gilson Scientific Ltd, Dunstable, UK). Samples were denatured at 100 °C and loaded onto polyacrylamide gels, and Western blotting was performed as detailed in 2.11.2 to 2.11.5.

2.12 Antibodies

2.12.1 Primary antibodies for immunofluorescence

Table 2.16: List of primary antibodies used for immunocytochemistry analysis.

Name	Species	Dilution	Supplier	Catalogue number
CHaT	Goat	1:100	Abcam	AB144P
HB9	Mouse	1:50	DSHB	81.5C10
ISLET 1/2	Mouse	1:200	DSHB	39.4D5
FOXP1	Mouse	1:150	R&D	MAB45341

NFH	Rabbit	1:500	Antibodies.com	A85336
Nanog	Rabbit	1:400	Cell Signalling Technologies	4903s
Oct4	Rabbit	1:1000	Cell Signalling Technologies	2840
SSEA3	Rat	1:10	In-house	(Shevinsky et al., 1982)
TRA 1-60	Mouse	1:10	In-house	(Badcock et al., 1999)
PAX6	Rabbit	1:350	Abcam	ab195045
Nestin	Mouse	1:100	Santa Cruz	Sc-377380
SOX17	Goat	1:100	R&D	AF1924
CXCR4	Chicken	1:100	Sigma	GW21075
TBXT	Rabbit	1:1000	Abcam	Ab209665
Vimentin	Chicken	1:5000	Abcam	Ab316214
PTPIP51	Mouse	1:1000	Abcam	Ab69337
VAPB	Rabbit	1:100	GeneTex	GTX131631

2.12.2 Primary antibodies for Western blotting

Table 2.17: List of primary antibodies used for Western blotting.

Name	Species	Dilution	Supplier	Catalogue number
MFN1	Rabbit monoclonal	1:1000	Cell Signalling Technologies	14739
MFN2	Rabbit monoclonal	1:1000	Cell Signalling Technologies	11925
B-actin	Mouse monoclonal	1:5000		
α-tubulin	Rabbit monoclonal	1:10000	Abcam	AB2288001

Acetylated α-tubulin	Mouse monoclonal	1:5000	Sigma	6-11B-1
GAPDH	Mouse	1:2000	Cell Signalling Technologies	14C10
HA	Rabbit	1:1000	Sigma	H6908
HA	Mouse	1:1000	Sigma	H3663
Myc	Mouse	1:1000	Cell Signalling Technologies	9B11
KIF5B	Rabbit	1:2000	Proteintech	21632-1-AP
Dynein	Mouse	1:1000	Genetex	GTX80684
DYNC1I2	Mouse	1:1000	Sigma	SAB1408953

2.12.3 Secondary antibodies for Western blotting

Table 2.18: List of secondary antibodies used for Western blotting.

Name	Species	Dilution	Supplier	Catalogue number
Secondary 800	mouse	1:50,000	Stratech	715-655-150-JIR
Secondary 700	Rabbit	1:50,000	Stratech	715-655-152-JIR

2.12.4 Secondary antibodies for Immunofluorescence

Table 2.19: List of secondary antibodies used for immunocytochemistry analysis.

Name	Species	Dilution	Supplier	Catalogue number
594	Goat	1:500	Invitrogen	A-11058
488	Mouse	1:500	Invitrogen	A-21202
647	Rabbit	1:500	Invitrogen	A-31573
594	Rabbit	1:500	Invitrogen	A-21207

2.13 Solutions and buffers

2.13.1 PBS

PBS was made by diluting 10x PBS (ThermoFisher, 15815418) 1:10 in double distilled water and then autoclaving for sterility.

2.13.2 4% PFA

37% formaldehyde solution (VWR, 1.04003.1000) was diluted in PBS to 4% and stored away from light at room temperature.

2.13.3 TBE

10x TBE solution was made by combining 108 g Tris base (Sigma, T1503), 55 g boric acid (Sigma, B0394), and 7.5 g EDTA (Sigma, E9884) in 800 ml of distilled water and mixed with a magnetic stir bar over gentle heat. Once dissolved, the solution was made up to 1 litre with distilled water. 10x TBE was diluted 1:10 for use in electrophoresis.

2.14 Statistical analysis

Statistics were performed using the means of each individual biologic replicate in each cell line, where a biological replicate was defined as an independent differentiation. For example, each cell line used has a N=3. When genotypes rather than cell lines were compared, the combined biological replicates were used. For example, the wild-type genotype consists of WT1 and WT2 which both have N=3, so combined have an N=6. For experiments where single neurons were measured (Chapter 4), 2 – 4 neurons were measured per cell line per biological replicate, and multiple recording were taken from each individual neuron (technical replicates).

Statistical analysis was performed using Graphpad Prism version 9.3.1 or RStudio by statistical tests as indicated in figure legends. Data was tested for normality via a Shapiro-Wilks test and distribution observations, and descriptive statistics were determined to examine the SD for each sample. If data was found to be normally distributed, then a Student's t Test or ANOVA with Dunnett's T3 multiple comparisons test was used. If data was found to not be normally distributed, a Wilcoxon rank sum test or a Kruskal-Wallis test with Dunn's multiple comparisons was performed. For all

the statistical tests $p<0.05$ was used as the criterion for statistical significance. Effect size (Wilcoxon effect size, *r;* Cohen's effect size, *d;* H statistic, *H*) was calculated alongside statistical significance for experiments with an $N \geq 3$. An *r* value of $0 < 0.3$ was defined as a small effect, $0.30 - < 0.5$ was a moderate effect, and ≥ 0.5 was a large effect. A *d* value of $0 < 0.2$ was defined as a small effect, $0.2 - < 0.5$ was a moderate effect, and ≥ 0.8 was a large effect. A *H* value of $0.01- < 0.06$ was defined as a small effect, $0.06 - < 0.14$ was a moderate effect, and $>= 0.14$ was a large effect.

Chapter 3 - Generation of hESC lines containing CMT2A-causing mutations via CRISPR-Cas9 gene editing:

3.1 Introduction:

Since its discovery, CRISPR-Cas9 has been used extensively for *in vitro* genome editing in multiple cell types (Adli, 2018). hPSCs are amenable to CRISPR-Cas9 editing and thus the technique has been used to model a variety of diseases, particularly neurodegenerative diseases such as Parkinson's Disease (Cuddy et al., 2019) and Alzheimer's disease (Wang et al., 2018). The CRISPR-Cas9 system employs a specific guide RNA (gRNA) that targets the Cas9 enzyme to a desired genomic site, making the system simpler to use than its predecessors zinc finger nucleases (ZFNs) (Urnov et al., 2010) and Transcription activator-like effector nucleases (TALENs) (Becker and Boch, 2021). The Cas9 enzyme recognises a downstream protospacer adjacent motif (PAM) in the genomic DNA and cleaves the DNA, giving rise to blunt-ended double-strand breaks (DSB). Cells go on to repair the breaks typically using either non-homologous end joining (NHEJ) or homology-directed repair (HDR) (Yang et al., 2020). NHEJ can occur without a template, which often leads to insertions or deletions (indels) at the breakage site. Indels can induce a frameshift mutation that impacts gene expression or function through premature stop codons and is preferred for the generation of knockout models (Bennett et al., 2020). HDR is often referred to as a non-mutagenic mechanism of DNA repair and uses a DNA template with homologous ends (either a sister chromatid or donor oligonucleotide) to fill the DSB. The provision of single-stranded oligodeoxynucleotides (ssODNs) during a CRISPR-Cas9 experiment permits the inclusion of a single point mutation or even an entire gene (Yoshimi et al., 2016, Okamoto et al., 2019). CRISPR-Cas9 gene editing can be tuned to a desired level of precision with considered gRNA and repair template design, choice of Cas enzyme, and choice of introducing CRISPR-Cas9 elements into cells (Wang and Doudna, 2023).

With the continued advancements in gene editing technology, the generation of disease models, specifically for CMT2A, has expanded rapidly and the popularity of

editing stem cells has risen. By having arrays of edited hPSCs, including wild-type, mutant, and knockout cells, one has access to all the cell types that hPSCs can generate through differentiation on a variety of genetic backgrounds.

However, hPSC models are known to be highly variable. hiPSC variability can be influenced by differences between donors, reprogramming techniques and genetic changes acquired through reprogramming or culturing of hiPSCs (Volpato and Webber, 2020; Rouhani, 2021). hESC variability is similarly influenced by genetic changes as a result of long-term culture and culture bottlenecks like cloning (Barbaric et al., 2014, Baker et al., 2016). This variation in hPSCs between institutions, and even within the same laboratory, limits reproducibility and progress (Drucker, 2016, Anderson et al., 2021, Glass et al., 2024). In a bid to improve reliability and reproducibility, the International Society for Stem Cell Research (ISSCR) published their Basic Research Standards document in 2023 (https://www.isscr.org/basic-research-standards). In this document, best practice recommendations for hPSC care and characterisation are put forward to 'establish the minimum characterisation and reporting criteria'. This includes the need for multiple clones, verifying the genetic stability of hPSCs, and demonstrating pluripotency through multiple surrogate assays. With the advent of stem cell therapies and personalised medicine, the need to standardise research practices, especially at the pre-clinical level, of stem cell research is clear in order to strengthen these upcoming therapies (Lee et al., 2013, Nature, 2013).

For disease modelling with hPSCs, it is essential that starting material is well characterised as variability in hPSC quality is known to negatively impact differentiation (Engel et al., 2016, Zhang et al., 2022b, Glass et al., 2024). Low reproducibility and quality in differentiations confound findings that could be attributed to disease-causing mutations or disease modifiers.

3.1.1 Aims

Previous work in the Barbarić lab began to generate a panel of hESC clones containing CMT2A-causing mutations in MFN2 using CRISPR-Cas9 (Butler, 2021). The mutation chosen was R94Q, as this mutation is one of the most commonly observed in the clinic and is associated with a more severe phenotype, thus would be more likely to show an observable phenotype *in* vitro (Neusch et al., 2007).

Through CRISPR-Cas9 editing of MasterSheff11 human embryonic stem cells, one clone with a heterozygous R94Q mutation in MFN2, referred to as Het1 (H1), was identified alongside one clone that remained wild-type after the editing event, referred to as WT2. These two clones were both screened for off-target mutations at the top five most susceptible sites as predicted by IDT's *in silico* prediction tool, were found to be unedited, and sub-cloned to ensure a homogenous population of the genotype. The unedited parental population of MasterSheff11 hESCs was referred to as WT1. One mutant clone was not sufficient to provide confidence for any future findings and so the first aim of this project was to expand and characterise the R94Q panel of clones. Furthermore, this chapter aimed to differentiate the expanded R94Q panel into spinal motor neurons (sMNs) using a previously optimised differentiation protocol (Butler, 2021). Finally, this section also aimed to generate a batch of hESC clones containing a different CMT2A-causing MFN2 mutation: T105M. The T105M mutation is associated with a milder phenotype in patients compared to R94Q but is still observed in a significant number of patients (Chung, 2006).

3.2 Generating and characterisation of CMT2A hESC sub-clones using CRISPR editing:

3.2.1 Generation and identification of CRISPR edited hESCs containing MFN2$^{R94Q/+}$

As previous work in the lab had already generated one R94Q clone successfully, it was possible to repeat the CRISPR experiment without the need to re-design and test guide RNAs (Figure 3.1A-C). The original guide RNA and HDR ssODN were electroporated into low-passage MasterSheff 11 hESCs that were ~70% confluent using the NEON transfection kit (Figure 3.1D). These cells were cultured for 48 hours before being single cell sorted, isolating each individual cell to one well of a 96-well plate. Each colony that grew within a single well was defined as a new clone, and each clone was expanded enough to gain material to extract DNA for screening and to cryopreserve for future expansion, if required. A total of 80 clones across four 96-well plates grew from the single cell sorting experiment.

The new clones were initially screened for potential on-target edits using a PCR and restriction digest (RD) screen (Figure 3.1E). A region of ~500 base pairs containing

the R94 site was amplified by PCR. If a successful edit had occurred (G281>A) then a new cut site would be introduced for the restriction enzyme BseMII in the PCR product. An unedited clone should only produce a band at ~500bp as there is no cut site for BseMII. A heterozygous clone should have bands at ~500 bp for the allele that was unedited and a band at ~250bp where BseMII has cut the PCR product in half. A homozygous clone should have one band at ~250bp where all PCR product contained the edit and thus the cut site, cleaving all the PCR product.

This first pass screen identified 28 clones that putatively contained the intended edit on one allele (Figure 3.1F). The PCR and RD screen lacks the ability to highlight any small indels that can also occur with successful editing. With that in mind, 10 of the 28 possible heterozygous clones were taken forward for Sanger sequencing, where the on-target mutation and ~150 bp each side of this site were visualised to single base pair resolution (Figure 3.1G). At this resolution small indels around the intended edit site were identified alongside the intended edit in 8 out of the 10 clones sequenced. The two clones that contained the intended edit without the presence of indels were then screened for any off-target editing that may have occurred. Faint bands were also present at ~500 bp and ~250 bp and this was most likely due to inefficient cutting by the restriction enzyme. Additional bands beyond these were presumably due to the presence of indels creating additional cut sites.

With the confirmation of the correct on-target mutation and the absence of off-target mutations, the two successful clones were subjected to another round of single cell cloning (Figure 3.2A). It is possible to have a mosaic population of cells after one round of cloning as the CRISPR components may still be active in the cells post-cloning, leading to a DSB break and repair event in a daughter cell. It is also possible that a single cell sort could be inaccurate due to mechanical error. Six subclones from each clone were carried forward and expanded in order to cryopreserve the material and extract DNA.

The top five sites most susceptible to off target editing using this guide RNA were predicted using IDT's *in silico* prediction tool (https://eu.idtdna.com/site/order/designtool/index/CRISPR_SEQUENCE). These top five predicted sites were amplified by PCR and analysed by Sanger sequencing. Off target sequencing showed that the two clones with the on-target mutation and no

indels around the intended edit site were also free of unwanted edits in these predicted off-target sites.

The PCR and RD screen was performed again on the 12 subclones. All subclones from the first clone (clone 2A8) showed clean bands at the ~500bp and ~250 bp mark indicating that the genotype of all these subclones was R94Q/+ (Figure 3.2B). The subclones from the second clone (clone 4G11) appeared to be a mix of wild-type and heterozygous, highlighting the necessity for the second round of cloning (Figure 3.2C). Two subclones from the first clone, now called Het3.1 (H3.1) and Het3.2 (H3.2) and one subclone from the second clone, now called Het4 (H4), were expanded for banking and further use. Het3.1, Het3.2, and Het 4 alongside the previously generated WT1, WT2, and Het1 constituted six hESC lines for the *in vitro* study of $MFN2^{R94Q/+}$. These six lines will be referred to at the R94Q panel from herein. The R94Q panel was sequenced for the on-target mutation once again at an early and late passage to confirm the presence of the G>A base pair change (Figure 3.2D). Material from the cell master banks were sent for low-pass whole genome sequencing to identify any chromosomal variations acquired during the CRISPR editing process (Figure 3.2E). The survival rate of hPSCs after single cell cloning is poor (Barbaric et al., 2014), and this selection bottleneck can favour genetic variants that confer growth advantages (Draper et al., 2004, Stavish et al., 2024). Manhattan plots of chromosomal copy number revealed that no gross chromosomal gains or losses had occurred in any of the R94Q panel after two rounds of single cell cloning. With the R94Q panel established, all six lines were sequenced for any off-target mutations to confirm the sub-clones were also free of unwanted edits that may not have been detected in parental clones (Figure 3.3A-E). All six lines showed no additional edits in the top 5 sites most susceptible to off target editing using the chosen guide RNA.

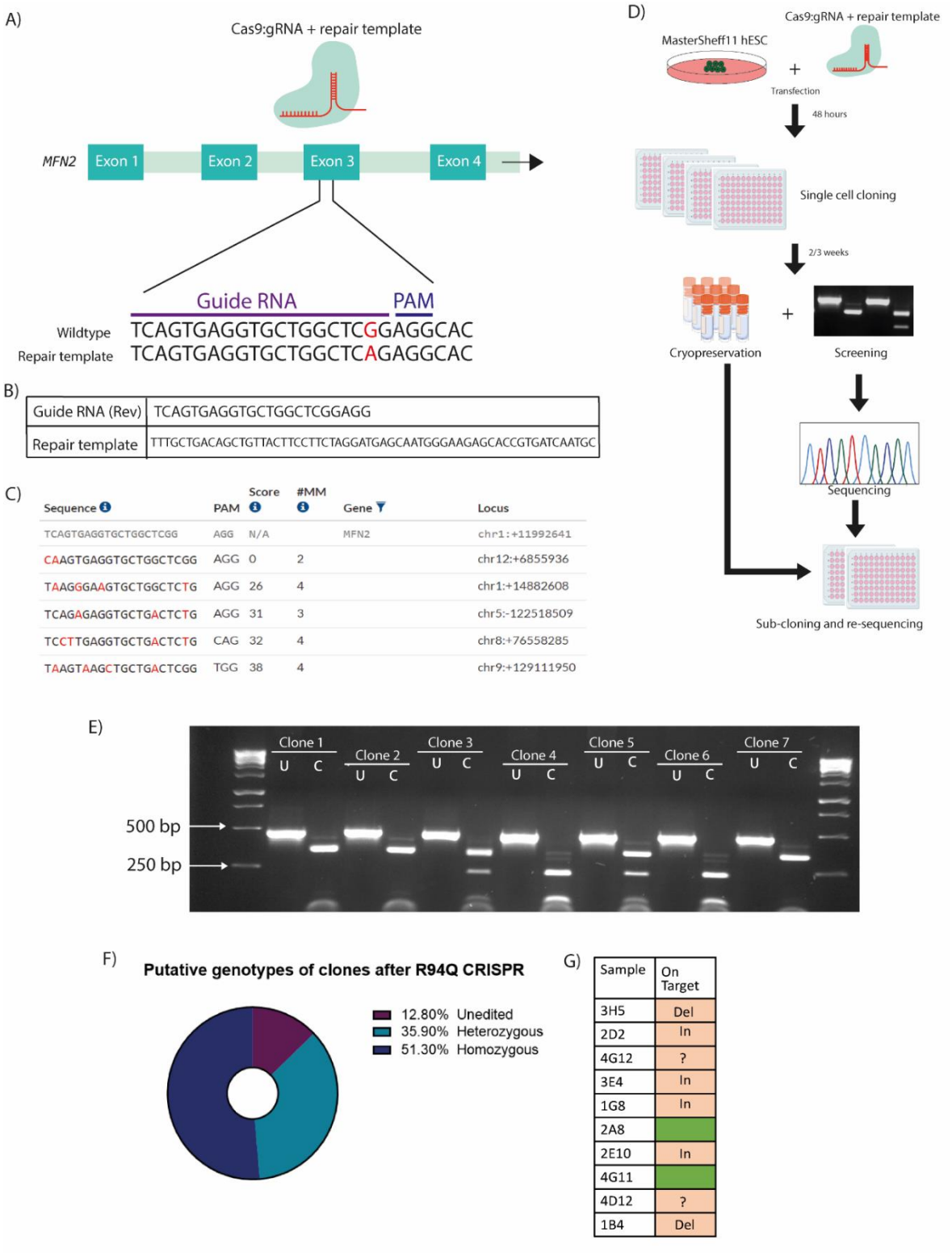


Figure 3.1: Generation of MFN2$^{R94Q/+}$ clones from MasterSheff11 hESCs using CRISPR-cas9 with no detected off-target editing. *(A) Schematic showing CRISPR-cas9 system targeting Exon 3 of MFN2 to generate the G>A base pair substitution. (B) Sequences of DNA oligos used to generate and validate the G>A base pair substitution. (C) Top five most likely off target sites as predicted in silico (D) CRISPR workflow schematic (E) Representative image of a PCR gel from the PCR/RD screen with anonymised clone names. U = uncut PCR fragment by RD. C= cut PCR fragment by RD (F) Putative genotypes of clones after CRISPR and first single cell clone (G) Overview of on-target edits in the ten sequenced clones (clones not shown in 3.1.E). Indels were detected using TIDER (http://shinyapps.datacurators.nl/tider/)*

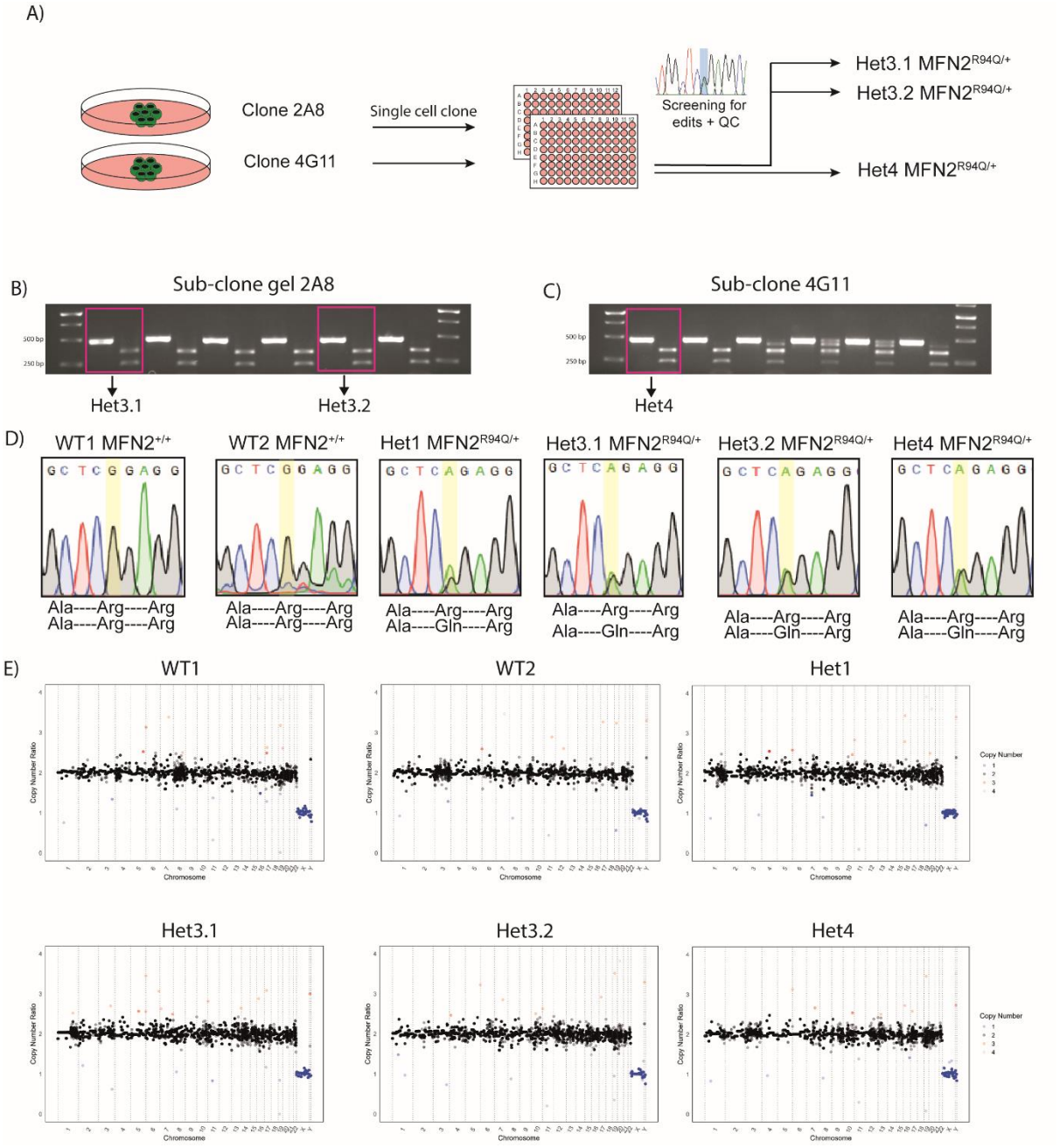


Figure 3.2: Sub-cloning of 2 putative MFN2$^{R94Q/+}$ clones. *(A) Schematic to show the generation of three MFN2$^{R94Q/+}$ sub-clones from two MFN2$^{R94Q/+}$ clones. (B) PCR/RD gel of six sub-clones from clone 2A8. Pink box denotes a sub-clone that was chosen for sequencing and further use. (C) PCR/RD gel of six sub-clones from clone 4G11. (D) Chromatograms generated by Sanger sequencing showing the on-target G>A base pair substitution, highlighted in yellow. Predicted amino acid sequence is shown below the sequence traces. (E) Copy number analysis of master banks of the MFN2$^{R94Q/+}$ panel by low-pass whole genome sequencing.*

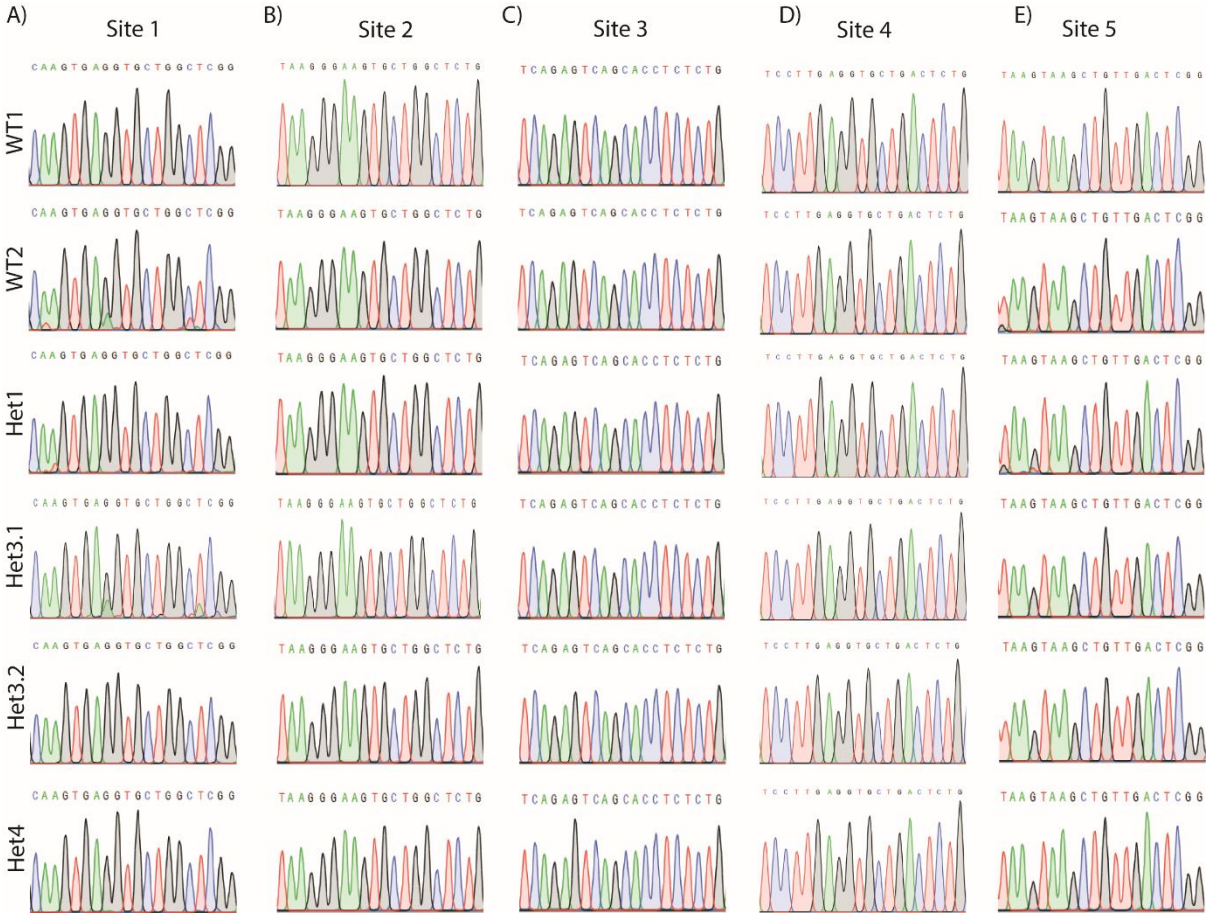


Figure 3.3: Screen for off-target mutations in MFN2$^{R94Q/+}$ sub-clones. *(A) Chromatograms generated by Sanger sequencing for the most likely site for off-target mutation by the chosen gRNA for introducing G281A in MFN2. (B) Sequencing of the second, third (C), fourth (D), and fifth (E) most likely sites for off-target mutation when generating MFN2$^{R94Q/+}$ in all lines.*

3.2.2 Characterisation of pluripotency of MFN2$^{R94Q/+}$ hESCs

Extensive characterisation of hESC lines is essential in determining their suitability for different applications. A pluripotent stem cell is typically identified by the co-expression of pluripotency-associated markers such as NANOG, Oct4, SSEA3, and TRA-1-85 (Andrews and Gokhale, 2024). However, pluripotency is defined as the ability of a cell to generate cells belonging to the three lineages: endoderm, ectoderm, and mesoderm. In order to show that introducing the heterozygous R94Q mutation into MFN2 had not changed the inherent stem cell characteristics of the cells, staining of the new lines for pluripotency-associated markers was performed alongside a trilineage differentiation.

All clones were immunoreactive for SSEA3 (Figure3.4A) and Tra-1-85 (Figure3.4B), with these cell-surface markers showing similar distributions across the colonies. Each clone showed no significant differences in NANOG or Oct4 expression across

the population, with all lines showing near 100% expression in nuclei (Figure3.4C, D).

Each clone was also capable of differentiating into each of the three germ layers. Suitable markers were chosen as read-outs for the different germ layers according to the ISSCR's Standards Document (Table A4.2 https://www.isscr.org/basic-research-standards) and available antibodies (Figure 3.5A). The 5-day mesodermal differentiation produced strong TBXT and CXCR4 expression in the nuclei and cytoplasm respectively of all clones (Figure 3.5B). The 7-day ectodermal differentiation produced cells that were immunoreactive to PAX6 and Nestin antibodies (Figure 3.5B). The 5-day endodermal differentiation produced mixed population of SOX17-positive and CXCR4-positive cells (Figure 3.5B). The efficiency of these germ layer differentiations was quantified by the percentage of positive nuclei by immunocytochemistry and by RT-qPCR analysis of mRNA. The ectodermal differentiation produced an average of 85.7% PAX6 positive nuclei across the R94Q panel paired with a low percentage of nuclei expressing Nanog (Figure 3.5C). RT-qPCR analysis of PAX6 and Nanog showed a similar trend, with an upregulation of PAX6 and down regulation of Nanog compared to Day 0 (Figure 3.5D). The mesodermal differentiation produced an average of 93.8% TBXT positive nuclei across the six lines with a concomitant loss of Nanog expression (Figure 3.5C). This was mirrored in RT-qPCR data, showing TBXT upregulation and Nanog downregulation compared to Day0 (Figure 3.5D). The endodermal differentiation was less efficient compared to the other germ layer differentiations, producing an average of 47.5% SOX17 positive nuclei across the R94Q panel (Figure 3.5C). The loss of Nanog immunoreactivity was also less profound. RT-qPCR analysis showed a modest and variable upregulation of FOXA2 and Nanog (Figure 3.5D). This result was consistent across all six lines indicating that the parental line (WT1) has a reduced capacity for the endodermal lineage and favours differentiations along the ectodermal or mesodermal routes. Differentiation bias is a well-documented phenomenon with hPSCs, with different hPSC lines having different capacities for certain differentiations owing to epigenetics (Kim et al., 2007, Osafune et al., 2008). Furthermore, this trilineage data plays into the initial choice of selecting MasterSheff 11 as the parental line for this project, as it has a higher propensity for neuronal differentiations deriving from the ectoderm.

Overall, these data show that introduction of the R94Q mutation did not significantly change the proportion of nuclei positive for the lineage markers compared to WT1, suggesting that the R94Q mutation in hESCs did not alter inherent stem cell characteristics.

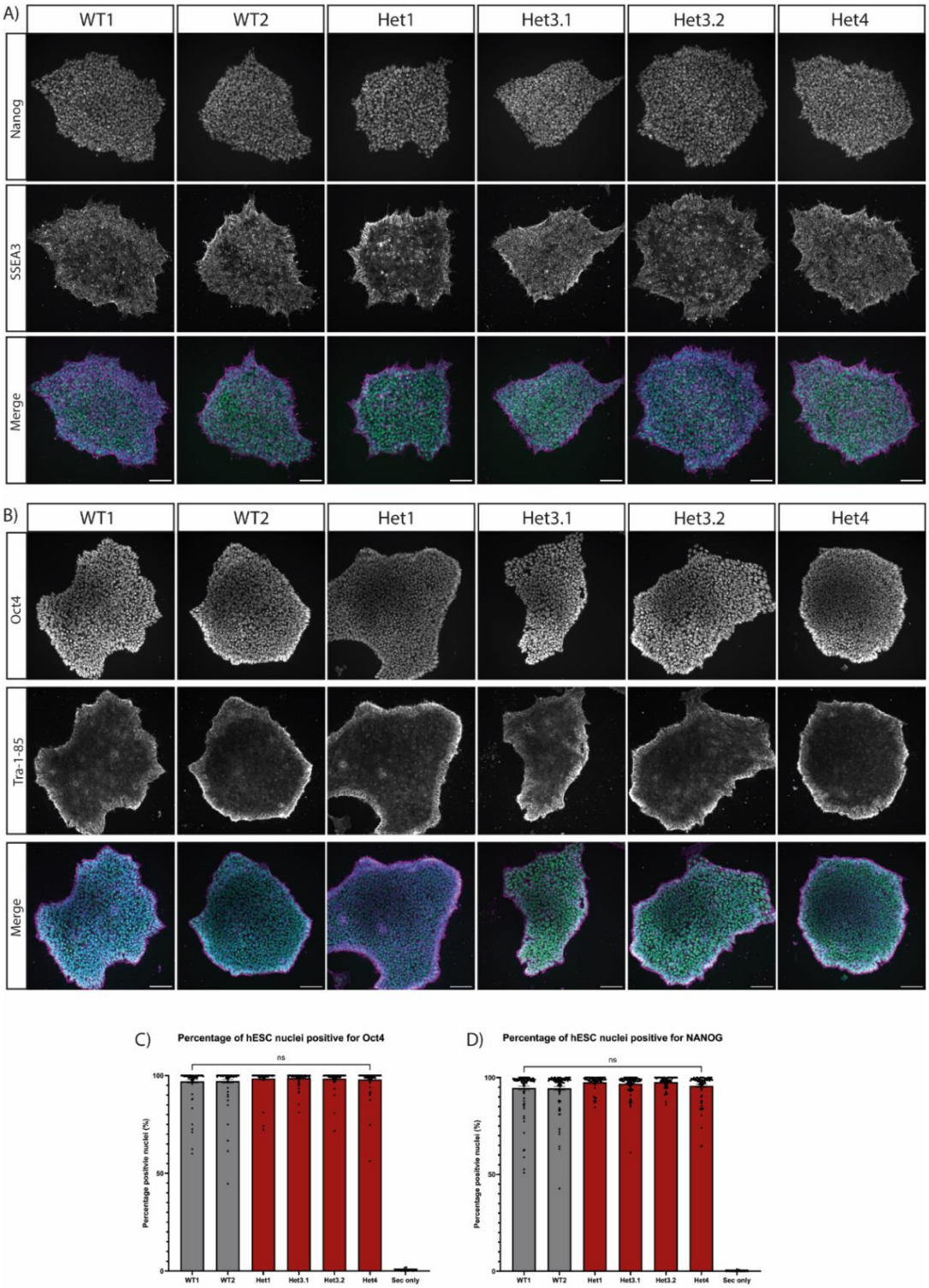


Figure 3.4: CMT2A pluripotency marker expression. *(A) Nanog and SSEA3 expression in clone panels. Scale bar = 100 µm. (B) Oct4 and Tra-1-85 expression in clone panel. Scale bar = 100 µm. (C) Quantification of number of nuclei positive for Nanog. Data is shown as the mean ± SEM. (N=3 biological repeats, each data point shown is one field of view, with ≥20 fields of view per biological replicate). NS = not significant, P=0.1092, H = 0.177, by Kruskal-Wallis test. (D) Quantification of number of nuclei positive for Oct4. Data is shown as the mean ± SEM. (N=3 biological repeats, each data point shown is one field of view, with ≥20 fields of view per biological replicate). NS = not significant, P=0.2204, H = 0.146, by Kruskal-Wallis test.*

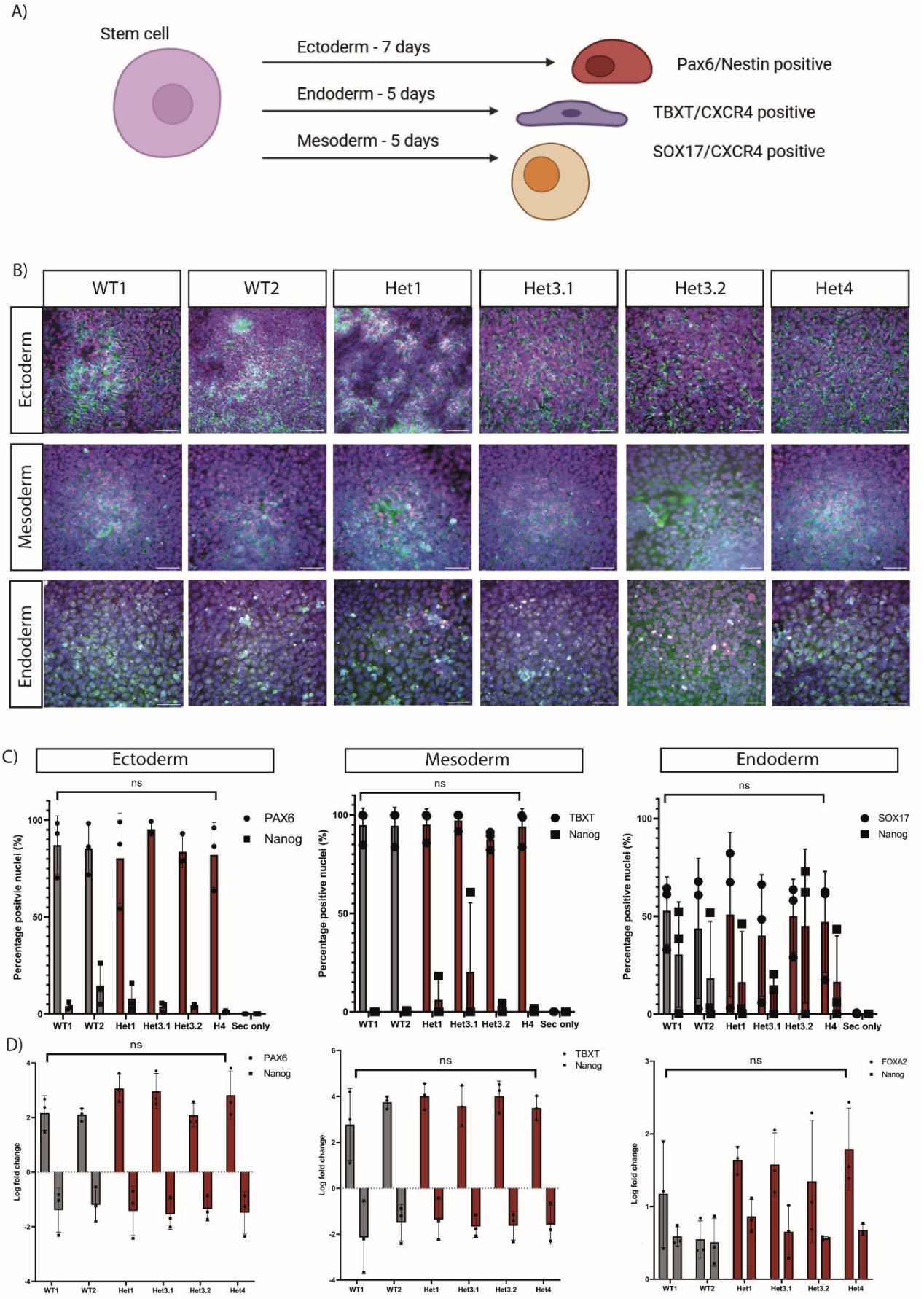

A)
Stem cell
Ectoderm - 7 days
Endoderm - 5 days
Mesoderm - 5 days
Pax6/Nestin positive
TBXT/CXCR4 positive
SOX17/CXCR4 positive
B)
WT1
WT2
Het1
Het3.1
Het3.2
Het4
Ectoderm
Mesoderm
Endoderm
C)
Ectoderm
Mesoderm
Endoderm
ns
PAX6
Nanog
TBXT
SOX17
Percentage positvie nuclei (%)
Percentage positive nuclei (%)
WT1 WT2 Het1 Het3.1 Het3.2 H4 Sec only
D)
Log fold change
FOXA2

Figure 3.5: Trilineage differentiation of the CMT2A hESC clone panel. *(A) Schematic depicting the trilineage differentiation protocol of the Stem Cell Technologies Trilineage Differentiation kit. (B) Immunofluorescence analysis of lineage markers in cells subjected to the differentiations highlighted in (A). Ectodermal cells were identified by expression of Nestin (green) and PAX6 (magenta). Mesodermal cells were identified by expression of Brachyury (magenta) and CXCR4 (green). Endodermal cells were identified by expression of SOX17 (magenta) and CXCR4 (green). Scale bars = 50µm. (C) Quantification of cells positive for the nuclear lineage marker as shown in (B) and nuclear stem cell marker Nanog. Data is shown as the mean ± SD (N=3 biological repeats). Kruskal-Wallis test with Bonferroni correction for multiple comparison for PAX6, TBXT, and FOXA2 fold change expression; ns = not significant. Ectoderm, p = 0.66, H = 0.142; mesoderm, p = 0.83, H = 0.0508; endoderm, p = 0.94, H = 0.337. (D) RT-qPCR gene expression analysis of lineage markers in the three lineages generated. Data is shown as the mean fold change relative to Day 0 of differentiation ± SD (N=3 biological repeats). Kruskal-Wallis test with Bonferroni correction for multiple comparison for PAX6, TBXT, and FOXA2 fold change expression; ns = not significant. Ectoderm, p = 0.454, H = 0.259; mesoderm, p = 0.454, H = 0.146; endoderm, p = 0.454, H = 0.357.TBXT=Brachyury*

3.2.3 MFN1/MFN2 expression in MFN2$^{R94Q/+}$ hESCs

The R94Q mutation in MFN2 is considered a dominant negative mutation and thus the introduction of a point mutation into MFN2 is not expected to impact the level of protein expression. Loss of MFN2 protein has been shown to have deleterious consequences in cells (Mou et al., 2020, Wojtyniak et al., 2022). Loss of MFN2 can also reduce the efficiency of hPSC differentiation into neurons (Fang et al., 2016). Additionally, MFN1 levels have been known to partially compensate for MFN2 loss (Sugiura et al., 2013, Stavropoulos et al., 2023). Loss of MFN1 can equally detrimental, with MFN1 knockdowns resulting in impaired neural induction and alter mitochondrial dynamics (Yamada et al., 2017, Zhang et al., 2020).

To confirm that the R94Q panel had unaltered expression levels of MFN1 and MFN2 after CRISPR-Cas9 editing, hESC lysates were analysed via Western blotting and probed for MFN1 or MFN2 alongside GAPDH as a loading control.

MFN1 expression was not changed by the introduction of MFN2$^{R94Q/+}$ as seen by Western blot analysis (Figure 3.6A). MFN1 signal was normalised to its loading control, and then to the relative MFN1 signal of WT1 (Figure 3.6B). No significant difference was found between the lines (p=0.617). When probing for MFN2 across the R94Q panel (Figure 3.6C), a similar trend was seen with no significant difference in expression across the cell lines (p=0.837) (Figure 3.6D), thus demonstrating no quantitative loss of protein.

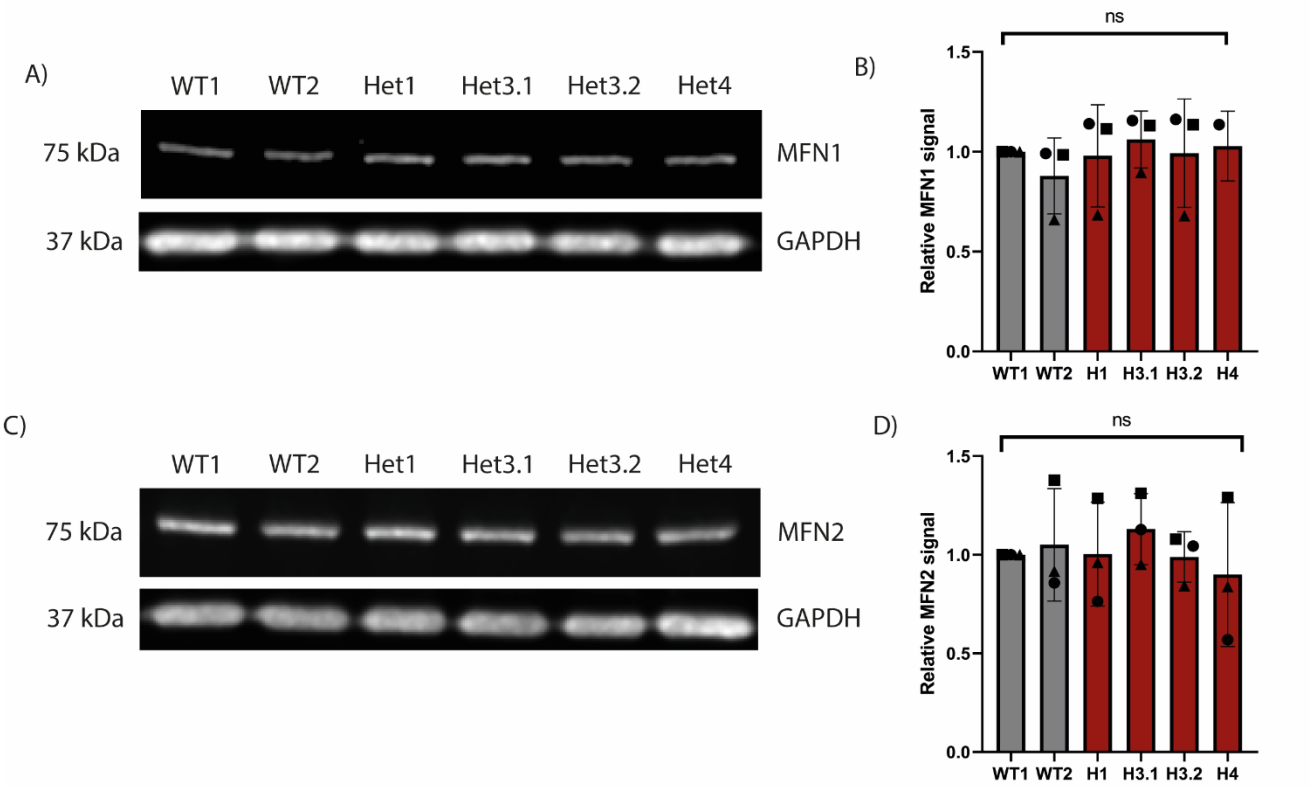


Figure 3.6: Expression of MFN1 and MFN2 in MFN2$^{R94Q/+}$ clone panel. *(A) Western blot analysis of MFN1 in hESCs. (B) Quantification of (A), normalised to WT1 hESCs. Kruskal-Wallis test, p = 0.84, H = 0.121. (C) Western blot analysis of MFN2 in hESCs. (D) Quantification of (C), normalised to WT1 hESCs. Kruskal-Wallis test, p = 0.62, H = 0.251. Data is shown as the mean ± SD (N=3 biological repeats).*

3.2.4 Generation and identification of CRISPR edited hESCs containing MFN2$^{T105M/+}$

Over 100 different mutations have been identified in MFN2 as causative for CMT2A. An allelic series of CMT2A-causing mutations on the same genetic background has not been generated before. A benefit to having this as a panel of cells is that this would eliminate any genetic or epigenetic variation between iPSC lines derived from different patients. In order to achieve this, CRISPR-Cas9 editing of different base pairs would need to be performed. From previous work in the lab, a guide RNA for the T105M mutation had already been designed and validated through a surveyor nuclease assay but never used to generate MFN2$^{T105M/+}$ hESCs (Figure 3.7A). In order to generate these cells now, this guide along with the pre-designed ssODN was electroporated into cells as before (Figure 3.7B). Cells were cultured for 48

hours before being single cell sorted and colony growth was monitored over two weeks.

As before, colonies were expanded enough to cryopreserve material and extract DNA. The PCR/RD screen was performed again, except this time the intended mutation introduced a new cut site for the restriction enzyme FokI (Figure 3.7D). The screen indicated that only 2 of the 59 clones had the on-target heterozygous mutation. These two clones (3B4 and 4H7) both showed two bands close together at the ~500bp mark, indicating that the primers were amplifying two products of very similar size and alluding to the presence of indels generating a slightly larger PCR product. This was confirmed by Sanger sequencing (Figure 3.7E). Sequencing of a suspected wild-type clone (2F10) also showed the presence of large indels.

CRISPR technology and *in silico* predictions of efficacy have increased exponentially over the last five years. The online program CRISPOR (https://crispor.gi.ucsc.edu/) is now capable of giving guide RNAs scores for their efficiency and their ability to generate indels. The previously generated guide for T105M scored highly for predicted generation of a frameshift after DNA strand break repair (Figure 3.8A). With the advancement of knowledge surrounding DNA editing and repair, alongside advancing CRISPR technology, a new guide (referred to as Guide 3) was suggested that had not been suggested by the program during the original guide design in 2018. This new guide was predicted to have a higher on-target efficiency with a lower off-target and frameshift score when compared to the original chosen guide.

The efficacy of this new guide RNA to guide the Cas9 enzyme to the intended DNA site was assessed using a surveyor nuclease assay (Figure 3.8B). Cells transfected with Cas9 and the guide RNA had their DNA harvested 48 hours post-transfection. The region of interest containing the intended edit site was amplified by PCR, and edited DNA was hybridised to wild-type DNA. The efficiency of the guide is determined by its ability to induce small indels by Cas9-induced DSB. When edited DNA is hybridised to wild-type DNA, there should be a mismatch in the sequence that can be detected by surveyor nucleases that cleave at sites of mismatch. Cleavage events generate smaller fragments of DNA that are detectable on agarose gels.

Transfection with the new T105M guide RNA did not generate any new bands indicating that it was not efficient at guiding the Cas9 to the intended site and therefore not suitable to use for a CRISPR editing experiment (Figure 3.8C). Due to time considerations and a lack of efficient guides suggested by online prediction tools, the generation of T105M clones was not pursued.

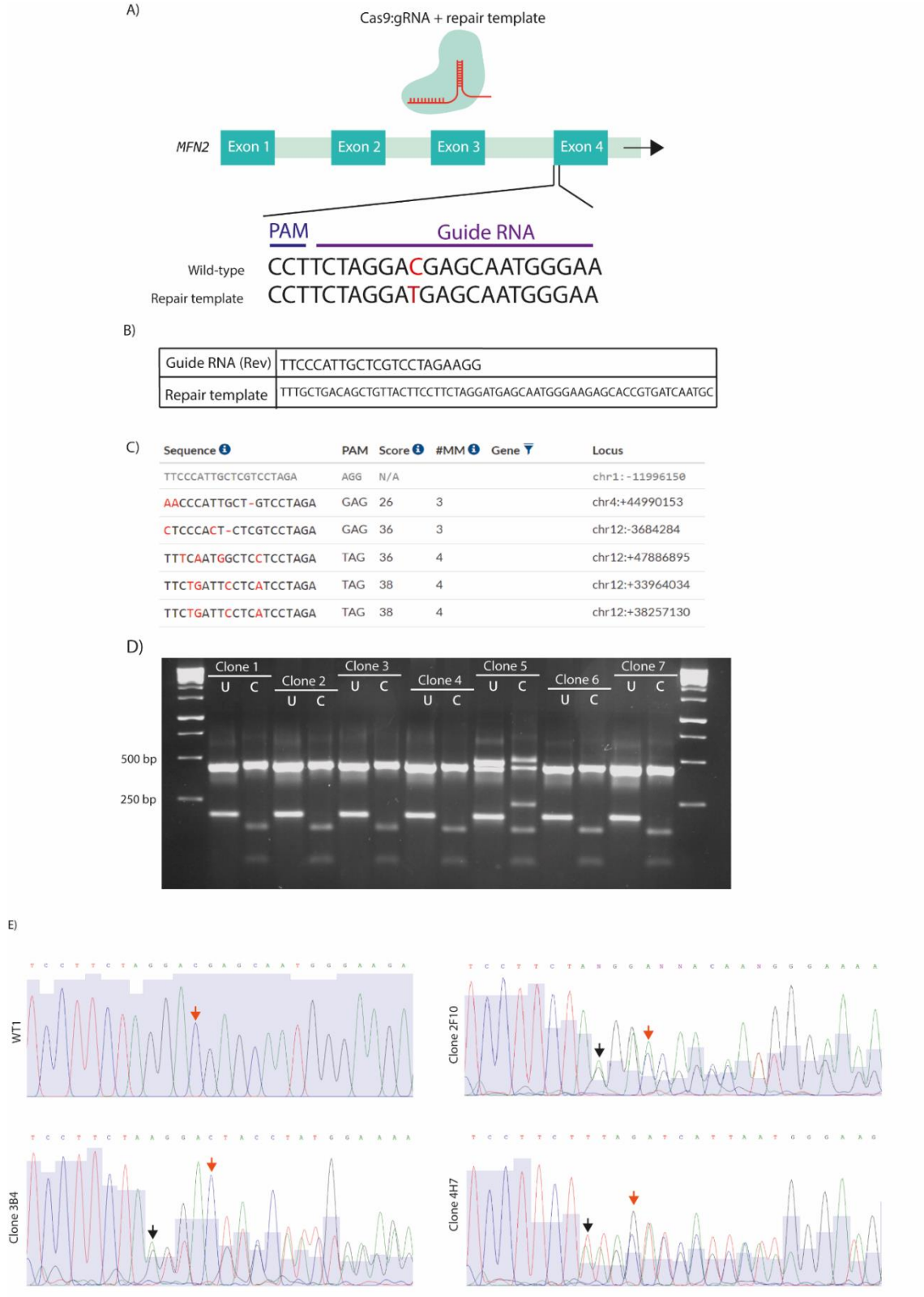
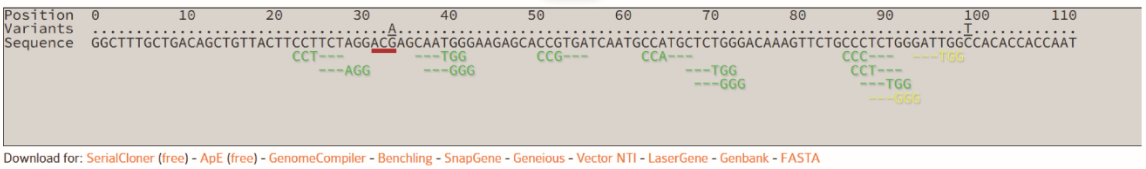


Figure 3.7: CRISPR-cas9 editing using previously generated guides for MFN2$^{T105M/+}$. *(A) Schematic showing CRISPR-cas9 system targeting Exon 4 of MFN2 to generate the C>T base pair substitution. (B) Sequences of DNA oligos used to generate and validate the C>T base pair substitution. (C) Top five most likely sites for off-target mutation using the chosen gRNA. (D) Example PCR/RD gel from screening for on-target edits in clones. U = uncut PCR fragment by RD, C = cut PCR fragment by RD. (E) Chromatograms generated by Sanger sequencing of the intended edit site. Black arrow indicates start of indel, red arrow indicates residue intended to be edited.*

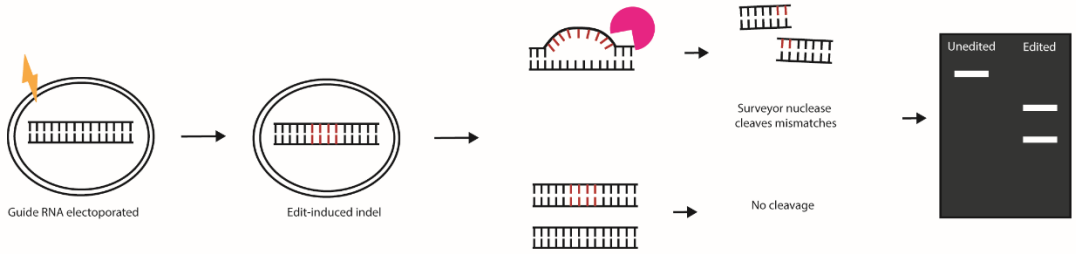
A)



Download for: SerialCloner (free) - ApE (free) - GenomeCompiler - Benchling - SnapGene - Geneious - Vector NTI - LaserGene - Genbank - FASTA

	Position/ Strand	Guide Sequence + *PAM* + Restriction Enzymes + Variants (Only G- / Only GG- / Only A-)	MIT Specificity Score	CFD Spec. score	Predicted Efficiency (Show all scores) Doench '16	Mor.-Mateos	Outcome Out-of-Frame	Lindel	Off-targets for 0-1-2-3-4 mismatches + next to PAM	Genome Browser links to matches sorted by CFD off-target score (exons only / chr1 only)
Guide 3	42 / fw	TTCCTTCTAGGACGAGCAAT *GGG* Enzymes: *BseMI, MboII* **Cloning / PCR primers**	89	93	48	56	46	54	0 - 0 - 5 - 9 - 69 0 - 0 - 0 - 0 - 0 83 off-targets	3:intergenic:RP11-371F15.3-RP11-577B7.1 4:intergenic:FMO9P-FMO10P 4:intergenic:ENPP7-CBX2 show all...
Guide 2	24 / rev	TTCCCATTGCTCGTCCTAGA *AGG* Enzymes: *MaeI* **Cloning / PCR primers**	81	90	47	48	78	87	0 - 0 - 3 - 21 - 80 0 - 0 - 0 - 0 - 0 104 off-targets	4:intergenic:RP6-1O2.1-MID1 3:exon:RP11-475O23.2 4:intergenic:RCAN1-CLIC6 show all...
Guide 1	72 / fw	CCGTGATCAATGCCATGCTC *TGG* Enzymes: *BslI, BslFI, Van91I* **Cloning / PCR primers**	80	92	43	36	63	74	0 - 0 - 0 - 6 - 68 0 - 0 - 0 - 0 - 3 74 off-targets	4:intergenic:RN7SL766P-LINC00424 4:exon:CCR7 4:intergenic:EYA2-RP5-1050K3.3/EYA2 show all...

B)



C)

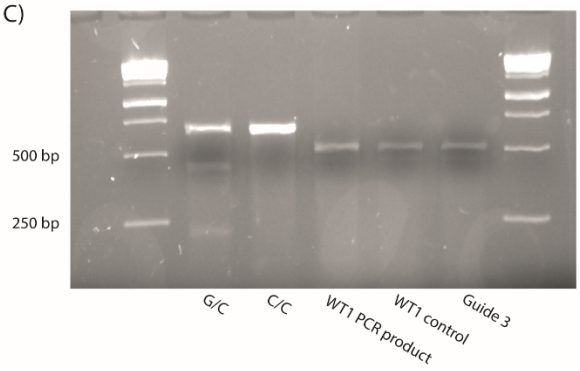


Figure 3.8: Generation of a new gRNA for MFN2$^{T105M/+}$. *(A) CRISPOR predictions of gRNA sequences for C314T showing a previously untested gRNA (Guide 3). (B) Schematic showing the workflow and premise of a surveyor nuclease assay for the detection of indels. (C) Electrophoresis gel of surveyor nuclease assay for assessing the activity of Guide 3.*

3.3 Generation of spinal motor neurons (sMNs) from MFN2$^{R94Q/+}$ hESCs:

3.3.1 Motor neuron differentiation protocol:

Motor and sensory neurons are the most affected cell types in CMT2A patients and are amongst the largest cells in the body, reaching from the spinal cord to the extremities of the limbs; in some humans, the longest motor neurons can be greater than a meter in length. Due to their impressive size and selective vulnerability in CMT2A, the hypothesis that neurons are affected in a length-dependent manner has gained traction (Ginsberg, 2020). These cell types are highly inaccessible within patients. Thus, stem cell models are ideal for generating these cell types and facilitating *in vitro* investigations that can be more accurately extrapolated to the disease in question. Dozens of protocols exist within the literature for differentiating hPSCs into a wide variety of neuronal cell types (Chang et al., 2021). We chose to focus on using hESC-derived sMNs for this project as these cultures are capable of generating large axonal projections in culture (>2mm in length) making them ideal for studying length-dependent processes. The impaired motor phenotype in CMT2A patients is also more consistently seen in patients compared to loss of proprioception and cutaneous sensation (Feely et al., 2011).

Previous work within the Barbaric lab successfully optimised a motor neuron differentiation protocol based on the Maury *et al* and Guo *et al* protocols (Figure 3.9A) (Maury et al., 2015, Guo et al., 2017, Butler, 2021)This optimised differentiation protocol begins with a 3D culture of embryoid bodies (EBs) of 3,000 cells. Dual SMAD inhibition by the small molecules LDN193189 and SB431542 pushes cells towards the early neuroectoderm (Chambers et al., 2009). WNT pathway activator CHIR99021 inhibits GSK3β and caudalises neural progenitors (Nordström et al., 2002, Xi et al., 2012). FGF2 is applied at a higher concentration than previously published protocols to guide progenitors further down the rostrocaudal axis (Figure 3.10) (Diez Del Corral and Morales, 2017). Sonic hedgehog (Shh) signalling is activated by Smoothened agonist (SAG) which is a known morphogen governing the dorsoventral axis of the spinal cord (Roelink et al., 1995). A low concentration of retinoic acid is used to push progenitors along the rostrocaudal axis of the spinal cord (Figure 3.10) (Patani et al., 2011). Notch inhibition is necessary for the maturation of motor neurons as it prevents continued

OLIG2 and Hes5 expression and a commitment to an oligodendrocyte fate (Ben-Shushan et al., 2015). This is achieved through γ-secretase inhibition by DAPT. Finally, the neurotrophic factors brain-derived neurotrophic factor (BDNF), glial-derived neurotrophic factor (GDNF), and ciliary neurotrophic factor (CNTF) promote survival and general neuronal health (Stansberry and Pierchala, 2023). This protocol produces OLIG2 expression in progenitors which induces expression of HB9 (Lee and Pfaff, 2003). HB9 is considered a pan-motor neuron marker however there are some sMN populations that are not characterised by HB9, including sMNs belonging to the medial lateral motor column (LMCm), the spinal accessory column (SAC), and the preganglionic motor column (PGC) (Stifani, 2014).

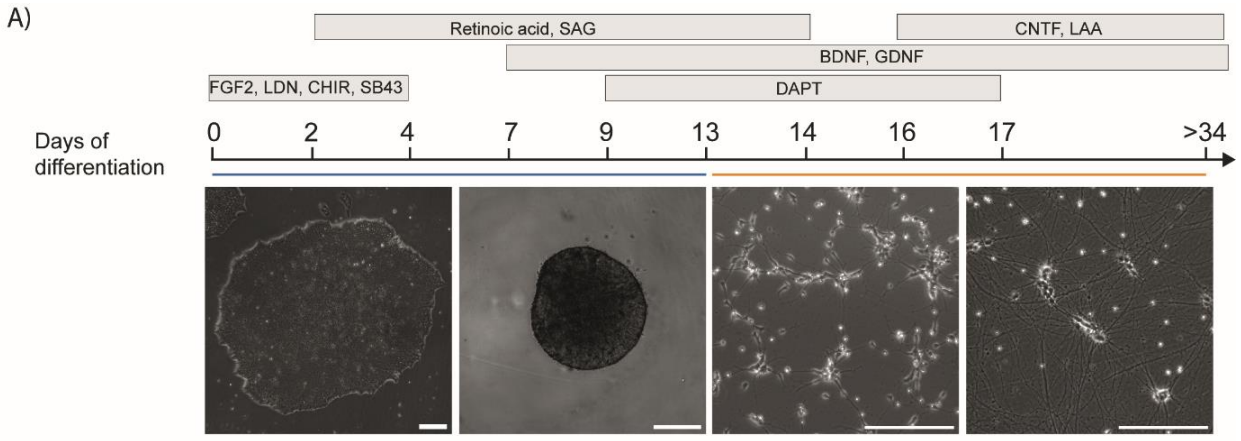


Figure 3.9: Optimised spinal motor neuron differentiation protocol. *(A) Differentiation schematic showing the application of small molecules across a 34-day differentiation. Blue line indicates the 3D portion of the differentiation, and the orange line indicates the 2D portion. Scale bar = 100 µm. SB43 = SB431542, LDN = LDN193189, CHIR = CHIR99021.*

sMNs belong to one of six motor columns which are arranged longitudinally along the rostrocaudal spinal axis and defined by their muscular targets (Figure 3.10). These include the SAC and PGC as well as the phrenic motor column (PMC), medial motor column (MMC), hypaxial motor column (HMC) and the lateral and medial lateral motor column (LMCl and LMCm respectively). The LMC contains limb-innervating neurons at the brachial and lumbar levels of the spine, corresponding with the upper and lower limbs respectively. Brachial and lumbar sMNs in the LMC are biochemically differentiated by the expression of HOX genes with brachial sMNs expressing HOX5-8 and lumbar neurons expressing HOX10-12. All LMC sMNs are

characterised by ISL1/2 and FOXP1 expression, with the LMCl also expressing LHX1 and HB9. These neurons are also cholinergic as they innervate muscles through cholinergic transmission and this is typified by expression of choline acetyltransferase – an enzyme that catalyses acetylcholine biosynthesis (Beigneux et al., 2004).

CMT2A is not considered a developmental disease and consequently one would expect that the introduction of the heterozygous R94Q mutation into wild-type hESCs would not impede their differentiation into motor neurons. In order to verify this assumption, the R94Q panel was subjected to our optimised differentiation protocol and analysed for the expression of mature motor neurons markers. In confirming that R94Q neurons develop similarly to wild-type neurons in culture, we can assume that any future findings are due to the exerted effects of MFN2$^{R94Q/+}$ on developed neurons, rather than a consequence of improperly formed or immature motor neurons.

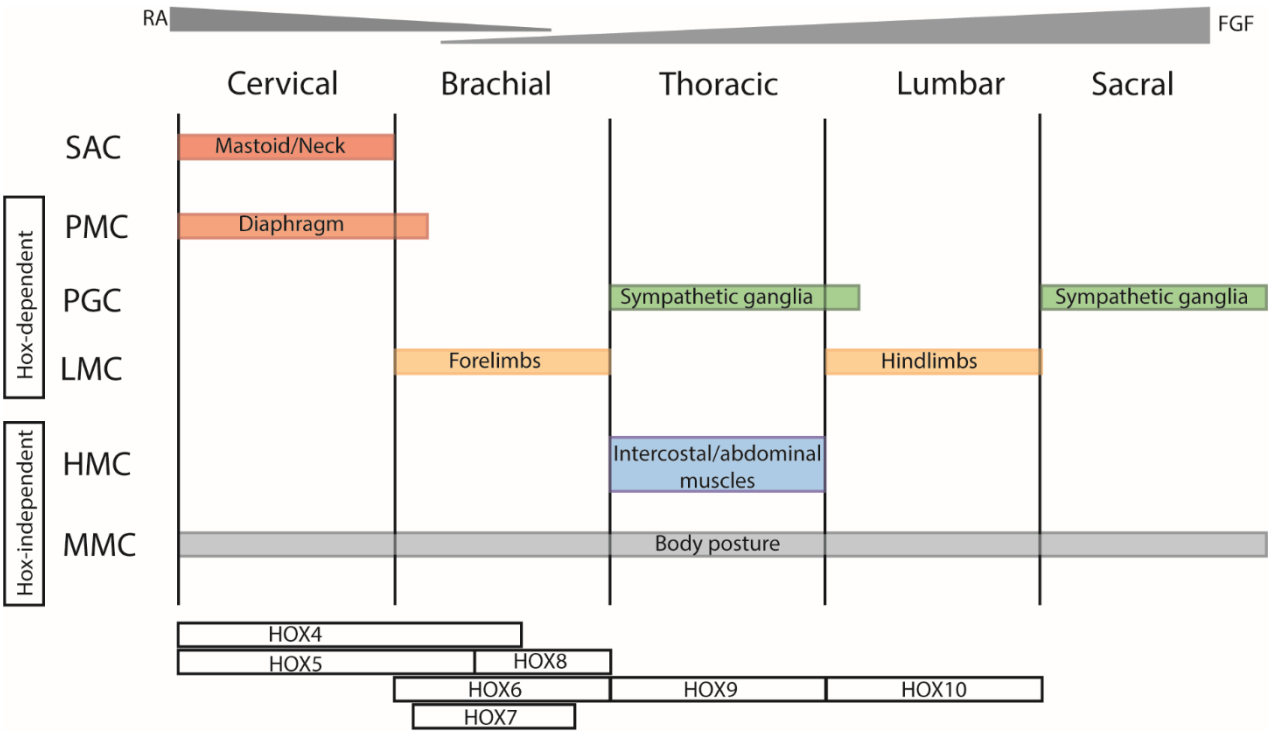


Figure 3.10: Organisation of the motor columns. *sMNs are organised into six motor columns: spinal accessory column (SAC), phrenic motor column (PMC), preganglionic motor column (PGC), lateral motor column (LMC), hypaxial motor column (HMC), and the medial motor column (MMC). The sMNs of each motor column target different groups of muscles within the body. Retinoic acid (RA) and FGF signalling gradients contribute to generation of the motor columns. HOX gene expression corresponds to different positions along the rostrocaudal axis, and some motor columns are dependent on HOX genes for their development.*

3.3.2 Expression of key sMN markers in neurons generated by the optimised sMN differentiation protocol

The R94Q panel was subjected to the optimised sMN differentiation protocol and neurons were assessed immunocytochemically for the expression of key sMN markers (ISL1/2, ChAT, FOXP1, HB9) at the final time point (Day 34) as well as mRNA expression at Day 0, Day 13, and Day 34.

Day 34 neurons were immunoreactive for ISL1/2 alongside the axonal marker Neurofilament Heavy Chain (NFH) (Figure 3.11A). When quantified as the percentage of positive nuclei, cells showed strong staining for ISL1/2 (WT1 88.1% ± 6.6, WT2 84.6% ± 6.2, Het1 83.7% ± 7.0, Het3.1 86.6% ± 10.7, Het3.2 83.7% ± 7.9, Het4 84.7% ± 4.1) with no significant difference identified between the lines (Figure 3.11B). RT-qPCR analysis of ISL1 across the course of the differentiation showed a strong increase in mRNA production between Day 0 and Day 34, with no differences identified between the lines at each time point (Figure 3.11C).

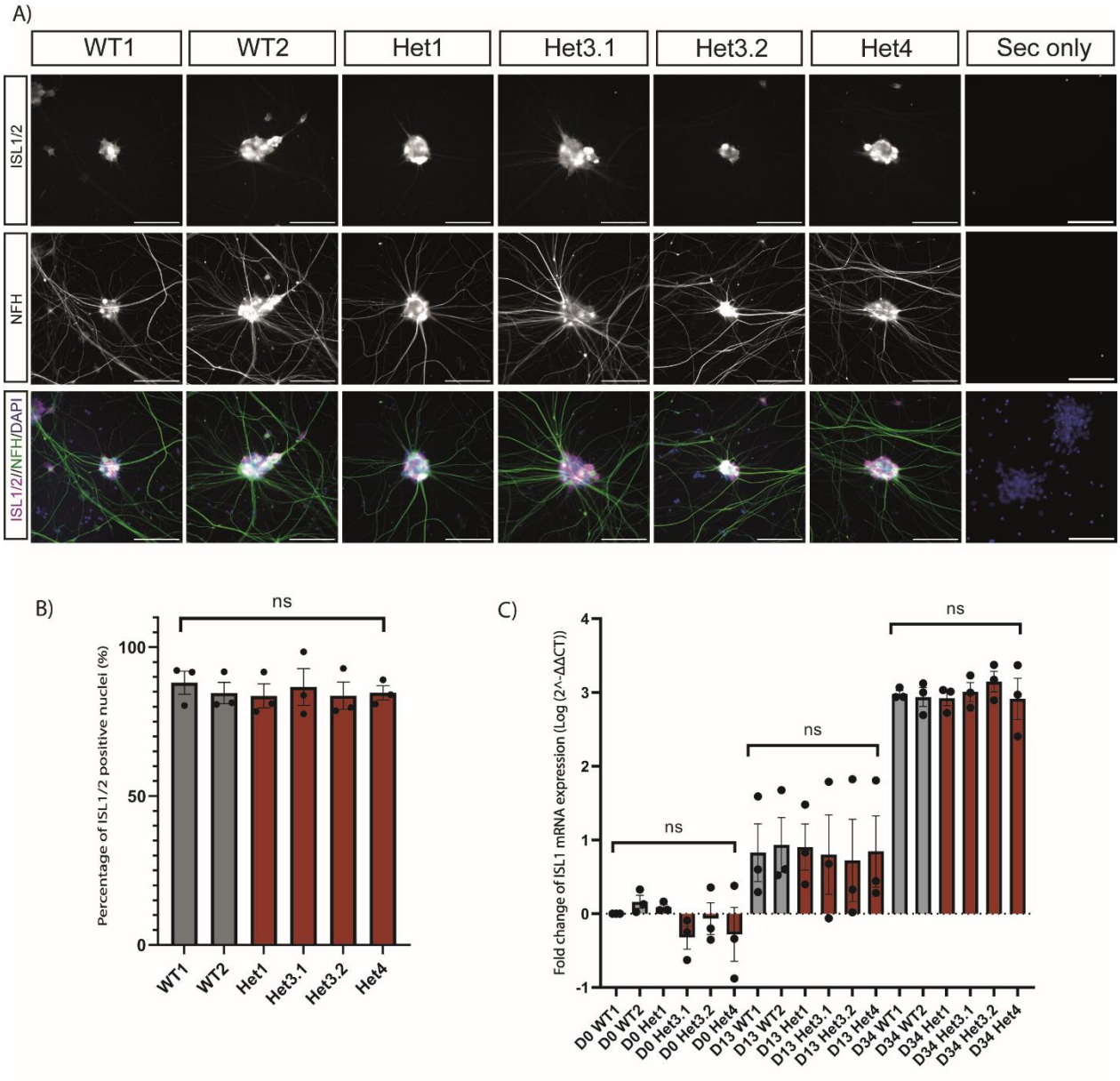


Figure 3.11: ISL1/2 expression in sMNs. *(A) Representative images from immunocytochemical analysis of Day 34 neurons. (B) Quantification of the number of positive nuclei as a percentage at Day 34. Data is shown as the mean ± SEM. Data points represent N = 3 biological repeats with ≥20 fields of view per biological replicate. Kruskal-Wallis test, p = 0.97, H = 0.164. (C) RT-qPCR analysis of ISL1 mRNA expression normalised to WT1 Day 0. Data shown as mean ± SEM, N = 3 biological repeats. Kruskal-Wallis test; Day 0, p = 0.277, H = 0.109; Day 13, p = 0.992, H = 0.374; Day 34, p = 0.93, H = 0.304.*

Day 34 neurons were also marked positive as cholinergic due to the presence of ChAT (Figure 3.12A). The majority of nuclei were ChAT+ (WT1 90.6% ± 4.9. WT2 92.0% ± 0.8, Het1 91.8% ± 1.6, Het3.1 94.4% ± 1.2, Het3.2 93.5% ± 2.4, Het4 88.9% ± 1.4) with no significant difference noted between the lines (Figure 3.12B). RT-qPCR showed a large upregulation of ChAT mRNA between Day 0 and Day 13, with

a small additional increase between Day 13 and Day 34 (Figure 3.12C). Again, there were no differences in ChAT mRNA expression between the lines at each time point.

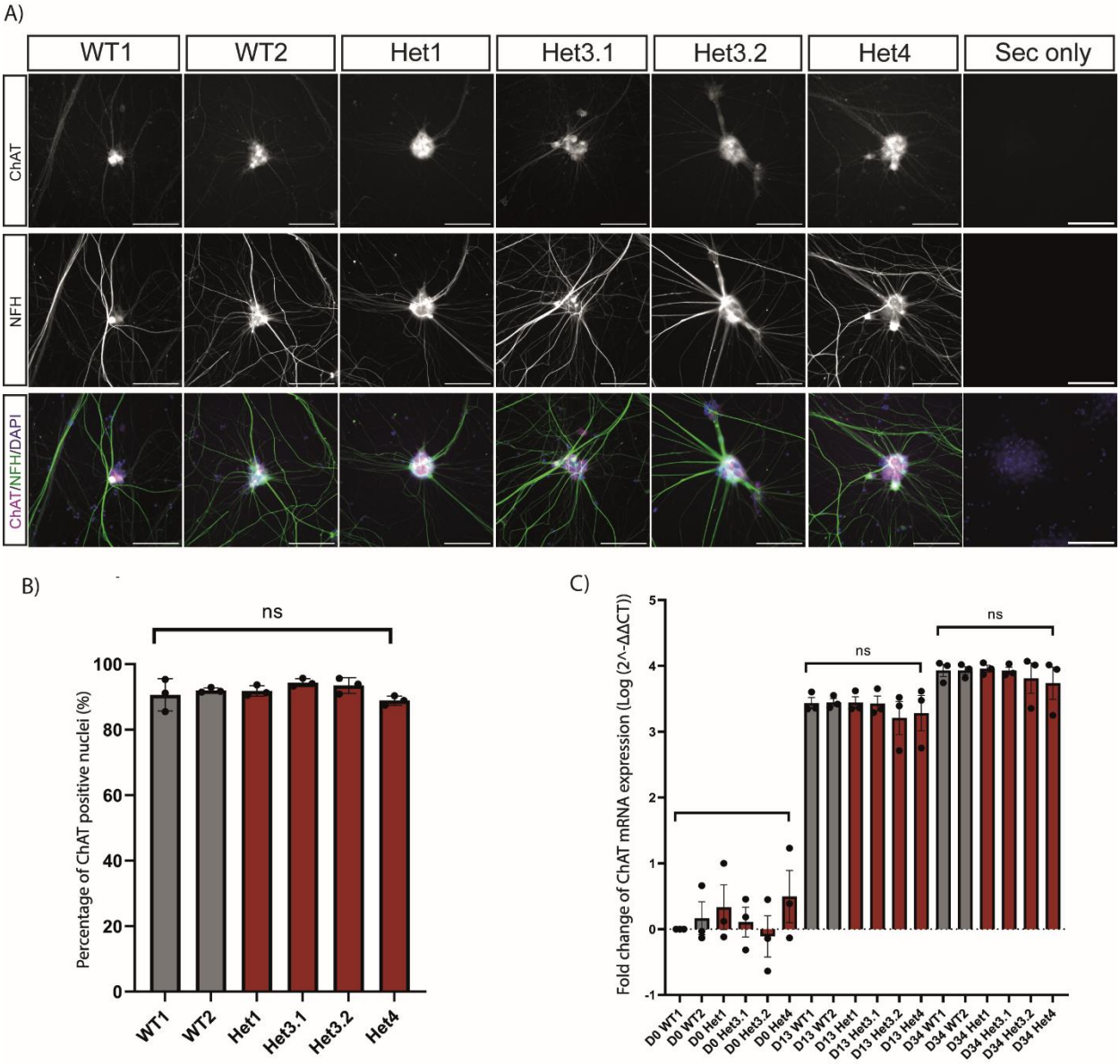


Figure 3.12: ChAT expression in sMNs. *(A) Representative images from immunocytochemical analysis of Day 34 neurons. (B) Quantification of the number of positive nuclei as a percentage at day 34. Data is shown as the mean ± SEM. Data points represent N=3 biological repeats with ≥20 fields of view per biological replicate. Kruskal-Wallis test; p = 0.117, H = 0.015. (C) RT-qPCR analysis of ChAT mRNA expression normalised to WT1 Day 0. Data shown as mean ± SEM, N = 3 biological repeats. Kruskal-Wallis test: Day 0, p = 0.797, H = 0.219; Day 13, p = 0.973, H = 0.345; Day 34, p = 0.966, H = 0.337.*

FOXP1 expression was also interrogated via immunocytochemistry in Day 34 neurons (Figure 3.13A). Quantification revealed no significant difference between the lines at Day 34 with all lines having >80% positive nuclei (WT1 80.2% ± 10.8, WT2 84.8% ± 10.0, Het1 86.2% ± 10.7, Het3.1 84.6% ± 11.0, Het3.2 83.2% ± 8.4, Het4

80.1% ± 8.8) (Figure 3.13B). RT-qPCR for FOXP1 was omitted due to a lack of efficient primers and time constraints. Alternatively, RNAseq data was used to look at FOXP1 transcripts (Figure 3.13C). Cultures used for the RNAseq were generated by Larissa Butler in 2021, according to 2.4.2, and sequencing and analysis was performed by Novogene. At the time of the RNAseq analysis, only WT1, WT2, and Het1 lines existed so FPKM (fragments per kilobase per million) values are only presented for these lines. In line with the immunofluorescence data, there was no difference found between lines. Observed FOPX1 intensity in Figure 3.13A appears lower than other MN-associated markers investigated in this chapter plus FPKM values are quite low. This may suggest that there is a reduced ability of cells to induce FOXP1 or that FOXP1 expression is being downregulated at this time point compared to prior time points in the differentiation. As time course data for FOXP1 expression in this differentiation protocol was not collected, it cannot be deduced whether expression peaked at an earlier timepoint or was never strongly induced.

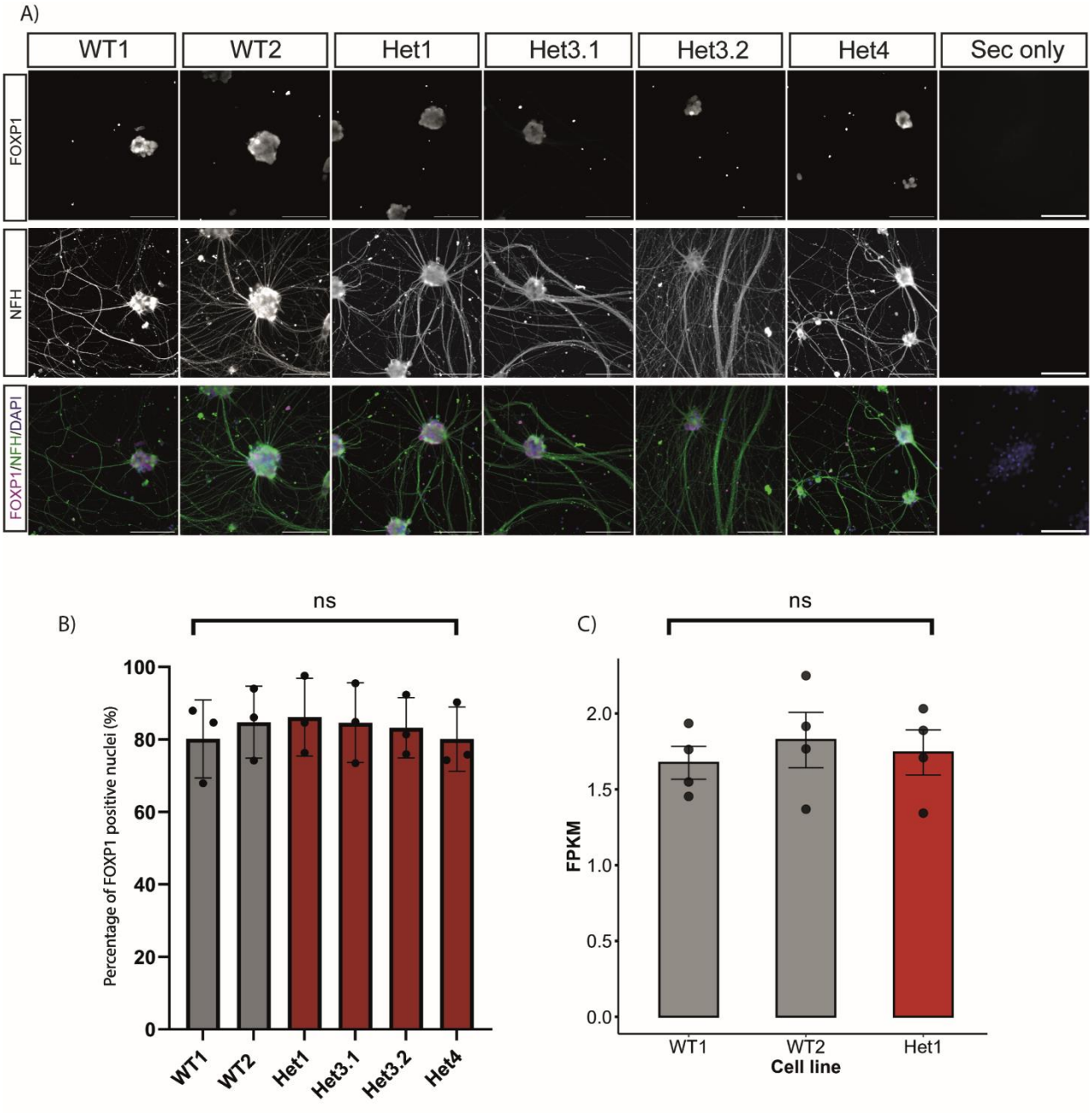


Figure 3.13: FOXP1 expression in sMNs. *(A) Representative images from immunocytochemical analysis of Day 34 neurons. (B) Quantification of the number of positive nuclei as a percentage at Day 34. Data is shown as the mean ± SEM. Data points represent N=3 biological repeats with ≥20 fields of view per biological replicate. Kruskal-Wallis test; p = 0.959, H = 0.329. (C) FPKM values for FOXP1 from RNAseq analysis performed on Day 34 neurons. N = 4 biological replicates. Kruskal Wallis test, p = 0.779, H = 0.167.*

Finally, HB9 expression was investigated at the protein and transcript level. Nuclei were marked positive for HB9 by immunocytochemistry at Day 34 (Figure 3.14A), with all lines showing >60% positive nuclei and no significant difference between the lines (WT1 64.3% ± 4.3, WT2 65.2% ± 4.9, Het1 72.4% ± 4.6, Het3.1 69.8% ± 11.3,

Het3.2 68.0% ± 8.4, Het4 66.1% ± 9.5) (Figure 3.14B). RT-qPCR analysis revealed an upregulation of HB9 at Day 13 and Day 34 compared to Day 0, with no differences identified between the lines at the measured time points (Figure 3.14C). Strong expression of ISL1/2, ChAT, and HB9, alongside FOXP1 in these neurons indicates a large population of sMNs that belong to the LMC.

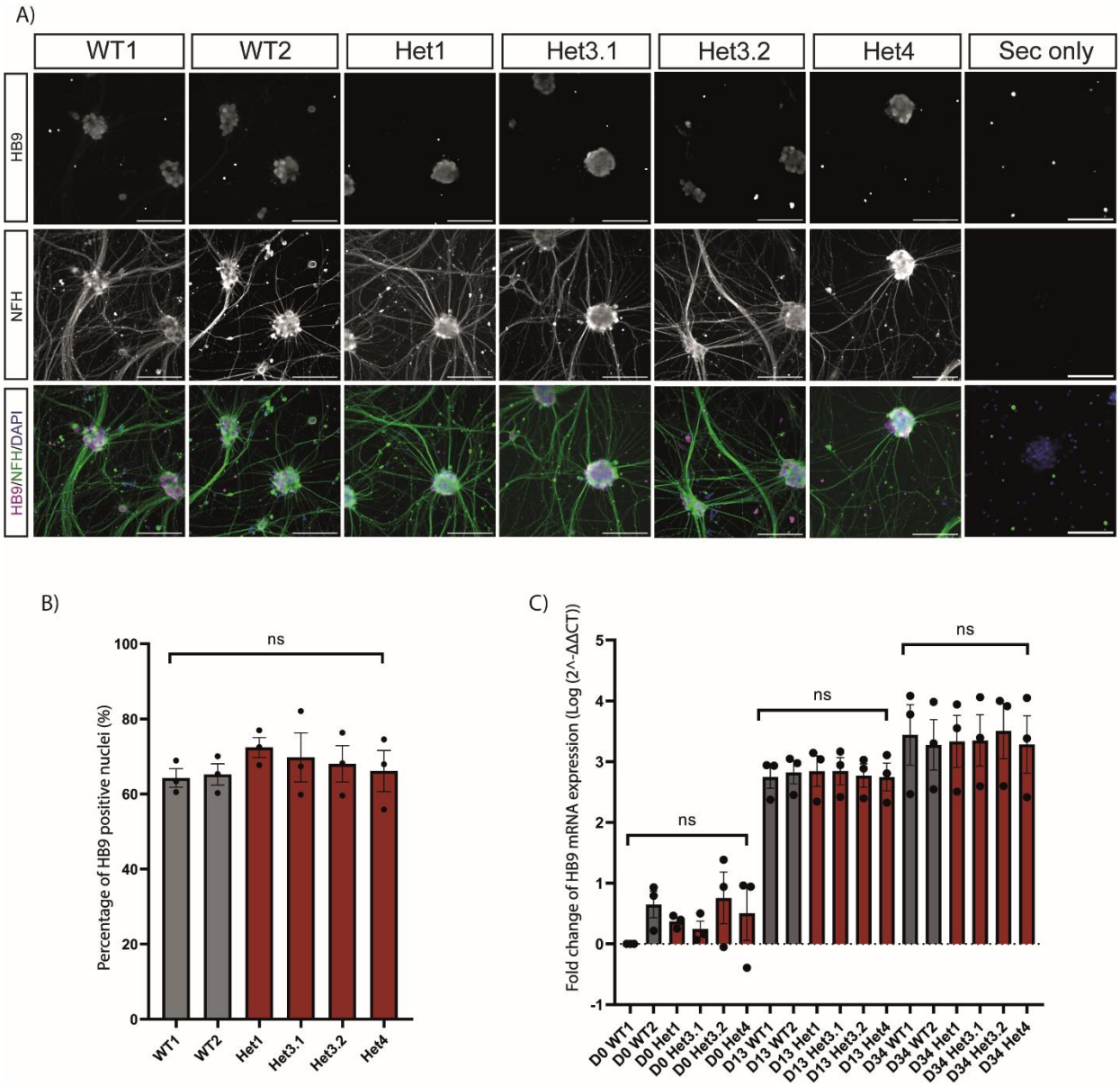


Figure 3.14: HB9 expression in sMNs. *(A) Representative images from immunocytochemical analysis of Day 34 neurons. (B) Quantification of the number of positive nuclei as a percentage at Day 34. Data is shown as the mean ± SEM. Data points represent N=3 biological repeats with ≥20 fields of view per biological replicate. Kruskal-Wallis test; p = 0.819, H = 0.0978. (C) RT-qPCR analysis of HB9 mRNA expression normalised to WT1 Day 0. Data shown as mean ± SEM, N = 3 biological repeats. Kruskal-Wallis test: Day 0, p = 0.452, H = 0.0237; Day 13, p = 0.889, H = 0.275; Day 34, p = 0.981, H = 0.355..*

3.3.3 Additional assessment of sMN markers by RT-qPCR

The previous assessment of the four main markers for sMNs indicates that the optimised differentiation protocol produces a high proportion of sMNs, but a more precise identity for these cells can be deduced through the expression profiles of additional sMN-associated genes and HOX genes.

All lines showed an equivalent decrease in NANOG mRNA expression at Day 13, which was sustained throughout the rest of the differentiation, corroborating that all lines had differentiated away from a stem cell identity (Figure 3.15A). The early motor neuron marker OLIG2 expression peaked at the Day 13 timepoint and showed a lower expression at Day 34 compared to Day 13 indicating that the neurons had exited a MN progenitor state and had begun to mature (Figure 3.15B). PHOX2B has previously been shown to be upregulated in cells generated by this protocol, suggesting that some of the neurons generated belong to the spinal accessory column (SAC) and are equivalent to neurons found at the cervical level of the human spinal cord that innervate the neck and shoulders (Butler, 2021). PHOX2B mRNA was upregulated at the progenitor stage, with a small decrease in expression as the cells matured to Day 34 suggesting that some SAC MNs were present in culture (Figure 3.15C). LHX1 mRNA expression was also interrogated as a specific marker for the lateral portion of the lateral motor column (LMCl) (Figure 3.15D). LHX1 expression was upregulated in Day 13 and Day 34 neurons indicating that neurons belonging to the LMCl were present in the culture. Importantly, there is no significant difference in the expression of any of these markers between lines at each measured timepoint.

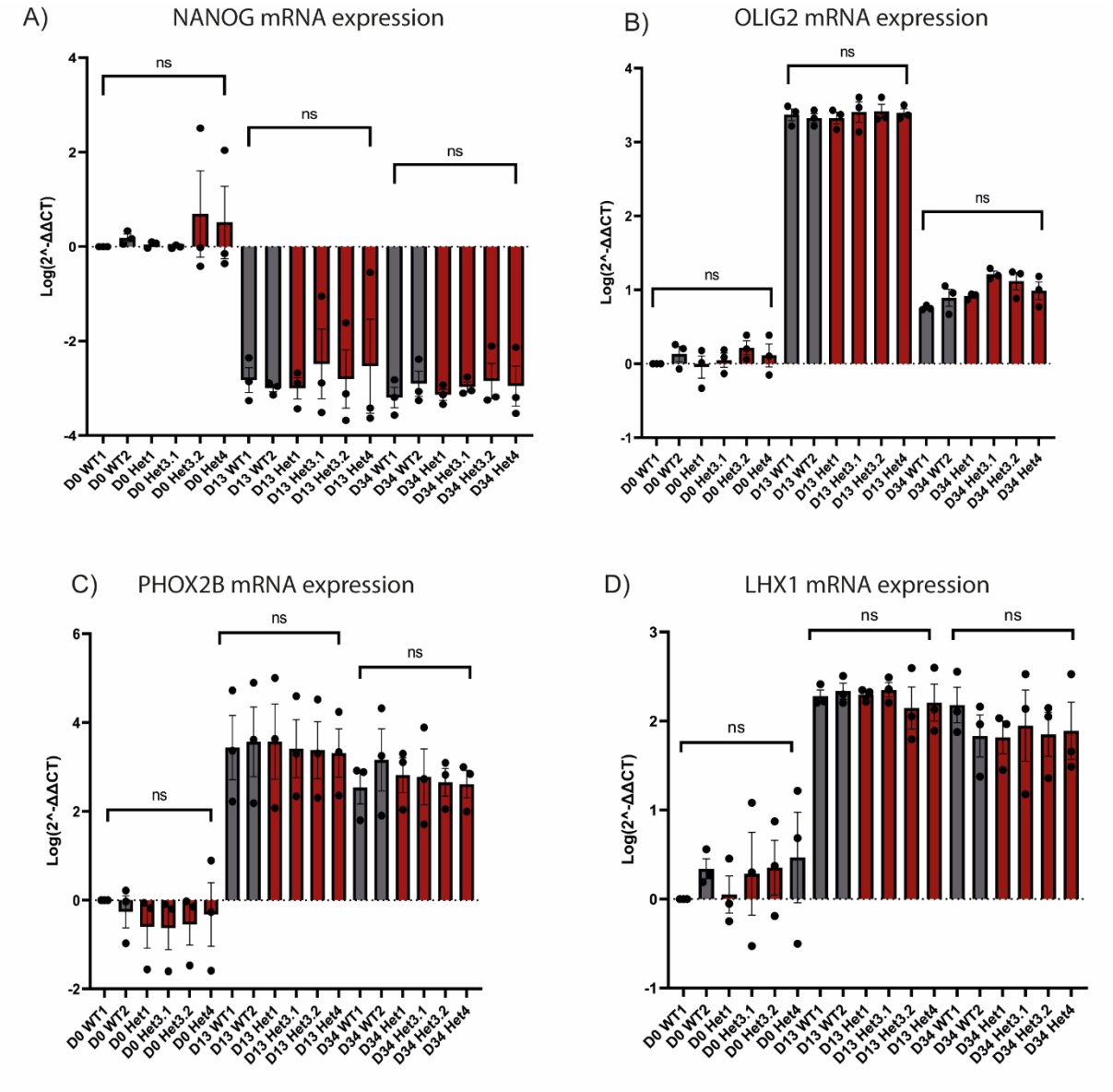


Figure 3.15: Expression of additional sMN markers across differentiation. *(A) RT-qPCR analysis of NANOG (Day 0, p = 0.582, H = 0.102; Day 13, p = 0.976, H = 0.349; Day 34, p = 0.880, H = 0.269), OLIG2 (Day 0, p = 0.495, H = 0.0511; Day 13, p = 0.966, H = 0.337; Day 34, p = 0.08, H = 0.404) (B), PHOX2B (Day 0, p = 0.359, H = 0.0409; Day 13, p = 0.999, H = 0.40; Day 34, p = 0.874, H = 0.265) (C), and LHX1 (Day 0, p = 0.821, H = 0.233; Day 13, p = 0.922, H = 0.298; Day 34, p = 0.925, H = 0.30) (D) mRNA expression throughout motor neuron differentiation, normalised to WT1 Day 0. Data shown as mean ± SEM, N = 3 biological repeats: Kruskal-Wallis test, ns = p>0.05.*

HOX gene expression is an additional measure for assessing the identity of the neurons generated by the optimised differentiation protocol by localising the cells to a specific area along the rostrocaudal axis of the spinal cord. Neurons showed a robust upregulation of the brachial- associated HOX paralogous groups HOXA4, HOXB5, HOXB6, and HOXB7 (Figure 3.16A-D). HOXC8 is considered as lower brachial and upper thoracic – its expression is present at Day 13 and Day 34 in all lines but shows a more variable expression profile compared to HOXPG4-7 (Figure

3.16E). HOXC9, which is exclusively expressed at the thoracic level of the spinal cord, was also expressed at Day 13 and Day 34 in all lines (Figure 3.16F). The relative fold change of HOXC9 expression was around half of that of the other HOXPG groups and considerably more variable, suggesting that only a small proportion of cells were expressing HOXC9 mRNA. Taken together, this HOX gene analysis suggests that the neurons generated by the optimised differentiation protocol are predominantly of the brachial identity. Pairing this with cells that are also ISL1/2+, FOXP1+, and HB9+ it can be concluded that the neurons generated here belong predominantly to the LMCl, the motor column that that innervates the dorsal region of the upper limbs. Critically, the expression of all sMN markers at the transcript level and protein level are unaltered by the introduction of $MFN2^{R94Q/+}$, further confirming that CMT2A is not a developmental disease. We can also infer that any future findings in neurons generated by applying this differentiation protocol to the R94Q panel is due to an effect exerted by $MFN2^{R94Q/+}$ in mature neurons and not due to starting differences in neuron identity.

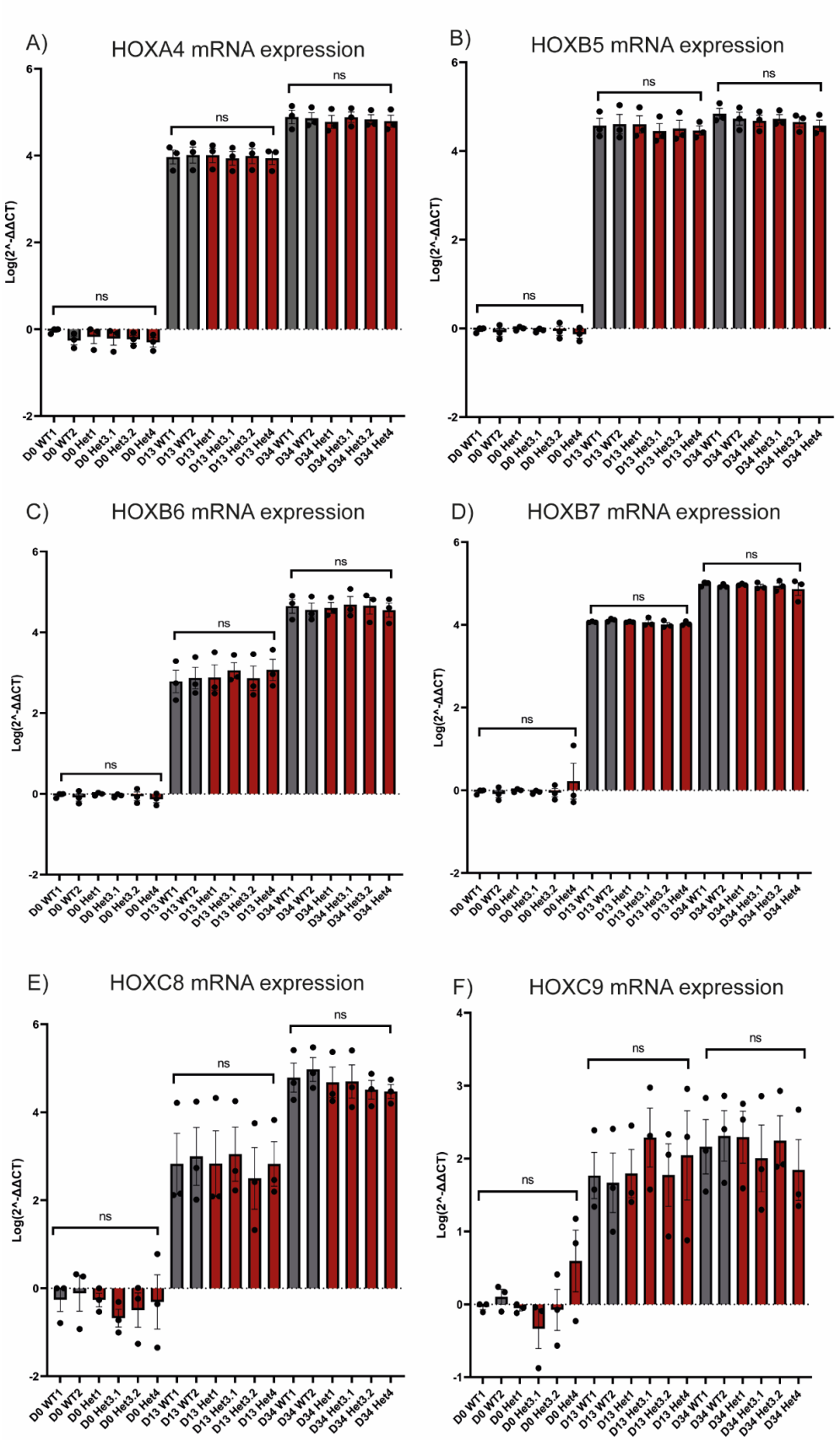


Figure 3.16: HOX gene expression across sMN differentiation. *(A) RT-qPCR analysis of HOXA4 (Day 0, p = 0.380, H = 0.0252; Day 13, p = 0.914, H = 0.292; Day 34, p = 0.927, H = 0.302), HOXB5 (Day 0, p = 0.831, H = 0.239; Day 13, p = 0.880, H = 0.269; Day 34, p = 0.839, H = 0.244) (B), HOXB6 (Day 0, p = 0.831, H = 0.239; Day 13, p = 0.805, H = 0.224; Day 34, p =*

0.990, H = 0.370) (C), HOXB7 (Day 0, p = 0.911, H = 0.290; Day 13, p = 0.473, H = 0.037; Day 34, p = 0.871, H = 0.263) (D), HOXC8 (Day 0, p = 0.810, H = 0.227; Day 13, p = 0.932, H = 0.306; Day 34, p = 0.687, H = 0.160) (E), and HOXC9 (Day 0, p = 0.689, H = 0.161; Day 13, p = 0.925, H = 0.30; Day 34, p = 0.784, H = 0.212) (F) mRNA expression throughout motor neuron differentiation, normalised to WT1 Day 0. Data shown as mean ± SEM from N = 3 biological repeats; Kruskal Wallis test..

3.3.4 Additional assessment of sMN function

Further preliminary investigations were made into the electrophysiological function of the sMNs generated by the optimised differentiation protocol and if the presence of the R94Q had any clear effect on these parameters. Patch-clamping to assess electrical activity was selected over the use of microarrays as sMNs do not typically have high network connectivity in monocultures; the neurons secrete the neurotransmitter acetylcholine but are only responsive to glutamine. Patch-clamp experiments were carried out to assess the electrical activity of WT1, WT2, and Het1 sMNs at Day 34. Only these lines were assessed as Het3.1, Het3.2, and Het4 did not exist at this time. All three lines produced sMNs that exhibited membrane potential responses in response to different current injections (Figure 3.17A). All sMNs displayed both fast inward Na^+ currents (Figure 3.17B, C) and outward K^+ currents (Figure 3.17B).

No clear differences were observed between $MFN2^{+/+}$ and $MFN2^{R94Q/+}$ sMN inward Na^+ currents, with voltage-dependent activation occurring at a threshold of ~ -50 mV, with a peak conductance of ~ -30 mV (Figure 3.17E). Additionally, no clear differences were observed between the resting membrane potentials of the sMNs analysed, which sat at ~ -65 mV (Figure 3.17F).

To further confirm no differences in the electrophysiology between $MFN2^{+/+}$ and $MFN2^{R94Q/+}$ sMNs, the axon initial segment (AIS) was investigated for any changes in length. The AIS is where action potentials are initiated in the proximal axon, thus this highly specialised area has a high density of voltage-gated ion channels and scaffolding proteins (Huang and Rasband, 2018). The AIS is identified by the presence of ankyrin G, which is considered the master organiser of AIS ion channel clustering (Huang and Rasband, 2018). Changes to the length of the AIS have been associated with alteration in the electrophysiological properties of neurons; for example, in hiPSC-derived sMNs from ALS patients neuronal hyperexcitability correlated with increased AIS length (Harley et al., 2023). To that end, Day 36 $MFN2^{+/+}$ and $MFN2^{R94Q/+}$ sMNs were stained for ankyrin G to identify the AIS and the

length of the AIS was measured (Figure 3.18A). The AIS was only measured when it had two clear ends and was in frame. The preliminary experiment revealed no obvious trends between the AIS length in $MFN2^{+/+}$ and $MFN2^{R94Q/+}$ sMNs, with each line having an average AIS length between 24 µm and 28 µm (Figure 3.18B).

With no clear differences in the electrophysiological properties of $MFN2^{+/+}$ and $MFN2^{R94Q/+}$ sMNs identified in these preliminary experiments, no further investigations were conducted.

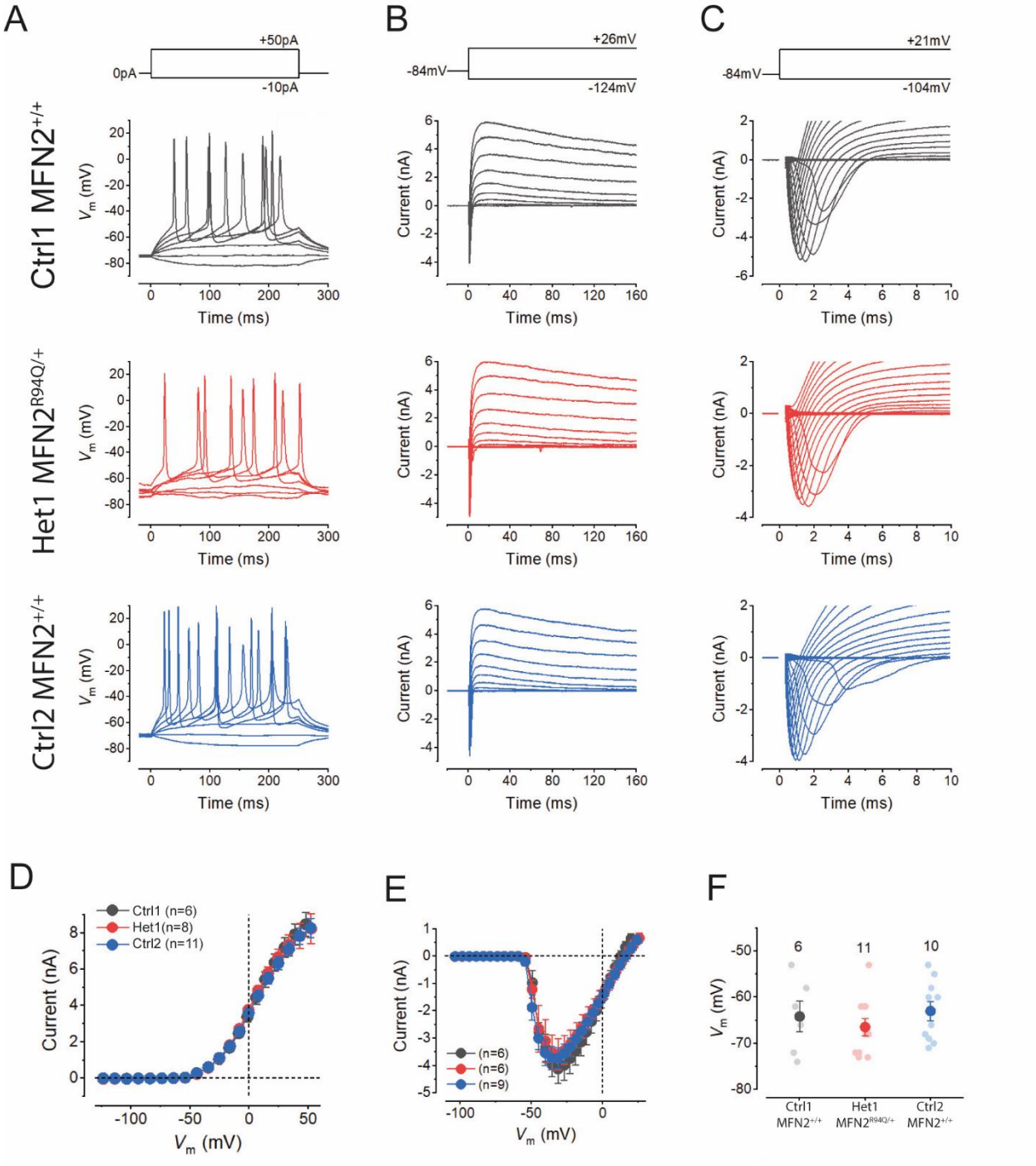


Figure 3.17: Electrophysiological characterisation of hESC-derived sMNs. *(A) Membrane potential responses from WT1 (black, upper panel) and Het1 (red, middle panel) and WT2 (blue, lower panel) neurons in response to depolarising current injection. Cells were stimulated with the current clamp protocol shown above. (B) Inward Na^+ (I_{Na}, negative) and outward K^+ (I_K, positive) currents from WT1 (black, upper panel) and Het1 (red, middle panel) and WT2 (blue, lower panel) neurons recorded in voltage clamp in response to the voltage protocol shown above. (C) Inward I_{Na} from WT1 (black, upper panel) and Het1 (red, middle panel) and WT2 (blue, lower panel) neurons in response to 10 ms voltage steps in 5 mV increments (voltage protocol shown above). (D) Average steady-state tail current-voltage (I-V) curves for I_K from all Ctrl $MFN2^{+/+}$ (black), Het1 $MFN2^{R94Q/+}$ (red) and Ctrl2 $MFN2^{+/+}$ (blue) neurons measured towards the end of the voltage protocol (E) Average peak I-V curves for I_{Na} from all all Ctrl $MFN2^{+/+}$, Het1 $MFN2^{R94Q/+}$ and Ctrl2 $MFN2^{+/+}$ neurons measured at the peak of the inward currents. (F) Resting membrane potentials from WT1 $MFN2^{+/+}$, Het1 $MFN2^{R94Q/+}$ and WT2 $MFN2^{+/+}$ neurons measured in current clamp at 0pA (in A). Cells were differentiated by Larissa Butler and electrophysiological experiments and data analysis were carried out by Stuart Johnson in 2021. N = 1 biological replicate with the number of neurons analysed per condition indicated in the figure.*

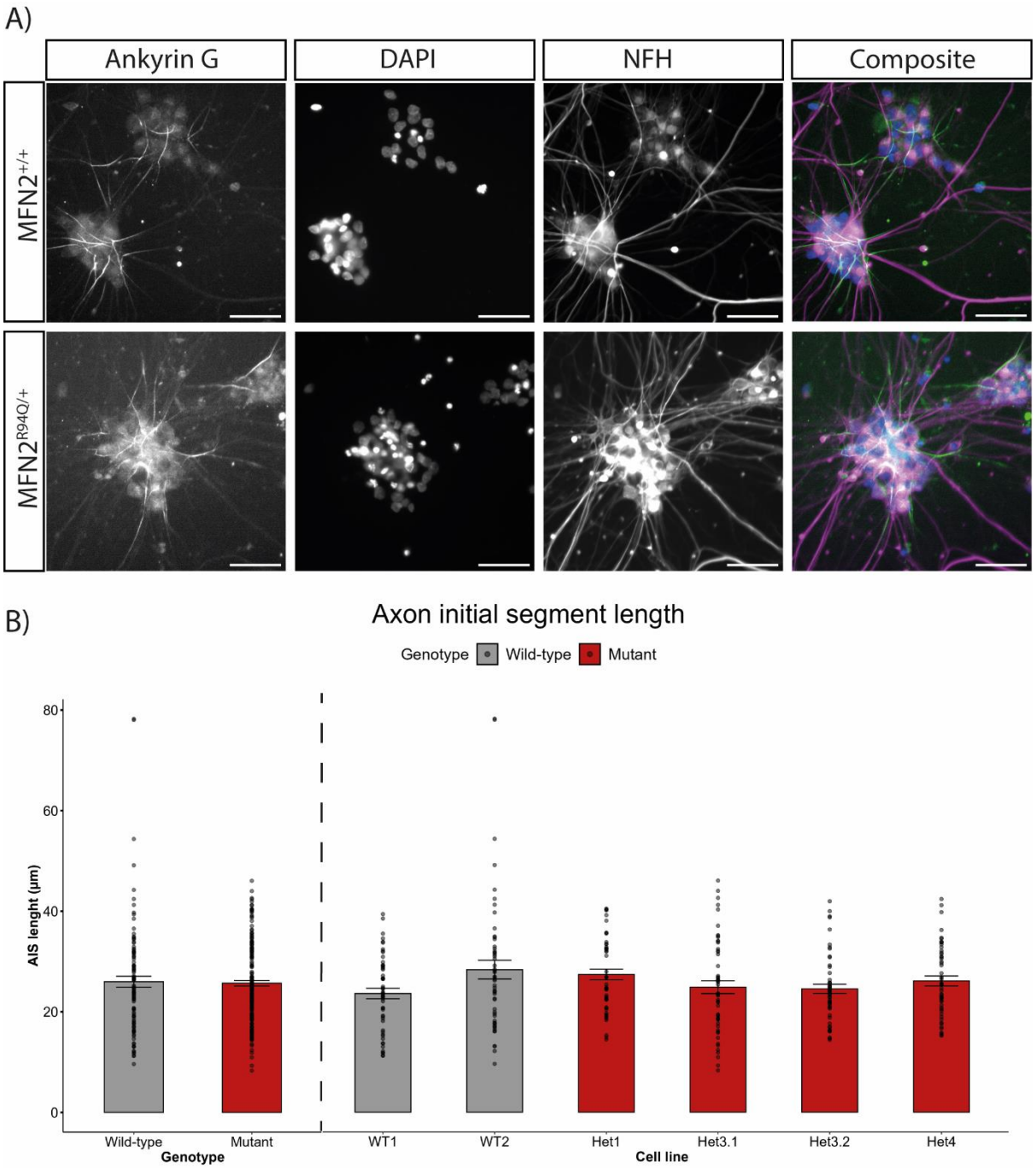


Figure 3.18: Characterisation of the axon initial segment in hESC-derived sMNs. *(A) Representative images of Ankyrin G staining in Day 36 MFN2$^{+/+}$ and MFN2$^{R94Q/+}$ sMNs. Scale bar = 50 µm. Nuclei are shown in blue, NFH in magenta, and Ankyrin G in green. (B) Quantification of the length of the AIS in µm. Data plotted as mean ± SD, N = 1 biological replicate, ≥ 50 AIS measured per cell line.*

3.4 Discussion

In summary, this chapter details the generation of three new MFN2$^{R94Q/+}$ sub clones through CRISPR-Cas9 editing of wild-type MasterShef11 hESCs. These three new clones, alongside WT1, WT2, and Het1 now comprise a panel of six hESC lines for

the *in vitro* study of CMT2A. All six lines maintained their inherent stem cell characteristics and were capable of generating sMNs that belong to the LMC at the brachial level.

Following on from Butler, 2021 this is still the only reported body of work that has produced CMT2A lines through the editing of wild-type hESCs. Thus far, all other hPSC models in the literature have utilised patient iPSCs paired with isogenic/sibling controls (Saporta et al., 2015, Rizzo et al., 2016, Van Lent et al., 2021) or MFN2 knockdown in hESCs (Mou et al., 2021). As discussed in Chapter 1, hiPSCs have been revolutionary as a disease-modelling resource but there is much benefit in having complementary hESC models of disease to corroborate results and allow access to different disease-causing mutations and genetic backgrounds. The use of hESCs independently or alongside iPSC-based models can control for inter-patient variability that arises from genetic and epigenetic memory, and from inefficient reprogramming (Ghosh et al., 2010, Scesa et al., 2021). Inter-patient and inter-clone variability is a well noted phenomenon within stem cell research, and is mainly attributed to epigenetics (Volpato and Webber, 2020). This variability can confound experimental findings, thus highlighting the need for hESC models like that described in Chapter 3 to independently demonstrate disease phenotypes.

In this chapter, a precise heterozygous point mutation (G281>A) was introduced into MFN2 in wild-type MasterShef11 hESCs using CRISPR-Cas9 editing. Screening revealed that a large percentage of clones that survived single-cell cloning post-editing were heterozygous or homozygous for the intended edit, with >50% of clones being putative homozygotes. The gRNA and ssODN used for generating this edit conferred strong activity and thus generating more heterozygous mutants could be achieved by using a less efficient guide. NHEJ is more likely to be the repair pathway for DSB generated by Cas9, and many of the putative heterozygotes had indels around the intended edit site. Two clones with the correct heterozygous mutation and no indels at the edit site were identified, and this was deemed to be sufficient for expanding the R94Q panel. Rates of HDR can be enhanced by using small molecule enhancers, cold shock post-electroporation, or alternative Cas species (Skarnes et al., 2019). The two correctly-edited clones were sub-cloned to ensure the lines were homogenous for the heterozygous mutation. The sub-cloning of the second clone revealed a mix of genotypes, highlighting the necessity for two rounds of single-cell

cloning. It is important to note that the mutant clones were not assessed for potential epigenetic changes.

CRISPR-Cas9 editing of hESCs to contain a MFN2$^{T105M/+}$ was tried using a previously validated gRNA. This gRNA and ssODN conferred a very low rate of HDR and an extremely high rate of NHEJ resulting in all surviving clones containing indels. Whilst generating MFN2$^{T105M/+}$ clones was not achieved during the given timeframe, the experiment does highlight the flexibility of hESC-based approaches for generating allelic series on the same genetic background and for modelling rare genotypes where patients cells are not available.

The successfully edited R94Q panel was differentiated into sMNs using a previously optimised differentiation protocol (Butler, 2021). All lines showed a comparable ability to differentiate along this lineage, indicating that MFN2$^{R94Q/+}$ does not impede differentiation. These results also highlight the importance of choosing a parental cell line that has an affinity for the ectodermal lineage. The sMNs generated mainly belonged to the LMCl at the brachial level, as determined by motor neuron marker expression and HOX gene expression. The expression pattern identified in the neurons generated in this chapter reflects that of the sMNs that innervate the dorsal muscles of the upper limbs. FOXP1 expression appeared to not be as strong as other motor neuron markers, as determined by RNAseq data and antibody staining. This may suggest a lack of upregulation or a downregulation at that time point; this could be clarified by analysing FOXP1 expression at different points throughout the differentiation. Whilst the expression of all other motor neuron markers suggest a primarily LMC identity and FOXP1 is present, this may present an avenue to further improve this differentiation protocol to increase FOXP1 expression, as FOXP1 expression is needed for LMC specification (Stifani, 2014).

HOX gene expression has mainly been studied within the context of embryonic development (Cooper and Tsakiridis, 2022, Hubert and Wellik, 2023) but roles for HOX genes in motor neuron specification and axial specification have been elucidated more recently (Catela et al., 2016, Kc et al., 2024). An anterior identity is the default for neuronal differentiations, with different signalling molecules needed such as increasing FGF and decreasing RA to generate more posterior cell populations (Gouti et al., 2014, Lippmann et al., 2015). In CMT2 and CMT2A, it is the

peripheral neurons emanating from the brachial and lumbar plexuses rather than the more anterior sensory and motor neurons at cervical levels of the spinal cord. In examining HOX gene expression and axial identity, human neurons can be generated from hPSCs that mimic those implicated in CMT2A more closely than other hPSC models of CMT2A which have not examined axial identity of neuronal cultures (Saporta et al., 2015, Rizzo et al., 2016, Van Lent et al., 2021).

Whilst an extensive analysis of motor neuron markers was undertaken, further investigations could be undertaken to characterise other facets of the neurons, including soma size, axonal and dendritic branching, and axonal length. Differences in neurite length between wild-type and MFN2$^{R94Q/+}$ hiPSC-derived neurons have been identified before, with CMT2A neurons having a reduced length (Van Lent et al., 2021). Conversely, no difference in axon length was observed between wild-type and MFN2$^{A383V/+}$ hiPSC-derived motor neurons (Rizzo et al., 2016). No clear and consistent morphological changes in hPSC-derived motor neurons have been identified, and consequently it would be useful to the field to analyse these parameters to move towards a consensus morphology for CMT2A *in vitro* motor neurons.

The sMNs generated in Chapter 3 were also shown to be electrophysiologically active and able to generate axon potentials. This data supports the notion that at Day 34 – 36, the sMNs are mature in terms of function, rather than age. Future work should look to create an aged phenotype in this model either through extended culturing of neurons alongside GenToniK (Hergenreder et al., 2024) or through the employment of i-neurons derived directly from patient fibroblast which are able to maintain the cellular age of the fibroblasts (Mertens et al., 2021). As CMT2A is progressive, it is important to consider the relative age that a CMT2A model mimics and how this may map onto disease initiation and progression. Furthermore, late-onset patients experience a different disease course and progression compared to early-onset, with only age of onset being a clear differentiator (instead of causal mutation for example). Including an aged phenotype into the model may give insights into any cellular or molecular differences between early-onset/hESC-derived sMNs and late-onset/induced sMNs.

Together, the data presented in this chapter shows that MFN2$^{R94Q/+}$ does not impact the pluripotency of hESCs and cells containing this mutation can successfully be used to generate limb-innervating sMNs that can be used for the *in vitro* study of CMT2A.

Chapter 4: Characterisation of mitochondrial transport in an hESC model of CMT2A

4.1 Introduction:

As previously detailed in Chapter 1, axonal transport is an essential process in polarised neurons and the efficiency of this transport will determine the health of a neuron. With disrupted axonal transport being a shared hallmark between multiple neurodegenerative diseases, multiple techniques for observing this process have been developed, with different techniques being able to pull out different parameters relating to axonal transport.

The simplest method for observing the transport of mitochondria is through the use of mitochondria-specific fluorescent probes known as MitoTracker (Chazotte, 2011). These dyes are simple to use, taken up quickly by organelles, and retained post-fixation, but they are only taken up by mitochondria with membrane potential meaning not all mitochondria may be visualised (Neikirk et al., 2023). As a method for observing mitochondrial transport MitoTrackers limit observations to bulk transport in dense cultures as segmenting and tracking individual mitochondria is not possible. In the case of neurons, this problem can be somewhat overcome with the use of microfluidic chambers. Here, neurons are seeded at one end of the chamber and their axons extended along a thin channel, organising the neurons so that they are all arranged in the same orientation. Using fluorescent probes with microfluidic chambers allows for the observation of bidirectional transport along an axon as the direction of the soma and the axon terminal is known. These axonal cultures are still dense and thus single organelle/particle tracking remains difficult. One technique that can be employed to better observe single organelle movement is the use of low efficiency transfection with a plasmid encoding a fluorescent probe that is targeted to an organelle of choice (Chudakov et al., 2007). This low efficiency transfection allows for the isolation of individual cells within a dense culture and consequently it is easier to isolate and track individual organelles.

When quantifying the axonal transport of a mitochondrion, there are many parameters that can be examined to give a detailed image of how mitochondria are being transported. The percentage of motile organelle is the most common

parameter to quantify and shows if there is an increase or decrease in general movement. If possible, this can then be broken down into percentage motile according to direction – anterograde or retrograde. Each direction employs a different set of motor proteins and differences here can indicate a motor protein-specific mechanism (Hancock, 2014). When considering motile organelles, velocity is a key measure that can point towards deficits in motor protein efficiency. Velocity can be broadly split into two measurements: whole track velocity and instantaneous velocity. Whole track velocity is an average of the velocity of a motile object across an entire trajectory and encompasses any pauses that may occur within that trajectory. Instantaneous velocity measures the velocity of a moving organelle between two points, and this is typically a short piece of track where the organelle if moving at a constant velocity. In the case of organelles that pause often, whole track velocity and instantaneous velocity can vary greatly and for organelles that move at a constant speed, whole track velocity and instantaneous velocity values will be similar. Pausing is an important parameter to quantify as this can indicate imbalances in calcium ions or increased detachment of motor proteins from organelles (Lovas and Wang, 2013).

In the case of mitochondria, changes in transport can impact morphology with altered transport and morphology being seen simultaneously in multiple neurodegenerative diseases (Magrané et al., 2014, Lavie et al., 2016). Mitochondrial morphology is linked to mitochondrial health and function, with mitochondrial morphology changing in response to stresses (Picard et al., 2013). Identifying morphology and size changes in mitochondria can indicate imbalances in the fission/fusion processes or the presence of new cellular stress. With the canonical role of MFN2 being to drive the fusion of the OMM alongside MFN1, changes in MFN2's capacity to perform this role would be reflected in mitochondrial morphology. Previous CMT2A modelling has suggested that CMT2A-causing mutation in MFN2 lead to a reduction in mitochondrial fusion, which leads to a fragmented mitochondrial network and smaller mitochondria (El Fissi et al., 2018, Zhou et al., 2019).

Mitochondrial morphology is most commonly quantified by shape descriptors and absolute size. In terms of shape, circularity measures how close a shape is to a circle, with 1 being a perfect circle and numbers closer to zero being non-circular. Aspect ratio relates the minor axis (width) and major axis (length) to giving a length to width ratio and thus an indication of how tubular or circular a mitochondrion is (Luz et al., 2015). Form factor integrates the perimeter and area of a mitochondrion and is a proxy measure of mitochondrial branching (Merrill et al., 2017). All these parameters give a read-out of how elongated or punctate a mitochondrion is, which can be related back to hypo- or hyper- fusion and fission.

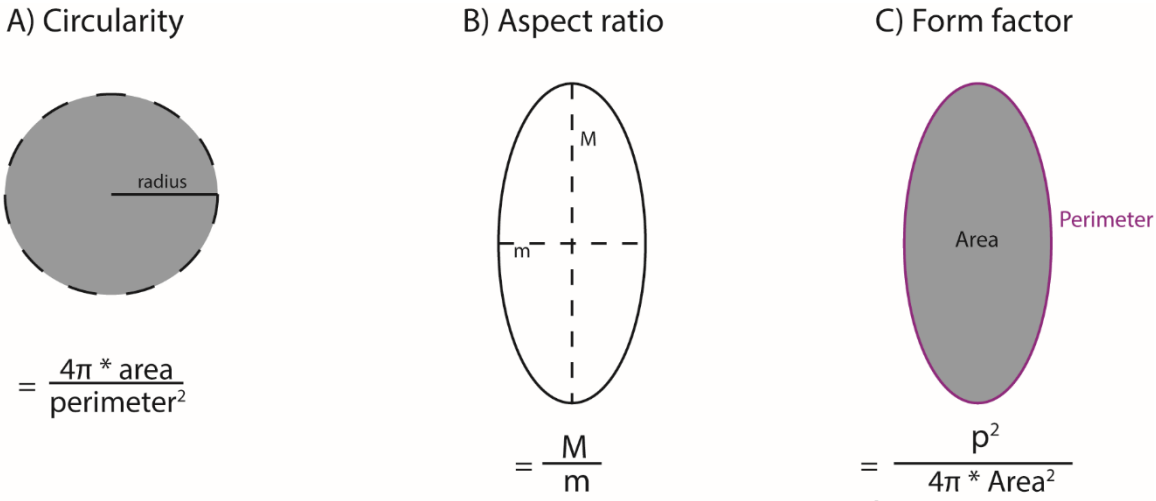


Figure 4.1: Mitochondrial shape descriptors. *(A) Circularity is calculated by dividing 4π*area by the perimeter squared. (B) Aspect ratio divided the major axis (M) by the minor axis (m). (C) Form factor divides the perimeter squared by 4π*area squared.*

In Chapter 3, a hESC-based model of CMT2A was generated using CRISPR-cas9 editing to introduce a CMT2A-causing heterozygous point mutation into MFN2 in hESCs. These hESCs can be differentiated into limb-innervating motor neurons that provide a disease-relevant platform to study neuronal biology and pathogenesis in CMT2A. Due to the location and canonical role of MFN2, a mitochondrial phenotype in hESC-derived motor neurons containing $MFN2^{R94Q/+}$ was thought to be highly likely as two of the most reported deficits in animal and cell models of CMT2A is an impairment of mitochondrial transport (Baloh et al., 2007, Misko et al., 2012, Adalbert et al., 2020, Van Lent et al., 2021) and mitochondrial fusion (Detmer et al., 2007, El Fissi et al., 2018, Das et al., 2024). With significant interplay between mitochondrial fusion and transport and a disease-relevant neuronal model with a large axonal

network, characterisation of mitochondrial transport in MFN2$^{R94Q/+}$ neurons was pursued.

Furthermore, some animal and cell models of CMT that have identified a mitochondrial trafficking deficit or a phenotype that may be related to a mitochondrial trafficking deficit have been able to improve the disease phenotype by way of small molecule inhibition of HDAC6. As previously mentioned in Chapter 1, HDAC6 is the predominant deacetylase of α-tubulin in neuronal microtubules, working in tandem with the acetylase αTAT1 to maintain α-tubulin acetylation levels which work to maintain microtubule architecture and long-range axonal transport. HSPB1 mutations lead to CMT2F, and are characterised by disturbed neuronal microtubule dynamics leading to impaired axonal transport (Almeida-Souza et al., 2011). Both mouse and iPSC-derived models of CMT2F have had transport and motor phenotypes rescued by multiple different small molecules HDAC6 inhibitors, which increase tubulin acetylation (D'Ydewalle et al., 2011, Kim et al., 2016, Benoy et al., 2017, Adalbert et al., 2020). HDAC6 inhibitors have also shown efficacy in CMT2 subtypes that do not have causal mutations that directly alter microtubule dynamics such as iPSC models of CMT2D (Mo et al., 2018, Smith et al., 2022) and mouse and immortalised cell line models of CMT2A (Picci et al., 2020, Shen et al., 2021, Kumar et al., 2024). Whether HDAC6 inhibition is targeting a common pathological pathway in CMT2 or is generally neuroprotective for peripheral nerves is yet to be determined, but a body of growing evidence suggests that HDAC6 inhibition may be a promising therapeutic pathway in CMT2. Importantly, the full effect of HDAC6 inhibition is yet to be quantified in a hESC-based model of CMT2A.

It was hypothesised that MFN2$^{R94Q/+}$ sMN axons would display a mitochondrial trafficking defect, and as a consequence mitochondria in these axons would be smaller in size and rounder in shape due to a lack of available fusion partners. Furthermore, it was hypothesised that the mitochondrial trafficking defect and mitochondrial morphology changes could be rescued by inhibiting HDAC6. This chapter describes a detailed analysis of mitochondrial morphology and transport in MFN2$^{+/+}$ and MFN2$^{R94Q/+}$ sMN axons and the consequence of HDAC6 inhibition on these parameters. Additionally, this chapter details a semi-automated analysis pipeline for kymograph analysis to extract mitochondrial transport data.

4.2 Results:

Establishing a mitochondrial trafficking assay and analysis pipeline

In order to assess mitochondrial transport in the axons of $MFN2^{+/+}$ and $MFN2^{R94Q/+}$ hESC-derived neurons, mitochondria needed to be tracked in the axons across a set period of time. Mature hPSC-derived sMNs exist in a dense axonal network with cell body clustering and axonal bundling, making it difficult to identify which mitochondria belong to a specific axon. Hence, to investigate transport direction and velocity in different axonal locations, previous work in the Barbarić lab optimised a low efficiency transfection of sMNs using Lipofectamine Plus (Butler, 2021) (Figure 4.1A). sMNs are transfected with both a plasmid encoding green fluorescent protein (GFP) under the CAG promoter and a plasmid coding for ds-RedMito under the CMV promoter (Figure 4.1B). The GFP allows for the visualisation of an entire axon and the ds-RedMito targets a red fluorophore to mitochondria, allowing the visualisation of mitochondria within a GFP axon.

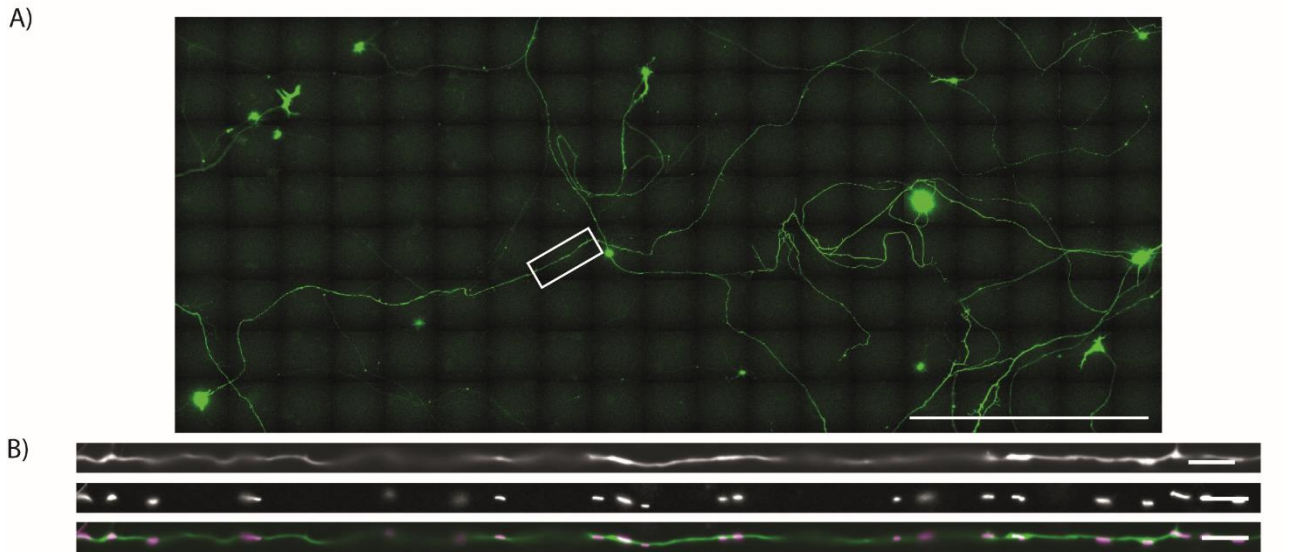


Figure 4.2: Low-efficiency transfection isolates neurons in dense cultures*. (A) Low-efficiency transfection of Day 36 sMNs. Scale bar = 1000 µm. (B) Magnified section of axon from (A). Axon shown in green and mitochondria in magenta. Scale bar = 10 µm.*

Ds-Red labelled mitochondria in GFP-labelled axons were recorded in proximal (0 to 500 µm from the soma), mid (500 to 1500 µm from the soma), and distal axonal portions (≥1500 µm from the soma) for 150 seconds. Timelapse images were first processed using FIJI. Timelapse images were segmented using the GFP axon as a

mask to isolate the mitochondria (Figure 4.3A.1,2). The axon was straightened and the timelapse video was maximum projected to generate a kymograph (Figure 4.3A.3). The first frame of the timelapse was used for morphological analysis of mitochondria (Figure 4.3.4). The final step of processing in FIJI required the segmenting of kymographs using the square region of interest (Figure 4.3.5). This was to reduce the size of the kymographs so that they could be analysed using KymoButler (Jakobs et al., 2019). KymoButler is an artificial intelligence-based software that automatically tracks movement on kymographs with a high level of accuracy. Kymograph segments that were smaller than 100,000 pixels were run through KymoButler to have predicted regions of interests of the kymograph tracks (Figure 4.3B.1,2). These predicted tracks were exported into R where kymograph segments were re-stitched with the predicted tracks from KymoButler. From here, track parameters were calculated such as motility, direction, and speed.

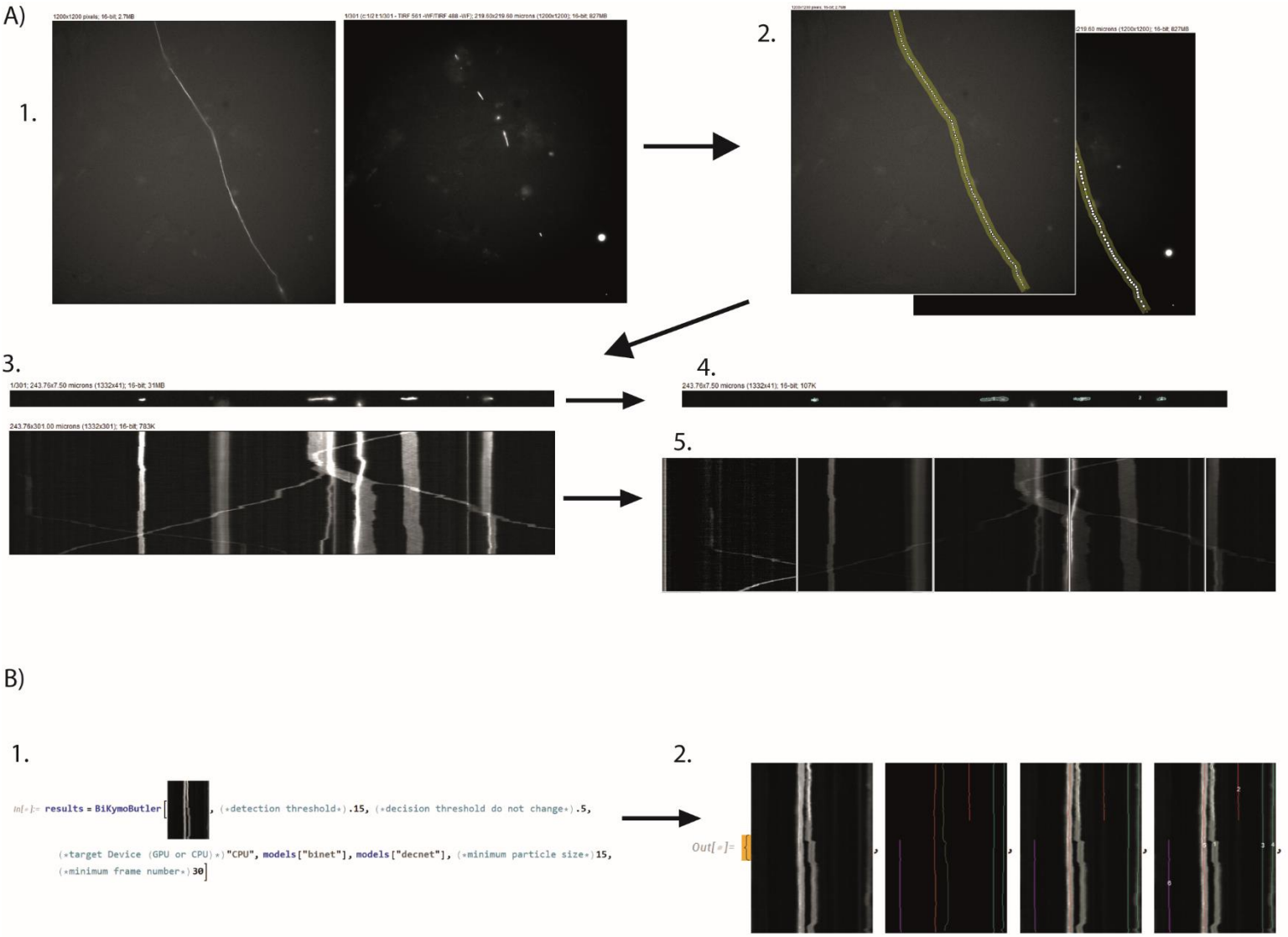


Figure 4.3: ImageJ processing and KymoButler analysis. *(A) 1. Timelapse videos are split into separate channels, separating axon and mitochondria. 2. GFP channel provides region of interest (ROI) of the axon path that is overlayed on mitochondria. 3. Mitochondrial channel and time series is straightened using ROI. Kymograph is generated by Z-projection of straightened mitochondria time series. 4. Mitochondrial shape descriptors are generated by ImageJ thresholding and measurements. 5. Kymographs are cut into chunks <100,000 pixels in preparation for KymoButler. (B) 1. Kymographs chunks generated in (A.5) are passed through KymoButler in Wolfram Mathematica. 2. KymoButler outputs an overlay of the detected ROIs for predicted tracks. Predicted tracks are exported as x,y coordinates.*

CMT2A motor neurons have reduced mitochondrial size in axons

To assess mitochondrial morphology in sMNs, the first frame of a timelapse was isolated and thresholded to convert mitochondria to measurable regions of interest. It was immediately noted that mitochondria in MFN2$^{R94Q/+}$ sMNs appeared to be spaced further apart (Figure 4.4A). This spacing was quantified by calculating the number of mitochondria per 100 µm. When comparing the number of mitochondria per 100 µm in MFN2$^{+/+}$ and MFN2$^{R94Q/+}$ sMN axons, there was a significant decrease in the number of mitochondria per 100 µm in MFN2$^{R94Q/+}$ sMN axons (Figure 4.4B),

suggesting that MFN2$^{R94Q/+}$ sMN axons may have a mitochondrial trafficking defect. This data was further binned into proximal, mid, and distal sections of the axons to assess a potential cumulative loss of mitochondria as a result of reduced trafficking. The biggest difference in mitochondria per 100 µm between MFN2$^{+/+}$ and MFN2$^{R94Q/+}$ sMN axons was seen in the most distal portion of axons (Figure 4.4B). The number of mitochondria per 100 µm in MFN2$^{+/+}$ sMNs was consistent across the proximal, mid, and distal regions of the axons (Figure 4.4B).

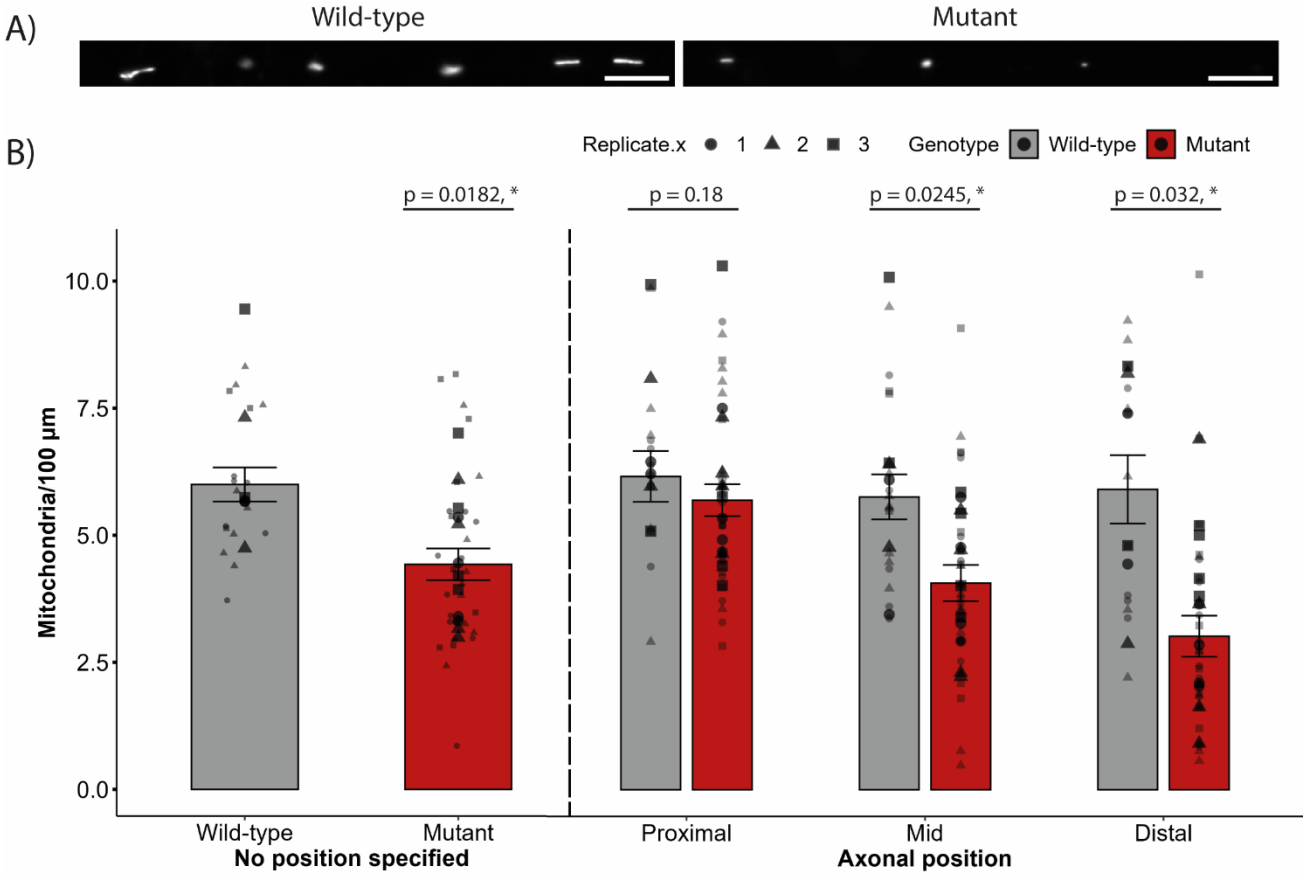


Figure 4.4: Mitochondrial spacing along the axon worsened by MFN2$^{R94Q/+}$. *(A) Representative images of dsRed mitochondria in an MFN2$^{+/+}$and MFN2$^{R94Q/+}$sMN axons. Scale bar = 10 µm. (B) Average number of mitochondria per 100 µm in proximal, mid, and distal segments. Data points represent individual neurons and data is plotted as mean ± SEM. No position, r = 0.552; proximal, r = 0.331; mid, r = 0.530; distal, r = 0.508. Wilcoxon rank sum test, N = 6 wild-type, 12 mutant from three independent differentiations; ns = p > 0.05, * = p ≤ 0.05,*

Mitochondrial shape and size also visually appeared to differ between wild-type and mutant axons, with mitochondria in mutant axons appearing smaller (Figure 4.4A). To quantify size, the area and length of mitochondria was compared between wild-type and mutant axons averaged across the axon and specifically in the proximal, mid, and distal regions. Quantification of mitochondrial area revealed a statistically

significant decrease in mitochondria in MFN2$^{R94Q/+}$ axons when axonal location was not considered, and this trend was consistent across all mutant cell lines (Figure 4.5A). When this data was split into axonal locations, a significant difference in average mitochondrial area was only seen between wild-type and mutant neurons in the distal region of the axon (Figure 4.5B). This trend was apparent across all cell lines, with MFN2$^{R94Q/+}$ neurons having a consistently lower mitochondrial area in the distal region whereas mitochondrial area in these same neurons was more variable in axonal locations closer to the soma (Figure 4.5C). It was noted that mitochondrial area in MFN2$^{+/+}$ axons decreased as mitochondria moved further away from to soma towards the distal region of the axons (Figure 45).

The same pattern was seen when average mitochondrial length was compared between MFN2$^{+/+}$ and MFN2$^{R94Q/+}$ sMN axons. When axonal position is not considered, there is a small but not statistically significant decrease in mitochondrial length from MFN2$^{+/+}$ to MFN2$^{R94Q/+}$ sMN axons, and this was consistent across all cell line (Figure 4.6A). When this data was broken down into different axonal positions, a statistically significant difference in length between MFN2$^{+/+}$ and MFN2$^{R94Q/+}$ sMN axons was seen in the distal portion of the axon (Figure 4.6B). No significant difference in mitochondrial length was seen between MFN2$^{+/+}$ and MFN2$^{R94Q/+}$ neurons in the proximal or mid portions of the axon (Figure 4.6B). As with mitochondrial area, mitochondrial length also decreased in MFN2$^{+/+}$ as mitochondria moved away from the soma towards the distal portion of the axons (Figure 4.6B). The average mitochondrial length in each axonal position for each cell line was also plotted to check for clonal variability (Figure 4.6C). There was very little variation in mitochondrial length in the mid and distal portions of all MFN2$^{R94Q/+}$ sMN axons and all MFN2$^{+/+}$ sMN axons. It was noted that there was variability in average mitochondrial length between WT1 and WT2 sMN axons in the proximal region, highlighting the importance of multiple clones.

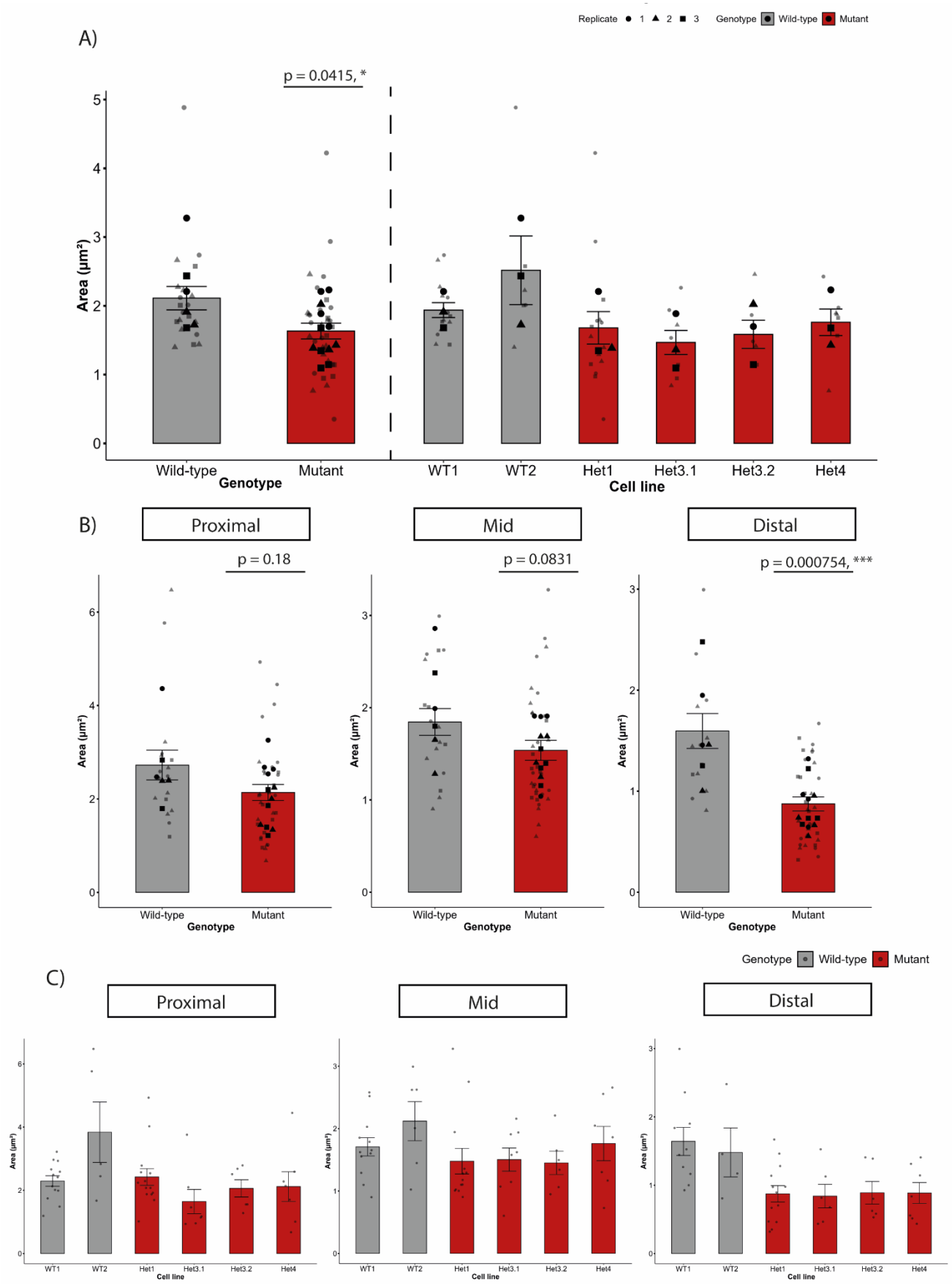


Figure 4.5: Reduction in MFN2$^{R94Q/+}$ mitochondrial area is most pronounced in the distal axon. *(A) Average area of mitochondria across the length of wild-type and mutant sMN axons. (B) Average area of mitochondria in the proximal, mid, and distal segments of wild-type and mutant sMN axons. r*

*= 0.486 (C) Average area of mitochondria in each cell line in the proximal (r = 0.331), mid (r = 0.419), and distal (r = 0.728) segments of sMNs axons. Each data point represents the average for a single neuron and plotted as mean ± SEM. Wilcox signed rank, N = 6 wild-type, 12 mutant from three independent differentiations; ns = p>0.05, * = P ≤ 0.05, *** = p ≤ 0.001,*

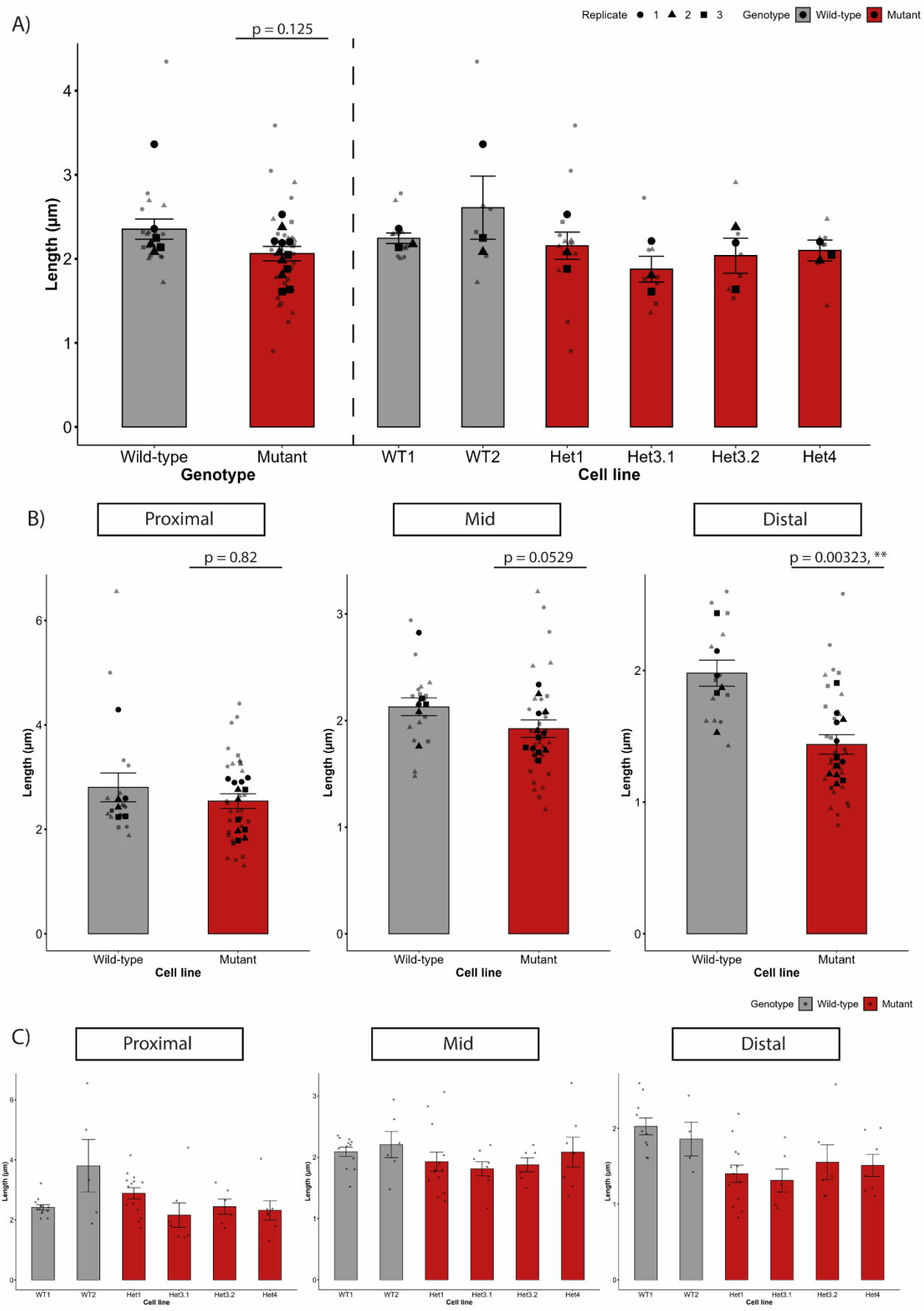


Figure 4.6: Mitochondrial length is reduced in MFN2$^{R94Q/+}$ sMNs. *(A) Average length of mitochondria across the length of wild-type and mutant sMN axons. r = 0.375. (B) Average length of*

*mitochondria in the proximal (r = 0.0662), mid (r = 0.464), and distal (r = 0.662) segments of wild-type and mutant sMN axons. (C) Average length of mitochondria in each cell line in the proximal, mid, and distal segments of sMNs axons. Each data point represents the average for a single neuron and plotted as mean ± SEM. Wilcox rank sum test, N = 6 wild-type, 12 mutant from three independent differentiations; ns = p>0.05, ** = p ≤ 0.01.*

Mitochondrial shape investigations revealed a lack of changes between $MFN2^{+/+}$ and $MFN2^{R94Q/+}$ mitochondria in contrast to the mitochondrial size analysis. Firstly, mitochondrial aspect ratio was interrogated. Average aspect ratio across the whole sMN axon did not differ between $MFN2^{+/+}$ and $MFN2^{R94Q/+}$ neurons, and this was consistent across all cell lines (Figure 4.7A). This data was broken down into the proximal, mid, and distal sections of the axons to see if the increased mitochondrial spacing impacted aspect ratio further away from the soma, but no differences were seen between $MFN2^{+/+}$ and $MFN2^{R94Q/+}$ mitochondria (Figure 4.7B). This pattern was seen in all cell lines at each axonal location, with all clones of each genotype acting similarly (Figure 4.7C).

Mitochondrial circularity was investigated next. Average circularity across the whole sMN axon did not differ between $MFN2^{+/+}$ and $MFN2^{R94Q/+}$ neurons, and this was consistent across all cell lines (Figure 4.8A). When examined by axonal location, no difference between the average circularity of $MFN2^{+/+}$ and $MFN2^{R94Q/+}$ mitochondria was identified but it was noted that mitochondrial circularity trended upwards as mitochondria moved away from the soma in both $MFN2^{+/+}$ and $MFN2^{R94Q/+}$ sMNs (Figure 4.8B). This pattern was seen in all cell lines at each axonal location, with all clones of each genotype acting similarly (Figure 4.8C).

Finally, mitochondrial form factor was compared between $MFN2^{+/+}$ and $MFN2^{R94Q/+}$ sMNs. No difference was seen between the average form factor of $MFN2^{+/+}$ and $MFN2^{R94Q/+}$ when axonal position was not considered, and this was consistent across all clones (Figure 4.9A). Similarly to mitochondrial circularity and aspect ratio, no differences between $MFN2^{+/+}$ and $MFN2^{R94Q/+}$ mitochondria appeared when considering axonal position (Figure 4.9B). Inter-clonal variability was also considered but no clone appeared to be an outlier of the trend (Figure 4.9C).

In summary, mitochondrial shape and size analysis revealed that mitochondria in $MFN2^{R94Q/+}$ sMNs were smaller than mitochondria in $MFN2^{+/+}$ sMNs, with decreases in area and length being most pronounced in the distal portions of sMN axons. However, mitochondrial shape was unaffected by the presence of $MFN2^{R94Q/+}$,

regardless of axonal position. This could indicate a potential fusion defect as mitochondria were smaller, but also suggests that mitochondria were not under significant stress due to no changes in mitochondrial shape.

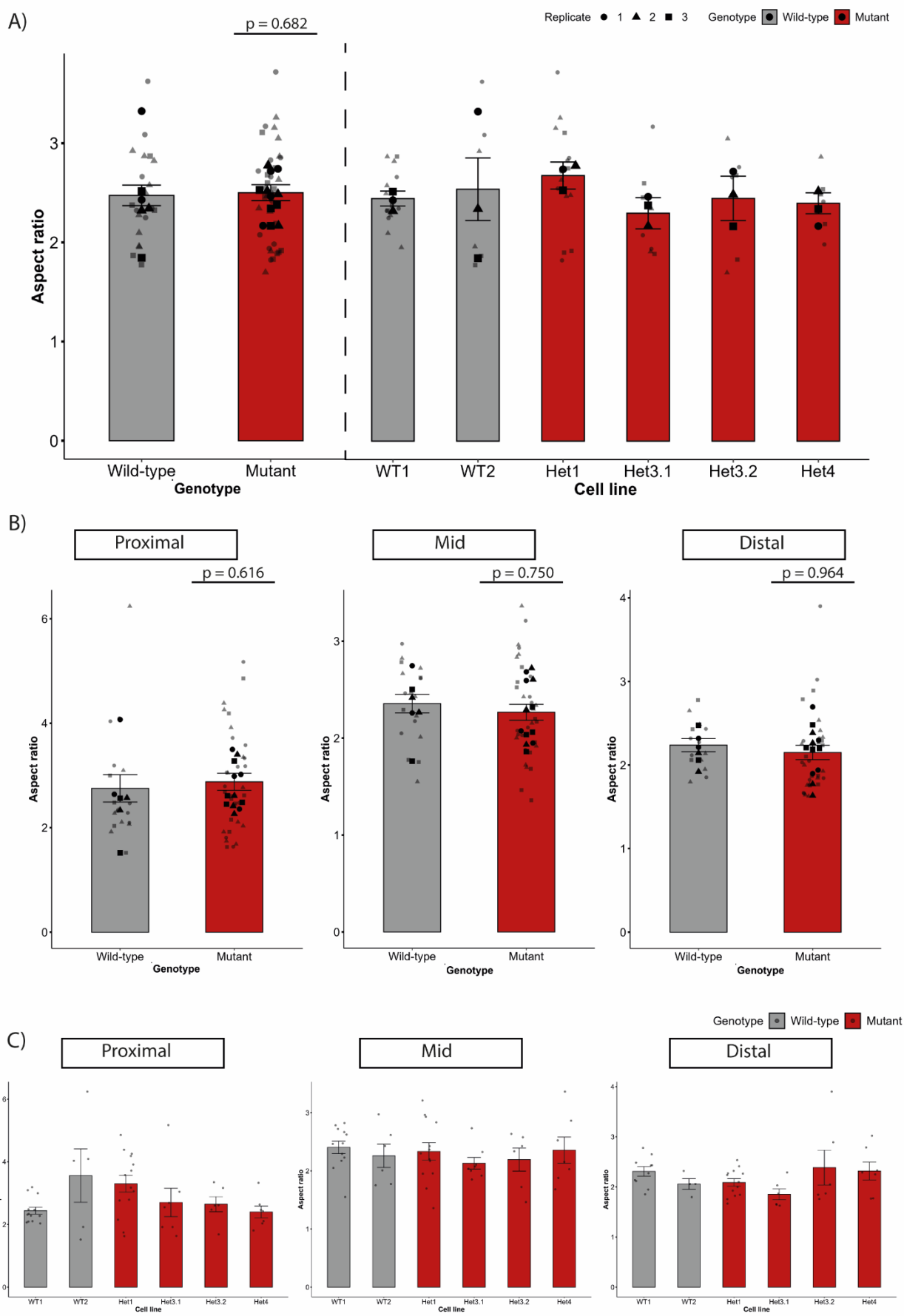


Figure 4.7: Mitochondrial aspect ratio is not altered in MFN2$^{R94Q/+}$ sMN axons. *(A) Average aspect ratio of mitochondria across the length of wild-type and mutant sMN axons. r = 0.110. (B)*

Average aspect ratio of mitochondria in the proximal (r = 0.132), mid (r = 0.0883), and distal (r = 0.0221) segments of wild-type and mutant sMN axons. (C) Average aspect ratio of mitochondria in each cell line in the proximal, mid, and distal segments of sMNs axons. Each data point represents the average for a single neuron and plotted as mean ± SEM. Wilcox rank sum test, N = 6 wild-type, 12 mutant from three independent differentiations; ns = p>0.05.

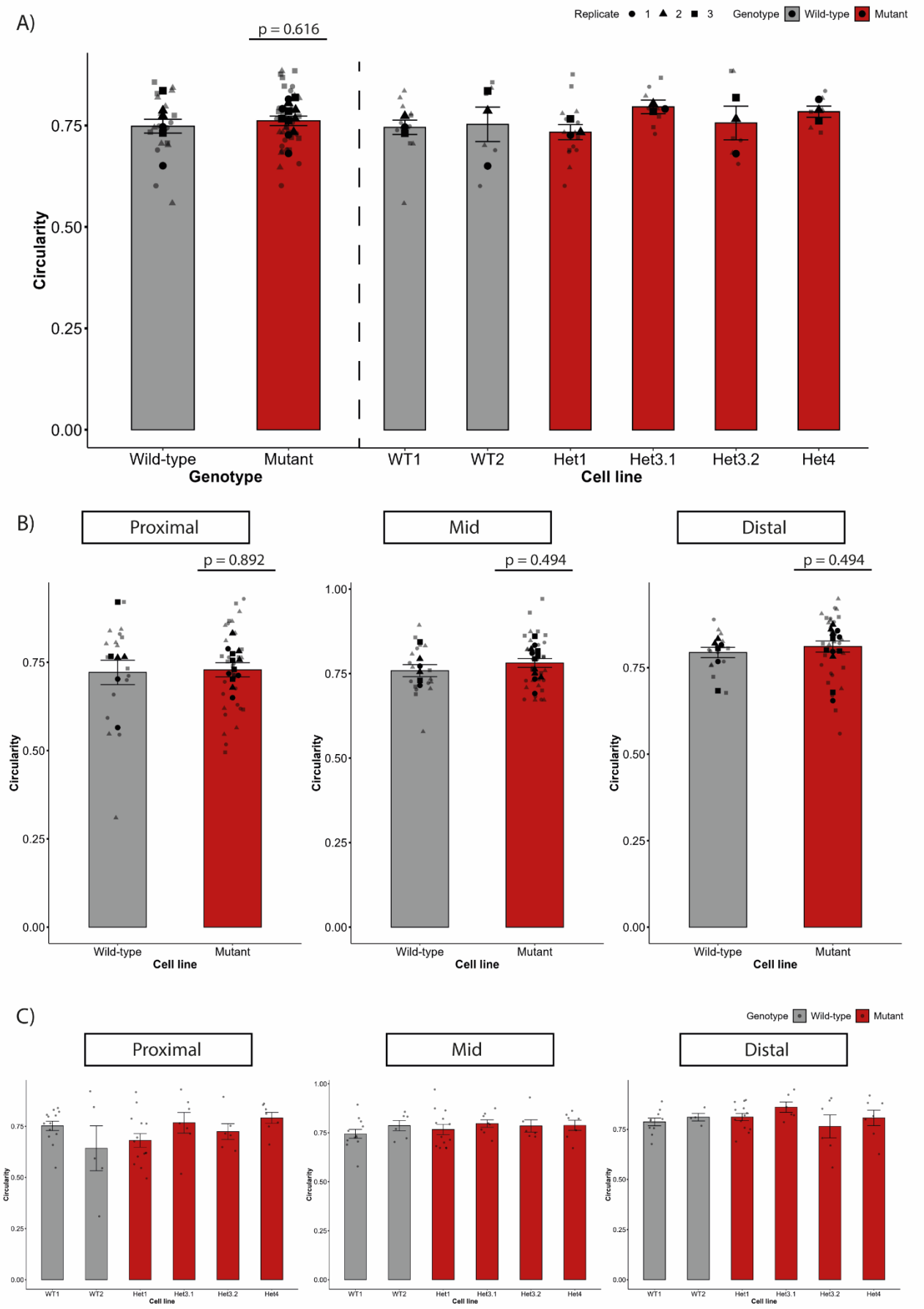


Figure 4.8: Mitochondrial circularity is not altered in MFN2$^{R94Q/+}$ sMN axons. *(A) Average circularity of mitochondria across the length of wild-type and mutant sMN axons. r = 0.132. (B)*

Average circularity of mitochondria in the proximal (r = 0.0442), mid (r = 0.177), and distal (r = 0.177) segments of wild-type and mutant sMN axons. (C) Average circularity of mitochondria in each cell line in the proximal, mid, and distal segments of sMNs axons. Each data point represents the average for a single neuron and plotted as mean ± SEM. Wilcox rank sum test, N = 6 wild-type, 12 mutant from three independent differentiations; ns = p>0.05.

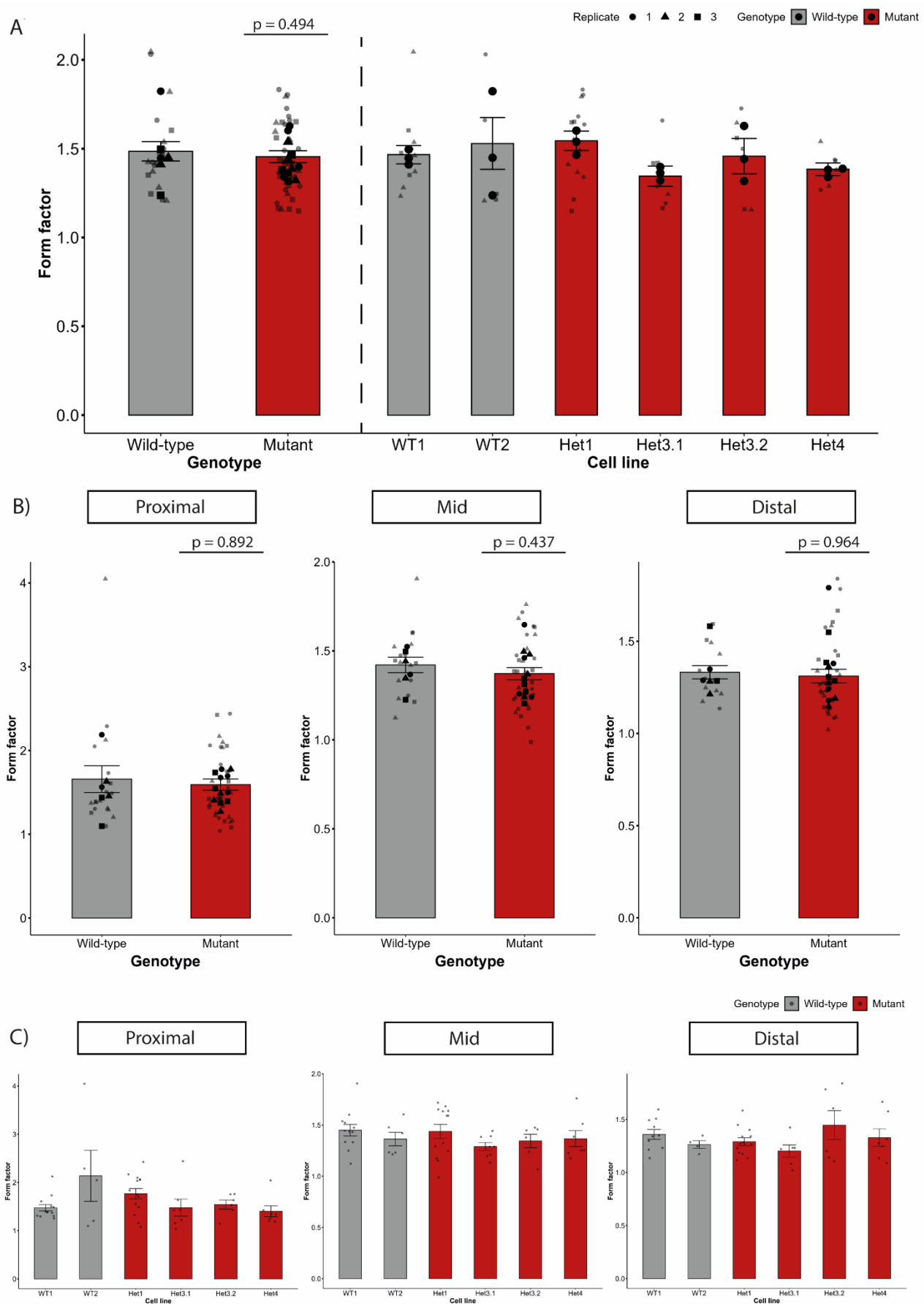


Figure 4.9: Mitochondrial form factor is not altered in MFN2$^{R94Q/+}$ sMN axons. *(A) Average form factor of mitochondria across the length of wild-type and mutant sMN axons. r = 0.177. (B) Average*

form factor of mitochondria in the proximal (r = 0.0442), mid (r = 0.199), and distal (r = 0.0221) segments of wild-type and mutant sMN axons. (C) Average form factor of mitochondria in each cell line in the proximal, mid, and distal segments of sMNs axons. Each data point represents the average for a single neuron and plotted as mean ± SEM. Wilcox rank sum test, N = 6 wild-type, 12 mutant from three independent differentiations; ns = p>0.05.

CMT2A motor neurons have a mitochondrial trafficking deficit

The increase in mitochondrial spacing in the distal portions of $MFN2^{R94Q/+}$ sMN axons shown in Figure 4.4 was indicative of a reduced delivery of mitochondria the distal portions of the axon. To confirm that this was the case, kymographs were generated from timelapse recordings of $MFN2^{+/+}$ and $MFN2^{R94Q/+}$ sMNs that had been transfected with GFP and MitoDsRed (as described in 2.9.1) and analysed using the semi-automated kymograph analysis pipeline detailed in Figure 4.3 (Figure 4.10A). As a broad measure of motility, the percentage of motile tracks in a kymograph was calculated and compared between genotypes which revealed a significant decrease in the average percentage of motile mitochondria (Figure 4.10B). This reduction in the percentage of motile mitochondria was seen at all axonal positions (Figure 4.10C) and in all $MFN2^{R94Q/+}$ cell lines (Figure 4.10D, E, F). Interestingly, the average percentage of motile mitochondria in $MFN2^{+/+}$ sMNs decreased slightly as mitochondria moved towards distal portions suggesting that a small reduction in motility in axonal regions far from the soma is normal for mitochondria.

It is important to consider the direction of motile mitochondria as different molecular motors are responsible for anterograde transport (away from the soma towards the distal axon) and retrograde transport (away from the distal axon towards the soma). Anterograde transport was interrogated first by calculating the average percentage of motile mitochondria moving in the direction. A significant decrease in the percentage of anterogradely moving mitochondria was seen in $MFN2^{R94Q/+}$ sMNs compared to $MFN2^{+/+}$ sMNs (Figure 4.11A). This was consistent across the proximal and mid, portions of the axons, with $MFN2^{+/+}$ sMNs showing a small trend downwards as mitochondria moved further away from the soma (Figure 4.11B). This was relatively consistent across all $MFN2^{R94Q/+}$ cell lines with some lines showing no movement in a specific location across the 2.5-minute recordings (Figure 4.11 C, D, E).

Quantification of retrograde mitochondrial movements revealed a different pattern to that of anterograde mitochondria. Whilst a significant decrease in the percentage of

motile retrograde mitochondria was still noted in MFN2$^{R94Q/+}$ sMNs compared to MFN2$^{+/+}$ sMNs (Figure 4.12A), this significant decrease was only maintained in the proximal and distal portion of MFN2$^{R94Q/+}$ sMNs (Figure 4.12B). This was mostly reflected by each cell line, though Het3.2 experienced some hypermotility in the distal portion of the axon (Figure 4.12C).

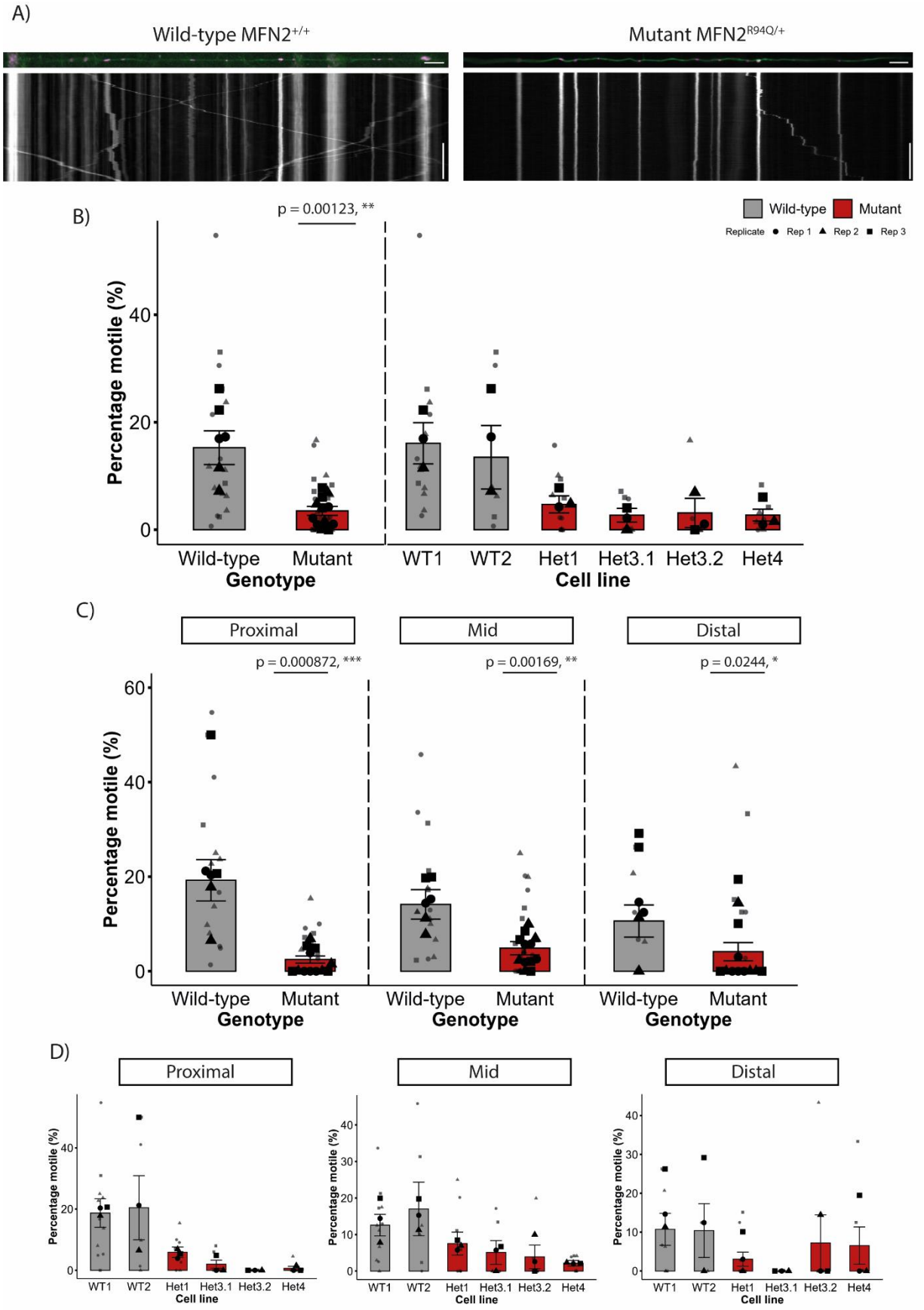

A)
Wild-type MFN2+/+
Mutant MFN2R94Q/+
B)
p = 0.00123, **
Wild-type
Mutant
Replicate
Rep 1
Rep 2
Rep 3
Percentage motile (%)
0
20
40
Wild-type
Mutant
Genotype
WT1
WT2
Het1
Het3.1
Het3.2
Het4
Cell line
C)
Proximal
Mid
Distal
p = 0.000872, ***
p = 0.00169, **
p = 0.0244, *
Percentage motile (%)
0
20
40
60
Wild-type
Mutant
Genotype
D)
Proximal
Mid
Distal
Percentage motile (%)
WT1
WT2
Het1
Het3.1
Het3.2
Het4
Cell line

Figure 4.10: MFN2$^{R94Q/+}$ sMNs have fewer motile mitochondria across the length of the axon. *(A) Representative kymographs from a MFN2$^{+/+}$ and MFN2$^{R94Q/+}$ axons. Axon shown in green, and mitochondria shown in magenta. Horizontal scale bar = 10 µm. Vertical scale bar = 100 seconds. (B) Percentage of motile mitochondria in wild-type and mutant sMNs. Each data point represents the average per neuron and plotted as the mean ± SEM. Data collected from three independent differentiations: N = 6 wild-type, 12 mutant. Wilcoxon rank sum test; **** = p ≤ 0.0001. r = 0.773. (C) Percentage motile mitochondria in wild-type and mutant sMNs in the proximal (r = 0.796), mid (r = 0.751), and distal (r = 0.542) segments of axons. Data points represent the average per neuron and plotted as mean ± SEM. Data collected from three independent differentiations: N = 6 wild-type, 12 mutant. Wilcoxon rank sum test; * = p ≤ 0.05, ** = p ≤ 0.01, **** = p ≤ 0.0001. (D) Percentage motile mitochondrial in each line in the R94Q panel in the proximal, mid (E), and distal (F) segments of the axons. Data points represent the average per neuron and plotted as mean ± SEM. Data collected from three independent differentiations: N = 6 wild-type, 12 mutant.*

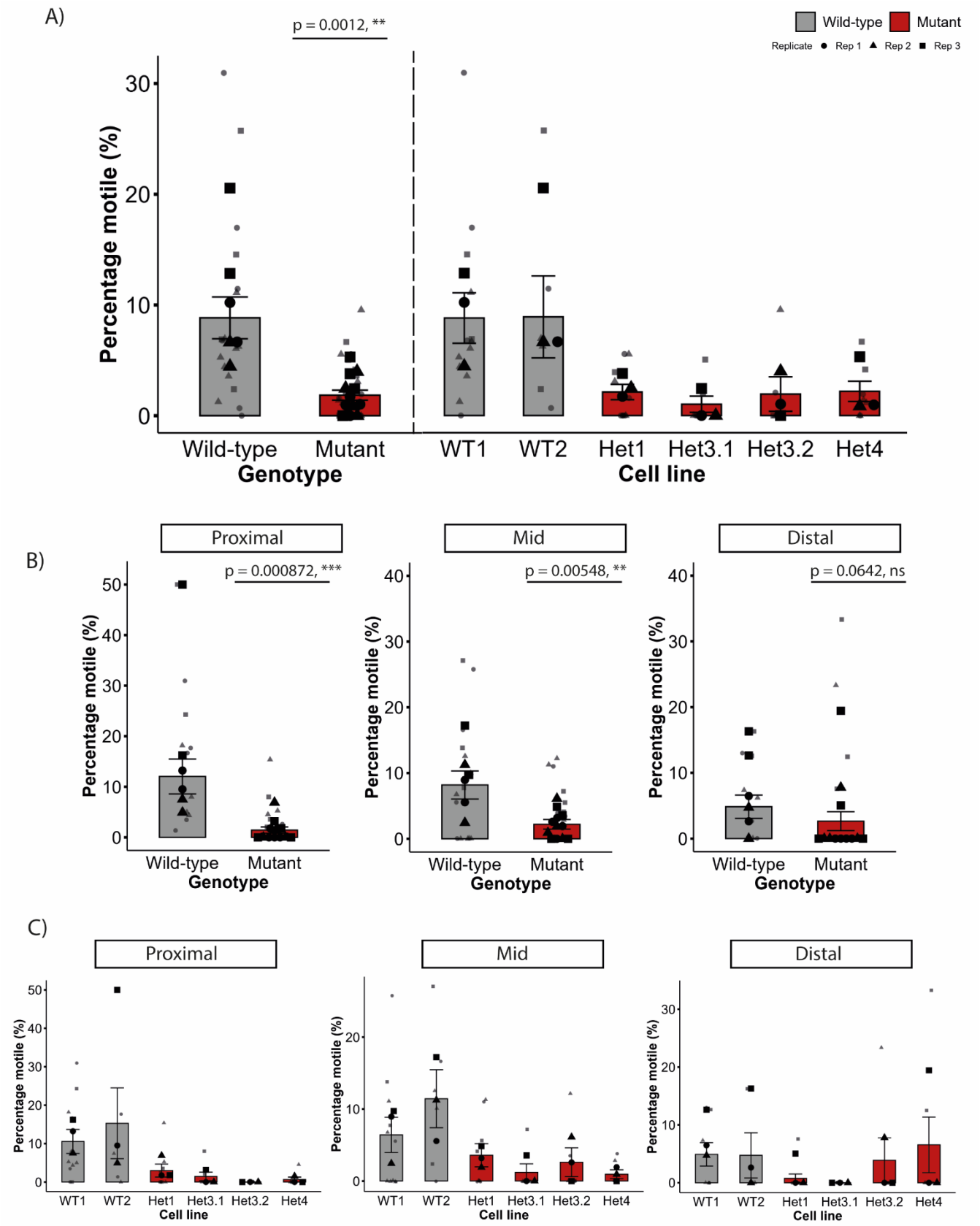


Figure 4.11: MFN2$^{R94Q/+}$ sMNs have fewer motile mitochondria moving in the anterograde direction across the length of the axon. *(A) Percentage of anterograde motile mitochondria in wild-type and mutant sMNs. Each data point represents the average per neuron. Data collected from three independent differentiations: N = 6 wild-type, 12 mutant. Wilcoxon rank sum test; ** = p ≤ 0.01, *** = p ≤ 0.001. r = 0.774. (B) Percentage anterograde motile mitochondria in wild-type and mutant sMNs in*

*the proximal (r = 0.796), mid (r = 0.666), and distal (r = 0.448) segments of axons. Data points represent the average per neuron. Data collected from three independent differentiations: N = 6 wild-type, 12 mutant. Wilcoxon rank sum test; ** = p ≤ 0.01, *** = p ≤ 0.001. (C) Percentage anterograde motile mitochondrial in each line in the R94Q panel in the proximal, mid (D), and distal (E) segments of the axons. Data points represent the average per neuron. Data collected from three independent differentiations: N = 6 wild-type, 12 mutant.*

The dynamics of mitochondrial transport were also analysed for any differences between $MFN2^{+/+}$ and $MFN2^{R94Q/+}$ mitochondria. Firstly, whole track velocity was calculated by dividing the total change in distance by total time of movement of KymoButler-detected tracks, generating an average velocity for a designated motile track. No significant differences were detected between $MFN2^{+/+}$ and $MFN2^{R94Q/+}$ whole track velocity in the anterograde (Figure 4.13A) or retrograde direction (Figure 4.13B). This was a surprising result as visually, $MFN2^{R94Q/+}$ motile tracks seemed to pause more often. To confirm that a lack of difference in whole track velocity was a true result, instantaneous velocity was calculated manually, whereby short straight lines were fitted to discrete movements on the kymographs (Figure 4.13C). Interestingly, instantaneous velocity was found to be significantly increased in the anterograde direction and trended upwards in the retrograde direction (Figure 4.13D). This finding was consistent across all cell lines in the anterograde direction (Figure 4.13E) but Het3.2 showed a decrease in the instantaneous retrograde velocity compared to the other cell lines (Figure 4.13F).

To resolve the difference between whole track and instantaneous velocity, pausing of motile tracks was analysed. An increase in pausing paired with an increased instantaneous velocity could equate to an equivocal whole track velocity. The percentage of motile tracks that paused was calculated first and this showed that $MFN2^{+/+}$ had a higher percentage of motile tracks that paused compared to $MFN2^{R94Q/+}$ (Figure 4.14A). However, percentage of motile tracks that pause does not consider the number of times a track pauses and the length of these pauses. In order to account for this, a pause coefficient was calculated by dividing the total time a motile track spent paused by the total length of the motile track (Figure 4.14B). When the average pause coefficient was compared between $MFN2^{+/+}$ and $MFN2^{R94Q/+}$ motile tracks, it was found that $MFN2^{R94Q/+}$ motile tracks had a larger average pause coefficient (although not statistically significant), indicating that these tracks tended to spend more time paused than $MFN2^{+/+}$ motile tracks.

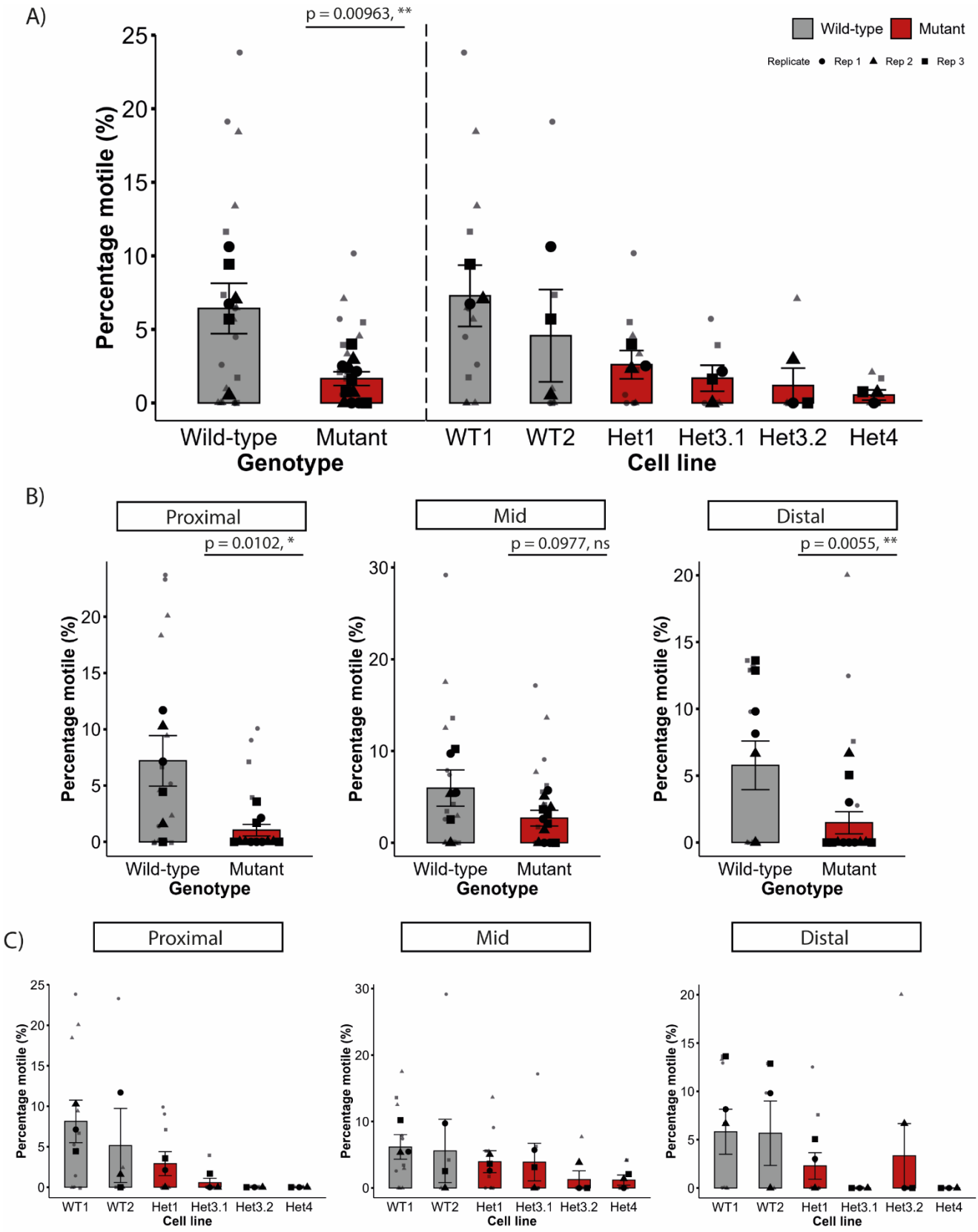


Figure 4.12: MFN2$^{R94Q/+}$ sMNs have fewer motile mitochondria moving in the retrograde direction across the length of the axon. *(A) Percentage of retrograde motile mitochondria in wild-type and mutant sMNs. Each data point represents the average per neuron. Data collected from three independent differentiations: N = 6 wild-type, 12 mutant. Wilcoxon rank sum test; **** = p ≤ 0.0001. r =*

*0.621. (B) Percentage retrograde motile mitochondria in wild-type and mutant sMNs in the proximal (r = 0.618), mid (r = 0.402), and distal (r = 0.666) segments of axons. Data points represent the average per neuron. Data collected from three independent differentiations: N = 6 wild-type, 12 mutant. Wilcoxon rank sum test; ns = p ≥ 0.05, *** = p ≤ 0.001. (C) Percentage retrograde motile mitochondrial in each line in the R94Q panel in the proximal, mid (D), and distal (E) segments of the axons. Data points represent the average per neuron. Data collected from three independent differentiations: N = 6 wild-type, 12 mutant.*

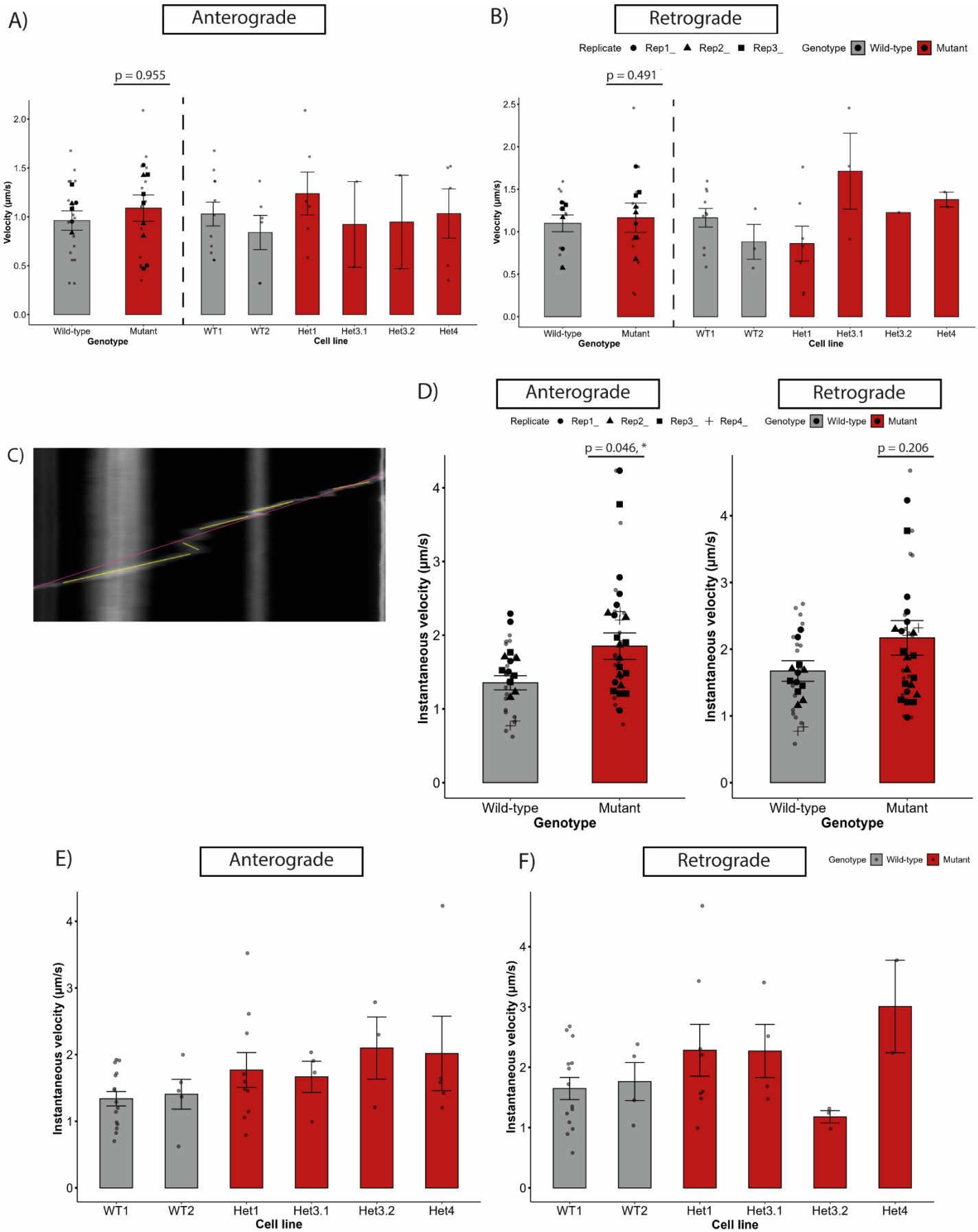


Figure 4.13: Mitochondrial velocity varies with direction and MFN2 status. *(A) Whole track velocity measurement of anterograde tracks (r = 0.0304) and retrograde (r = 0.207) (B) in MFN2$^{+/+}$*

*and MFN2$^{R94Q/+}$ sMNs at Day 36. Each data point represents the average per neuron and plotted as mean ± SEM. Data collected from three independent differentiations: N = 6 wild-type, 12 mutant. Wilcoxon rank sum test; ns = p ≥ 0.05. (C) Yellow lines represent instantaneous velocity measurements. Pink line represents whole track velocity. (D) Instantaneous velocity measurements of anterograde (r = 0.330) and retrograde (r = 0.267) movements in Day 36 sMNs. Each data point represents the average per neuron and plotted as mean ± SEM. Data collected from three independent differentiations: N = 6 wild-type, 12 mutant. Wilcoxon rank sum test; ** = p ≤ 0.01, *** = p ≤0.001. (E) Instantaneous velocity measurements of anterograde movements of mitochondria in each cell line. Mean ± SEM, each data point represents the average per neuron. (F) Instantaneous velocity measurements of retrograde movements of mitochondria in each cell line. Mean ± SEM, each data point represents the average per kymograph.*

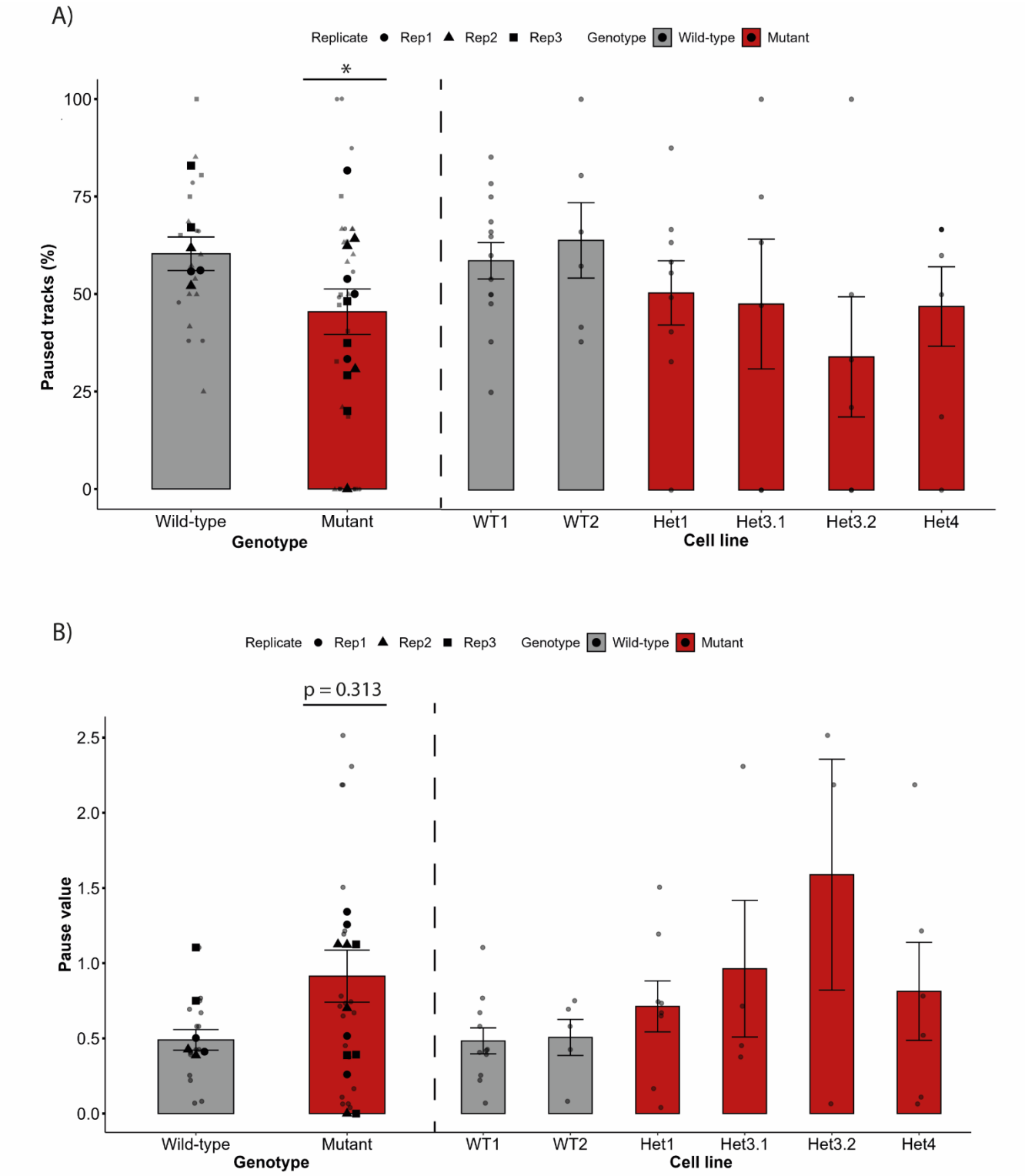


Figure 4.14: Pausing of motile mitochondria in CMT2A sMN axons. *(A) Average percentage of paused mitochondrial tracks per kymograph of MFN2$^{+/+}$ and MFN2$^{R94Q/+}$ sMNs. Data shown as mean ± SEM, each data point represents an individual neuron. Wilcoxon rank sum test: N = 6 wild-type, 12 mutant; * = p ≤ 0.05. r = 0.486. (B) Average pause value for motile mitochondria per kymograph of MFN2$^{+/+}$ and MFN2$^{R94Q/+}$ sMNs. Data shown as mean ± SEM, each data point represents an individual neuron. Wilcoxon rank sum test: N = 6 wild-type, 12 mutant. r = 0.232.*

It was also noted from visual inspection of kymographs that motile tracks were capable of switching direction, and that it may be more common in $MFN2^{R94Q/+}$ motile tracks. To quantify this, a sliding window of five seconds was run over each motile track to calculate velocity along a motile track (Figure 4.15A). This sliding window assigned anterograde speeds a positive integer and retrograde speeds were given a negative integer. Direction switching was equated to differences between maximum and minimum speeds. A motile track that moved at a fairly consistent speed in the same direction for the duration of the recording would have a difference close to zero between maximum and minimum speeds. A motile track that switched directions and achieved high speeds in both directions would have a difference > 5 for example. When this analysis was performed on $MFN2^{+/+}$ and $MFN2^{R94Q/+}$ motile tracks, the $MFN2^{R94Q/+}$ histogram had a longer tail to the right showing that more tracks were achieving high speeds in both the anterograde and retrograde direction (Figure 4.15B).

The final parameter of mitochondrial motile tracks that was considered was the motile track length – the distance covered by a single motile track. The average length of motile tracks of $MFN2^{R94Q/+}$ mitochondria was compared to that of $MFN2^{+/+}$ mitochondria, with no specified direction, and found that there was no change in motile track length (Figure 4.156). When considering only anterograde tracks, no significant difference was found between $MFN2^{+/+}$ and $MFN2^{R94Q/+}$ motile track length (Figure 4.16B). Anterograde track length appeared to increase as mitochondria moved further away from the soma (Figure 4.16B). No significant difference was seen between retrograde $MFN2^{+/+}$ and $MFN2^{R94Q/+}$ motile track length either, although these $MFN2^{R94Q/+}$ motile tracks trended towards being shorter than their $MFN2^{+/+}$ counterparts (Figure 4.16C).

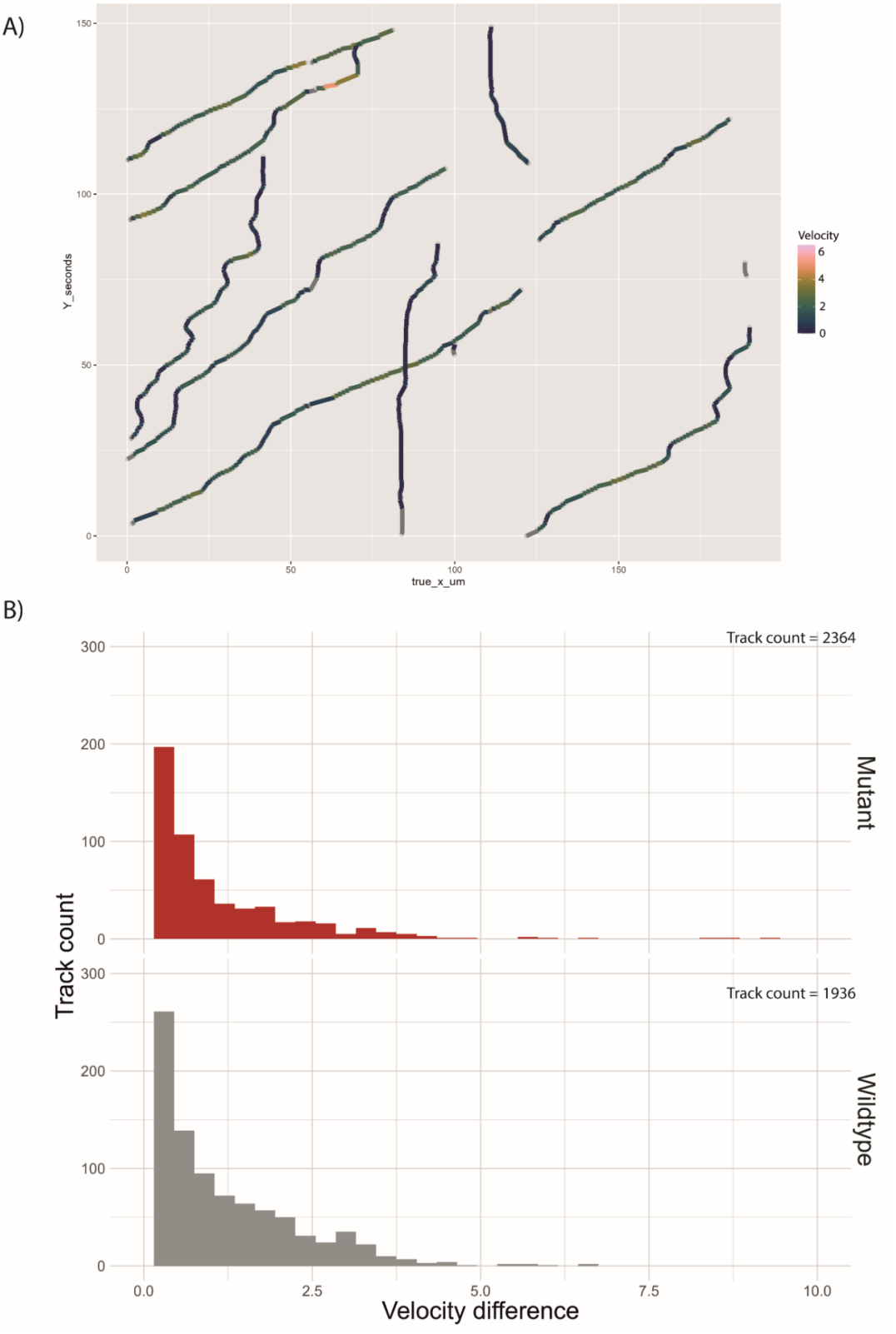


Figure 4.15: Velocity variation in motile mitochondria in MFN2$^{+/+}$ and MFN2$^{R94Q/+}$ sMNs. *(A) Sliding windows analysis of velocity shows that tracks have a varied velocity. Dark blue indicates velocity values closer to 0 µm/s and yellow/pink indicates velocity values closer to 6 µm/s. (B) Histogram of the difference between maximum anterograde and maximum retrograde speeds for motile tracks in MFN2$^{+/+}$ and MFN2$^{R94Q/+}$ sMNs.*

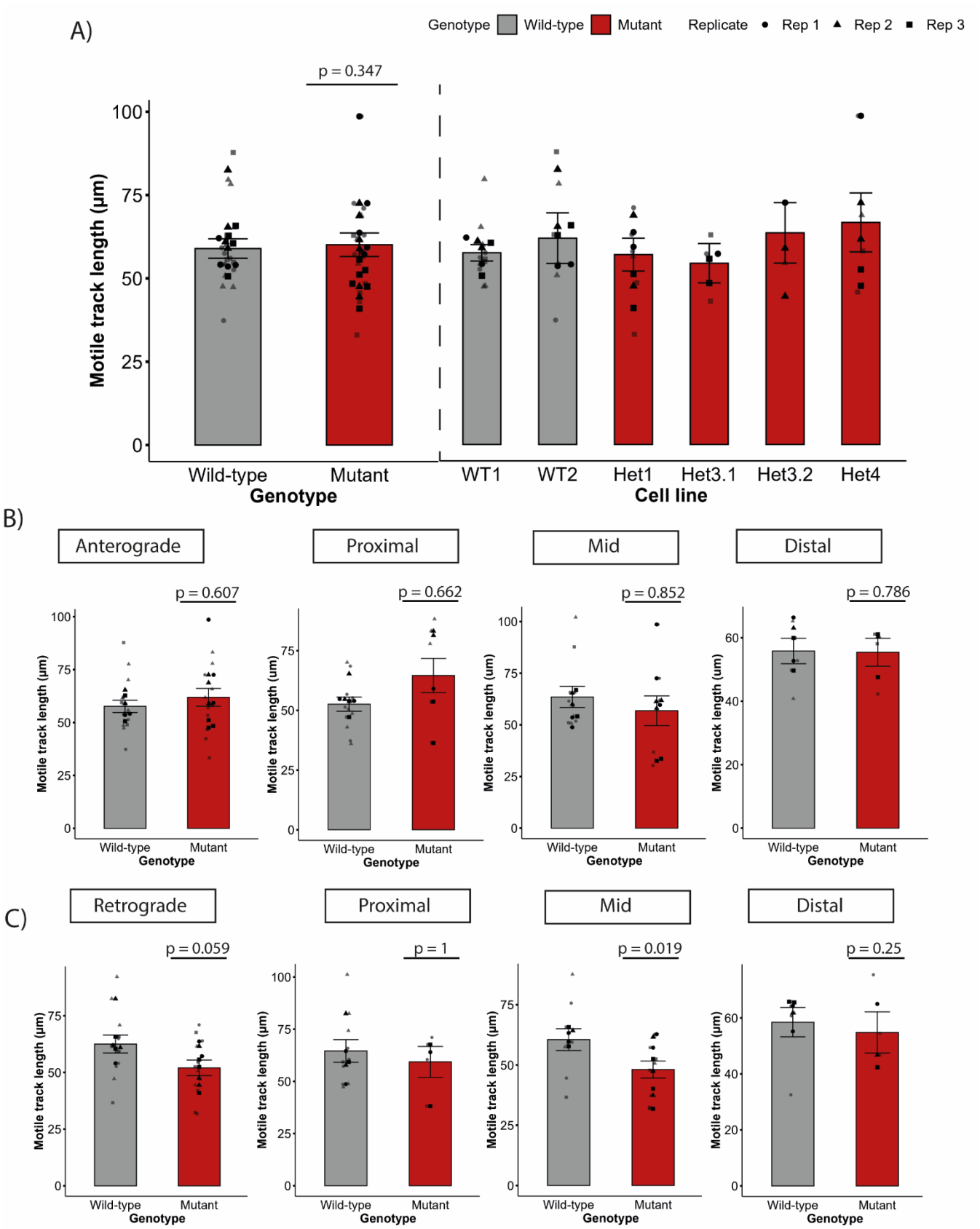


Figure 4.16: Motile track length in MFN2$^{+/+}$ and MFN2$^{R94Q/+}$ sMNs. *(A) Mean motile track length (direction unspecified) in MFN2$^{+/+}$ and MFN2$^{R94Q/+}$ sMNs. Each data point represents an individual neuron and data is plotted as mean ± SEM. Wilcoxon rank sum test: N = 6 wild-type, 12 mutant from three independent differentiations. r = 0.181. (B) Mean motile track length in the anterograde direction across the whole axon (r = 0.152) and in proximal (r = 0.165), mid (r = 0.0690), and distal (r = 0.158)*

*sections. Each data point represents an individual neuron and data is plotted as mean ± SEM. Wilcoxon rank sum test: N = 6 wild-type, 12 mutant from three independent differentiations. (C) Mean motile track length in the retrograde direction across the whole axon (r = 0.518) and in proximal (r = 0.0527), mid (r = 0.650), and distal (r = 0.474) sections. Data points represent the mean for a neuron across three independent differentiations. Wilcoxon rank sum test: N = 6 wild-type, 12 mutant; ns = p>0.05, * = p<0.05.*

Mitochondrial size in CMT2A axons is rescued by HDAC6 inhibition

As previously highlighted, it was hypothesised that inhibiting HDAC6 would rescue the mitochondrial trafficking deficit in hESC-derived MFN2$^{R94Q/+}$ sMNs. To inhibit HDAC6, the aromatic hydroxamic acid-derived small molecule ACY-738 was selected (Xiao and Zhang, 2020). ACY-738 has an attractively low IC_{50} for HDAC6 (1.7 nM) and is highly selective for Class II HDACs over Class I. ACY-738 has been shown to rescue the axonal transport in an iPSC-based model of CMT2F (Benoy et al., 2017) and improve multiple disease read-outs in models of MS (Lopresti, 2019) and ALS (Majid et al., 2015, Guo et al., 2017). Furthermore, ACY-738 has been used to successfully rescue the motor phenotype of a zebrafish model of CMT2A (Butler et al., 2022). Previous work in the Barbarić lab titrated ACY-738 in Day 36 hESC-derived sMNs to determine the optimal concentration of ACY-738 that would significantly increase α-tubulin acetylation without impacting neuronal survival. It was found that 100 nM of ACY-738 could increase α-tubulin acetylation in sMNs, and higher doses began to initiate neuronal death (Butler, 2021). Thus, this dose was taken forward for the experiments detailed in this section.

In order to test the hypothesis that HDAC6 inhibition could rescue the mitochondrial trafficking deficit in hESC-derived MFN2$^{R94Q/+}$ sMNs, sMNs were treated with 100 nM ACY-738 or vehicle control (0.01% DMSO) for 24 hours then imaged on Day 36 of differentiation to analyse mitochondrial shape, size, and transport dynamics.

Thresholding of the mitochondria revealed that whilst ACY-738 treatment had no effect on the average area of MFN2$^{+/+}$ mitochondria in the axon, it increased the average area of mitochondria in the MFN2$^{R94Q/+}$ sMN axons, with two out of four mutant lines following this trend (Figure 4.17A, B). When broken down into axonal regions, the most significant increase in mitochondrial area in MFN2$^{R94Q/+}$ sMN axons was seen in the distal portions of the axons (Figure 4.17C). Mitochondria in the distal portions of MFN2$^{+/+}$ sMN axons also experienced an increase in average size with ACY-738 treatment. Increases in mitochondrial size were seen in all

$MFN2^{R94Q/+}$ cell lines except for Het3.2 in the proximal, mid, and distal axonal portions (Figure 4.17D).

HDAC6 inhibition exerted a similar effect on mitochondrial length. Whilst no change in length was observed for $MFN2^{+/+}$ mitochondria treated with ACY-738, $MFN2^{R94Q/+}$ mitochondria did increase slightly in length with ACY-738 treated with three out of four lines following this trend (Figure 4.18A). When this data was broken down into axonal locations, only $MFN2^{R94Q/+}$ mitochondria in the distal portion of the axon experienced a significant increase in length after ACY-738 treatment (Figure 4.18B). When this was broken down further into each cell line, increases and decreases to mitochondrial length did not correspond to genotype in the proximal region of the axon (Figure 4.18C). In the mid section, all lines experienced an increase in mitochondrial length with ACY-738 treatment and all but one line (Het3.2) experienced an increase in mitochondrial length with ACY-738 treatment (Figure 4.18C).

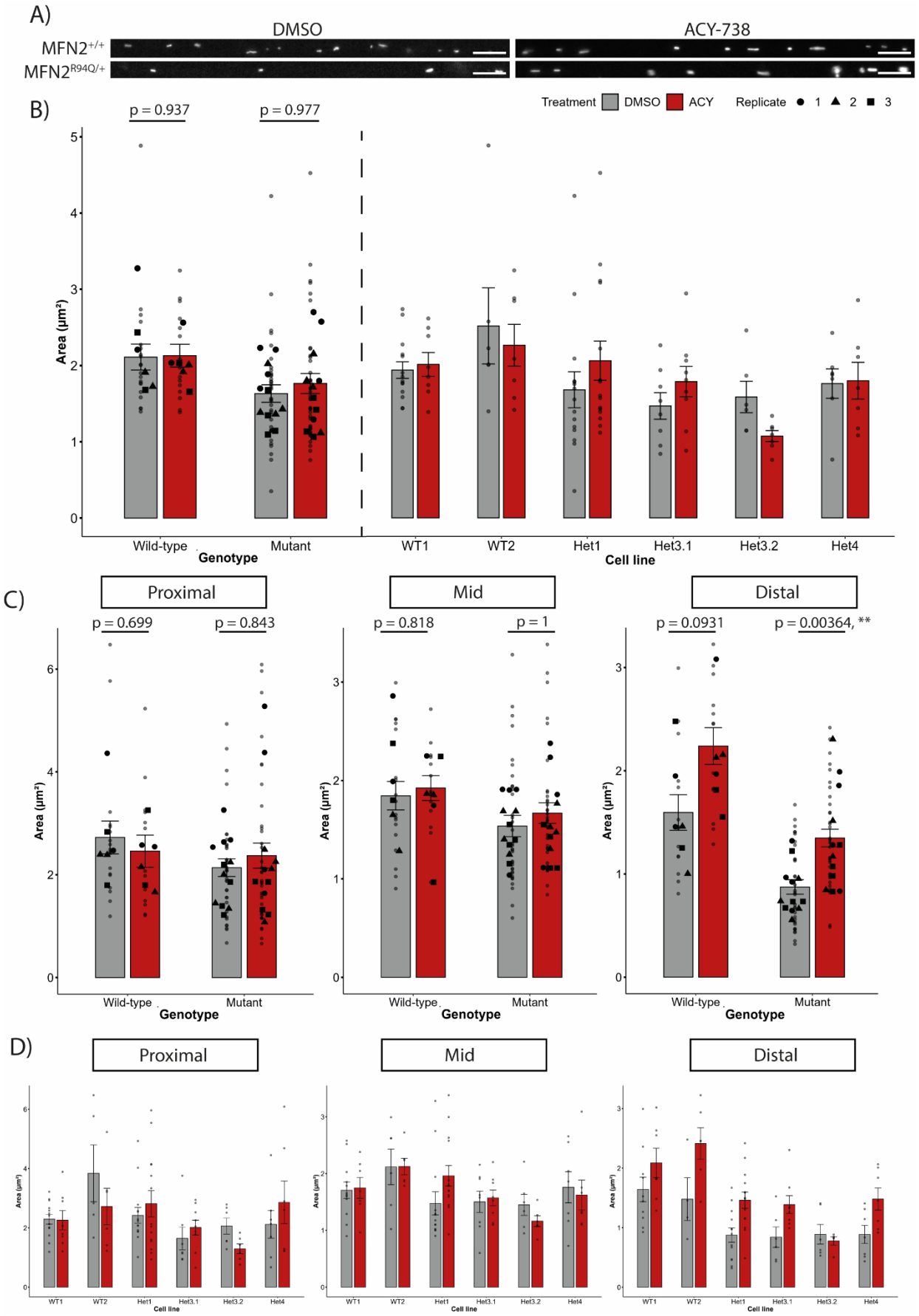


Figure 4.17: HDAC inhibition increases mitochondrial area in MFN2$^{R94Q/+}$ in the distal axon. *(A) Representative images from the mid axon of MFN2+/+ and MFN2R94Q/+ neurons treated with either*

*0.01% DMSO or 100 nM ACY-738. Scale bar = 10 µm. (B) Average area of mitochondria across the length of wild-type (r = 0.0462) and mutant (r = 0.0118) sMN axons when treated with 0.01% DMSO or 100 nM ACY-738. (C) Average area of mitochondria in the proximal (r = 0.139 wild-type, 0.0471 mutant), mid (r = 0.0925 wild-type, 0 mutant), and distal (r = 0.508 wild-type, 0.577 mutant) segments of wild-type and mutant sMN axons when treated with 0.01% DMSO or 100 nM ACY-738. (D) Average area of mitochondria in each cell line in the proximal, mid, and distal segments of sMNs axons when treated with 0.01% DMSO or 100 nM ACY-738. Each data point represents the average for a single neuron and plotted as mean ± SEM. Wilcox rank sum test: N = 6 wild-type, 12 mutant from three independent differentiations; ns = p>0.05, ** = p ≤ 0.01.*

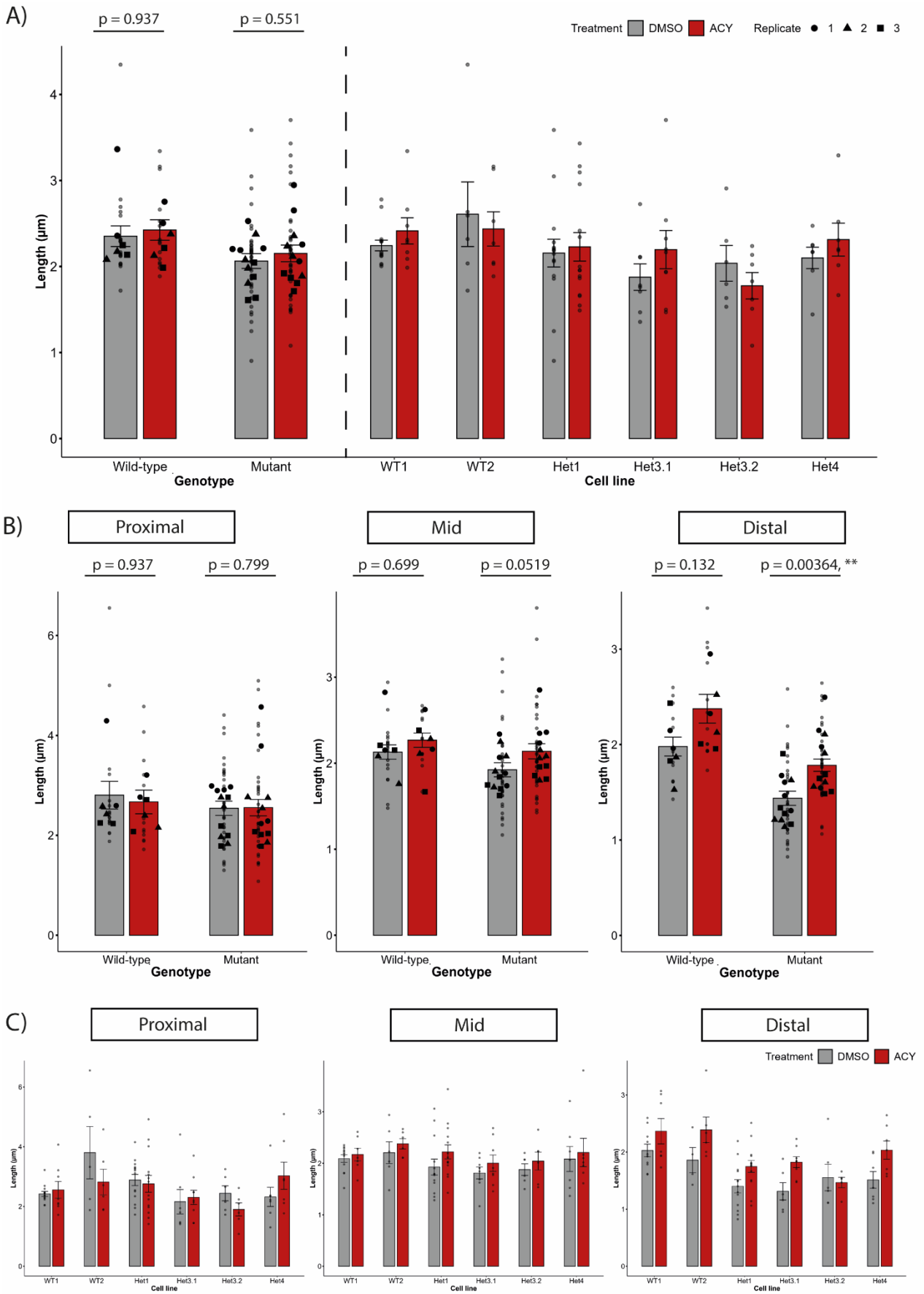


Figure 4.18: HDAC inhibition increases mitochondrial length in MFN2$^{R94Q/+}$ in the distal axon.
(A) Average length of mitochondria across the length of wild-type (r = 0.0.462) and mutant (r = 0.130)

*sMN axons when treated with 0.01% DMSO or 100 nM ACY-738. (B) Average length of mitochondria in the proximal (r = 0.0462 wild-type, 0.0589 mutant), mid (r = 0.139 wild-type, 0.401 mutant), and distal (r = 0.462 wild-type, 0.577 mutant) segments of wild-type and mutant sMN axons when treated with 0.01% DMSO or 100 nM ACY-738. (C) Average length of mitochondria in each cell line in the proximal, mid, and distal segments of sMNs axons when treated with 0.01% DMSO or 100 nM ACY-738. Each data point represents the average for a single neuron and plotted as mean ± SEM. Wilcox rank sum test: N = 6 wild-type, 12 mutant from three independent differentiations; ns = p>0.05, ** = p ≤ 0.01.*

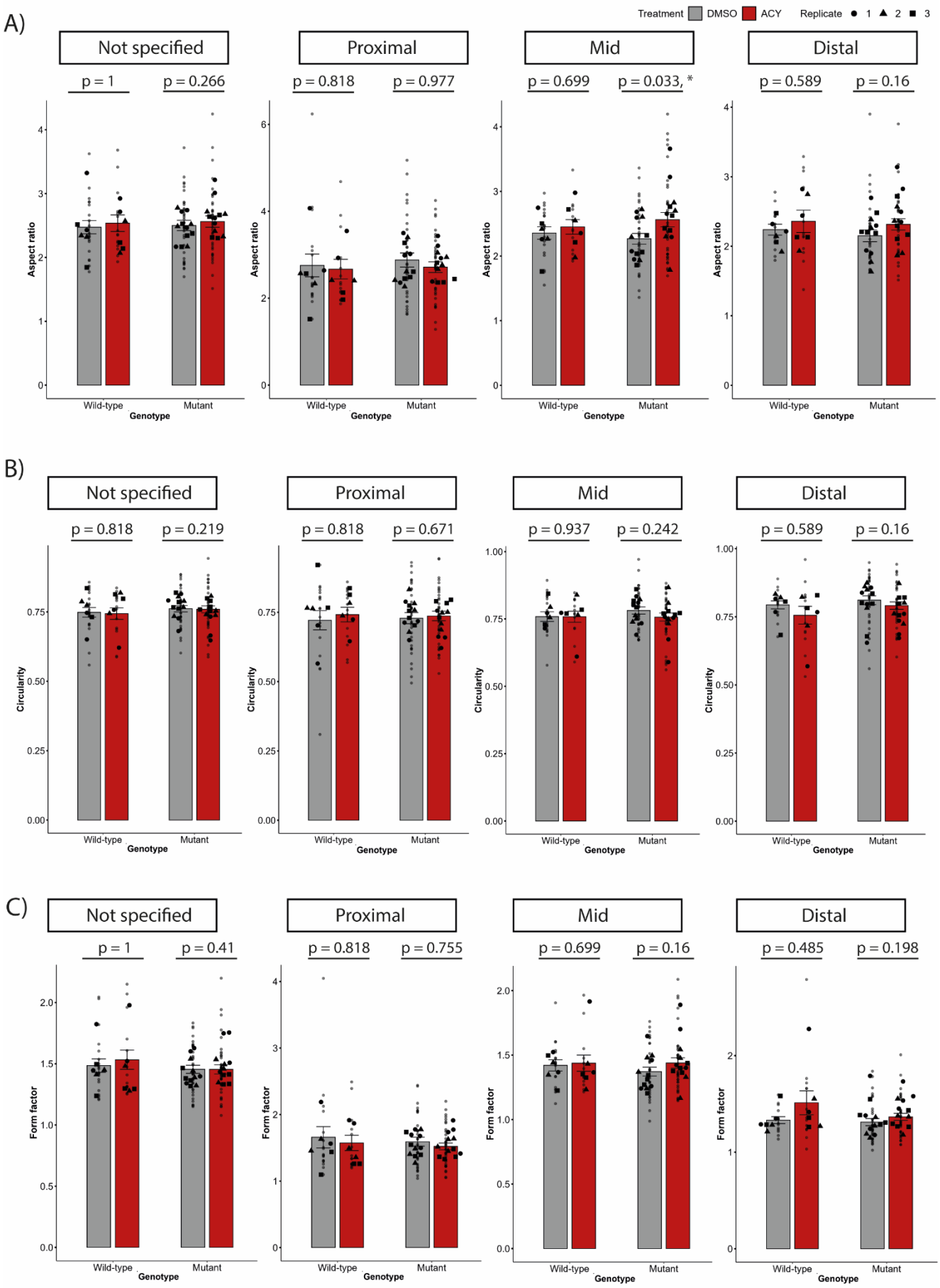


Figure 4.19: HDAC6 inhibition does not alter mitochondrial shape descriptors. *(A) Average*

aspect ratio of mitochondria in the proximal, mid, and distal segments of wild-type and mutant sMN axons when treated with 0.01% DMSO or 100 nM ACY-738. Wild-type effect sizes: whole axon, r = 0; proximal, r = 0.0925; mid, r = 0.139; distal, r = 0.185. Mutant effect sizes: whole axon, r = 0.236; proximal, r = 0.0118; mid, r = 0.436; distal, r = 0.295.(B) Average circularity of mitochondria in the proximal, mid, and distal segments of wild-type and mutant sMN axons when treated with 0.01% DMSO or 100 nM ACY-738. Wild-type effect sizes: whole axon, r = 0.0925; proximal, r = 0.0925; mid, r = 0.0462; distal, r = 0.185. Mutant effect sizes: whole axon, r = 0.259; proximal, r = 0.0943; mid, r = 0.247; distal, r = 0.295. (C) Average form factor of mitochondria in the proximal, mid, and distal segments of wild-type and mutant sMN axons when treated with 0.01% DMSO or 100 nM ACY-738. Wild-type effect sizes: whole axon, r = 0; proximal, r = 0.0925; mid, r = 0.139; distal, r = 0.231. Mutant effect sizes: whole axon, r = 0.177; proximal, r = 0.0707; mid, r = 0.295; distal, r = 0.271. Each data point represents the average for a single neuron and plotted as mean ± SEM. Wilcox rank sum test: N = 6 wild-type, 12 mutant from three independent differentiations; ns = p>0.05.

Mitochondrial shape was also assessed after ACY-738 treatment. Neither $MFN2^{+/+}$ and $MFN2^{R94Q/+}$ mitochondria showed a change in aspect ratio across the axon with ACY-738 treatment except for $MFN2^{R94Q/+}$ mitochondria in the mid section of the axon which saw an increase in aspect ratio (Figure 4.19A). No change in $MFN2^{+/+}$ and $MFN2^{R94Q/+}$ mitochondria was noted for form factor (Figure 4.19B) or circularity (Figure 4.19C) either.

In summary, 100 nM ACY-738 increased mitochondrial size (area and length) in the distal portions of $MFN2^{R94Q/+}$ sMN axons but had no effect on mitochondrial shape in either $MFN2^{+/+}$ and $MFN2^{R94Q/+}$ sMNs. This indicates that mitochondria may able to increase their size in the distal axon via fusion if more fusion partners are delivered to the distal axon.

CMT2A mitochondrial trafficking deficit is rescued by HDAC6 inhibition

Previous work in the Barbarić lab demonstrated that HDAC6 inhibition by ACY-738 could rescue the mitochondrial trafficking deficit in one $MFN2^{R94Q/+}$ clone. In order to see if this effect was shared by the newly created clones, $MFN2^{+/+}$ and $MFN2^{R94Q/+}$ sMNs were treated with 100nM ACY-738 for 24 hours and mitochondrial movement in axons was recorded for two and a half minutes as before to determine the percentage of motile mitochondria and motility dynamics.

Upon first inspection, kymographs derived from $MFN2^{R94Q/+}$ treated with ACY-738 appeared to have more diagonal lines (motile mitochondria), comparable to kymographs derived from $MFN2^{+/+}$ recordings (Figure 4.20A). When quantified as the percentage of motile tracks, $MFN2^{R94Q/+}$ showed a significant increase in the percentage of motile tracks with ACY-738 treatment, bringing the average to a

similar level as DMSO-treated $MFN2^{+/+}$ mitochondria (Figure 4.20B). This was consistent across all $MFN2^{R94Q/+}$ cell lines (Figure 4.20B). When the percentage of motile mitochondria was examined in the proximal, mid, and distal regions of the axons, $MFN2^{R94Q/+}$ sMNs exhibited a significant increase in the percentage motile mitochondria (Figure 4.20C). In the proximal and mid regions, ACY-738 treatment brought the average percentage of motile mitochondria in $MFN2^{R94Q/+}$ lines close to that of $MFN2^{+/+}$ (Figure 4.20C). Interestingly, ACY-738 treatment increased the average percentage motility of $MFN2^{R94Q/+}$ beyond that of DMSO-treated $MFN2^{+/+}$ (Figure 4.20C). When considering each cell line individually in the three axonal regions, all $MFN2^{R94Q/+}$ lines responded consistently to HDAC6 inhibition whereas $MFN2^{+/+}$ showed increases and decreases in percentage motility after HDAC6 inhibition (Figure 4.20D, E, F). This suggests that increasing α-tubulin acetylation is capable of increasing mitochondrial transport but is only beneficial in the presence of $MFN2^{R94Q/+}$.

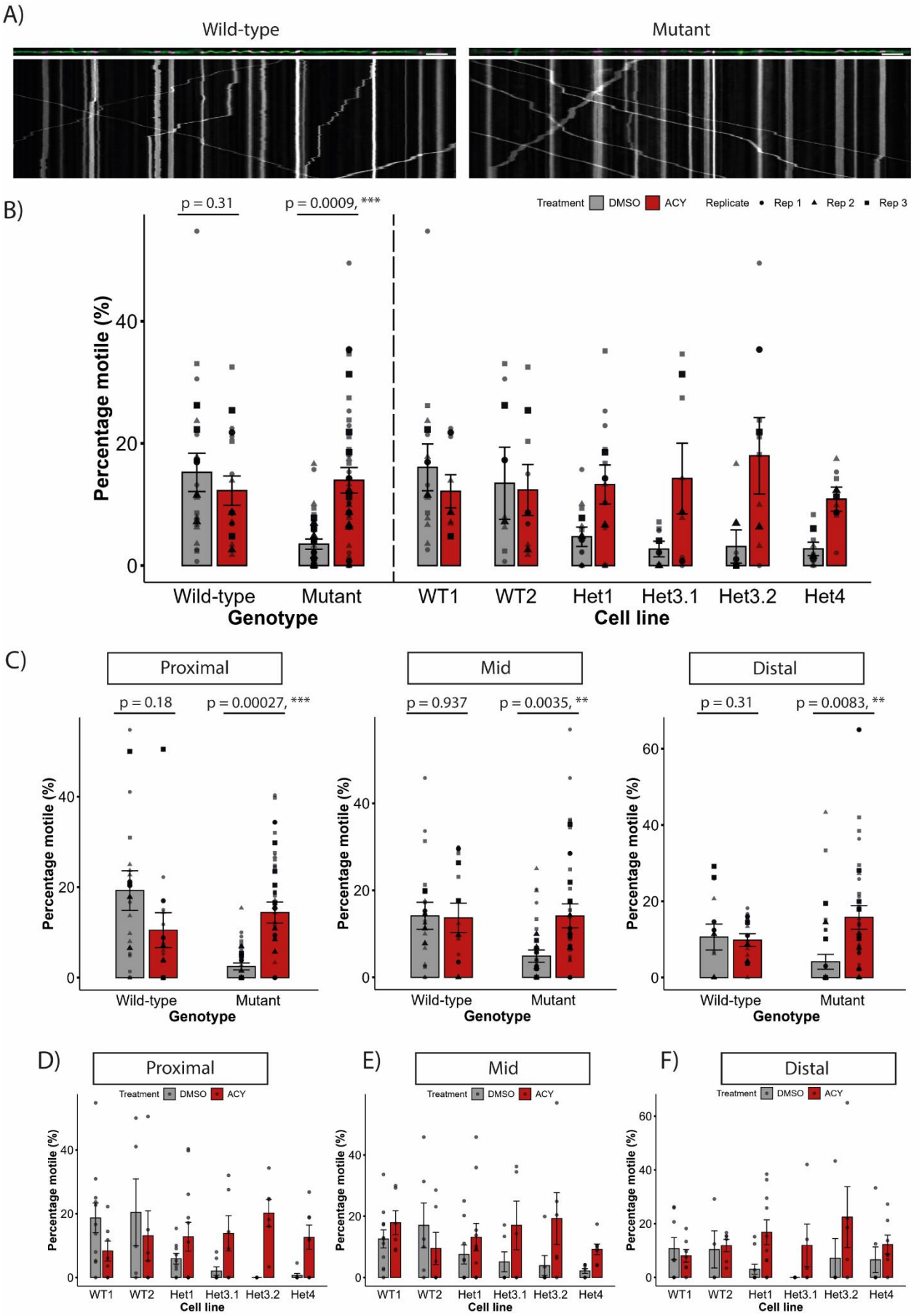


Figure 4.20: HDAC6i rescues trafficking defect in MFN2$^{R94Q/+}$ sMNs. *(A) Representative*

*kymographs and the corresponding axon of wild-type and mutant sMNs treated with 100 nM ACY-738. Vertical scale bar = 100 seconds, horizontal scale bar = 10 µm. (B) Average percentage motile mitochondria in wild-type (r = 0.324) and mutant (r = 0.684) sMNs that have been treated with 0.01% DMSO or 100 nM ACY-738 (ACY). (C) Average percentage motile mitochondria in the proximal (wild-type, r = 0.416; mutant, r = 0.750), mid (wild-type, r = 0.0462; mutant, r = 0.602), and distal (wild-type, r = 0.324; mutant, r = 0.545) portions of wild-type and mutant sMN axons that have been treated with 0.01% DMSO or 100 nM ACY-738. (D) Average percentage of motile mitochondria in each cell line in the proximal, mid, and distal portions of the axons. Each data point represents the average for single neuron and plotted as mean ± SEM. Wilcox rank sum test: N = 6 wild-type, 12 mutant from three independent differentiations; ns = p>0.05, ** = p ≤ 0.01, *** = p ≤ 0.001.*

The percentage of motile mitochondria was again broken down into anterograde and retrograde mitochondria to see if HDAC6 inhibition impacted the two mechanisms of mitochondrial transport differentially. The anterograde direction was interrogated first, and it was found that ACY-738 treatment significantly increased the average percentage of anterograde mitochondria in MFN2$^{R94Q/+}$, which was seen in all cell lines (Figure 4.21A). Interestingly, MFN2$^{+/+}$ sMNs showed a decrease in the percentage of anterograde mitochondria but this appeared to be mainly due to WT2 exhibiting a decrease in anterograde mitochondria (Figure 4.21A). The increase in the percentage of anterograde mitochondria in MFN2$^{R94Q/+}$ sMNs was consistent across the length of the axons (Figure 4.21B) and each of the MFN2$^{R94Q/+}$ cell lines (Figure 4.21C).

The average percentage of retrograde mitochondria in MFN2$^{R94Q/+}$ followed a similar pattern to that of anterograde mitochondria, with ACY-738 treatment significantly increasing the percentage of retrograde mitochondria in MFN2$^{R94Q/+}$ sMNs across all lines (Figure 4.22A). This increase was maintained across the proximal, mid, and distal portions of the axons in all MFN2$^{R94Q/+}$ lines (Figure 4.22B, C).

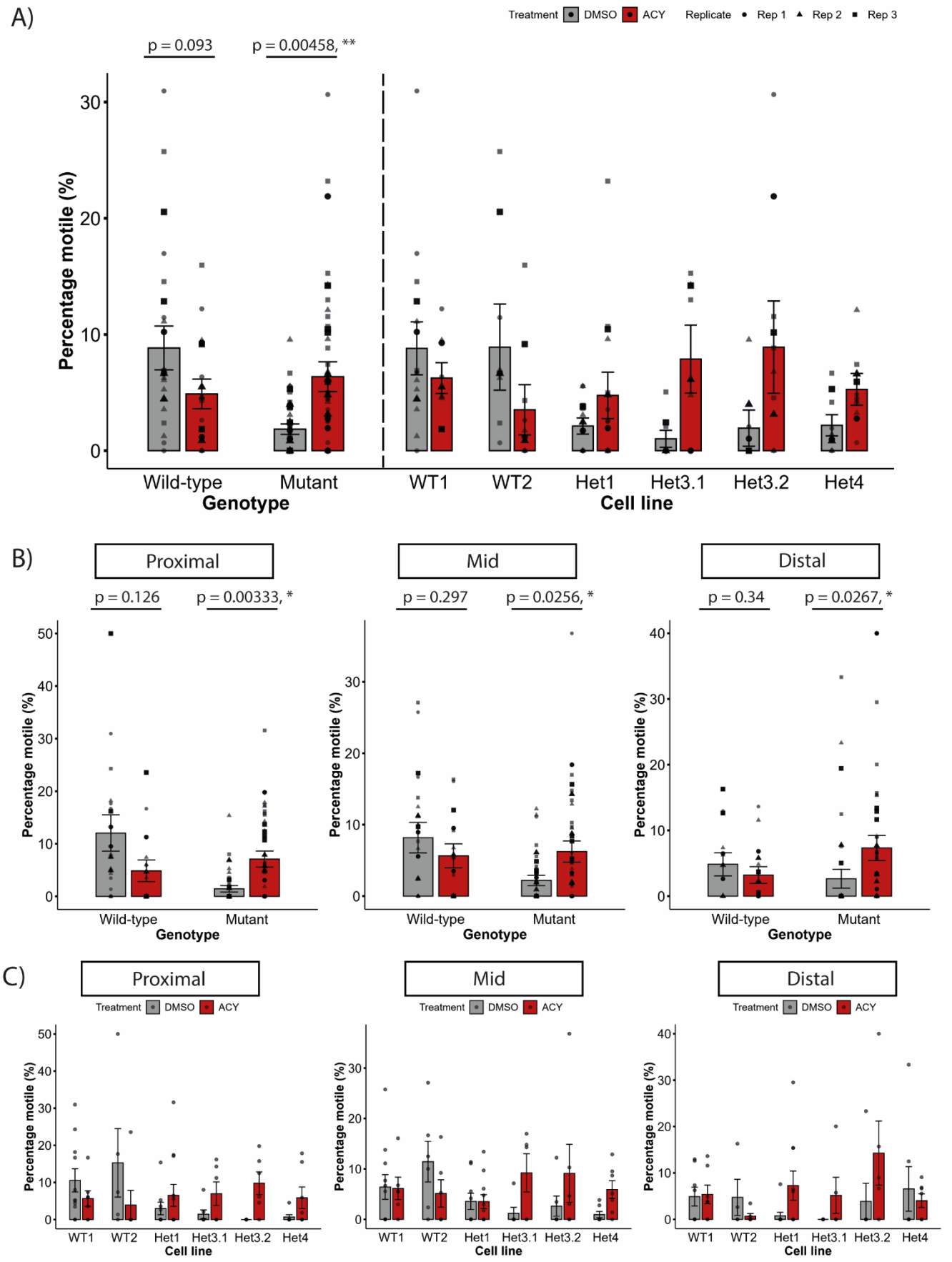


Figure 4.21: HDAC6i increases anterograde transport in MFN2$^{R94Q/+}$ sMNs. *(A) Average percentage motile anterograde mitochondria in wild-type (r = 0.508) and mutant (r = 0.585) sMNs*

*that have been treated with 0.01% DMSO or 100 nM ACY-738 (ACY). (B) Average percentage motile anterograde mitochondria in the proximal (wild-type, r = 0.466; mutant, r = 0.605), mid (wild-type, r = 0.324; mutant, r = 0.462), and distal (wild-type, r = 0.301; mutant, r = 0.459) portions of wild-type and mutant sMN axons that have been treated with 0.01% DMSO or 100 nM ACY-738. (C) Average percentage motile anterograde mitochondria in each cell line in the proximal, mid, and distal portions of the axons. Each data point represents the average for a single neuron and plotted as mean ± SEM. Wilcoxon rank sum test: N = 6 wild-type, 12 mutant; ns = p>0.05, * = p ≤ 0.05, ** = p ≤ 0.01.*

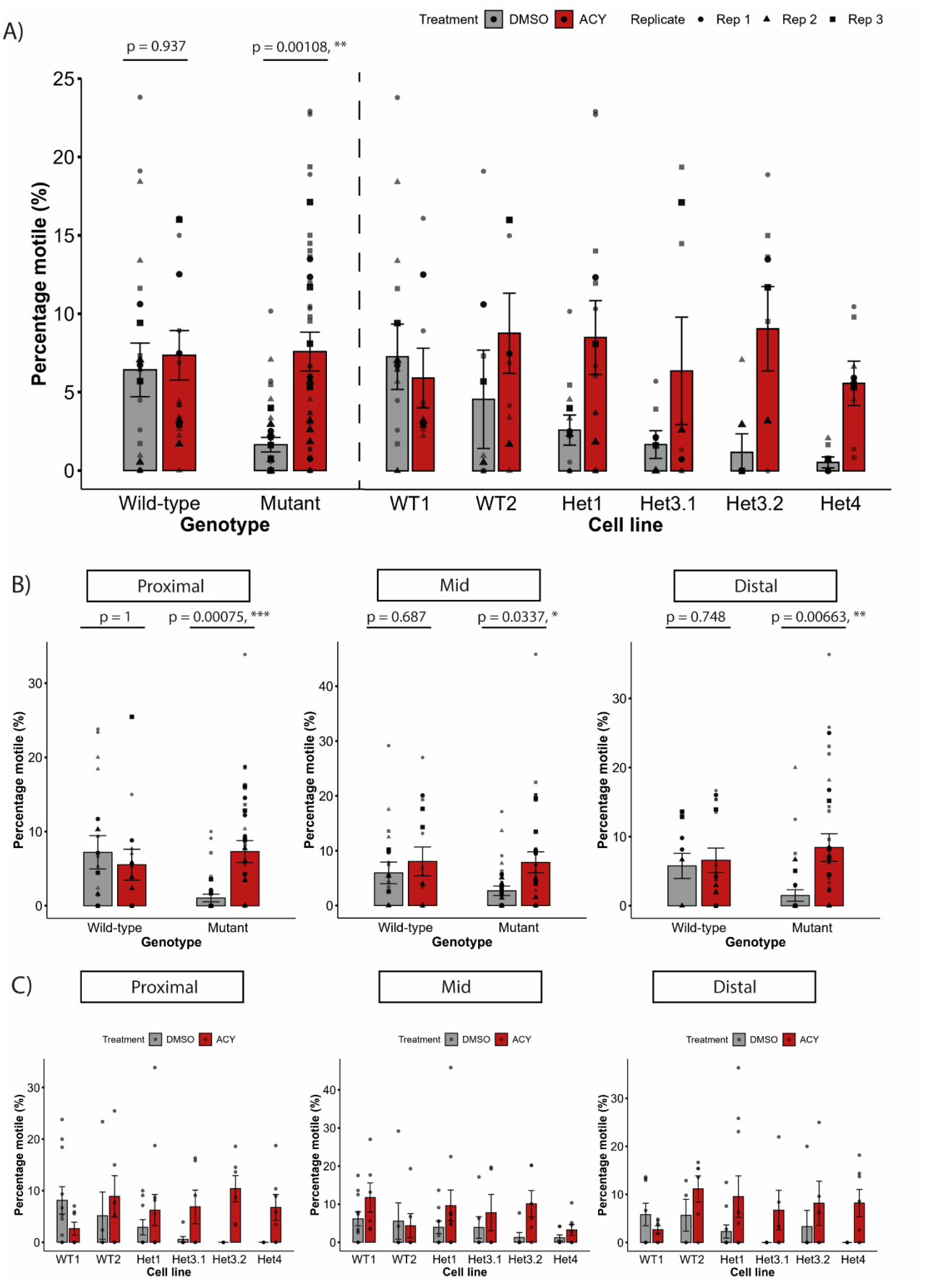

A)
Treatment DMSO ACY
Replicate Rep 1 Rep 2 Rep 3
p = 0.937
p = 0.00108, **
Percentage motile (%)
Wild-type
Mutant
Genotype
WT1
WT2
Het1
Het3.1
Het3.2
Het4
Cell line
B)
Proximal
Mid
Distal
p = 1
p = 0.00075, ***
p = 0.687
p = 0.0337, *
p = 0.748
p = 0.00663, **
C)
Proximal
Mid
Distal

Figure 4.22: HDAC6i increase retrograde transport in MFN2$^{R94Q/+}$ sMN axons. *(A) Average percentage motile retrograde mitochondria in wild-type (r = 0.0462) and mutant (r = 0.673) sMNs that have been treated with 0.01% DMSO or 100 nM ACY-738 (ACY). (B) Average percentage motile retrograde mitochondria in the proximal (wild-type, r = 0.0232; mutant, r = 0.694), mid (wild-type, r = 0.140; mutant, r = 0.439), and distal (wild-type, r = 0.116; mutant, r = 0.560) portions of wild-type and mutant sMN axons that have been treated with 0.01% DMSO or 100 nM ACY-738. (C) Average percentage of motile retrograde mitochondria in each cell line in the proximal, mid, and distal portions of the axons. Each data point represents the average for a single neuron and plotted as mean ± SEM. Wilcoxon rank sum test: N = 6 wild-type, 12 mutant from three independent differentiations; ns = p>0.05, * = p ≤ 0.05, ** = p ≤ 0.01, *** = p ≤ 0.001.*

Next, the effect of ACY-738 treatment on mitochondrial movement dynamics was assessed. Whole track velocity was calculated as before and compared between DMSO- and ACY-738-treated MFN2$^{+/+}$ and MFN2$^{R94Q/+}$ sMNs. No significant difference was found between DMSO- and ACY-738-treated MFN2$^{R94Q/+}$ motile tracks in the anterograde (Figure 4.23A) or retrograde direction (Figure 4.23B). Measuring instantaneous velocity revealed that ACY-738 treatment significantly reduced the average value in both MFN2$^{+/+}$ and MFN2$^{R94Q/+}$ sMNs in both the anterograde (Figure 4.23C) and retrograde direction (Figure 4.23D). Velocity difference was calculated as before as a proxy for direction switching and it was found that whilst ACY-738 had no effect on the distribution of MFN2$^{+/+}$ velocity difference, it did shift the distribution of MFN2$^{R94Q/+}$ to the right (Figure 4.23E). This suggests that MFN2$^{R94Q/+}$ motile tracks were less likely to travel at a consistent velocity and that there may be impairments with motor proteins interacting with the mitochondria or microtubules.

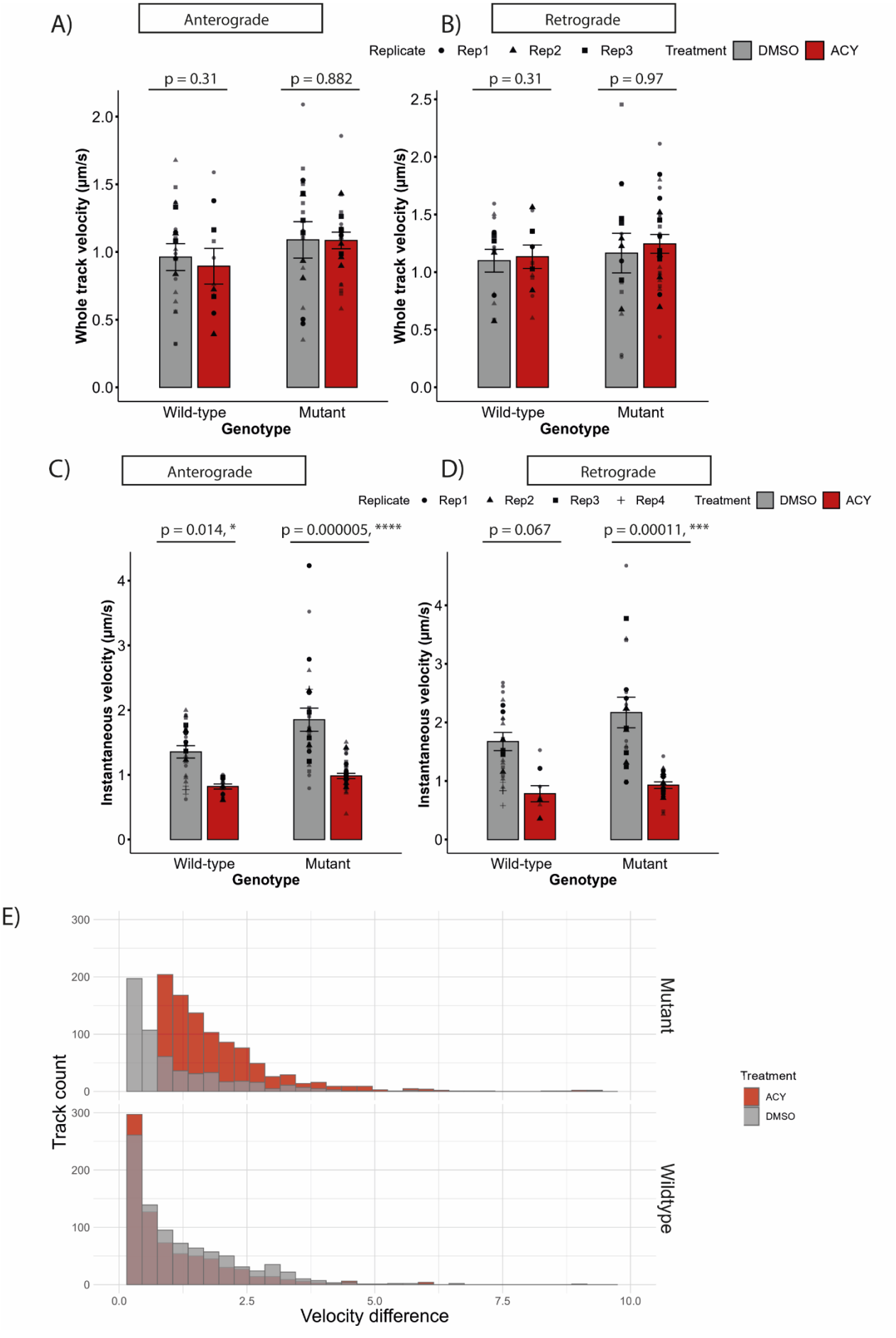

A)
Anterograde
B)
Retrograde
Replicate Rep1 Rep2 Rep3
Treatment DMSO ACY
p = 0.31
p = 0.882
p = 0.31
p = 0.97
Whole track velocity (µm/s)
Wild-type
Mutant
Genotype
C)
Anterograde
D)
Retrograde
Replicate Rep1 Rep2 Rep3 Rep4
Treatment DMSO ACY
p = 0.014, *
p = 0.000005, ****
p = 0.067
p = 0.00011, ***
Instantaneous velocity (µm/s)
E)
Track count
Mutant
Wildtype
Velocity difference
Treatment
ACY
DMSO

Figure 4.23: HDAC6 inhibition alters the velocity of motile mitochondria in sMN axons. *(A) Average whole track velocity of anterograde mitochondria in wild-type (r = 0.324) and mutant (r = 0.0425) sMN axons treated with 0.01% DMSO or 100 nM ACY-738 (ACY). (B) Average whole track velocity of retrograde mitochondria in wild-type (r = 0.324) and mutant (r = 0.0172) sMN axons treated with 0.01% DMSO or 100 nM ACY-738. (C) Average instantaneous velocity of anterograde mitochondria in wild-type (r = 0.674) and mutant (r = 0.813) sMN axons treated with 0.01% DMSO or 100 nM ACY-738. (D) Average instantaneous velocity of retrograde mitochondria in wild-type (r = 0.613) and mutant (r = 0.768) sMN axons treated with 0.01% DMSO or 100 nM ACY-738. Each data point represents the average for a single neuron and plotted as mean ± SEM. Wilcoxon rank sum test: N = 6 wild-type, 12 mutant from three independent differentiations; ns = p>0.05, * = p ≤ 0.05, *** = p ≤ 0.001, **** = p ≤ 0.0001. (E) Histogram of the difference between maximum anterograde and maximum retrograde speeds for motile tracks in wild-type and mutant sMNs axons treated with 0.01% DMSO or 100 nM ACY-738 (ACY).*

The effect of ACY-738 on the pausing of motile mitochondria was quantified next. ACY-738 treatment significantly increased the average percentage of motile tracks that paused in $MFN2^{R94Q/+}$ sMNs, bringing it to a comparable level of DMSO-treated $MFN2^{+/+}$ sMNs (Figure 4.24A). This trend was present in all $MFN2^{R94Q/+}$ lines (Figure 4.24A). The pause coefficient was calculated as before, and no significant difference was observed in $MFN2^{+/+}$ or $MFN2^{R94Q/+}$ motile mitochondria after ACY-738 treatment, although $MFN2^{+/+}$ motile tracks experienced a small increase after ACY-738 treatment (Figure 4.24B).

Finally, motile track length in $MFN2^{+/+}$ and $MFN2^{R94Q/+}$ sMNs after ACY-738 treatment was calculated. No significant difference was detected between DMSO- and ACY-738 treated $MFN2^{+/+}$ and $MFN2^{R94Q/+}$ sMNs (Figure 4.25A). When the motile tracks were divided into direction and axonal location, no differences in the motile track length of anterograde mitochondria were seen in the proximal, mid, or distal portions of the axon after HDAC6 inhibition (Figure 4.25B). Motile track length of retrograde mitochondria also remained unchanged by HDAC6 inhibition in the proximal, mid, and distal portions of the sMNs (Figure 4.25C).

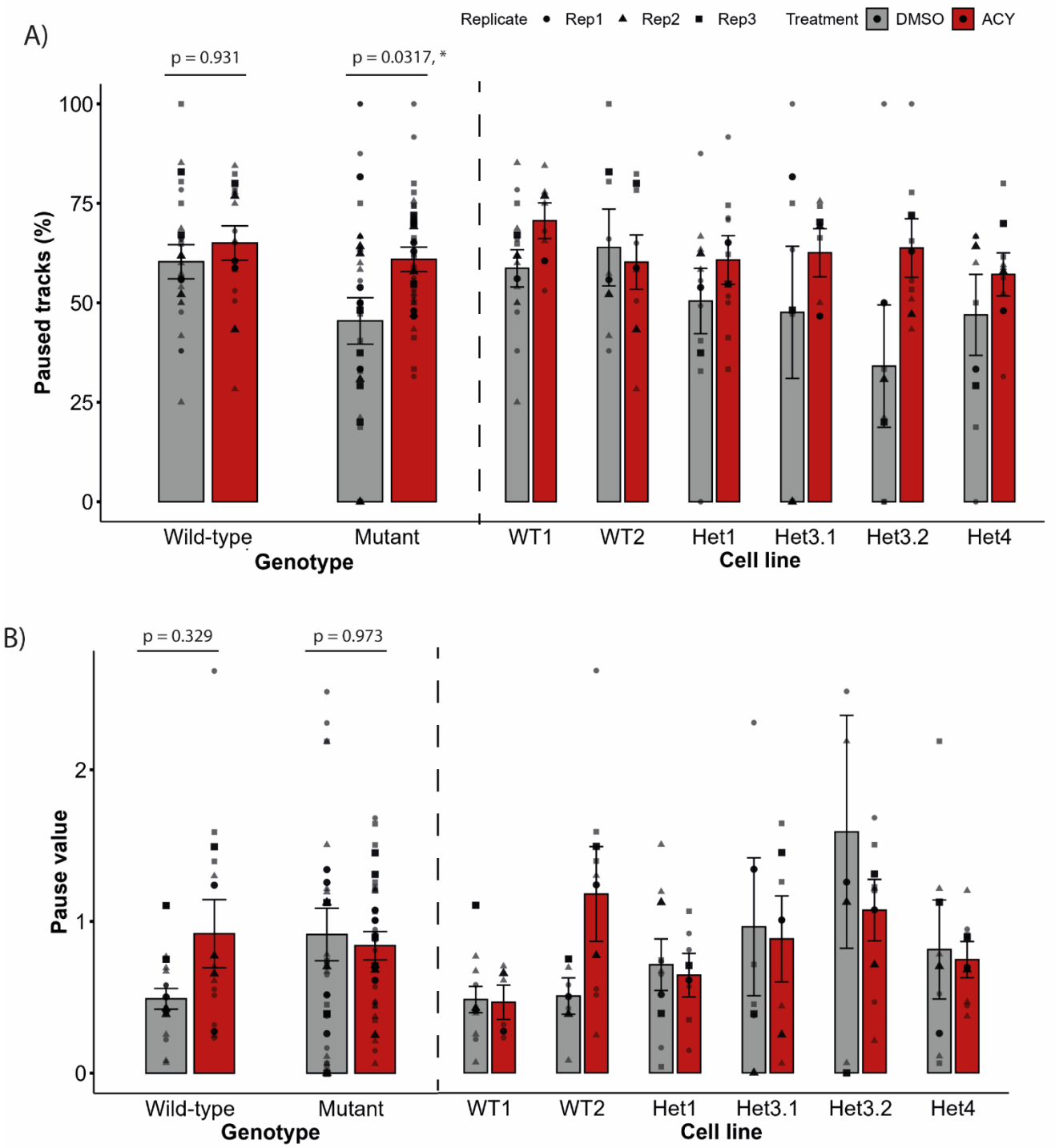


Figure 4.24: Pausing of motile mitochondria in sMNs treated with ACY-738. *(A) The average percentage of motile tracks that paused in wild-type (r = 0.0550) and mutant (r = 0.449) sMN axons treated with 0.01% DMSO or 100 nM ACY-738 (ACY). (B) Average pause coefficient of motile mitochondria in wild-type (r = 0.330) and mutant (r = 0.0154) sMN axons treated with 0.01% DMSO or 100 nM ACY-738 (ACY). Data plotted as mean ± SEM and each data point represents an individual Neuron. Wilcoxon rank sum test: N = 6 wild-type, 12 mutant from three independent differentiations; ns = p 0.05, * = p ≤ 0.0.5.*

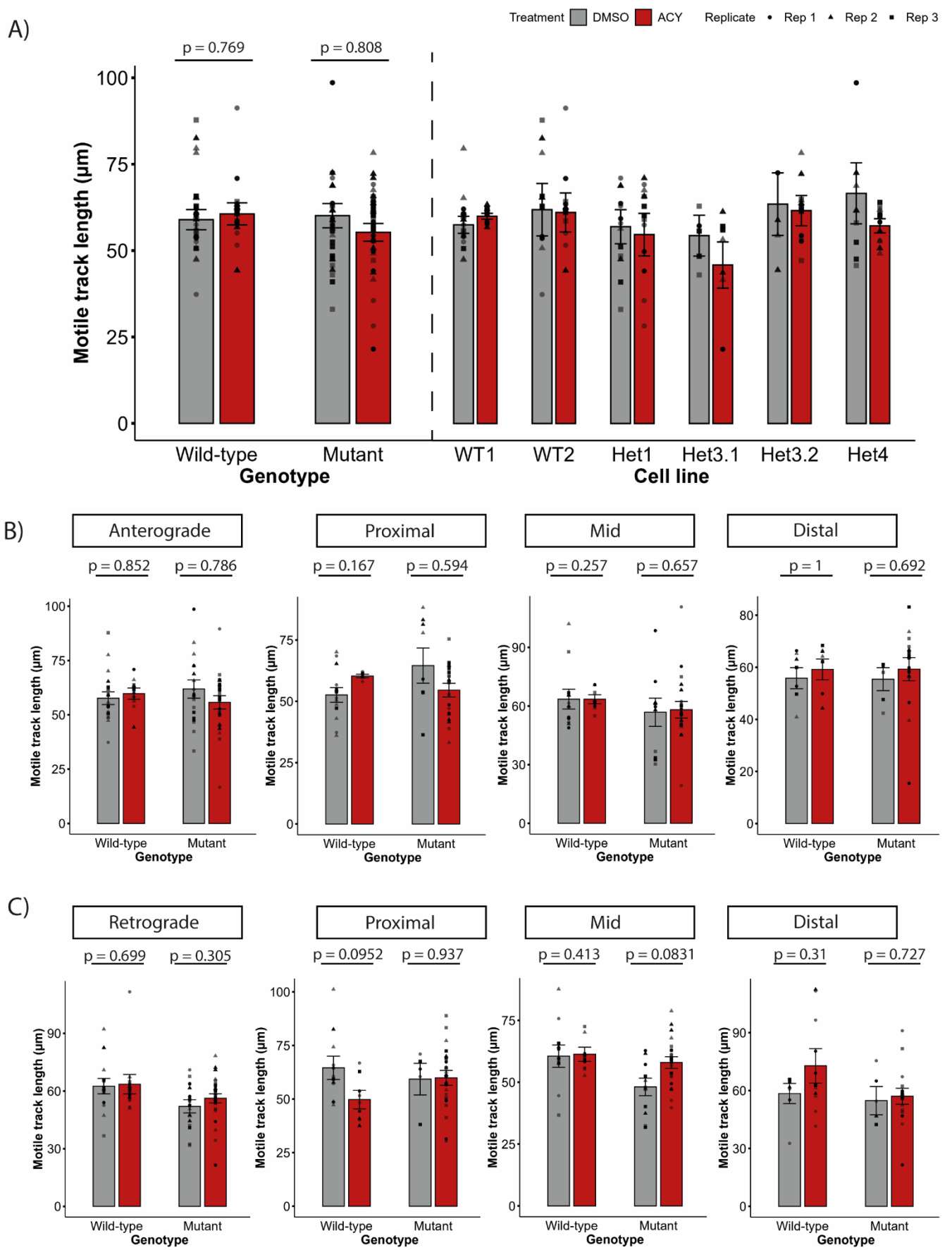


Figure 4.25: HDAC6i does not alter motile track length. *(A) Average motile track length of mitochondria in wild-type (r = 0.0653) and mutant (r = 0.0411) sMN axons treated with 0.01% DMSO*

or 100 nM ACY-738 (ACY). (B) Average motile track length of anterograde mitochondria across the axon (wild-type, r = 0.185; mutant, r = 0.195) and in the proximal (wild-type, r = 0.516; mutant, r = 0.158), mid (wild-type, r = 0.405; mutant, r = 0.114), and distal (wild-type, r = 0.0330; mutant, r = 0.141) portions of the axon. (C) Average motile track length of retrograde mitochondria across the axon (wild-type, r = 0.139; mutant, r = 0.242) and in the proximal (wild-type, r = 0.561; mutant, r = 0.0469), mid (wild-type, r = 0.327; mutant, r = 0.419), and distal (wild-type, r = 0.363; mutant, r = 0.133) portions of the axon. Each data point represents the average for a single neuron and plotted as mean ± SEM. Wilcoxon rank sum test: N = 6 wild-type and 12 mutant from three independent differentiations; ns = p>0.05.

4.3 Discussion

In conclusion, the work in this chapter has demonstrated that sMNs derived from MFN2$^{R94Q/+}$ hESCs have a mitochondrial trafficking defect in their axons. These mitochondria are smaller in size compared to those in MFN2$^{+/+}$ sMN axons, specifically in the distal regions of axons, but do not differ in shape. HDAC6 inhibition by 100 nM ACY-738 is sufficient to restore mitochondrial movement in MFN2$^{R94Q/+}$ sMNs and increase mitochondrial size in the distal portions of the sMN axons.

4.3.1 MFN2$^{R94Q/+}$ mitochondria are smaller and display an axonal transport defect

The results presented in this chapter highlight that MFN2$^{R94Q/+}$ mitochondria are smaller than MFN2$^{+/+}$ mitochondria, but only in the most distal portions of sMN axons. This reduction in area and length was not mirrored in shape descriptors of mitochondria suggesting that the mitochondria themselves were not excessively stressed. Mitochondrial shape has typically been used as a read-out of mitochondrial fusion/fission balance and consequently mitochondrial bioenergetics and health. However, mitochondria in axons have been found to have a more punctate morphology compared to the soma and dendrites and thus morphology changes moving closer to perfectly circular may be harder to detect (Lewis et al., 2018). Morphology changes here may also be a less suitable surrogate for mitochondrial health due to this. The progressive loss in size of MFN2$^{R94Q/+}$ mitochondria from soma to distal axon paired with an increased inter-mitochondrial distance suggested a reduction in the delivery of mitochondria to the distal portions of the axons. Mitochondria aim to maintain even spacing across the length of an axon and thus MFN2$^{R94Q/+}$ may be smaller to facilitate uniform spacing in the face of reduced

numbers (Miller and Sheetz, 2004). A reduction in the number of mitochondria per 100 µm along the axon was thought to be indicative of a transport defect, as axonal transport deficits have been identified in previous models of CMT2A (Misko et al., 2012, Van Lent et al., 2021, Kumar et al., 2024). However, a reduction in mitochondrial content in the cells could also contribute to a reduced number of mitochondria in the distal portions of neurons; future work should look to quantify mitochondrial mass in $MFN2^{+/+}$ and $MFN2^{R94Q/+}$ neurons to see if differences are present that could minimise the contribution of trafficking deficits on CMT2A pathogenesis.

When live mitochondrial transport was observed, $MFN2^{R94Q/+}$ motor neurons exhibited significant defects. Specifically, a reduction in the percentage of motile mitochondria in both the anterograde and retrograde direction compared to wild-type controls was observed, indicating impaired mitochondrial trafficking. This finding was consistent with previous observations in a complementary human induced pluripotent stem cell (hiPSC)-based model of CMT2A (Van Lent et al., 2021), further supporting the hypothesis that mitochondrial transport defects are a core feature of CMT2A pathology. The reduction in mitochondrial numbers in the distal axon paired with a reduction in mitochondrial size may explain the loss of distal muscle innervation seen in *in vivo* models and patients; with fewer, smaller mitochondria being delivered to the synapse there may be a reduction in ATP production which would affect synaptic vesicle recycling (Pathak et al., 2015), or a reduction in calcium buffering which could affect neurotransmitter release and post-release recovery (White and Reynolds, 1997, Verma et al., 2022). These events could lead to synaptic death and a reduction in distal muscle innervation. Future work may benefit from observing the neuromuscular junction to visualise mitochondrial delivery to the synapse, mitochondrial health at the synapse, and if synaptic death occurs in the presence of $MFN2^{R94Q/+}$. This could be achieved by co-culturing the cells generated in this body of work with skeletal muscle cells differentiated from the same hESC source.

To further dissect the underlying mechanisms of this transport impairment, various aspects of mitochondrial motility were analysed. Whole-track velocity was unchanged by $MFN2^{R94Q/+}$ but $MFN2^{R94Q/+}$ mitochondria spent more time paused. This discrepancy can be explained by noting that $MFN2^{R94Q/+}$ mitochondria had

increased instantaneous velocity, with faster movements with more pauses averaging out to a similar whole-track velocity as $MFN2^{+/+}$ neurons. The increased instantaneous velocity may be explained by a greater reliance on kinesin motors that travel faster than kinesin-1; for example, kinesin-3 contributes to axonal mitochondrial transport and can reach speeds of ≥ 3.0 μm/s (Hirokawa et al., 2009, Guedes-Dias et al., 2019). $MFN2^{R94Q/+}$ mitochondria were also more likely to move bidirectionally within recording periods, suggesting that opposing motor proteins may not achieving the required balance in order to facilitate long-range consistent transport (Bocanegra et al., 2020).

This project has focussed specifically on the transport of mitochondria in the context of a CMT2A-causing MFN2 mutation, but future work should also ascertain if the transport of other organelles is impacted in this model or another hPSC-based model of CMT2A. There is conflicting literature surrounding the axonal transport of other organelles: Misko et al. saw no changes to endosomal or peroxisomal transport in murine dorsal root ganglion neurons expressing MFN2-R94Q but Van Lent et al. showed a reduction in lysosomal transport in hiPSC-derived $MFN2^{R94Q/+}$ sMNs (Misko et al., 2010, Van Lent et al., 2021). This may be due to differences between species and cell types, differences in the way that these organelles are transported along an axon, and the age of the cells (Maday et al., 2014). It would be important to determine if the transport of other organelles is impacted and when this occurs in relation to the reduction in mitochondrial transport to see if there are shared mechanisms that point towards a pathomechanism governed by MFN2.

It should also be acknowledged that the $MFN2^{R94Q/+}$ sMNs could be metabolically compromised as a consequence of mutated MFN2, and this could contribute towards reduced axonal transport, which is an intensively energy-dependent process. Indeed, a MFN2 deficiency from knock-out or knockdown can lead to decreased expression of respiratory complex subunits, reduced oxygen consumption rates, and reduced mitochondrial membrane potential (Pich et al., 2005, Jiang et al., 2018). When observing the effects of MFN2 point mutations on mitochondrial metabolism and oxidative phosphorylation (OXPHOS), published results begin to echo this. In some patient fibroblast lines, a decrease in coupling efficiency with no differences in ATP production was identified (Loiseau et al., 2007, Guillet et al., 2010) whereas other patient fibroblast lines displayed no deficits in mitochondrial respiration rates (Amiott

et al., 2008). CMT2A iPSC-derived motor neurons containing the A383V mutation displayed a reduction in the activity of respiratory complexes II and III (Rizzo et al., 2016). Conversely, DRG cells expressing CMT2A-associated mutations had no alterations in mitochondrial membrane potential or reduced ATP production (Baloh et al., 2007). Similarly, expression of CMT2A-associated mutations in HEK293 cells did not affect endogenous or maximal oxygen consumption rates, suggesting unimpaired OXPHOS (Baloh et al., 2007). Alterations in the oxygen consumption rate and OXPHOS have been identified in iPSC-derived neurons from multiple CMT2 subtypes, which perhaps suggests that this is a common pathomechanism that occurs downstream as most CMT2-causing genes are not directly linked to mitochondria (Van Lent et al., 2021).

As mitochondrial metabolism and mitochondrial motility are intrinsically linked, in most cases it is difficult to distinguish the initiating and consequential deficit between the two (Nasrallah and Horvath, 2014, Chen et al., 2023). Future work should investigate the metabolic health of the mitochondria in the hESC-based model detailed in this body of work to identify any deficits, and if any deficits are uncovered whether HDAC6 inhibition can rescue these. This model may also provide a platform to investigate the interplay between mitochondrial metabolic health and long-range axonal transport of mitochondria, alongside other organelles.

4.3.2 HDAC6 inhibition alleviates MFN2$^{R94Q/+}$ mitochondrial transport defect

HDAC6 inhibition has been shown to be effective in reducing motor and sensory pathology in both mouse (Picci et al., 2020, Shen et al., 2021) and zebrafish models of CMT2A (Jestice et al., in preparation). ACY-738 was used to inhibit HDAC6 in hESC-derived MFN2$^{R94Q/+}$ sMNs to test the hypothesis that HDAC6 inhibition is a viable target for the treatment of CMT2A. A 24-hour treatment with 100 nM of ACY-738 was able to restore the average percentage of motile mitochondria in MFN2$^{R94Q/+}$ sMNs to a level comparable to MFN2$^{+/+}$ sMNs. This rescue was bidirectional and not specified to any axonal position. HDAC6 inhibition by ACY-738 increases α-tubulin acetylation in axonal microtubules, and is posited to increase kinesin-1 binding to microtubules (Reed et al., 2006). This theory is not fully accepted in the field, however, as α-tubulin acetylation occurs within the microtubule

polymer whereas kinesins and other microtubule-protein interactions occur on the outer surface of microtubules (Nogales et al., 1998b).

HDAC6 inhibition by ACY-738 exerted an interesting effect on the velocity of anterograde and retrograde mitochondria in both wild-type and mutant sMNs, reducing the instantaneous velocity of all mitochondria to ~1 µm/s with much smaller variation compared to DMSO-treated cultures. This also reduced the difference between the whole track and instantaneous velocities, indicating that there were fewer pausing events which was confirmed by calculating the pause coefficient of ACY-738 treated motile mitochondria. No clear link has been made between α-tubulin acetylation and kinesin-1 velocity, with several groups presenting evidence that the two are not linked (Walter et al., 2012, Kaul et al., 2014). Conversely, HDAC6 inhibition was shown to increase kinesin-1-driven velocity of BDNF vesicles in a model of Huntington's disease (Dompierre et al., 2007) and loss of α-tubulin acetylation was shown to reduce kinesin-1 velocity (Reed et al., 2006). Similarly, loss of tubulin acetylation has been shown to reduce axonemal dynein velocity (Alper et al., 2014). Kinesin-1 is thought to be the primary motor that moves mitochondria anterogradely but both kinesin-1 and kinesin-3 are involved in the axonal transport of mitochondria, and it is not possible to determine the extent to which each motor is involved in moving the mitochondria that have been analysed in this chapter (Nangaku et al., 1994). The reduction seen in velocity after HDAC6 inhibition may be due to a change in motor protein preference, with the slower kinesin-1 predominating over the faster kinesin-3 rather than a singular motor protein moving slower.

HDAC6 inhibition was also shown the increase the area and length of mitochondria in the distal portions of MFN2$^{R94Q/+}$ sMNs. This most likely due to the increased delivery of mitochondria to the distal portions of sMN axons, allowing mitochondria to undergo more kiss-and-run fusion/fission events and retain size whilst maintaining equal spacing along the axon (Liu et al., 2009). This also suggests that there may not be a fusion deficit in MFN2$^{R94Q/+}$ mitochondria as fusion, measured by mitochondrial size, increases with the delivery of mitochondrial fusion partners to the distal axon. This is in contrast to the hypo- and hyperfusion phenotypes have been reported in CMT2A models investigating different MFN2 mutations (Das et al., 2024, Zhang et al., 2024). Mitochondrial fusion and fission are governed by multiple factors beyond MFN2, including mitochondrial membrane potential, mitochondrial DNA

integrity, and mitochondrial transport (Westermann, 2012, Ul Fatima and Ananthanarayanan, 2023). This interplay makes it difficult to isolate fusion defects within cells that may also have a mitochondrial trafficking defect; cell-free assays could be employed to isolate these factors.

4.3.3 HDAC6 inhibition as a potential therapeutic for CMT2A

This is the first piece of work that demonstrates that HDAC6 inhibition can ameliorate a CMT2A phenotype in human neurons *in vitro*. HDAC6 inhibition has been shown to successfully rescue pathological phenotypes in a CMT2A mouse model using SW-100 and SW-101 (Picci et al., 2020, Shen et al., 2021). ACY-738, SW-100, and SW-101 are all aromatic hydroxamic acid-derived HDAC6 inhibitors with a high affinity for HDAC6 compared to other HDACs (Yufeng and Xuan, 2020, Shen et al., 2021). Selectivity for HDAC6 proves necessary for the development of small molecules for neurodegenerative disorders as pan-HDAC inhibitors developed as chemotherapeutic agents display aggressive side effects (Subramanian et al., 2010).

In conclusion, the data in this chapter demonstrates that MFN2$^{R94Q/+}$ sMNs display a mitochondrial trafficking deficit, with less motile mitochondria and altered velocity. HDAC6 inhibition by ACY-738 is able to restore mitochondrial motility to that of wild-type sMNs.

Chapter 5: Linking MFN2 to mitochondrial transport

5.1 Introduction:

With an established mitochondrial trafficking deficit in hESC-derived MFN2$^{R94Q/+}$ motor neurons, the obvious question remains: how does MFN2$^{R94Q/+}$ cause a mitochondrial trafficking deficit in neurons?

The canonical role of MFN2 is in facilitating outer mitochondrial membrane fusion alongside MFN1. Whilst some other published models of CMT2A have shown a reduction in mitochondrial fusion in the presence of CMT2A-causing mutations, previous work in the Barbarić lab found that the mitochondrial morphology in hESCs and in the soma of Day 16 hESC-derived neurons containing MFN2$^{R94Q/+}$ was not significantly different from that of the wild-type controls. This indicated that a defect in mitochondrial fusion was not present at these time points in the model. Furthermore, mitochondrial size does not significantly differ between the proximal sections of MFN2$^{+/+}$ and MFN2$^{R94Q/+}$ hESC-derived motor neurons, suggesting that a mitochondrial fusion deficit is not the cause of the mitochondrial trafficking deficit. The field has many hypotheses for how mutant MFN2 may disturb normal cell physiology outside of its canonical role, and three possibilities will be explored in this chapter including α-tubulin acetylation, mitochondria-ER contact sites (MERCS), and MFN2-TRAK1 interactions.

As outlined in Chapter 1, MFN2 plays many roles within eukaryotic cells beyond its canonical role of driving outer mitochondrial membrane fusion alongside MFN1. The prevalence of each of these roles is likely to be context-dependent, with different cell types having different homeostatic and metabolic needs. This supports the notion that peripheral neurons have a selective vulnerability in CMT2A, and this may be due to a particular reliance on a facet of MFN2's function that may have some redundancy in other cell types.

As the largest neurons in the body, peripheral neurons are profoundly reliant on a stable cytoskeleton to provide structure and facilitate outgrowth and axonal transport. Disruption to the cytoskeleton has been reported in multiple neurodegenerative

diseases, highlighting its importance in normal axonal physiology (Wurz et al., 2022). As outlined in Chapter 1, neuronal microtubules are subject to post-translational modifications which regulate their stability (Eshun-Wilson et al., 2019). A dysregulation of one such modification – α-tubulin acetylation – has been linked to a loss of axonal transport and neurodegeneration (Dompierre et al., 2007, Neumann and Hilliard, 2014, Guo et al., 2017). Microtubule tubulin acetylation is primarily governed by two opposing enzymes; the deacetylase HDAC6 and the acetylase α-TAT1 work in tandem to maintain a set level of acetylation. Loss of α-tubulin acetylation has been proposed as a possible pathogenic mechanism of CMT2A. In 2020, Picci et al showed a progressive reduction in α-tubulin acetylation only in the distal sciatic nerve of MitoCharc1 mice – mice with one copy of human $MFN2^{R94Q}$ under the neuron specific enolase promoter (Cartoni et al., 2010). This deficit in acetylation could be rescued via HDAC6 inhibition by SW-100, allowing α-TAT1 activity to exceed HDAC6 activity resulting in an increase in tubulin acetylation which correlated with a rescue of the motor phenotype of the mouse. Kumar et al (2024) also showed that α-tubulin acetylation could be reduced by overexpression of MFN2 containing the CMT2A-causing mutations R94Q or T105M in mouse embryonic fibroblasts (MEFs) (Kumar et al., 2024). The same reduction in acetylation was also achieved by MFN2 knockout in MEFs. Kumar et al. also showed using the same model that HDAC6 inhibition could rescue the motility of MFN2-null mitochondria (Kumar et al., 2024). A reduction in α-tubulin acetylation levels in the hESC-derived model of CMT2A outlined in this body of work may explain why HDAC6 inhibition can rescue the mitochondrial trafficking deficit.

Another possible mechanism by which mutant MFN2 may be generating a mitochondrial trafficking deficit is by perturbation of mitochondria-ER contact sites (MERCS). MERCS are involved in lipid metabolism (Petrungaro and Kornmann, 2019), the unfolded protein response (Verfaillie et al., 2012), mitochondrial fusion and fission (Friedman et al., 2011), as well as calcium transfer between the two organelles, thus helping to maintain tight intracellular calcium concentrations (Giacomello et al., 2010). Intracellular calcium concentrations are critical modulators of axonal transport – MIRO, which alongside TRAK1 links mitochondria to motor proteins, is a calcium-sensitive Rho-like GTPase on the OMM (Eberhardt et al., 2020). Increases in Ca^{2+} result in increased Ca^{2+} binding to MIRO and the

subsequent conformational changes lead to a cessation of axonal transport (MacAskill et al., 2009, Wang and Schwarz, 2009). MFN2 has been proposed to participate in MERCS, though the nature of this role is debated in the literature. Increases or decreases in MERCS number may be seen with the presence of a CMT2A-causing mutation in MFN2, which would alter intracellular Ca^{2+} leading to alterations in axonal transport.

One other direct link between MFN2 and axonal transport is the interactions between MFN2 and axonal transport-associated proteins TRAK, and MIRO. MFN2 has been shown to interact with the Drosophila homologues of TRAK1 and TRAK2, as well as MIRO1 and MIRO2 (Misko et al., 2010, Lee et al., 2018a). These interactions are not ablated in the presence of CMT2A-causing mutations but the extent to which these interactions are maintained has not yet been quantified (Misko et al., 2010).

In this chapter, the pathogenic possibilities outlined above will be explored using the hESC-based model of CMT2A described in the previous two chapters.

5.2 Results:

5.2.1 Assessing α-tubulin acetylation is MFN2$^{R94Q/+}$ motor neurons

As previously established in Chapter 4, inhibition of HDAC6 via ACY-738 is capable of rescuing the mitochondrial trafficking deficit present in MFN2$^{R94Q/+}$ hESC-derived limb innervating motor neurons, presumably through increasing tubulin acetylation in microtubules. This raises the question of whether a deficit in tubulin acetylation is present in MFN2$^{R94Q/+}$ neurons prior to HDAC6 inhibition.

Day 35 neurons were treated with ACY-738 or 0.01% DMSO for 24 hours then immunoblotted for tubulin and acetylated tubulin to establish native acetylated tubulin levels in the presence and absence of ACY-738 (Figure 5.1A). The ratio of acetylated tubulin to tubulin was not altered by the presence of MFN2$^{R94Q/+}$ (Figure 5.1B). Additionally, the ACY-738 treatment increased the proportion of acetylated α-tubulin in all the cell lines, although this was not found to be statistically signifcant (Figure 5.1A, C). These findings indicate that MFN2$^{R94Q/+}$ does not affect α-tubulin acetylation and that ACY-738 treatment is an effective means of increasing α-tubulin acetylation.

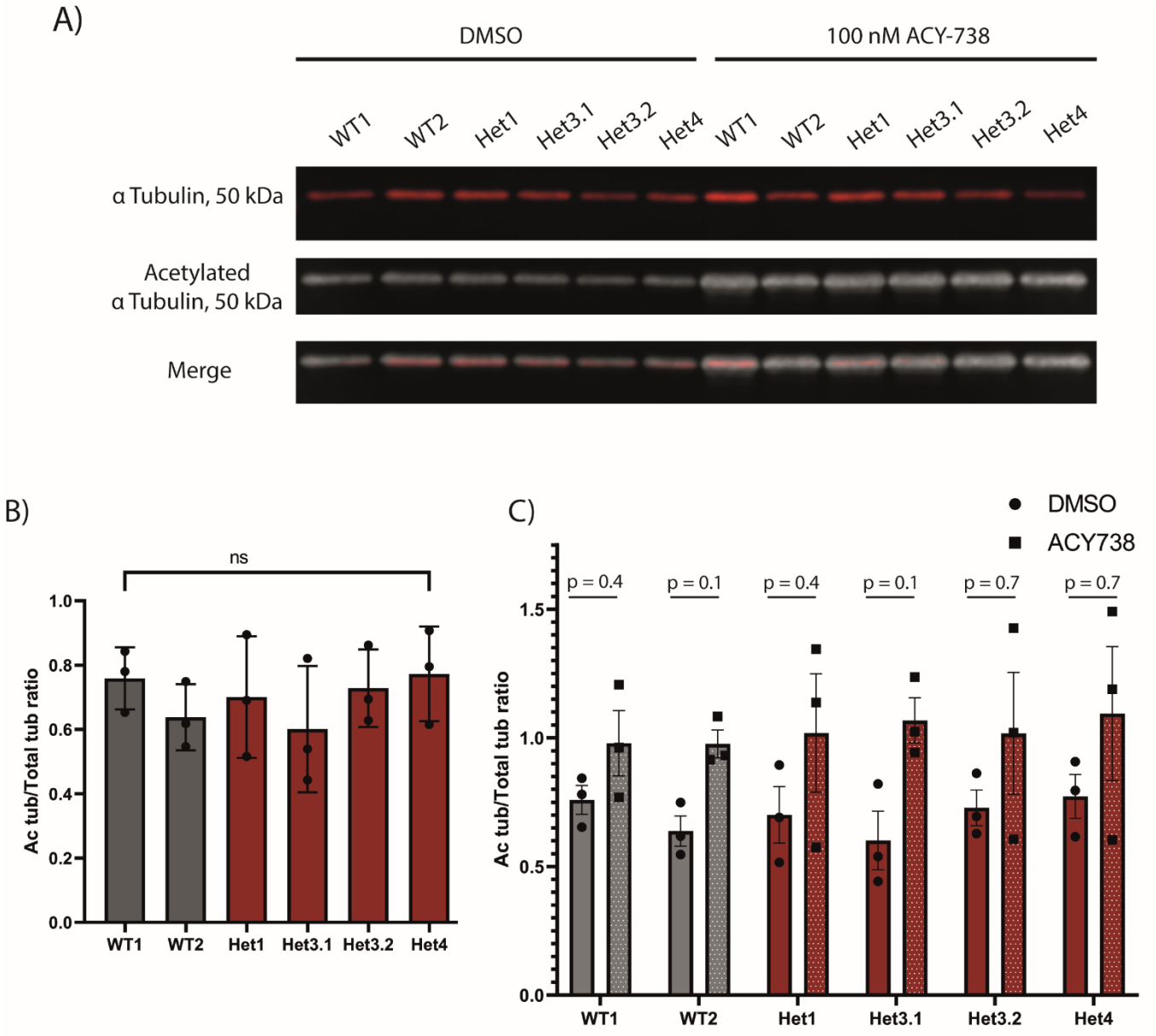


Figure 5.1: Tubulin acetylation is increased by HDAC6 inhibition but not altered by MFN2$^{R94Q/+}$. *(A) Immunoblot of Day 36 limb-innervating hESC-derived motor neurons that had been treated with 0.01% DMSO or 100 nM ACY-738 for 24 hours. Lysates were probed for α-tubulin and acetylated α-tubulin. (B) Quantification of the ratio of acetylated α-tubulin (Ac tub) to α-tubulin (Total tub) in neurons treated with 0.01% DMSO for 24 hours. Data shown as mean ± SD. Kruskal Wallis test; ns = not significant, p = 0.648, H = 0.138. (C) Quantification of the ratio of acetylated α-tubulin (Ac tub) to α-tubulin (Total tub) in neurons treated with 0.01% DMSO (circles) or 100 nM ACY-738 (squares) for 24 hours. Data shown as mean ± SEM. Wilcoxon rank sum test, N = 3 biological replicates: r = 0.445, 0.802, 0.445, 0.802, 0.802, 0.267.*

5.2.2 ER-mitochondrial contacts are unaffected by R94Q

Proximity ligation assays (PLA) are a modified form of immunocytochemistry used as a surrogate for identifying protein-protein interaction in situ (Figure 5.2). PLAs start with primary antibodies raised in different hosts identifying the cellular targets proposed to be interacting. Secondary antibodies that are conjugated to short oligonucleotide linkers bind the primary antibodies and if the DNA linkers are within 40 nm of each other, then hybridisation of the linkers can take place. An amplification step generates a singular fluorescent punctum through rolling circle amplification incorporating fluorescent molecules. Each punctum indicates a site within the cell where by two proteins are close enough to interact, therefore acting as a measure for interaction.

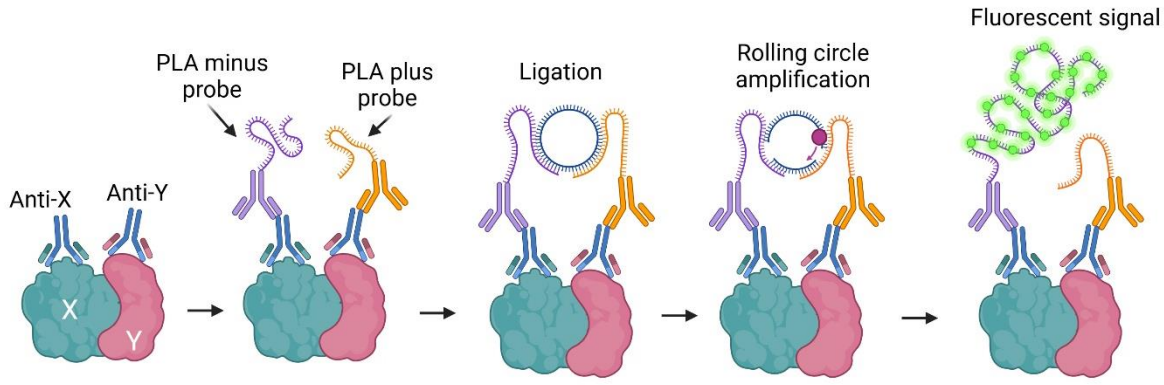


Figure 5.2: Proximity ligation assay. *Two primary antibodies identify two proteins: protein X and protein Y. Secondary antibodies tagged with complimentaryDNA oligonucelotides (PLA plus and minus probes) recognise the primary antibodies. If the PLA plus and minus probes are within 40 nM of each other, the oligonucleotides can be ligated and through rolling circle amplification a fluorescent signal is produced. Schematic made using Biorender.com.*

PLAs can be used to quantify the number of MERCS in a cell by using antibodies against bone fide MERCS tether proteins pairs, like VAPB on the ER and PTPIP51 on mitochondria (De Vos et al., 2012, Stoica et al., 2014). To investigate whether the presence of $MFN2^{R94Q/+}$ in hESCs altered the number of MERCS present, a PLA between VAPB and PTPIP51 was performed (Figure 5.3).

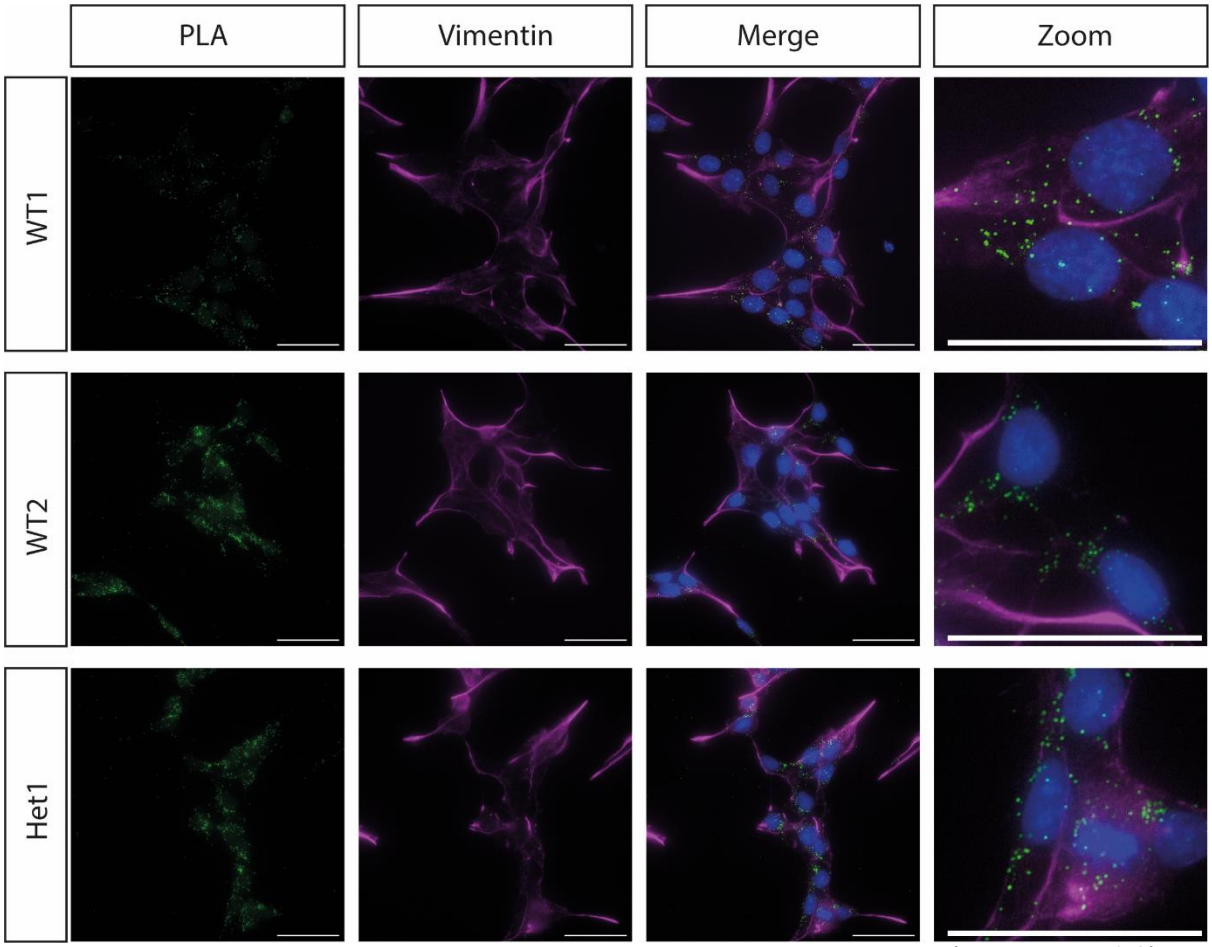


Figure 5.3: PLA between VAPB and PTPIP51 to visualise MERCS in $MFN2^{+/+}$ and $MFN2^{R94Q/+}$ hESCs. *Representative images of PLA in WT1, WT2, and Het1. PLA signal shown in green, and vimentin as a cell mask is shown in magenta. Scale bar = 50 µm.*

Quantification of PLA is typically shown as puncta per cell, but this can be calculated through multiple methods. Both a manual and an automated approach using FIJI were trialled to see which, if either, method was capable of detecting any differences in the number of puncta per cell in $MFN2^{+/+}$ and $MFN2^{R94Q/+}$ hESCs.

The manual approach involved separating the channel containing the puncta and channels containing the cell mask (vimentin) and nuclei. First, an outline of the cell was made around using the cell mask and nuclei and saved as a region of interest (Figure 5.4A). The puncta were then passed through a convolving filter to enhance the signal and manually thresholded. The region of interest was applied to the

thresholded puncta to isolate the puncta belonging to said cell. The number of puncta was then measured by FIJI's 'Analyze Particles' function. This manual approach gave an average of ~20 PLA puncta per cell, and this was not significantly altered by the presence of the R94Q mutation in MFN2 (Figure 5.4B).

Next, the automated analysis in FIJI was performed using a previously established macro and using the same image sets (Figure 5.5A). First, thresholds for the puncta and nuclei were established on a random image set from one replicate, as this would vary between experiments. PLA puncta were identified by 'Find Maxima', and prominence was altered until a balance was reached between the most true signal being detected and least background signal being detected. The prominence level was then entered into the macro. Next, nuclei were blurred using 'Gaussian Blur', and the sigma value needed for sufficient blurring was entered into the macro. The blurred nuclei were then identified using 'Find Maxima', and the prominence value required to correctly identify the nuclei was entered into the macro. The macro was then run on all images from a replicate, and the process was repeated for each replicate. The macro calculates the average number of PLA puncta per cell per image. Analysis using the FIJI macro gave an average of ~25 PLA puncta per cell, and this was not significantly altered by the presence of the R94Q mutation (Figure 5.5B).

When comparing the two analysis approaches, it was clear that whilst absolute values of PLA puncta per cell varied slightly depending on the approach, neither could detect a difference in the number of PLA puncta per cell between $MFN2^{+/+}$ and $MFN2^{R94Q/+}$ genotypes. Consequently, it was concluded that the presence of $MFN2^{R94Q/+}$ in hESCs did not change the number of MERCS.

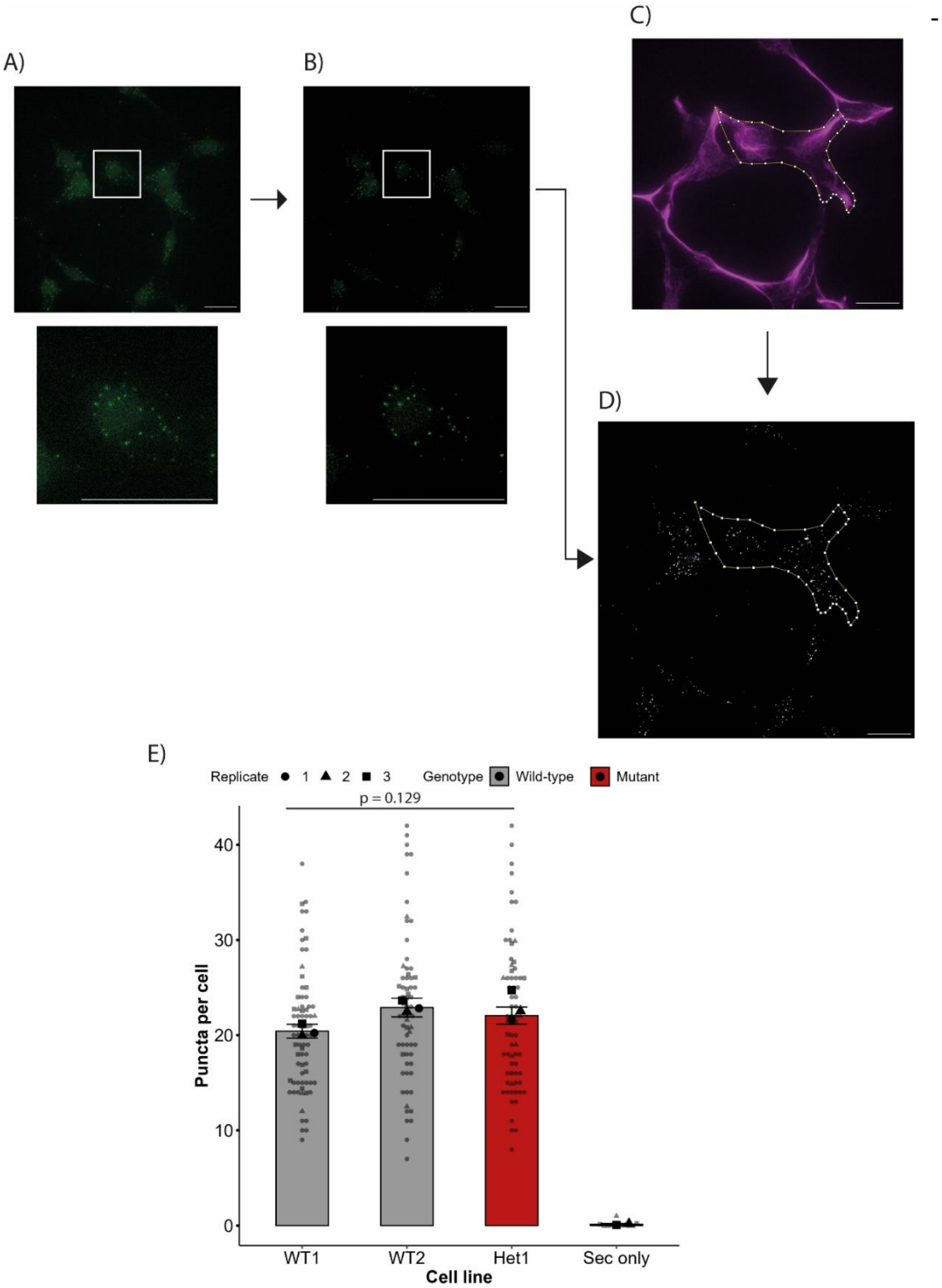


Figure 5.4: Manual analysis of PLA images in CMT2A hESCs. *Schematic showing the manual ImageJ pipeline which begins with the raw image (A) and convolving the PLA signal (B) and then thresholding the signal (D). Scale bar = 50 µm. The region of interest to measure is determined by a cytoplasmic stain (Vimentin) (C) and this ROI is applied to the threshold image to measure the number of puncta between 20 -100 pixels in size. (E) Quantification of the number of puncta per cell using the manual analysis method. Data shown as mean ± SEM and each data point corresponds to a field of view. Kruskal-Wallis test; ns = not significant. N = 3 biological repeats, 6-54 cells analysed per cell line per replicate. H = 0.230.*

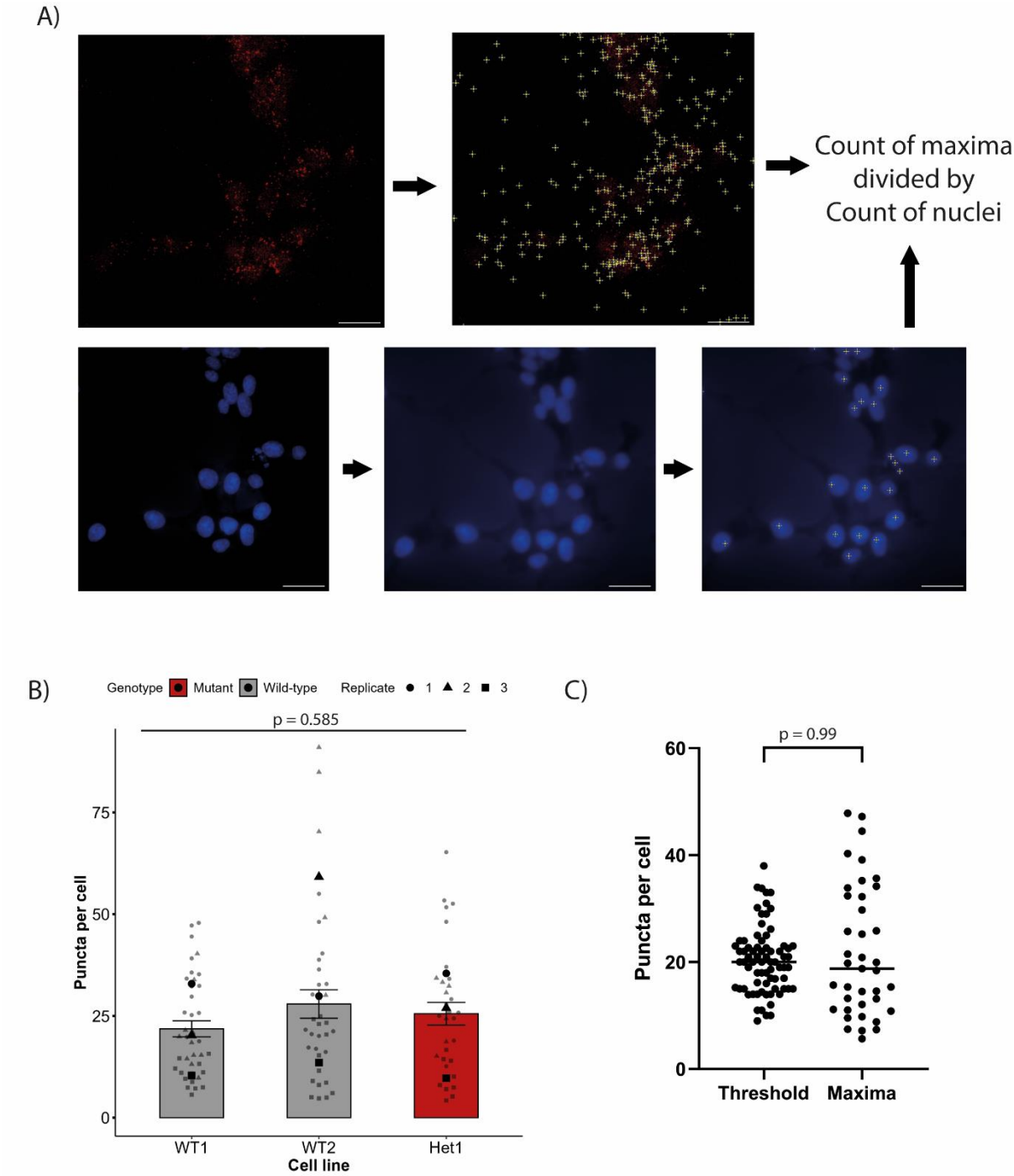


Figure 5.5: PLA quantification using establish ImageJ macro. *(A) Schematic showing the ImageJ macro steps. The PLA signal contrast is enhanced, then 'find maxima' is used to count the puncta. Nuclei count is done by applying a gaussian blur to the image and finding the maxima within the nuclei. Scale bar = 50 µm. (B) Quantification of the number of PLA puncta per cell per image using the ImageJ macro. N=3 biological replicates, ns = not significant, Kruskal-Wallis test. H = 0.570 (C) Different detection methods for the fluorescent puncta were tested. ns = not significant, Wilcoxon rank sum test, r = 0.187, N = 3 biological replicates.*

Whilst PLAs have been used extensively as a measure for the number of MERCS present in a cell, it is only a surrogate as proteins can be within close proximity

without truly interacting (Alsemarz et al., 2018). Furthermore, the role of MFN2 in MERCS may be cell type specific as suggested by discordant data in the literature (De Brito and Scorrano, 2008, Filadi et al., 2015). Consequently, the no observed changes in the number of MERCS between $MFN2^{+/+}$ and $MFN2^{R94Q/+}$ hESCs may not hold true when investigating at a higher resolution or in a more-disease-relevant cell type. Therefore, transmission electron microscopy (TEM) was performed on Day 34 $MFN2^{+/+}$ and $MFN2^{R94Q/+}$ hESC-derived motor neurons to visualise MERCS *in situ* (Figure 5.6A).

TEM allows for high magnification, high resolution of MERSC and thus more informative parameters. The length of MERCS gives a representation of the degree of association between the two organelles, which can change whilst still maintaining contact (and giving a signal on a PLA) (Figure 5.6B). When measured, there was no significant difference in the percentage of a single mitochondrial membrane in contact with the ER between $MFN2^{+/+}$ and $MFN2^{R94Q/+}$ lines (Figure 5.6C). Furthermore, no significant changes in the absolute contact length were seen between $MFN2^{+/+}$ and $MFN2^{R94Q/+}$ neurons (Figure 5.6D).

TEM also allows for analysis of mitochondrial shape within the cell body of neurons; changes in mitochondrial morphology have been reported in other non-neuronal cell models of CMT2A (El Fissi et al., 2018, Rocha et al., 2018). As in Chapter 4, mitochondrial area, perimeter, circularity, and aspect ratio were measured from TEM images of $MFN2^{+/+}$ and $MFN2^{R94Q/+}$ hESC-derived motor neurons (Figure 5.7A-D). From one biological replicate, no differences between $MFN2^{+/+}$ and $MFN2^{R94Q/+}$ neurons were identified for any mitochondrial shape descriptor, further suggesting that there is no imbalance between mitochondrial fusion and fission.

Taken together, this data suggests that the presence of $MFN2^{R94Q/+}$ in hESCs or hESC-derived motor neurons does not significantly alter the physical properties of MERCS. Additionally, mitochondrial morphology in hESC-derived neurons remains unaltered in the presence of $MFN2^{R94Q/+}$ when assessed at a high magnification.

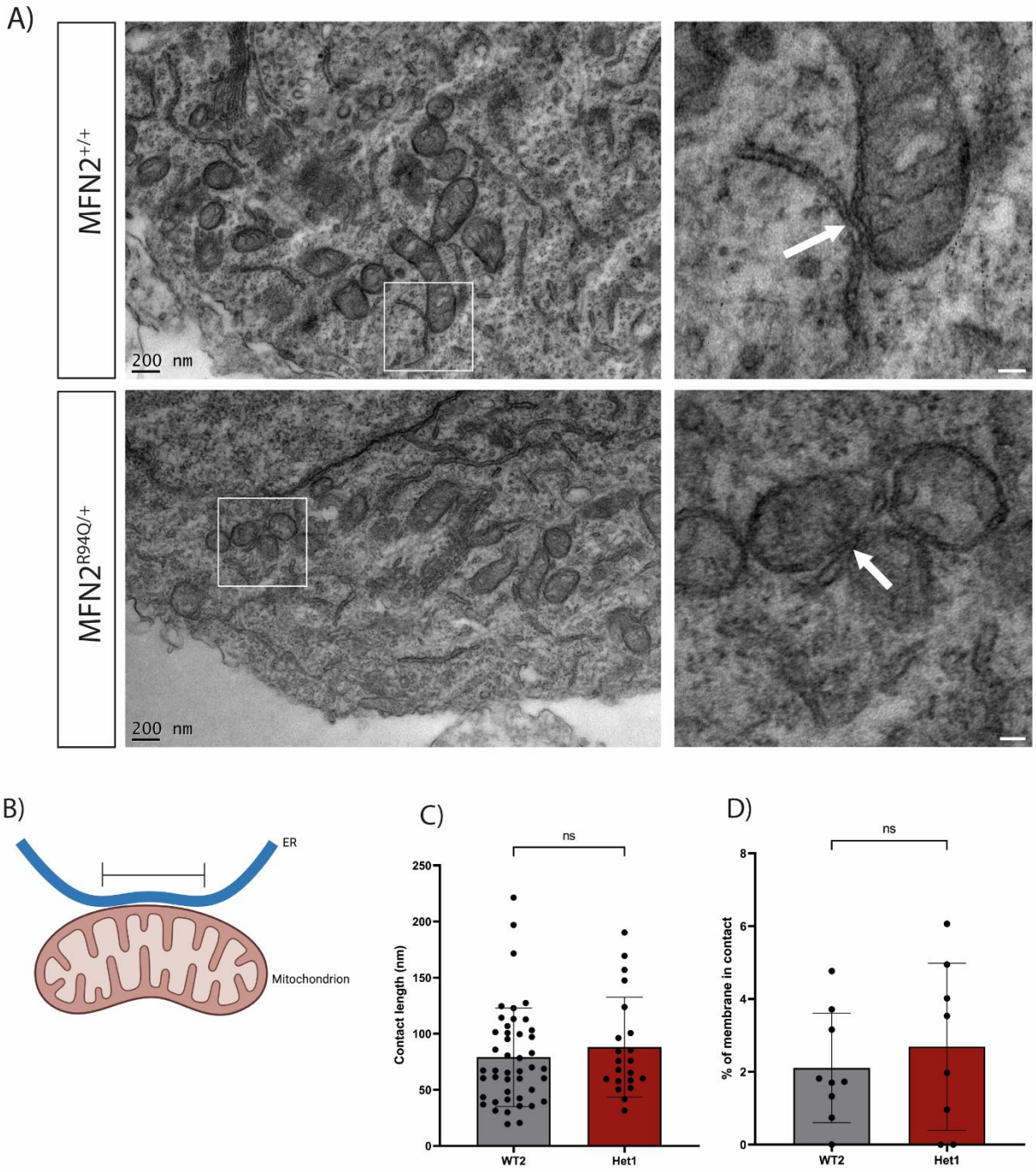


Figure 5.6: TEM images of Day 34 hESC-derived limb innervating motor neurons. *(A) Representative TEM images of Day 34 hESC-derived limb innervating motor neurons. Zoom regions highlight a contact site between mitochondria and the ER, as shown by the white arrow (scale bar = 50 nm unless indicated otherwise). (B) Schematic showing mitochondrion (brown) and the ER (blue) in contact. Bar shows the length of the contact that can be measured. (C) Quantification of the average length of individual contacts in nm and the percentage of the mitochondrial membrane in one image in contact with the ER (D). Data expressed as mean ± SD. Mann Whitney test; P>0.05 = ns. N=8-10 cells from 1 biological replicate.*

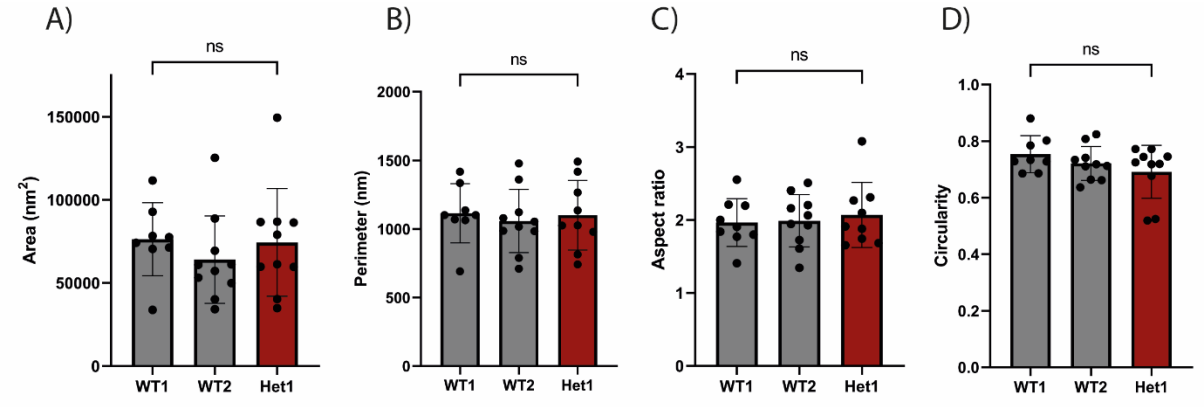


Figure 5.7: Analysis of mitochondrial morphology from TEM images. *(A) Quantification of mitochondrial parameters from TEM images of Day 34 hESC-derived limb innervating motor neurons including mitochondrial area, perimeter, circularity, and aspect ratio. Data shown as mean ± SD. N=8-10 cells from 1 biological replicate.*

5.2.3 MFN2 interactions with TRAK1 are altered by R94Q

With no observed differences in MERCS that could explain the mitochondrial trafficking defect in MFN2$^{R94Q/+}$ hESC-derived motor neurons, MFN2-protein interactions were examined next, focusing on interactions with the trafficking adaptor protein TRAK1.

To investigate the possible change in interaction between TRAK1 and MFN2 in the presence of a CMT2A-causing mutation, a plasmid encoding MFN2 containing a CMT2A-causing mutation needed to be generate. pcDNA3.1-Mfn2-10xMyc-His underwent primer directed site mutagenesis to generate a R94Q version of the plasmid. Successful editing was confirmed via whole plasmid sequencing (Figure 5.8). The wild-type plasmid will be referred to as Myc-MFN2-WT and the mutated plasmid as Myc-MFN2-R94Q.

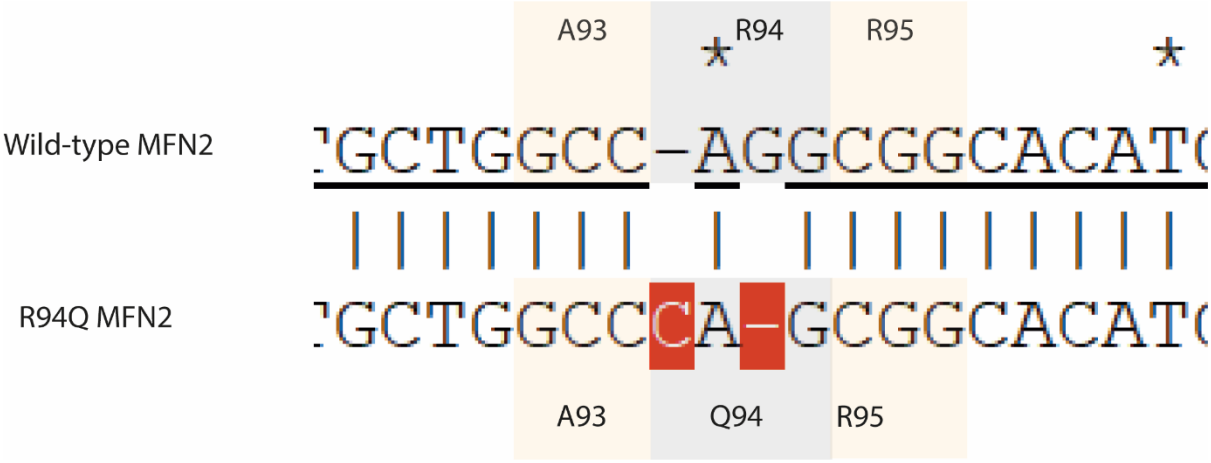


Figure 5.8: Generation of R94Q MFN2 encoding plasmid. *Primer directed site mutagenesis was performed on the pcDNA3-MFN2-10xMyc plasmid, changing the arginine (R) at amino acid position 94 to a glutamine (Q).*

Once the R94Q plasmid had been generated, HEK293 cells were transfected with pRK5-TRAK1-HA and either Myc-MFN2-WT or Myc-MFN2-R94Q. Cell lysates were harvested 24 hours post-transfection and incubated with an anti-HA antibody overnight. Magnetic beads were used to pulldown the anti-HA antibody, the HA-TRAK1 bound to the anti-HA antibody, and any other proteins bound to HA-TRAK1. This immunopellet was run on an immunoblot and probed for HA-TRAK1 and Myc-MFN2. MFN2 co-immunoprecipitated with TRAK1 as expected (Figure 5.9A). Interestingly, more Myc-MFN2-R94Q was pulled down by HA-TRAK1, indicating a stronger interaction between the two proteins in the presence of the CMT2A-causing mutation (Figure 5.9B).

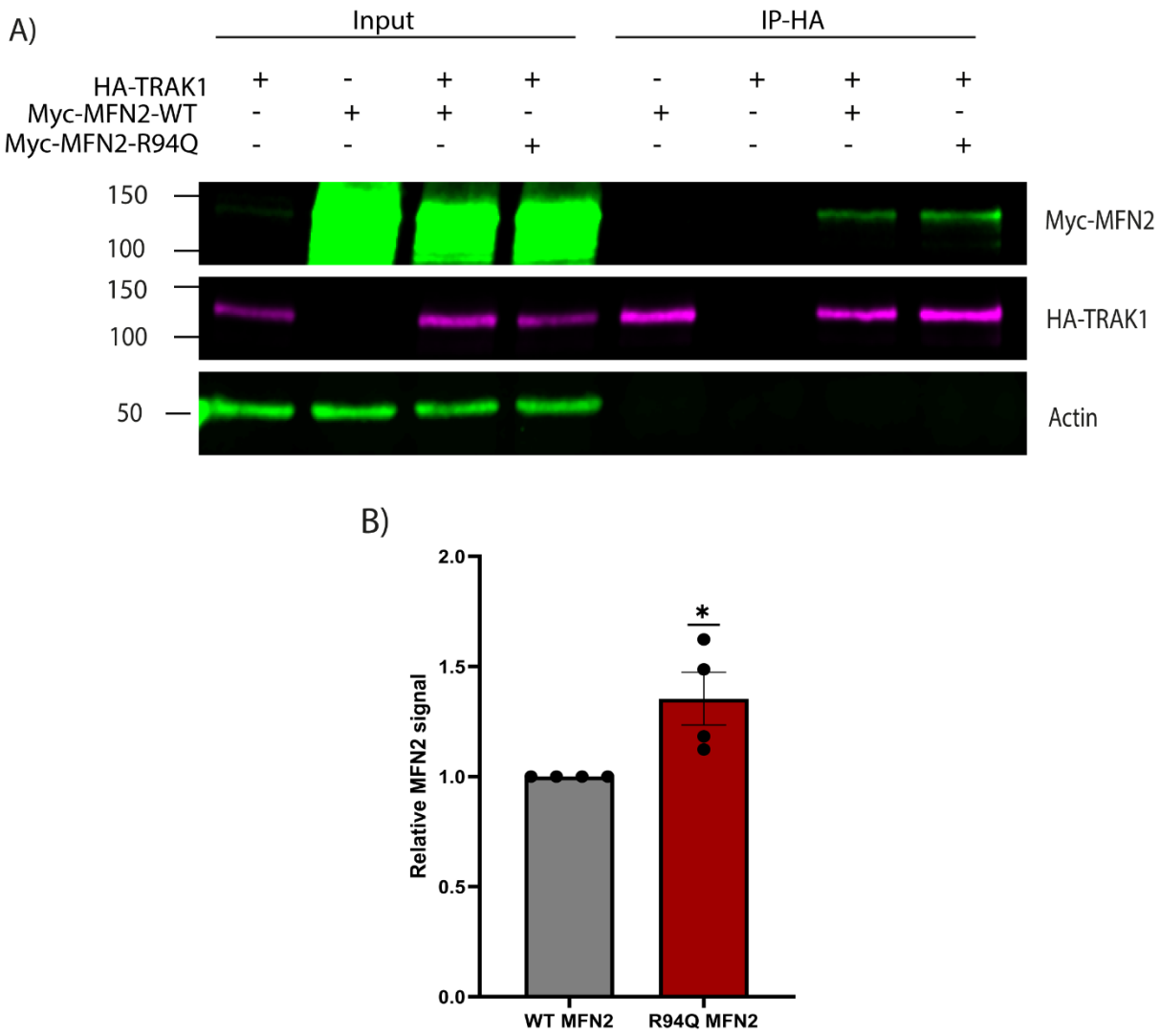


Figure 5.9. Myc-MFN2 interacts with HA-TRAK1 and a CMT2A-causing mutation increases this interaction. *(A) Lysates of HEK293T cells co-transfected with HA-TRAK1 and either empty vector (-), Myc-MFN2-Wild-type (Myc-MFN2-WT), or Myc-MFN2-R94Q were immunoprecipitated using an anti-HA antibody. Input and immune pellets were probed with anti-Myc, anti-HA, and anti-Actin antibodies. (B) Quantification of (A) shows the ratio of anti-Myc signal to anti-HA signal in the immune pellets normalised to the Myc-MFN2-WT condition. Data points represent mean ± SEM from M= 4 independent biological repeats. Statistical significance was calculated by an unpaired T-test (*P<0.05; ns, not significant). d = 1.47.*

As previously mentioned, TRAK1 is an adaptor protein that links mitochondria to the motor protein kinesin, which drives anterograde transport. Multiple genes comprise the kinesin family, with kinesin-1 genes (KIF5A, KIF5B, and KIF5C) generating the kinesin primarily responsible for axonal transport. To investigate whether the altered interaction between MFN2-R94Q and TRAK1 also impacted the interaction between TRAK1 and kinesin-1, the co-immunoprecipitation experiment from Figure 5.9 was repeated except the amount of endogenous KIF5B that was immunoprecipitated by HA-TRAK1 in the presence of wild-type MFN2 or MFN2-R94Q was quantified

(Figure 5.10A). Endogenous KIF5B was immunoprecipitated by HA-TRAK1, and this immunoprecipitation was reduced in the presence of Myc-MFN2-R94Q compared to Myc-MFN2-WT (Figure 5.10B). This suggests that TRAK1 has a weaker interaction with KIF5B in the presence of MFN2-R94Q compared to wild-type MFN2.

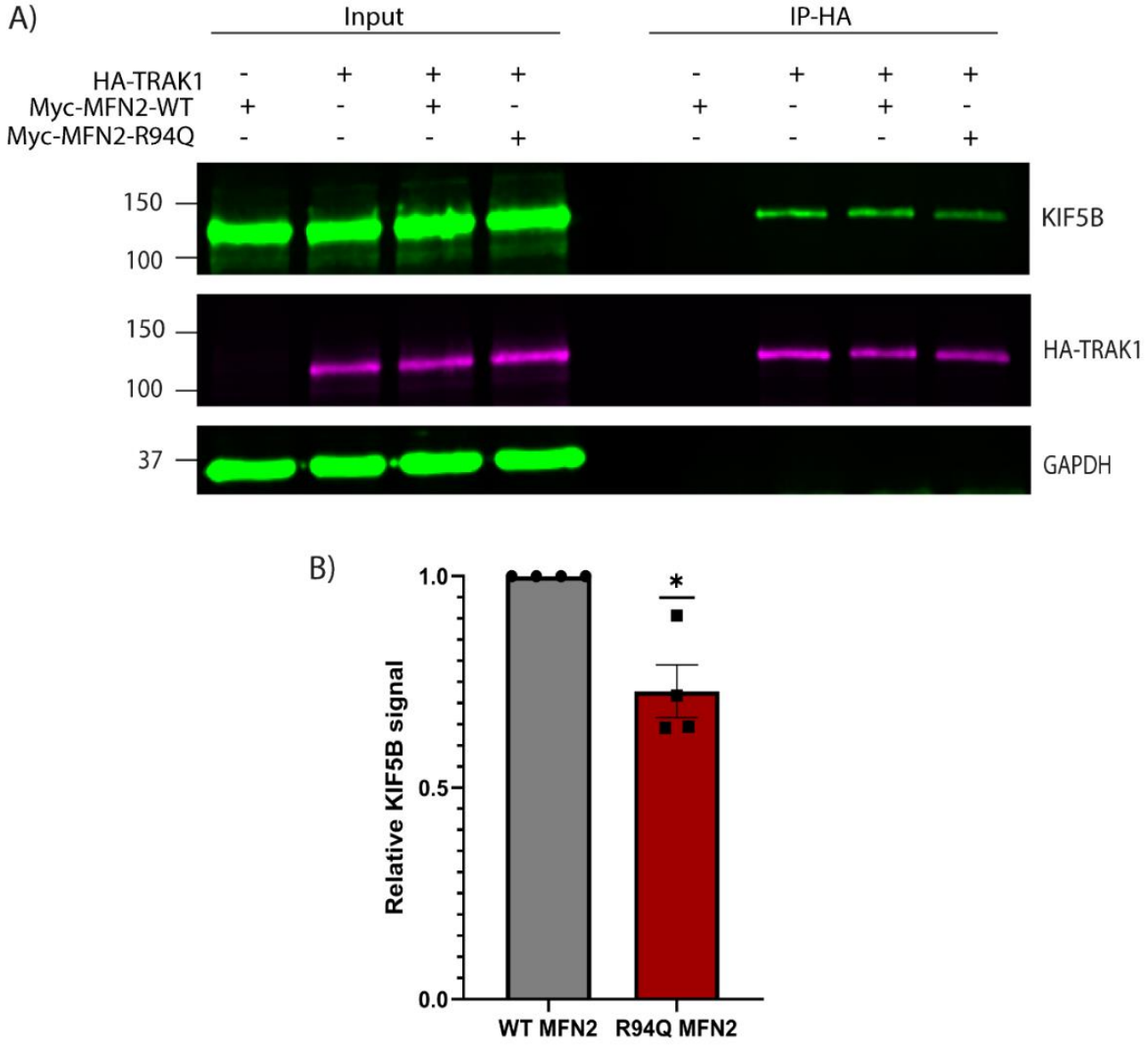


Figure 5.10: Less KIF5B is pulled down by TRAK1 in the presence of R94Q MFN2. *(A) Lysates of HEK293 cells co-transfected with TRAK1-HA and either MFN2- WT-Myc or MFN2- R94Q-Myc were immunoprecipitated using an anti-HA antibody. Immune pellets were probed for TRAK1-HA, KIF5B, and GAPDH on immunoblots. (B) Quantification of (A) shows the ratio of anti-Myc signal to anti-HA signal in the immune pellets normalised to the Myc-MFN2-WT condition. Data points represent mean ± SEM from N = 4 independent biological repeats. Statistical significance was calculated by an unpaired T-test (*P<0.05; **P<0.01; ns, not significant). d = 2.19.*

Having ascertained that TRAK1 and MFN2 interacted, and TRAK1 and KIF5B interacted in the cells, the question remained whether the TRAK1 was interacting with MFN2 and KIF5B at the same time. To test this hypothesis, HEK293 cells were transfected with HA-TRAK1 and either wild-type or R94Q Myc-MFN2 and lysates were immunoprecipitated using anti-Myc beads. KIF5B was not immunoprecipitated by Myc-MFN2, indicating that TRAK1 was not capable of linking the two proteins simultaneously and TRAK1 only interacted with MFN2 or KIF5B at any given time (Figure 5.11). Pairing this with the previous data showing mutant MFN2 reduces the TRAK1-KIF5B interaction, it would suggest that MFN2 indirectly reduces the TRAK1-KIF5B interaction.

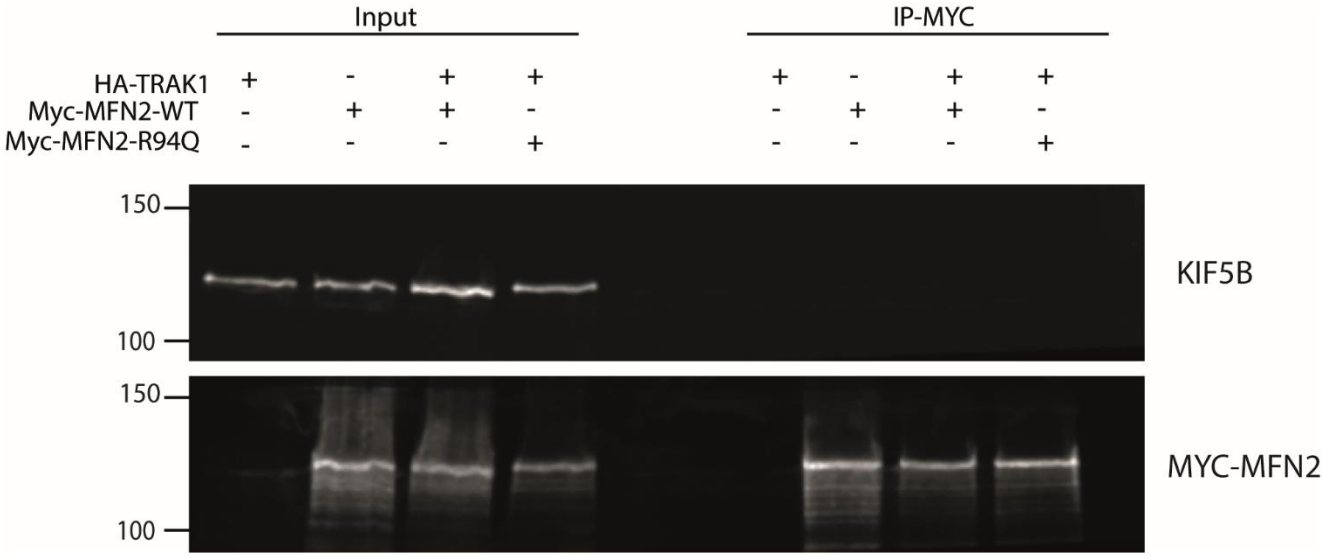


Figure 5.11: KIF5B is not precipitated by Myc-Mfn2. *Lysates of HEK293 cells co-transfected with TRAK1-HA and either MFN2-WT-Myc or MFN2-R94Q-Myc were immunoprecipitated using anti-Myc tag beads. Immune pellets were probed for KIF5B, and Myc-Mfn2.*

TRAK1 interacts with multiple other proteins to facilitate the transport of mitochondria and it is possible that as MFN2 is an interactor of TRAK1, MFN2 mutations may also alter other TRAK1 interactions. Amongst these TRAK1 interactions is the dynein complex, which facilitates retrograde transport in the axon. TRAK1 interacts with the light intermediate chain of dynein via its Hook domain (Lee et al., 2018b, Canty et al., 2023). To see if dynein was interacting with HA-TRAK1, and if this interaction was impacted by mutated MFN2, HEK293 cells were transfected with HA-TRAK1 and

either wild-type or R94Q Myc-MFN2 and lysates were immunoprecipitated using an anti-HA antibody. Using antibodies that had been previously validated in the host lab, immunopellets were probed for dynein intermediate chain (DYNC1I2) (Figure 5.12A) and dynein light chain (DNLC1) (Figure 5.12B). Neither DYNC1I2 or DNLC1 was seen on immunoblots from the HA-TRAK1 pull down, indicating that endogenous dynein was not interacting with HA-TRAK1.

TRAK1 also interacts with MIRO on the outer mitochondrial membrane to dock mitochondria to kinesin-1. To investigate whether endogenous MIRO could be pulled down by HA-TRAK1 and if this interaction was impacted by mutant MFN2, HEK293 cells were transfected with HA-TRAK1 and either wild-type or R94Q Myc-MFN2 and lysates were immunoprecipitated using an anti-HA antibody, then immunopellets were probed for endogenous MIRO. Endogenous MIRO was expressed at a very low level, and was not immunoprecipitated by HA-TRAK1. With such low levels of endogenous expression, it is difficult to discern whether that lack of immunoprecipitation of MIRO is due to low protein availability or due to a lack of interaction. Due to time restrictions, HA-TRAK1 interactions with dynein and MIRO were not pursued within this body of work.

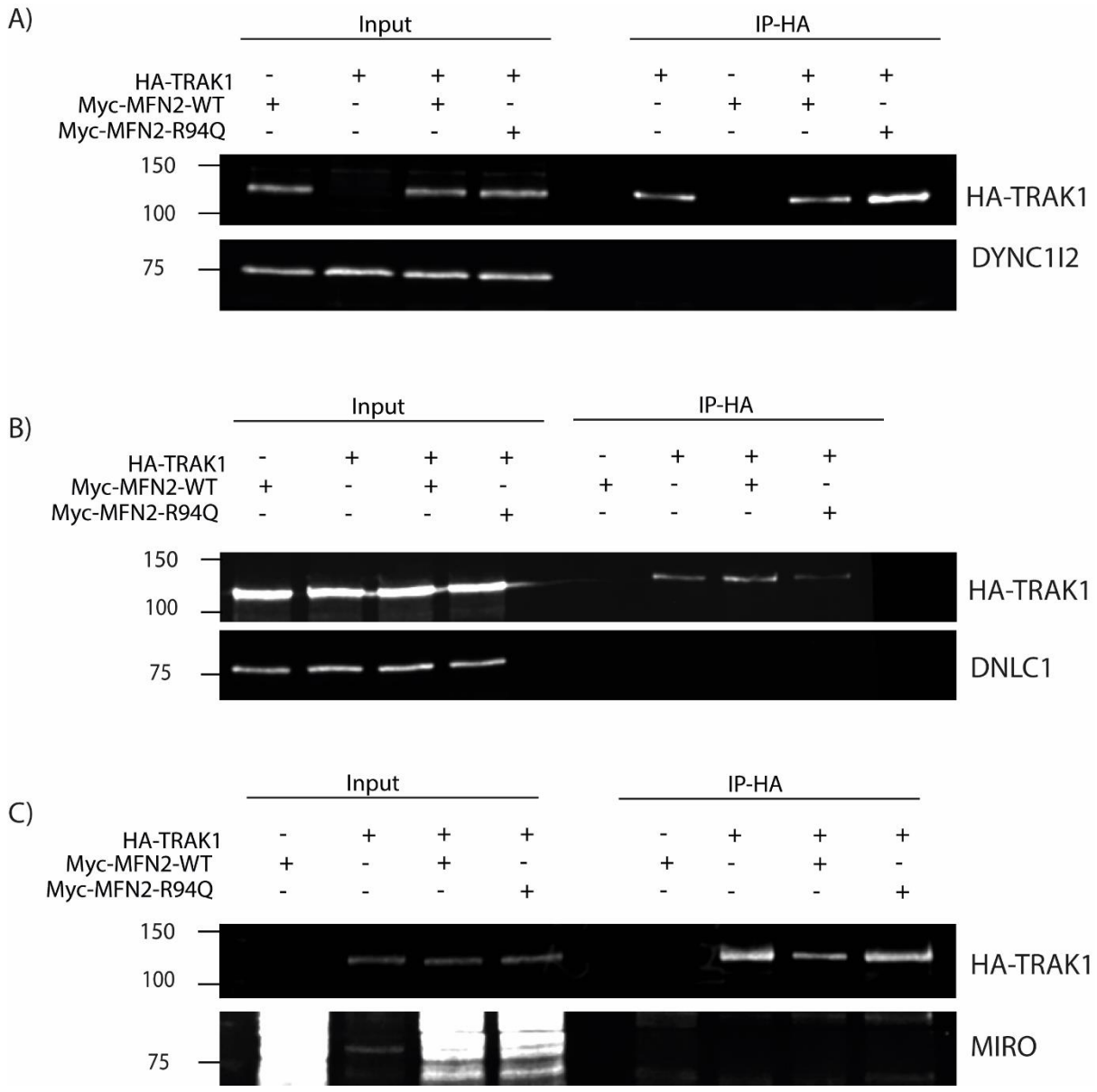


Figure 5.12: Neither endogenous cytoplasmic dynein nor endogenous MIRO are pulled down by HA-TRAK1. *(A) Lysates of HEK293 cells co-transfected with TRAK1-HA and either MFN2- WT-Myc or MFN2- R94Q-Myc were immunoprecipitated using an anti-HA antibody. Immune pellets were probed for TRAK1-HA and DYNC1I2 on immunoblots. (B) Lysates of HEK293 cells co-transfected with TRAK1-HA and either MFN2- WT-Myc or MFN2- R94Q-Myc were immunoprecipitated using an anti-HA antibody. Immune pellets were probed for TRAK1-HA and DNLC1 on immunoblots. (C) Lysates of HEK293 cells co-transfected with TRAK1-HA and either MFN2- WT-Myc or MFN2- R94Q-Myc were immunoprecipitated using an anti-HA antibody. Immune pellets were probed for TRAK1-HA and MIRO on immunoblots.*

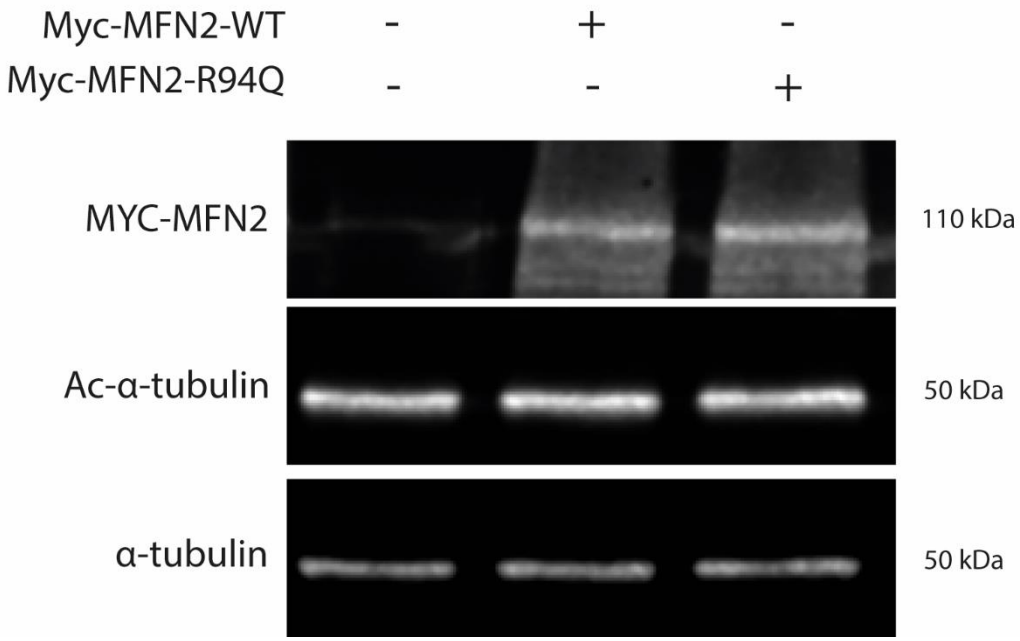


Figure 5.13: MFN2 R94Q overexpression in HEK293 cells does not reduce α-tubulin acetylation. *Western blot analysis of HEK293 lysates that were transfected with empty vector, Myc-MFN2-WT, or Myc-MFN2-R94Q. Immunoblots were probed for Myc-MFN2, α-tubulin, and acetylated α-tubulin.*

Having identified some modified protein-protein interactions relating to MFN2 R94Q that could govern the mitochondrial trafficking deficit characterised in Chapter 4, the effect of ACY-738 treatment on these interactions was investigated as this compound could rescue the mitochondrial trafficking deficit. Firstly, α-tubulin acetylation in the presence of the Myc-MFN2 plasmids was assessed because α-tubulin acetylation is proposed to decrease in the presence of overexpressed mutant MFN2 compared to wild-type (Kumar et al., 2024). HEK293 cells were transfected with Myc-MFN2-WT, Myc-MFN2-R94Q, or an empty vector and lysed 24 hours later. Immunoblotting of the samples revealed no changes in the levels of α-tubulin acetylation, mirroring α-tubulin acetylation ratios in Figure 5.1A (Figure 5.13).

In hESC-derived motor neurons, 100 nM of ACY-738 treatment for 24 hours was sufficient to mildly increase tubulin acetylation ratios without inducing cell death (Figure 5.1C) and rescue the mitochondrial trafficking defect. However, 100 nM of ACY-738 for 24 hours in HEK293 cells was not sufficient to increase tubulin acetylation (Figure 5.14A). A titration of ACY-738 treatment on HEK293 cells was

performed to find an ACY-738 concentration that could increase tubulin acetylation ratios to a comparable level of that seen in neurons treated with 100 nM of ACY-738 (Figure 5.14B). Acetylated tubulin bands appeared larger at ACY-738 doses of 2.5 µM and above, suggesting this was the minimum concentration needed to increase acetylated tubulin after a 24-hour treatment. Thus, this concentration was used for future experiments.

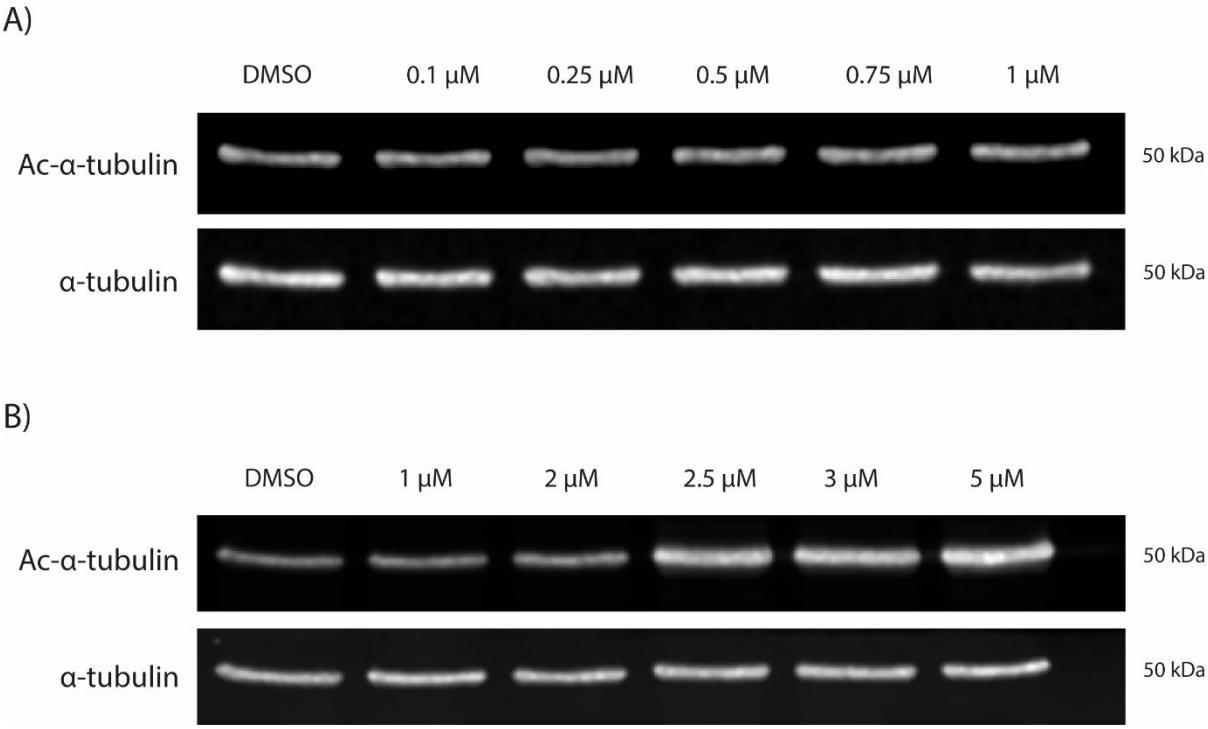


Figure 5.14: Western blot analysis of α-tubulin acetylation in HEK293 cells treated with increasing ACY-738 concentrations. *Immunoblot showing the amount of α-tubulin and acetylated α-tubulin in HEK293 lysates that had been treated with 0.5% DMSO or between 1 µM to 10 µM ACY-738.*

To see if increasing tubulin acetylation levels via HDAC6 inhibition using ACY-738 restored TRAK1-MFN2 interactions in the presence of the R94Q mutation back to a level comparable to wild-type MFN2, the experiment shown in Figure 5.9 was repeated. HEK293 cells were transfected with pRK5-TRAK1-HA and either Myc-MFN2-WT or Myc-MFN2-R94Q and treated with 2.5 µM ACY-738 or 0.2% DMSO. Cell lysates were harvested 24 hours post-transfection and post-treatment and incubated with an anti-HA antibody overnight. Magnetic beads were used to

pulldown the anti-HA antibody. The immunopellet was run on an immunoblot and probed for HA-TRAK1 and Myc-MFN2 (Figure 5.15A). Quantification of these immunoblots showed a small non-significant increase in TRAK1-WT MFN2 interactions after ACY-738 treatment (Figure 5.15B). There was also a small decrease in TRAK1-R94Q MFN2 interactions after ACY-738 treatment, which was now not statistically significant from the TRAK1-WT MFN2 interactions in the DMSO condition (Figure15.B).

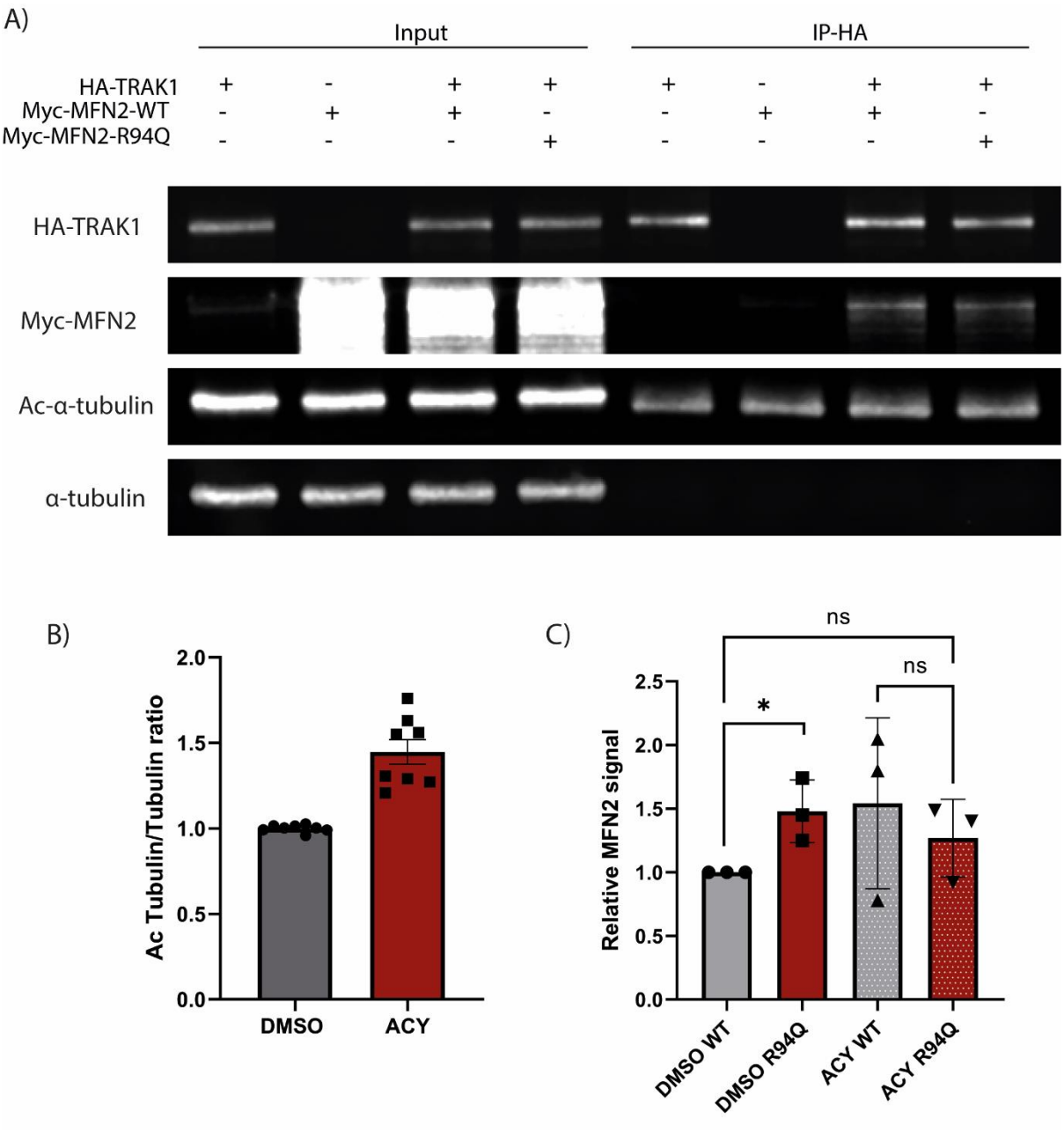


Figure 5.15: ACY-738 treatment has a modest effect on TRAK1-MFN2 interactions. *(A) Lysates of HEK293 cells treated for 24 hours with 2.5 μM ACY-738 co-transfected with TRAK1-HA and either MFN2- WT-Myc or MFN2- R94Q-Myc were immunoprecipitated using an anti-HA antibody. Immune pellets were probed for TRAK1-HA, Myc-MFN2, α-tubulin, and acetylated α-tubulin. (B) Quantification*

*of α-tubulin acetylation in lysates of HEK293 cells co-transfected with TRAK1-HA and either MFN2-WT-Myc or MFN2- R94Q-Myc and treated with either 0.2% DMSO or 2.5 μM ACY-738. N = 3 biological repeats. (C) Quantification of (A) shows the ratio of anti-Myc signal to anti-HA signal in the immune pellets normalised to the Myc-MFN2-WT DMSO condition in DMSO and ACY-738 conditions. Data points represent mean ± SEM from N = 3 independent biological repeats. Statistical significance was calculated by an unpaired T-test (*P<0.05; ns, not significant). DMSO WT vs DMSO R94Q, d = 1.95; ACY WT vs ACY R94Q, d = 0.525; DMSO WT vs ACY R94Q, d = 0.881.*

The experiment was repeated again, this time blotting for KIF5B that was interacting with TRAK1 in the presence of WT or R94Q MFN2 (Figure 5.16A). ACY-738 treatment created a small but insignificant increase in TRAK1-KIF5B interactions in the presence of WT MFN2 compared to the DMSO condition (Figure 5.16B). ACY-738 treatment did not increase TRAK1-KIF5B interactions in the presence of R94Q MFN2 (Figure 5.16).

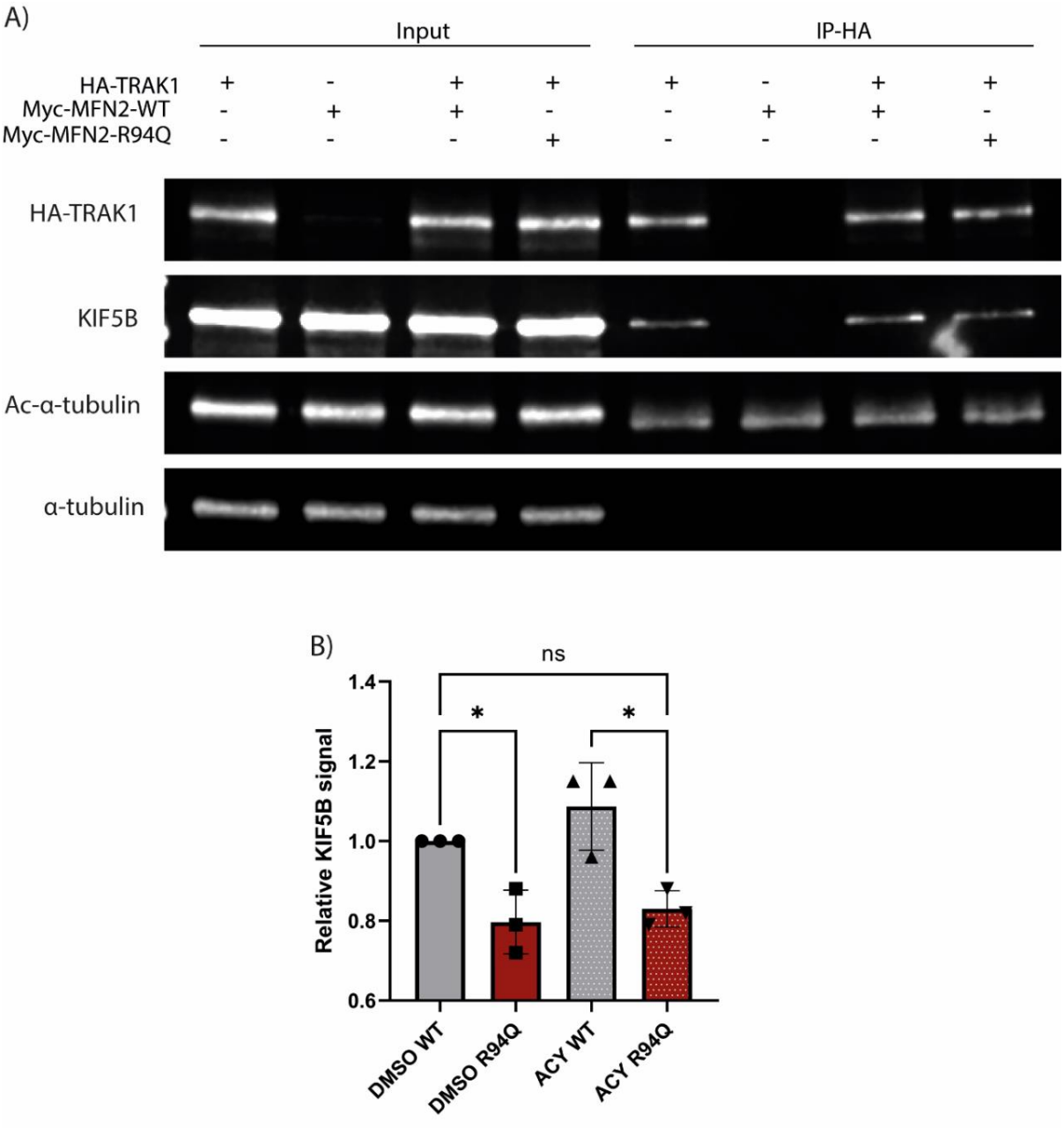


Figure 5.16: ACY-738 treatment does not increase TRAK1-KIF5B interactions in the presence of R94Q MFN2. *(A) Lysates of HEK293 cells treated for 24 hours with 2.5 µM ACY-738 co-transfected with TRAK1-HA and either MFN2- WT-Myc or MFN2- R94Q-Myc were immunoprecipitated using an anti-HA antibody. Immune pellets were probed for TRAK1-HA, KIF5B, α-tubulin, and acetylated α-tubulin. (B) Quantification of (A) shows the ratio of anti-KIF5B signal to anti-HA signal in the immune pellets normalised to the Myc-MFN2-WT DMSO condition in DMSO and ACY-738 conditions. Data points represent mean ± SEM from N = 3 independent biological repeats. Statistical significance was calculated by an unpaired T-test (*P<0.05; ns, not significant). DMSO WT vs DMSO R94Q, d = 2.54; ACY WT vs ACY R94Q, d = 3.05; DMSO WT vs ACY R94Q, d = 3.71.*

5.3 Discussion

In summary, this chapter sought to find a possible link between mutant MFN2 and the mitochondrial trafficking outlined in Chapter 4. These possibilities included altered α-tubulin acetylation, altered MERCs, and altered protein interactions between MFN2 and TRAK1. No aberrations were found in tubulin acetylation or MERCS in $MFN2^{R94Q/+}$ hESC-derived neurons. Interestingly, an increase in MFN2-TRAK1 interactions was identified when the R94Q mutation was present. This coincided with a reduction in TRAK1-KIF5B interactions in the presence of R94Q MFN2. HDAC6 inhibition via ACY-738 did not significantly rescue these altered proteins interactions.

5.3.1 α-tubulin acetylation ratios are unaffected in $MFN2^{R94Q/+}$ motor neurons

Western blot analysis of α-tubulin in hESC-derived motor neurons highlighted no clear differences in the acetylation ratios between $MFN2^{+/+}$ and $MFN2^{R94Q/+}$. This is in contrast to previous models of CMT2A that have shown a reduction in tubulin acetylation (Picci et al., 2020, Kumar et al., 2024). This may be a species-specific effect or a consequence of overexpressing mutant MFN2 – Picci et al used a mouse model of CMT2A that overexpressed MFN2 R94Q in neurons, and Kumar et al used MEFs that overexpressed either MFN2 R94Q or MFN2 T105M. Kumar et al also showed that overexpressing MFN2 R94Q in MEFs resulted in a reduction of acetylated α-tubulin. This is in direct contrast to the α-tubulin acetylation levels in HEK293 cells overexpressing MFN2 R94Q (Figure 5.13). The discrepancy between this data may also be explained by species specificity, further highlighting the importance of using human-based models for *in vitro* studies of CMT2A.

Disruption to microtubules has been noted in several models of CMT2 which most likely contributes to impaired axonal transport. Mutations in glycyl-tRNA synthetase (GARS) lead to CMT2D, and aberrant interactions with HDAC6 were identified in a mouse model of CMT2D (Mo et al., 2018). This correlated with an increase HDAC6 activity and a reduction in the acetylation of microtubules in the sciatic nerve (Mo et al., 2018). Interestingly, inhibition of HDAC6 via a small molecule proved effective in rescuing motor function of CMT2D mice whereas HDAC6 knockout mice showed no rescue (Mo et al., 2018, Tadenev et al., 2024). HDAC6 inhibition was also effective

in restoring electrophysiological deficits in an iPSC model of CMT2D (Smith et al., 2022). CMT2F is caused by HSPB1 mutations which can lead to reduced microtubule dynamics through increased HSPB1-tubulin interaction (Almeida-Souza et al., 2011). Inhibition of HDAC6 in a mouse model of CMT2F via a small molecule proved effective in rescuing motor function (D'Ydewalle et al., 2011).

5.3.2 MERCS number and contact size is unaffected in MFN2$^{R94Q/+}$ motor neurons

Inter-organelle contacts are an ever expanding area of cell biology, with new contact sites and protein tethers uncovering additional regulation of cellular functions still being defined (Huang et al., 2020). Contact sites between mitochondria and the ER are some of the most well characterised contacts, and MFN2 has been identified within these contacts, leading to the possibility that mutated MFN2 may alter MERCS in CMT2A.

PLA and TEM analyses using the hESC-based model of CMT2A did not show any statistically significant differences in the number of MERCS per cell nor the size of the MERCS. This data does not provide any further clarity on the role of MFN2 in MERCS in neurons specifically. The role of MFN2 in MERCS has been debated in the literature; some posit that MFN2 is a positive regulator, and loss of MFN2 correlates with loss of MERCS (De Brito and Scorrano, 2008). Others present data showing MFN2 as a negative regulator, with the loss of MFN2 correlating with an increase in opposition between the organelles (Filadi et al., 2015).

Due to the quality and magnification of TEM images, MERCS width could not be quantified in this body of work, but future work should consider quantifying this parameter of MERCS. MERCS width is considered to be key in determining the primary functional role of a single MERCS (Giacomello and Pellegrini, 2016). Furthermore, due to time constraints, the functional roles of MERCS were not measured here such as calcium transfer between the ER and mitochondria.

Though TEM was employed primarily to visualise MERCS, it also provided high magnification images of mitochondria that could be used for mitochondrial morphology analyses with the neuronal cell body. No clear differences were identified between wild-type and mutant cells when measuring area, perimeter,

circularity, or aspect ratio. This data suggests that there is no gross imbalance between mitochondrial fusion and fission, and that MFN2$^{R94Q/+}$ does not generate a detectable mitochondrial fusion deficit in this cell model. Hypofusion and fragmentation of mitochondria has been reported in multiple models of CMT2A (). Most of these models rely on overexpression of mutant MFN2, which may prevent compensation by MFN1 in mitochondrial fusion. The lack of a clear fusion deficit in the hESC-based model presented here may be due to MFN1 compensation or the loss of function generated by a heterozygous mutation in the GTPase domain of MFN2 is not sufficient impairment of MFN2 GTPase activity to impact mitochondrial fusion.

5.3.3 The R94Q mutation alters MFN2-TRAK1-KIF5B interactions

Mitochondria are typically transported along axons by kinesin-1 and dynein via interactions with TRAK1 and Miro (van Spronsen et al., 2013). MFN2 is known to interact with TRAK1 but the effect of mutations in MFN2 on this interaction have never been quantified (Misko et al., 2010, Lee et al., 2018a). This work adds confirmation that TRAK1 and MFN2 interact via co-immunoprecipitation. Furthermore, this work has shown for the first time that the common CMT2A-causing mutation R94Q can increase this interaction and this occurs alongside a decrease in the interaction between TRAK1 and kinesin-1. At the time of writing, this is the first piece of work to identify a differential TRAK1-kinesin-1 interaction within an *in vitro* disease model.

Miro-TRAK1 interactions allow kinesin-1 and dynein to transport mitochondria, but short-range movement of mitochondria has been identified in MIRO1/2 knockout cells, suggesting that TRAK1/2 can binds alternative OMM proteins (López-Doménech et al., 2018). OMM candidates include DISC1 (Norkett et al., 2016), syntaphilin (Chen and Sheng, 2013), Armcx proteins (López-Doménech et al., 2012), and MFN1 and MFN2 (Misko et al., 2010). Whilst this chapter shows that TRAK1 interacts with MFN2, KIF5B is not part of that complex suggesting that TRAK1-MFN2 interactions do not contribute to mitochondrial trafficking via direct coupling to kinesin-1.

This gives rise to a new mechanistic possibility underpinning mitochondrial trafficking deficits in CMT2A (Figure 5.16 A, B). The mitochondrial trafficking deficit shown in

Chapter 4 is bidirectional, but protein-protein interactions in this chapter have focused on the predominant anterograde motor in neurons – kinesin-1. Whether the increased interaction between TRAK1 and MFN2 affects TRAK1-dynein interactions is yet to be elucidated. Anterograde and retrograde axonal transport are mostly inter-dependent, thus if TRAK1-dynein interactions are unaffected in the presence of CMT2A-causing mutations, a downregulation of retrograde transport could occur from a reduction in anterograde transport caused by reduced TRAK1-kinesin-1 interactions (Jean and Kiger, 2012, Bekku and Salzer, 2020).

The protein-protein interactions investigated in this chapter capitalised on the HEK293 cells' amenability to protein overexpression and speed of growth. To this end, HEK293 cells are ideal for preliminary investigations into protein interactions. However, this system does not accurately reflect the neuronal context that is most relevant to the proposed protein-protein interactions – HEK293 cells are immortalised and derived from a human embryonic kidney, thus incapable of fully recapitulating neuronal biology. Furthermore, whilst protein overexpression facilitates easier observations of interactions, it does not reflect endogenous protein levels and how these proteins may interact *in situ*. With this in mind, further work should seek to characterise TRAK1-MFN2 interactions and TRAK1-KIF5B interactions within a neuronal model such as the one generated in Chapter 3, through endogenous co-immunoprecipitation, proteomics, and proximity ligation assays. Work should also look at TRAK1-KIF5A and RAK1-KIF5C interactions in the presence of MFN2 mutations with a neuronal cell model, as KIF5A and KIF5C are enriched in neurons (Kanai et al., 2000).

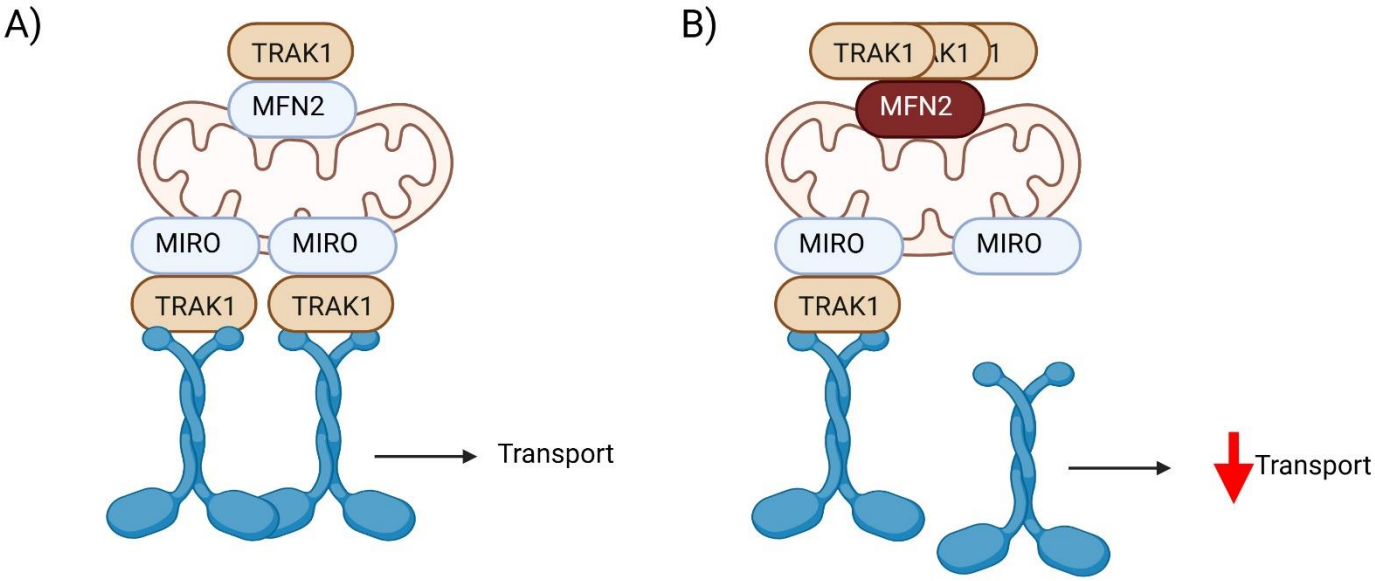


Figure 5.17: Proposed model for MFN2/TRAK1/KIF5B interactions in CMT2A. *(A) TRAK1 interacts with MIRO and MFN2 on the mitochondria, with MIRO-TRAK1 interactions allowing kinesin-1 to bind to TRAK1. (B) In CMT2A, mutated MFN2 traps TRAK1 and prevents it from interacting with MIRO and kinesin-1, leading to decreased transport. Schematic made using Biorender.com.*

HDAC6 has been shown to deacetylate Miro1 - deacetylation corresponded with decreased mitochondrial transport suggesting that this acetylation was necessary for Miro-dependent mitochondrial trafficking (Choudhary et al., 2009, Kalinski et al., 2019). Many questions remain around the role of acetylation of Miro including its impact on Ca^{2+} binding, Miro GTPase activity, and Miro1-TRAK1 interactions. Furthermore, whether the acetylation status of Miro1 is impacted by the presence of mutations in MFN2 has not been determined, but if it is altered this could further contribute to the mitochondrial trafficking deficit. This could also add a further dimeson to rescuing the mitochondrial trafficking deficit in the hESC-derived neurons via HDAC6 inhibition. Indeed, any neuronal model of disease that benefits from HDAC6 inhibition may also be benefitting from increased Miro1 acetylation.

In brief, this chapter has shown that the presence of $MFN2^{R94Q/+}$ in hESC-derived motor neurons does not significantly alter α-tubulin acetylation or MERCS. Overexpression experiments have shown an increase in the interaction between TRAK1 and MFN2 R94Q compared to wild-type MFN2, and the occurs with a decrease in the interaction between TRAK1 and KIF5B.

Chapter 6: General discussion and concluding remarks

The overarching aim of this body of work was to generate a hESC-based *in vitro* model of CMT2A that could be used to identify phenotypic and mechanistic differences between wild-type and CMT2A mutant cells. Previous models of CMT2A have centred around mouse models and immortalised cell lines (Abati et al., 2024), with some human iPSC models appearing in the last ten years (Saporta et al., 2015, Rizzo et al., 2016, Van Lent et al., 2021). The mix of models has highlighted the many facets of MFN2, but also brought discordant data regarding how MFN2 mutations affect normal cell physiology. A greater focus on using human-based neuronal *in vitro* models can bring consensus on disease mechanisms and facilitate drug screening. To that end, the common CMT2A-causing mutation in MFN2 – R94Q – was introduced into hESCs that were consequently differentiated into limb-innervating motor neurons. CMT2A neurons displayed a mitochondrial trafficking deficit and a new link between MFN2 and TRAK1 in CMT2A was highlighted.

6.1 A novel hESC model of CMT2A

In Chapter 3, a hESC-based model of CMT2A was generated by introducing the R94Q heterozygous mutation into MFN2 in hESCs and differentiating these stem cells into a disease-relevant cell type – limb-innervating motor neurons. At time of writing, this is the first hESC-based model of CMT2A to be reported, using hESCs that have had a CMT2A-causing mutation introduced. The only previous use of hESCs for the modelling of CMT2A has employed MFN2 knockdown in hESC-derived motor neurons, but this does not fully recapitulate disease as MFN2 protein expression is not reduced in disease (Mou et al., 2021). By opting to introduce one of the most common and severe mutations in MFN2, the model characterised in Chapter 3 is directly comparable to others which have used the same mutation. Doing so highlights commonalities between the models, namely mitochondrial trafficking deficits (Misko et al., 2012, Van Lent et al., 2021). It also highlights divergences in phenotypes between models, including mitochondrial fusion deficits which have not been identified in this model, but have been reported in different CMT2A models (El Fissi et al., 2018, Das et al., 2022b). This discordance in phenotypes between models further highlights the need human models of CMT2A in

disease-relevant cell types. Whilst some hiPSC models of CMT2A exist, a hESC-based model complements this by offering greater control of genetic background and an increased differentiation capacity (Halevy and Urbach, 2014). Furthermore, this hESC-based model permits the generation of an allelic series to study multiple, rarer MFN2 mutations on the same genetic background, allowing for a more powerful characterisation and comparison between MFN2 mutations. Whilst this was attempted but not achieved in this body of work due to time constraints, future work would benefit from doing so; comparing a variety of mutations across the length of MFN2 could determine if mutations in different domains contribute to CMT2A pathology in similar or divergent mechanisms. At present, there is little data comparing different mutated domains within cellular models. Cell-free assays have begun to investigate the effects of different CMT2A-associated mutations on the GTP turnover rates and dimerisation of MFN2; each mutation investigated had a different impact highlighting variable intra- and intermolecular mechanisms that may be driving disease and giving rise to variable patient phenotypes (Li et al., 2019). Whilst cell-free assays provide a strong biochemical lens to CMT2A pathogenesis, cell-based assays using the hESC model outlined in Chapter 3 would allow for the consequences of altered intra- or intermolecular interactions to play out within a disease-relevant cell type, uncovering their importance in disease phenotypes.

The use of a hPSC-based model allows for the generation of specific cell types which are not accessible in the human body, which is of particular use for the study of neurodegenerative diseases where tissue of interest is either inaccessible or not available to be biopsied in large quantities. In Chapter 3, limb-innervating motor neurons were generated through a previously optimised protocol from within the Barbarić lab. Neurons were immunoreactive for Isl1/2, HB9, ChAT, FOXP1, and NFH with an efficiency comparable to other publications using a similar protocol (Rizzo et al., 2016, Bhinge et al., 2017, Guo et al., 2017, Van Lent et al., 2021, Sainio et al., 2022). The neurons generated were also electrophysiological active,

In contrast to other protocols shown in the literature, this high-yield protocol includes the addition of FGF-2 for the first four days of differentiation which contributes to a more posterior axial identity of the neurons (Gouti et al., 2014, Lippmann et al., 2015, Butler, 2021). Consequently, HOX gene expression of the neurons generated in Chapter 3 shows that these *in vitro* neurons are equivalent to limb-innervating

neurons belonging to the brachial plexus in humans. HOX gene expression is not typically characterised in hPSC-derived neuronal models of neurodegeneration. This differentiation protocol may also be of use for *in vitro* modelling of other neurodegenerative diseases that exhibit brachial neuron degeneration, such as ALS or brachial neuritis.

Future work should capitalise on the differentiation potential of this hESC-based model; sensory neurons and retinal ganglion cells are also subject to degeneration in CMT2A, and all these cell types could be generated from a single source on the same genetic background. This plethora of disease-relevant cell types paired with the ability to generate an allelic series on a single genetic background means that this hESC-based model can directly compare different CMT2A-associated mutations in different cellular contexts. This is useful for understanding why certain mutations are associated with more severe clinical phenotypes or uncommon symptoms such as optic nerve degeneration or vocal cord involvement.

CMT2 and CMT2A specifically impacts the peripheral neurons of the limbs and being able to generate these cell types *in vitro* increases the translatability of the model and may bring consensus to the discordant data surrounding CMT2A phenotypes and mechanisms presented in the literature.

6.2 Characterising mitochondrial trafficking in hESC-based MFN2$^{R94Q/+}$ neurons

In order for any disease model to be useful, it needs a clear phenotype distinguishing it from a control. To that end, MFN2$^{+/+}$ and MFN2$^{R94Q/+}$ hESCs were differentiated into limb-innervating motor neurons and mitochondrial transport in the axon was investigated, as axonal transport defects had been reported in previous CMT2A models of both rodent and human origin (Picci et al., 2020, Van Lent et al., 2021). In Chapter 4, a clear mitochondrial transport deficit was identified in MFN2$^{R94Q/+}$ neurons, with fewer motile mitochondria. in the anterograde and retrograde directions. This is line with models that show a reduced delivery of mitochondria to the neuromuscular junction (El Fissi et al., 2018, Picci et al., 2020) or show a reduction in mitochondrial motility (Baloh et al., 2007, Misko et al., 2012, Rocha et al., 2018, Franco et al., 2020, Van Lent et al., 2021). The ability of the hESC-based model to replicate this consensus phenotype indicates that this model is accurately

depicting a facet of CMT2A pathogenesis and is consequently a useful platform for investigating upstream cellular and/or molecular events. The hESC-based model of CMT2A also highlighted differences in mitochondrial velocity between $MFN2^{+/+}$ and $MFN2^{R94Q/+}$ sMNs, namely no differences in average track velocity were identified but the presence of $MFN2^{R94Q/+}$ resulted in an increase in instantaneous velocity. Previous quantification of mitochondrial velocity in neuronal models of CMT2A have shown a reduction in velocity in the presence of CMT2A-associated or -causing mutations (Misko et al., 2010, Van Lent et al., 2021, Franco et al., 2022). This could indicate differences in the instantaneous velocities between the models or differences in pausing between the models; without quantification on motile mitochondria pausing or instantaneous velocities from these other neuronal CMT2A models, it is difficult to draw comparisons. The previously published experiments also report a lower average velocity of mitochondria in wild-type hiPSC motor neurons (~0.5 – 0.7 µm/s) compared to the hESC-derived sMNs (~1.0 µM/s) (Van Lent et al., 2021, Franco et al., 2022). The differences in wild-type mitochondrial velocity between the models may be explained in part by imaging temperature being lower and the number of frames per second used to capture also being too low resulting in a loss of resolution.

In Chapter 4 it was identified that mitochondria got progressively smaller and spaced out further along the axon, but mitochondrial shape was unchanged. Similar observations regarding mitochondrial area, length, and distribution have been reported in sural nerve biopsies, DRG cultures expressing $MFN2^{R94Q}$, and patient iPSC-derived motor neurons. (Vallat et al., 2008, Misko et al., 2012, Guo et al., 2023). Multiple studies have reported mitochondrial shape changes in the presence of CMT2A-associated mutations, with mitochondria becoming more spherical compared to the elongated mitochondria seen in control cells (El Fissi et al., 2018, Van Lent et al., 2021, Guo et al., 2023).

It is yet to be determined if all CMT2A-causing or -associated mutations in MFN2 lead to a mitochondrial trafficking deficit *in vitro*, although the hESC-based model presented here is well situated to do so through the generation of an allelic series. It is becoming increasingly accepted that different MFN2 mutations impact MFN2 function and the axonal transport of mitochondria to different extents (El Fissi et al., 2018, Li et al., 2019, Kumar et al., 2024). It would be important to determine this as

any pharmacological treatments targeting mitochondrial trafficking may not be effective in all CMT2A patients.

With the canonical role of MFN2 being to drive outer mitochondrial membrane fusion, previous CMT2A models have focussed on and identified deficits in mitochondrial fusion, as measured by fragmented mitochondrial morphology (Detmer et al., 2007, Rocha et al., 2018). However, previous data from the Barbarić lab and data shown in this thesis suggest that there is no significant impairment of mitochondrial fusion. Rat DRG cultures with MFN2$^{R94Q/+}$ displaying a mitochondrial trafficking deficit also did not have a significant mitochondrial fusion deficit (Baloh et al., 2007). The GTPase activity of MFN2 is significantly less than that of MFN1 (Ishihara et al., 2004, Li et al., 2019), making it less likely that impaired mitochondrial fusion is a key driver of CMT2A pathology. Furthermore, mitochondrial fusion and mitochondrial transport are somewhat interlinked – mitochondria need to be moved in order to fuse with other mitochondria. In order to further detangle the role of MFN2 mutations in mitochondrial transport and fusion, cell-free assays should be employed to separate the two.

Disrupted axonal transport is hypothesised to be unifying feature of CMT2 models. Van Lent et al demonstrated a mitochondrial and lysosomal trafficking defect in CMT2A (MFN2$^{R94Q/+}$), CMT2E (NEFL$^{P8R/+}$), CMT2L (HSPB8$^{K141N/+}$), and CMT2F (HSPB1$^{G84R/+}$ and HSPB1$^{P182L/+}$) hiPSC-derived motor neurons (Van Lent et al., 2021). Axonal transport deficits have also been identified in models of CMT2B (Zhang et al., 2013) and CMT2D (Sleigh et al., 2023). Whether disrupted axonal transport is an initiating event or a consequence of neuronal dysfunction in each CMT2 subtype is yet to be determined but could provide a targetable pathway for multiple CMT subtypes. Disturbed axonal transport has become a hallmark of neurodegeneration but in-depth characterisation of the dynamics of axonal transport in models of neurodegeneration are often missing.

6.3 Molecular mechanisms driving axonal transport defects in an *in vitro* CMT2A model

At present, there is no consensus on the molecular mechanisms driving reduced axonal transport and consequently nerve degeneration in CMT2A. In Chapter 5,

pathogenic events that may occur upstream of a reduction in mitochondrial trafficking as a result of MFN2$^{R94Q/+}$ were explored.

Firstly α-tubulin acetylation levels were investigated as reductions in α-tubulin acetylation have been reported in other CMT2/CMT2A models (Benoy et al., 2017, Picci et al., 2020, Van Lent et al., 2021, Kumar et al., 2024) and HDAC6 inhibition, which increases α-tubulin acetylation, was able to rescue the mitochondrial trafficking deficit in MFN2$^{R94Q/+}$ hESC-derived sMNs in Chapter 4. Western blot analysis of hESC-derived sMNs showed no differences in α-tubulin acetylation between MFN2$^{+/+}$ and MFN2$^{R94Q/+}$ sMN cultures. Furthermore, HEK293 cells overexpressing MFN2 R94Q also showed no changes in α-tubulin acetylation. Reductions in α-tubulin acetylation have been identified in the distal sciatic nerve of CMT2A mice and MEFs expressing CMT2A-causing mutations (Picci et al., 2020, Shen et al., 2021, Kumar et al., 2024). The lack of reduced α-tubulin acetylation in the hESC-based CMT2A may suggest that loss of α-tubulin acetylation occurs downstream of the mitochondrial trafficking deficit and culturing the hESC-derived sMNs beyond Day 36 of differentiation may begin to uncover this phenotype. Alternatively, it may be that loss of α-tubulin acetylation is a feature of CMT2A pathogenesis that the hESC-based model cannot recapitulate or loss of α-tubulin acetylation does not occur in human-based models of CMT2A, as previous reports have focused on murine models. It would be important to ascertain whether loss of α-tubulin acetylation precedes or follows axonal transport deficits, or never occurs in human *in vitro* models of CMT2A to further understand how HDAC6 inhibition rescues the mitochondrial transport deficit and if it provides a neuroprotective effect.

Changes to MERCS were also investigated as a potential molecular mechanism driving decreased mitochondrial motility. MFN2 has been identified as a component of MERCS, but its exact role in these contacts remains unclear and controversial (De Brito and Scorrano, 2008, Filadi et al., 2015, Casellas-Díaz et al., 2021). No clear trends were identified in MERCS length, number, or percentage of mitochondrial membrane in contact between MFN2$^{+/+}$ and MFN2$^{R94Q/+}$ hESCs or hESC-derived sMNs. In contrast, other publications have identified changes that appear to be MFN2-mutation dependent. MFN2 mutations R364W, M376V, and W740S resulted in increased association between mitochondria and the ER (Larrea et al., 2019, Das et al., 2022a), whereas the R94Q and T105M mutations decreased the number and

size of MERCS as well as the ability of MERCS to mediate lipid metabolism (Bernard-Marissal et al., 2019, Kumar et al., 2024). Perhaps what is more important than physical characterisation of MERCS is characterisation of MERCS function within CMT2A models. Larrea et al saw different impacts on function depending on the MFN2 mutation present, with phospholipid and cholesterol synthesis, calcium handling, and lipid droplet accumulation differentially altered between patient fibroblasts (Larrea et al., 2019). MERCS function was not characterised in this body of work thus it cannot be assumed that any aspect of MERSC function is unaltered in $MFN2^{R94Q/+}$ hESC-derived sMNs. Future work should look to investigate this to add further insight into the impact of the R94Q mutation on MERCS, as well as other mutations. This future work would also add insight into the role of MERCS in sMNs, as it is believed that different facets of MERCS function may be more important in neuronal subtypes (An et al., 2024, Kuijpers et al., 2024).

MFN2 has been shown to interact with the axonal transport cargo adaptor TRAK1, but the impact of MFN2 mutations on this interaction has never been quantified. Co-immunoprecipitation experiments indicated that MFN2 R94Q interacted more strongly with TRAK1 than MFN2 WT, and the increased interaction with TRAK1 occurred at the same time as a reduction in TRAK1 interactions with kinesin-1. This data suggests that a CMT2A-causing mutations has a toxic gain-of-function by indirectly decreasing mitochondrial coupling to kinesin-1. Further work should establish if this hypothesis holds true for other MFN2 mutations and whether these altered interactions are occurring within cells using the hESC-based model of CMT2A. This is because co-immunoprecipitation relies on overexpression of proteins with tags, which does not recapitulate protein levels found within the cell.

6.4 Future therapies for CMT2A

This PhD project was pursued because there are no treatments available for CMT2A, and thus there is a need for disease-relevant *in vitro* models that can provide a platform to test potential therapies and provide mechanistic insights to further inform pharmacological targeting. With a clear mitochondrial trafficking deficit identified in $MFN2^{R94Q/+}$ hESC-derived motor neurons, phenotypic rescue via pharmacological inhibition of HDAC6 was tested. HDAC6 inhibition has been shown to increase transport of mitochondria in multiple neurodegenerative conditions, most likely through increasing α-tubulin acetylation (Dompierre et al., 2007, Kim et al.,

2016, Benoy et al., 2017, Guo et al., 2017, Mo et al., 2018). HDAC6 inhibition by ACY-738 was able to significantly increase the number of motile mitochondria in MFN2$^{R94Q/+}$ hESC-derived motor neurons. HDAC6 inhibition has been shown to rescue the motor phenotype in a mouse model of CMT2A, presumably through a restoration of mitochondrial transport as reported here and in other *in vitro* models (Shen et al., 2021). The effectiveness of HDAC6 in an *in vivo* model of CMT2A suggests that restoring axonal transport of mitochondria can positively impact patient phenotypes. The work presented in this thesis contributes to the growing interest of pharmacological inhibition of HDAC6 for CMT2A and other diseases involving mitochondrial trafficking defects. However, it should be kept in mind that HDAC6 has multiple deacetylation targets beyond α-tubulin, which could lead to potentially dangerous side effects.

Pharmacological interventions are often the most popular routes for treatments of neurodegenerative diseases due to the need to access the nervous system; the blood-brain-barrier (BBB) poses a significant hurdle in drug delivery and small molecules are often more likely to be BBB-penetrant compared to peptide or gene therapies. Despite this, efforts towards long-lasting single-dose gene therapies for CMT and CMT2A are increasing. Recently, MFN2 knockdown and replacement via AAV-vectors was shown to improve mitochondrial density and distribution in CMT2A iPSCs showing proof of concept (Rizzo et al., 2023). Furthermore, increasing MFN1 expression in mice models of CMT2A was shown to be effective in reducing the motor phenotype, presenting a different therapeutic angle to MFN2 replacement (Zhou et al., 2021, Shahin et al., 2023). MFN1/MFN2 ratios vary between cell types, with MFN2 being expressed more highly than MFN1 in peripheral neurons; increasing MFN1 may therefore compensate for the loss-of-function of mutant MFN2. Advances in alternative therapeutic options for CMT2A include the development of cell-permeant minipeptides that act as mitofusin activators, increasing their activity (Rocha et al., 2018, Dang et al., 2022).

6.5 Closing remarks

This body of work has described the creation and characterisation of a hESC-based model of CMT2A with one of the most prevalent and severe mutations – MFN2$^{R94Q/+}$. A mitochondrial trafficking deficit was identified in MFN2$^{R94Q/+}$ motor neurons that could be rescued by pharmacological inhibition of HDAC6. Furthermore, the

presence of the R94Q mutation altered key TRAK1 interactions which may underpin the mitochondrial trafficking deficit. Future work should capitalise on this platform, utilising it for further characterisation and treatment screening.

I hope that this model can be used for future CMT2A research and that the findings presented in this body of work may be of use for the study of other neurodegenerative diseases, ultimately aiding the quest for effective and life-improving treatments for patients and their families.

Appendix 1

Nucleotide Change	Amino Acid Change	Domain	Age at Onset (Years)	Transmission	Reference	Severity
c.50C>T					(Al-Harbi et al., 2019)	
c.152C>T	S51F		56		(Bergamin et al., 2014)	Mild
	Q65STOP				(Sitarz et al., 2012)	
c.205G>T	V69F		1, 5		(Züchner et al., 2004)	
227T>C	L76P	7 to 44		Dominant	(Züchner et al., 2004),(Verhoeven et al., 2006)	
c.262A>T	I88F				(Antoniadi et al., 2015)	
c.275T>C	L92P	GTPase	Early, 1, 1, 1, 3	De novo	(Chung et al., 2006), 2006),(Choi et al., 2015), (Chung et al., 2010) (Verhoeven et al.,	Severe, Mild
c.275T>G	L92R		3		(McCorquodale et al., 2011)	Severe
c. 281 G<C	R94P	GTPase	16	(Bergamin et al., 2014)	Severe	
281G>A	R94Q	GTPase	1, 4-15, 6-17, 3-15, 4, <10, 7, 5, 3, 2, Early	Dominant, De novo	(Feely et al., 2011), (Ando et al., 2017), (Züchner et al., 2004), (Sitarz et al., 2012), (G J Braathen, 2012), (Casasnovas et al., 2010), (Verhoeven et al., 2006), (Kijima et al., 2005), (Sole et al., 2009), (Geir J Braathen et al., 2010), (Kotruchow et al., 2015), (Neusch et al., 2007)	Moderate/ Severe, Severe

c.280C>T	R94W	GTPase	2, 3, Early, 9, 4, 8, 1, 5, 3-5, 1-4, <10	De novo, Dominant	(Verhoeven et al., 2006), (Chung et al., 2006), (Choi et al., 2015), (Ando et al., 2017), (Antoniadi et al., 2015), (G J Braathen, 2012), (Feely et al., 2011), (Calvo et al., 2009), (Sitarz et al., 2012), (Casasnovas et al., 2010), (G J Braathen, 2012), (Chung et al., 2010), (Cho, Sung, Kim, & Ki, 2007)	
	R94G	GTPase	3		(Ando et al., 2017)	
c. 283A>G	R95G	GTPase			(Dankwa et al., 2019)	
c.292A>G + c.1168 T>C	K98E +C390R		14	Recessive	(Vallat et al., 2008)	
c.292A>C	K98Q	GTPase	8, 9		(Choi et al., 2015), (Nakhro et al., 2012)	Moderate, Moderate/ Severe
c.299C>G	A100G	GTPase	10	Dominant	(Sitarz et al., 2012),(Verhoeven et al., 2006)	
	R104L	GTPase			(Sitarz et al., 2012), (Ando et al., 2017)	
c.310C>T	R104W	GTPase	4, 20, <5, <10, 2-4, 3, 2, 6	De novo, autosomal Dominant	(Choi et al., 2015), (Del Bo et al., 2008), (Calvo et al., 2009),(Brockmann et al., 2008), (Abe et al., 2011), (Ando et al., 2017), (Nakhro et al., 2012), (Chung et al., 2010), (Vallat et al., 2008), (Sitarz et al., 2012), (Genari et al., 2011)	Moderate, Severe
c.311+1G>T		4th intron, Exon 4 skipped, prem stop	>50	Dominant	(Kotruchow et al., 2013)	Mild
	T105A	GTPase			(Sitarz et al., 2012)	

c.314C>T	T105M	GTPase	Early, 11, 25, 4, 1	Dominant	(Chung et al., 2006), (Choi et al., 2015), (Ando et al., 2017), (Lawson, Graham, & Flanigan, 2005), (Feely et al., 2011), Xu et al., 2024)	Mild
c.322G>A	G108R+R707W	GTPase	<10	Recessive	(Calvo et al., 2009)	Moderate
c.326A>G	K109R		10		(Ando et al., 2017)	
c. 334 G>A	V112M	GTPase	<1	Recessive	(Asif et al., 2023, Kanwal et al., 2021)	Mod/Severe
c.368C>T	P123L	GTPase	2, 30	Dominant	(Verhoeven et al., 2006), (Sole et al., 2009)	
c.371C>T	T124M		50		(Bergamin et al., 2014)	Moderate
c.467G>T	S125I	GTPase	<10		(Calvo et al., 2009)	Moderate
c.380G>A	G127D	GTPase	16, Late	De novo	(Chung et al., 2006), (Choi et al., 2015)	Mild
c.380G>T	G127V	GTPase	48		(Engelfried et al., 2006)	Mild
c.383A>G	H128R	GTPase	<5	De novo	(Calvo et al., 2009), (Ando et al., 2017)	Severe
c.475-1G>T; (c.475_486del ACTGT-GAACCAG)	pT159-Q162del	Intron 5 splicing	13		(Lin et al., 2011)	Mild
c.491C>T	A164V+T362M	GTPase	<5	Recessive	(Calvo et al., 2009, Nicholason et al. 2008, Vallat et al, 2008).	Severe
c.493C>G	H165D	GTPase			(Zhu et al., 2005)	Severe
c.494A>G	H165R	GTPase	Late, 35, 57, 6, 5, 10, 50, 14, 21	De novo, Dominant	(Chung et al., 2006),(Bergamin et al., 2014), (Ando et al., 2017), (Verhoeven et al., 2006) (Choi et al., 2015), (Chung et al., 2010), (Cho, Sung, Kim, & Ki, 2007)	Mild, Moderate, Mild/ Moderate
c.494A>G	H165R		21		(Ando et al., 2017),(Verhoeven et al., 2006),(Choi et al., 2015),(Chung et al., 2010), (Zhu et al., 2005)	Moderate
c.493C>T	H165Y	GTPase	12	Dominant	(Sitarz et al., 2012),(Verhoeven et al., 2006)	

c.526G>A	G176S		<1	Recessive	(Iapadre et al. 2018)	Severe
c.559A>G	K187D	GTPase	12		(Choi et al., 2015)	Mild
c. 581 A>C	D194A	GTPase			(Vinciguerra et al., 2023)	Moderate
	G202A	GTPase			(Sitarz et al., 2012)	
	I203M		<20	Dominant	(Casasnovas et al., 2010)	Moderate
c. 600-31T>G					(Stergachis et al., 2023	
c.617C>T	T206I	GTPase	3, 4, 2, 7	De novo	(Verhoeven et al., 2006), (Züchner et al., 2006), (Choi et al., 2015), (Sitarz et al., 2012), (Oh et al. 2014)	Severe, optic atrophy
c. 629A>T	D210V			Early	(Rouzier et al., 2012)	Severe
c.638T>C	I213T	GTPase	5, 12		(Lawson, Graham, & Flanigan, 2005, Yang et al., 2021)	No mild phenotype all severe.
c.640G>A	D214N+C390R	GTPase	<5	Recessive	(Calvo et al., 2009, Nicholason et al. 2008, Vallat et al, 2008).	Severe
c.671T>C	F216S		6, 13	Recessive	(Vallat et al., 2008)	
c.669T>A	F223L		7		(Kijima et al., 2005)	Severe
c.474+4A>G;668T>A	p.Thr105LeufsX2 and p.Phe223Ty	Splicing, Exon 5 skipped, Exon 7 mutation	12-42		(Park et al., 2012)	Moderate
c.694A>G	T232A		6, 12	Dominant	(Sole et al., 2009)	
	T232N	GTPase			(Sitarz et al., 2012)	
c.707C>T	T236M	GTPase	<10	Dominant	(Calvo et al., 2009), (Kijima et al., 2005)	Moderate, Moderate/ Severe
c. 984_986delAGA	E239del			1	(Bergamin et al., 2014)	Severe
c.730G>A	V244M	GTPase	<5, 10		(Calvo et al., 2009), (Kijima et al., 2005)	Moderate, Moderate/ Severe
	V244L				(Pehlivan et al., 2016)	
	L248V		1		(Feely et al., 2011)	Moderate/ Severe
c.	S249C	GTPase	17		(Abati et al., 2022)	Mild/moderate
c.476C>T	S249F		<20, 2		(Abe et al., 2011)	Severe

c.749G>A	R250Q	GTPase	21, 12	Unknown	(Verhoeven et al., 2006), (Sitarz et al., 2012), (McCorquodale et al., 2011)	Moderate/ Severe
c.748C>T	R250W	GTPase	4	Unknown	(Verhoeven et al., 2006)	
751C>G	P251A	GTPase	1, 8		(Züchner et al., 2004)	
c.752C>T	P251L		22		(Sivera et al., 2013)	Moderate
c.752C>G	P251R		2, 1		(Feely et al., 2011), (McCorquodale et al., 2011)	Severe, Moderate/ Severe
	N252L		<20	Dominant	(Casasnovas et al., 2010),	Severe
	R259C	GTPase	1, 11		(Sitarz et al., 2012), (Ando et al., 2017)	
c.776G>A	R259H	GTPase	17, 15		(Wu et al., 2018) (Ando et al., 2017), (Choi et al., 2015)	Mild, Moderate. Also seen with extreme sensory symptoms.
c.780G>A		Abloishs donor splice site for Ex7, Ex7 skipped, frameshift early stop in Ex8	22		(Martikainen et al., 2014)	Mild/moderate
c.787T>C	S263P	GTPase	12, Late, 13	Dominant	(Chung et al., 2006), (Cho et al., 2007), (Ando et al., 2017), (Choi et al., 2015)	Mild, Moderate
c.809T>C	M270T				(Antoniadi et al., 2015)	
c.818T>G	V273G	GTPase	1, 5		(Lawson et al., 2005)	Significant variability
c.820C>T	R274W		59	De novo	(Ando et al., 2017), (Kotruchow, Kabzińska, & Kochański, 2015)	Severe
c.827A>G	Q276R		10	Dominant	(Verhoeven et al., 2006),(Züchner et al., 2006), (Calvo et al., 2009)	Mild + optic atrophy, Moderate

	Q276H		<30	Dominant	(Casasnovas et al., 2010)	Mild
c.830A>G	H277R		10; 15	Dominant	(Verhoeven et al., 2006)	
c.829C>T	H277Y		>10	Dominant	(Calvo et al., 2009)	Moderate
c.839G>A	R280H	GTPase	11-35, 45, 24, 21, 5, 6, 7, 55, 11-34, 7, 45, 10, late, 12-32, 7, 45, 8	Dominant	(Ando et al., 2017), (Choi et al., 2015), (Nakhro et al., 2012), (Züchner et al., 2004), (Chung et al., 2006)	Mild, Moderate/ Severe, Moderate
	G280H	GTPase			(Sitarz et al., 2012)	
c. 865G>C	E288D			29	(Bergamin et al., 2014)	Moderate
C.851T>A	F284Y		4, 9		(Ando et al., 2017), (Kijima et al., 2005)	Severe
	G298R	GTPase	<20	Dominant	(Sitarz et al., 2012), (Casasnovas et al., 2010)	Moderate
	K307E		10		(Ando et al., 2017)	
	E308Stop	GTPase			(Sitarz et al., 2012)	
c.1029_1032delGAG	R344del				(Antoniadi et al., 2015)	
c1040A>T	E347V	Linker	childhood		(Engelfried et al., 2006)	Severe
c.1048T>C	S350P	GTPase	3		(Choi et al., 2015), (Nakhro et al., 2012), (Chung et al., 2010), (Cho et al., 2007)	Moderate/ Severe, Severe, Mild/ Moderate, Moderate
	p.K357E			(Abati et al., 2022)		
c.1071G>C	K357N		4	de novo	(Kijima et al., 2005)	Severe
c.1081C>T	H361Y		2, 1	De novo	(Verhoeven et al., 2006), (Feely et al., 2011),(Züchner et al., 2006)	Severe
c.1085>T	T362M		22, 42, Early, 0	Dominant	(Choi et al., 2015), (Chung et al., 2006), (Ando et al., 2017)	Mild, Severe
c.1085C>G	T362R		30		(Ando et al., 2017), (Antoniadi et al., 2015)	

c1091G>C	R364P	HR1	<5, 2	Dominant	(Sitarz et al., 2012), (Calvo et al., 2009), (Feely et al., 2011)	Severe
c01091G>A	R364Q	HR1	>10, <30, Late and early	Dominant	(Sitarz et al., 2012), (Calvo et al., 2009), (Casasnovas et al., 2010), (Banchs, Casasnovas, Montero, Martínez-Matos, & Volpini, 2008)	Moderate, Mild, Severe
C.1090C>T	R364W	HR1	1, 2, 3, 4, 5, 8, 6, Early	Dominant	(Sitarz et al., 2012), (Chung et al., 2006), (Ando et al., 2017), (Feely et al., 2011), (Züchner et al., 2006)	Severe, Moderate, Mild/ Moderate
	Met376O	HR1			(Sitarz et al., 2012)	
	M375V	HR1			(Sitarz et al., 2012)	
c.1128G>A	M376I	Linker	35, 22, 18-20	Dominant	(Engelfried et al., 2006)(Verhoeven et al., 2006), (Ando et al., 2017)	Moderate/ Severe
c.1125A>C	M376L		26		(McCorquodale et al., 2011)	Moderate/ Severe
c.11247T>C	M376T		39, late	Dominant	(Choi et al., 2015),(Chung et al., 2010)	Mild
c.1126A>G	M376V		4-6, <30	Dominant	(Ando et al., 2017), (Casasnovas et al., 2010), (Antoniadi et al., 2015)	Severe
c.1132T>C	S378P		Early, 44		(Brockmann et al., 2008), (Ando et al., 2017)	Mild
c.1134_1142del9	L379_M381del		3	Dominant	(Verhoeven et al., 2006)	
c.1148C>T	A383V	HR1	36, 15		(Sitarz et al., 2012), (Muglia et al., 2007), (Bergamin et al., 2014)	Mild/ Various
c.[1157A>C;1158G>T]	Q386P		1.5	De novo	(Verhoeven et al., 2006)	
c.1168T>C	C390R		3	Dominant	(Vallat et al., 2008)	Severe
	C390F		1		(Feely et al., 2011)	Moderate/ Severe
c.1190G>C;	R397P	HR1	3-4 males, 7-8 females	Dominant	(You et al., 2018)	Severe

c.1198C>T	R400X		4	Unknown	(Verhoeven et al., 2006)	
c. 1241A>T	D414V	HR1	8		(Sharma et al., 2022)	Severe
c.1253G>A	R418Q	HR1	37		(Choi et al., 2015)	Mild
C.1252C>T	R418X	Truncation - lacking transmem brane	1, 2		(Züchner et al., 2006), (Chung et al., 2010), (Ando et al., 2017)	Severe
c.1271A>G	E424G		10		(Kijima et al., 2005)	Moderate
c.1287+50G>T					(Kotruchow et al., 2015)	
c.1367C>T	RP456L		12		(Choi et al., 2015)	Mild
c.1392+2T>C		Splicing	50	Dominant	(Bergamin et al., 2014)	Severe
c.1397C>T	P456L		47		(Chung et al., 2008)	
c.1403G>A	R468H	Between TM and coiled coil	26, Childhood, <30, <50	Dominant	(Engelfried et al., 2006), (McCorquodale et al., 2011), (Sitarz et al., 2012), (Casasnovas et al., 2010),(G J Braathen, 2012), (Geir J Braathen, Sand, Lobato, Høyer, & Russell, 2010), (Antoniadi et al., 2015)	Moderate/ Severe, Mild, Moderate
	D496G				(Sitarz et al., 2012)	
c.1525G>C	V509L		37		(Choi et al., 2015)	Mild
	R519P				(Sitarz et al., 2012)	
c.1709A>G	N570S		63		(G J Braathen, 2012; Geir J Braathen et al., 2010)	
c.1717G>A	V573I				(Kotruchow et al., 2015)	
c.1717-274_1734del	p.Q574_V624del	Ex16 skipped, in-frame loss of 50aa, TM1 and PRD loss	0	Recessive	(Chevrollier et al., 2024)	Severe
c.1894C>T	R632W	Transmem brane	41, 42	Recessive	(Hikiami et al. 2018)	
c..1930_1932delCTC	L644del	TM	1		(Choi et al., 2015),(Feely et al., 2011)	Moderate
c.1994T>C	F665S		<10	Dominant	(Calvo et al., 2009)	
	L673P				(Sitarz et al., 2012)	Moderate/ Mild

c.2096T>6	L699P		<16 and late		(Kang et al. 2019)	
c.2113G>A	V705I	HR2	10, 47, 6, 5		(G J Braathen, 2012; Geir J Braathen et al., 2010), (Kotruchow et al., 2015), (Engelfried et al., 2006), (McCorquodale et al., 2011), (Sitarz et al., 2012)	Severe, Moderate - Benign?
c.2116A>C	T706P		7, 10		(Bergamin et al., 2014), (Ando et al., 2017), (Mathis et al., 2014)	Mild, Severe
c.2120delGGGAGAAACC	R707_N709del		12		(McCorquodale et al., 2011)	Moderate
	R707P	HR2			(Sitarz et al., 2012)	
c.2119C>T	R707W	HR2	44		(Sitarz et al., 2012), (Geir J Braathen et al., 2010), (Antoniadi et al., 2015)	
c.2119C>T	R707W	HR2	3	Recessive	(Nicholson et al 2008)	Severe
c.2129T>C	L710P	HR2	6, 1-2	Unknown	(Verhoeven et al., 2006), (Ando et al., 2017)	Severe
c.2140A>G	I714V	HR2	9		(Benedetti et al., 2010)	Moderate
c.2146G>A	A716T	HR2	2, 23, 50		(Sitarz et al., 2012), (Geir J Braathen, Sand, Lobato, Høyer, & Russell, 2010), (Feely et al., 2011), (G J Braathen, 2012)	Severe
C.2171T>C	L724P		<20		(Abe et al., 2011)	
c.2194A>G	K732Q				(Antoniadi et al., 2015)	Mild
c.2213C>T	A738V		9	Dominant	(Benedetti et al., 2010, Bergamin et al., 2014)	Mild-moderate
c.2220G>C	W740C		<10, 13	Dominant	(Calvo et al., 2009), (Ando et al., 2017)	Mild, Moderate
c.2219G > C	W740S	HR2	5-52, 5-33	Dominant	(Züchner et al., 2004), (Feely et al., 2011), (Verhoeven et al., 2006)	Mild/ Moderate
c.2222T>G	L741W	HR2	~20	Dominant	(Dankwa et al. 2018, Lin et al., 2019))	Moderate
c.2230G>A	E744K	HR2	8		(Choi et al., 2015)	
c.2230G>A	Q744K				(Antoniadi et al., 2015)	Mild
C.2234T>C	L745P		<10	Dominant	(Calvo et al., 2009)	Moderate
c.2240T>C	M747T		>10	De novo	(Calvo et al., 2009)	Severe

	H750P		6		(Sitarz et al., 2012),(Feely et al., 2011)	
c.2251C>T	Q751X		4, 5	De novo, Dominant	(Verhoeven et al., 2006)	
	Q751Stop				(Sitarz et al., 2012)	Mild
	Y752Stop				(Sitarz et al., 2012)	
	Y752X		14		(Feely et al., 2011)	Severe
c.2258_2259insT(L753fs)	L753fs	FRAME SHIFT	62		(Engelfried et al., 2006)	
IVS5-1G>C		Affects splice site	Early, 7		(Brockmann et al., 2008), (Chung et al., 2010)	Moderate/ Severe

Appendix 2

Figure 3.6.A, C:

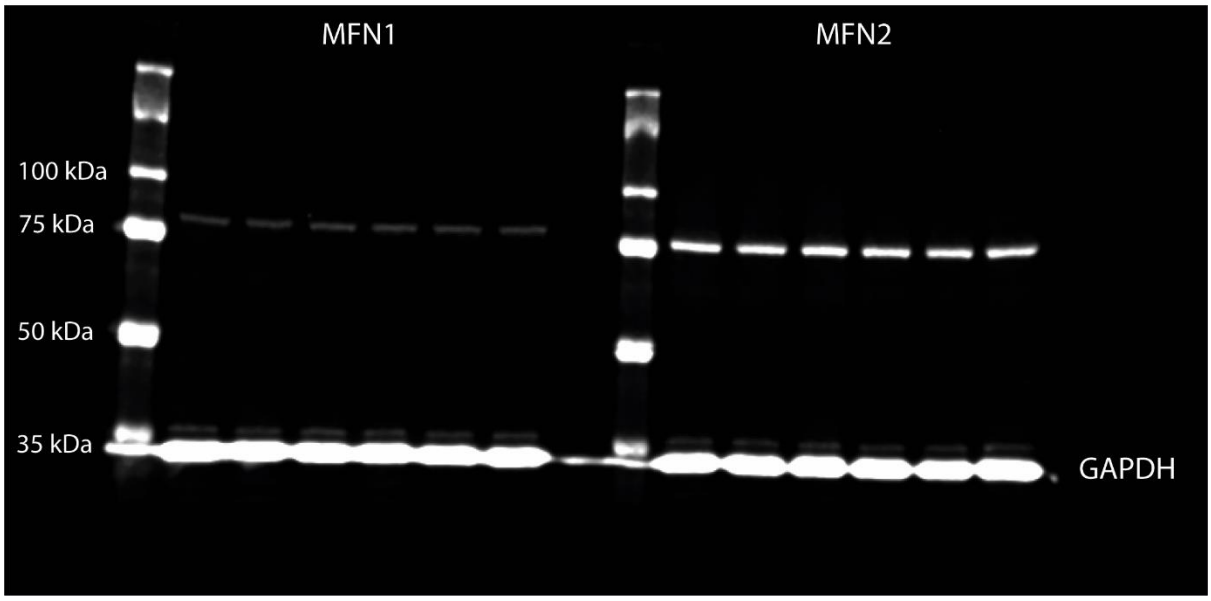


Figure 5.1.A:

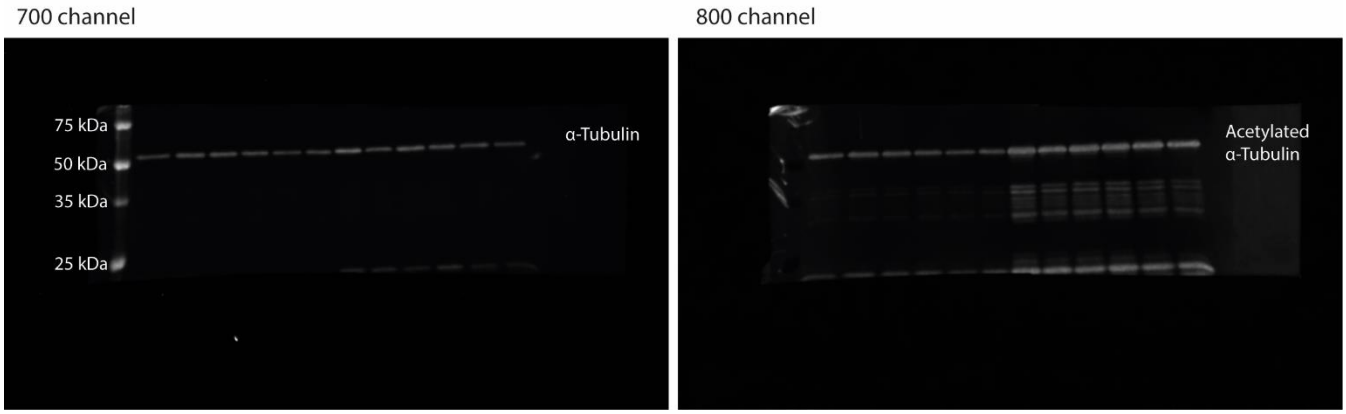


Figure 5.9.A:

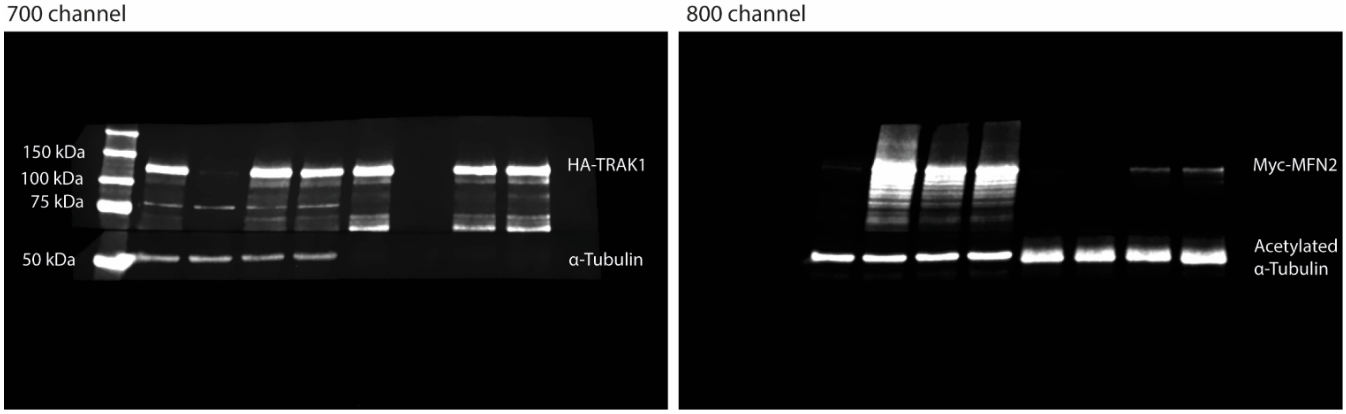


Figure 5.10.A:

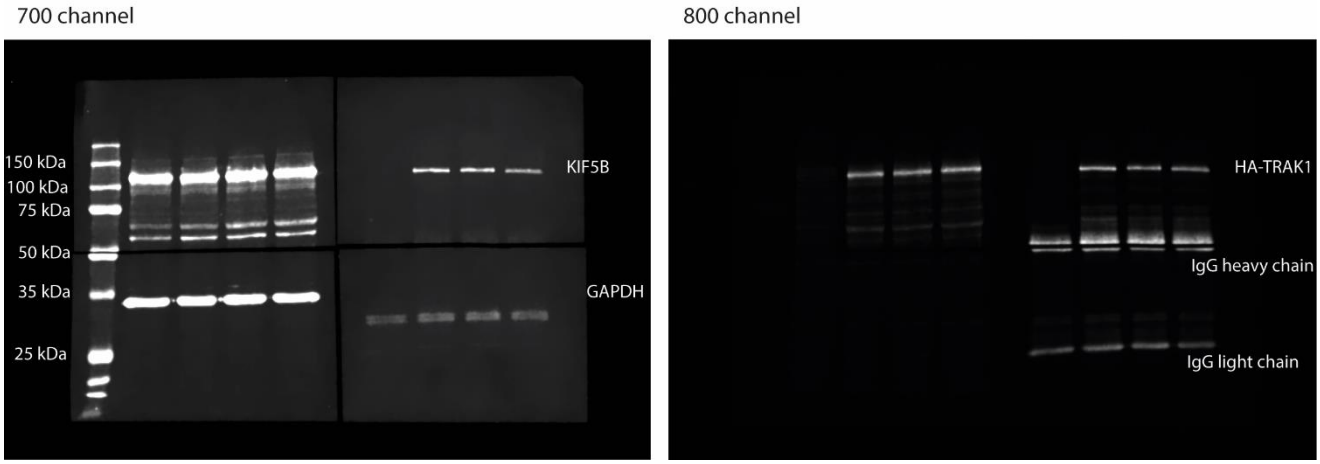


Figure 5.11:

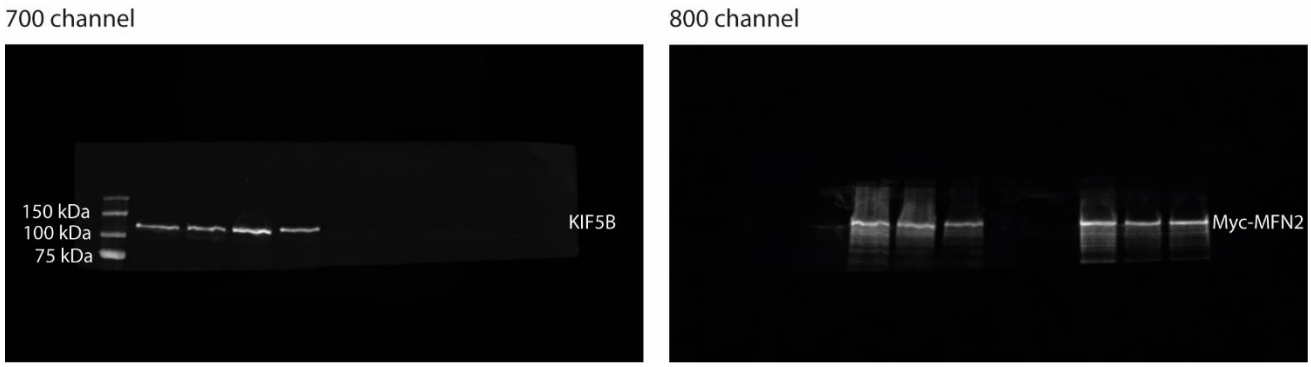


Figure 5.12.A:



Figure 5.12.B:

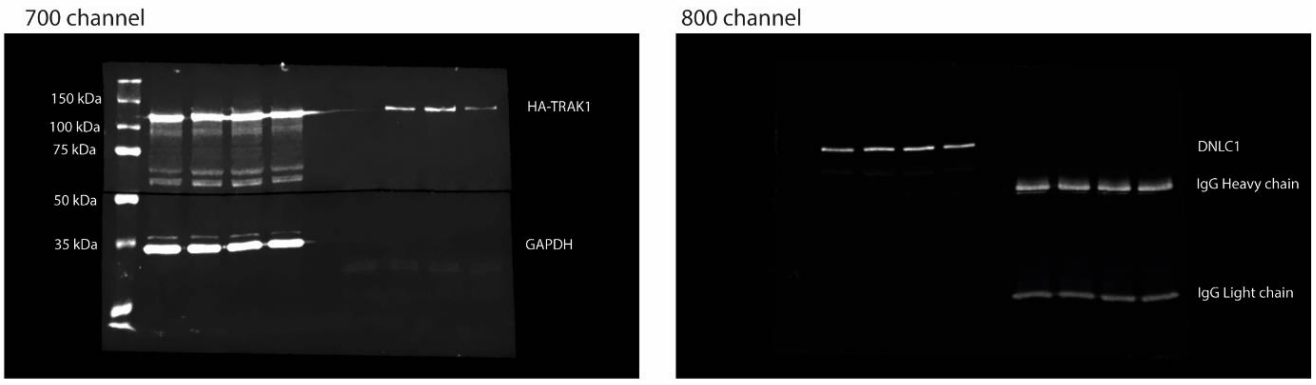


Figure 5.12.C

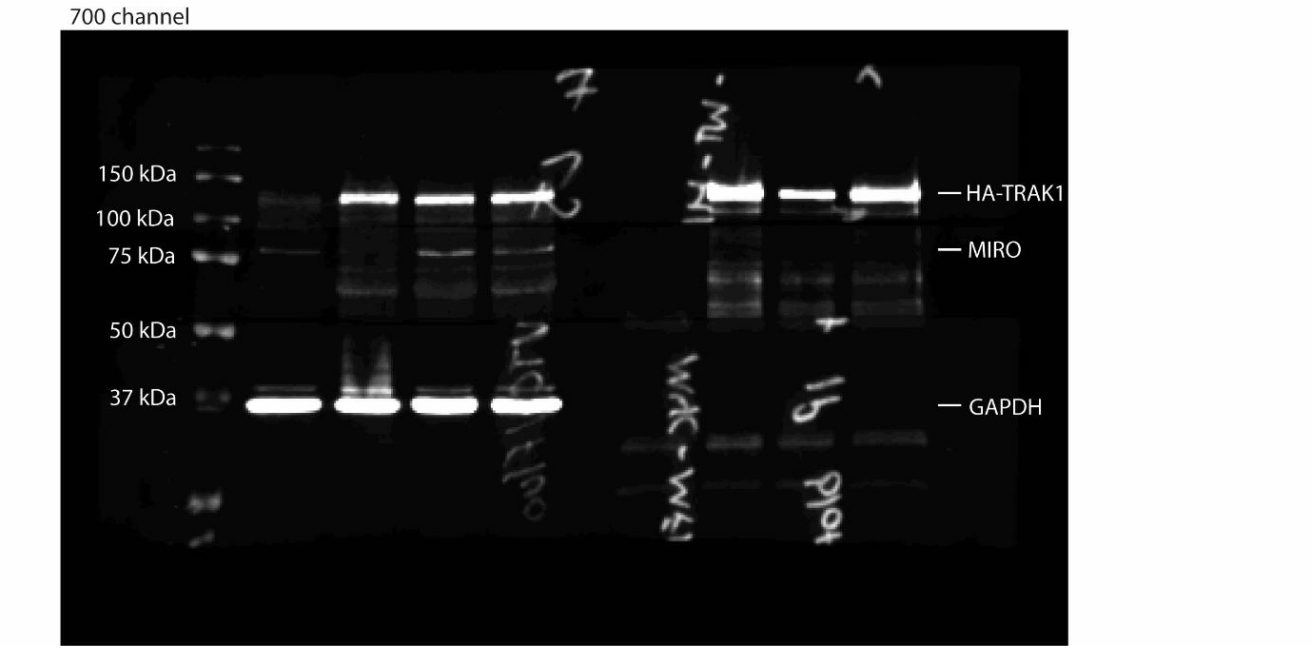
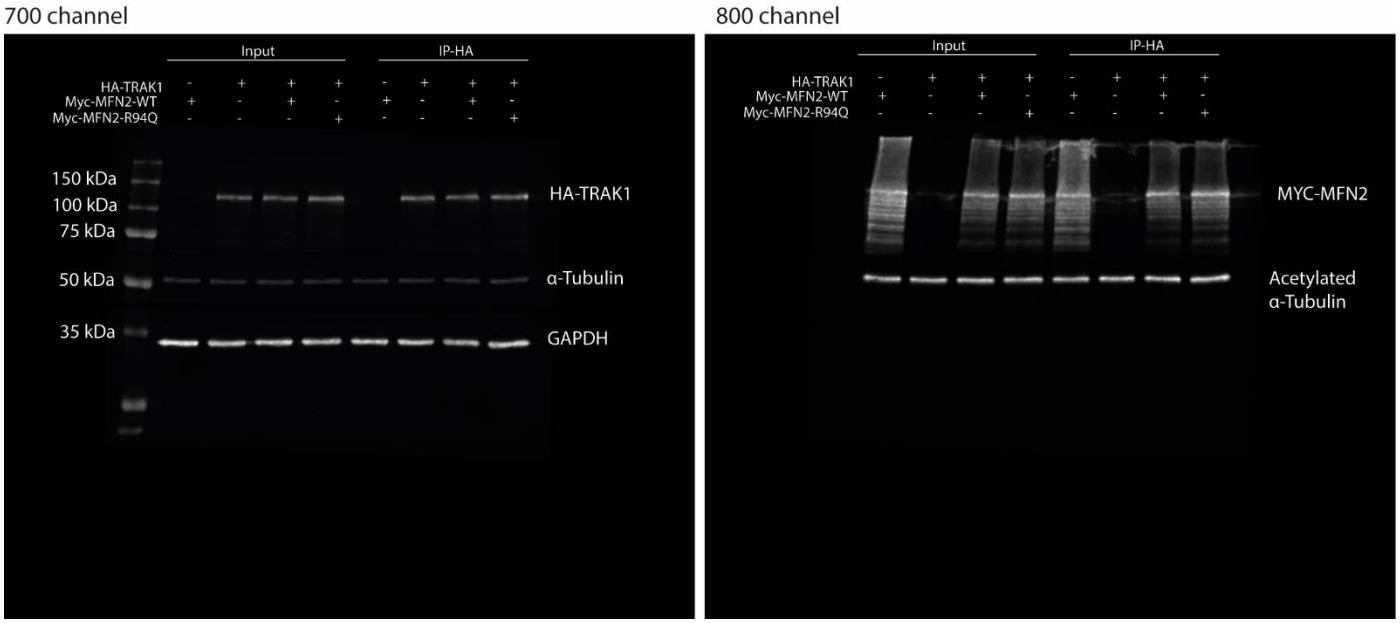


Figure 5.13:



Bibliography

ABATI, E., MANINI, A., VELARDO, D., DEL BO, R., NAPOLI, L., RIZZO, F., MOGGIO, M., BRESOLIN, N., BELLONE, E., BASSI, M. T., D'ANGELO, M. G., COMI, G. P. & CORTI, S. 2022. Clinical and genetic features of a cohort of patients with MFN2-related neuropathy. *Scientific Reports,* 12.

ABATI, E., RIZZUTI, M., ANASTASIA, A., COMI, G. P., CORTI, S. & RIZZO, F. 2024. Charcot–Marie-Tooth type 2A in vivo models: Current updates. *Journal of Cellular and Molecular Medicine,* 28.

ADALBERT, R., KAIEDA, A., ANTONIOU, C., LORETO, A., YANG, X., GILLEY, J., HOSHINO, T., UGA, K., MAKHIJA, M. T. & COLEMAN, M. P. 2020. Novel HDAC6 Inhibitors Increase Tubulin Acetylation and Rescue Axonal Transport of Mitochondria in a Model of Charcot–Marie–Tooth Type 2F. *ACS Chemical Neuroscience,* 11**,** 258-267.

ADLI, M. 2018. The CRISPR tool kit for genome editing and beyond. *Nature Communications,* 9.

AJROUD-DRISS, S., FECTO, F., AJROUD, K., YANG, Y., DONKERVOORT, S., SIDDIQUE, N. & SIDDIQUE, T. 2009. A novel de novo MFN2 mutation causing CMT2A with upper motor neuron signs. *neurogenetics,* 10**,** 359-361.

ALAMI, H., NAEL, SMITH, B., REBECCA, CARRASCO, A., MONICA, WILLIAMS, A., LUIS, WINBORN, S., CHRISTINA, HAN, S. W., STEVE, KISKINIS, E., WINBORN, B., FREIBAUM, D., BRIAN, KANAGARAJ, A., CLARE, J., ALISON, BADDERS, M., NISHA, BILICAN, B., CHAUM, E., CHANDRAN, S., SHAW, E., CHRISTOPHER, EGGAN, C., KEVIN, MANIATIS, T. & TAYLOR, P., J. 2014. Axonal Transport of TDP-43 mRNA Granules Is Impaired by ALS-Causing Mutations. *Neuron,* 81**,** 536-543.

ALAVI, M. V. & FUHRMANN, N. 2013. Dominant optic atrophy, OPA1, and mitochondrial quality control: understanding mitochondrial network dynamics. *Molecular Neurodegeneration,* 8**,** 32.

ALMEIDA-SOUZA, L., ASSELBERGH, B., D'YDEWALLE, C., MOONENS, K., GOETHALS, S., DE WINTER, V., AZMI, A., IROBI, J., TIMMERMANS, J.-P., GEVAERT, K., REMAUT, H., VAN DEN BOSCH, L., TIMMERMAN, V. & JANSSENS, S. 2011. Small Heat-Shock Protein HSPB1 Mutants Stabilize Microtubules in Charcot-Marie-Tooth Neuropathy. *The Journal of Neuroscience,* 31**,** 15320-15328.

ALPER, J. D., DECKER, F., AGANA, B. & HOWARD, J. 2014. The motility of axonemal dynein is regulated by the tubulin code. *Biophys J,* 107**,** 2872-2880.

ALSAYYAH, C., SINGH, M. K., MORCILLO-PARRA, M. A., CAVELLINI, L., SHAI, N., SCHMITT, C., SCHULDINER, M., ZALCKVAR, E., MALLET, A., BELGAREH-TOUZÉ, N., ZIMMER, C. & COHEN, M. M. 2024. Mitofusin-mediated contacts between mitochondria and peroxisomes regulate mitochondrial fusion. *PLOS Biology,* 22**,** e3002602.

ALSEMARZ, A., LASKO, P. & FAGOTTO, F. 2018. Limited significance of the in situ proximity ligation assay. Cold Spring Harbor Laboratory.

AMIOTT, E. A., LOTT, P., SOTO, J., KANG, P. B., MCCAFFERY, J. M., DIMAURO, S., ABEL, E. D., FLANIGAN, K. M., LAWSON, V. H. & SHAW, J. M. 2008. Mitochondrial fusion and function in Charcot–Marie–Tooth type 2A patient fibroblasts with mitofusin 2 mutations. *Experimental Neurology,* 211**,** 115-127.

AN, G., PARK, J., SONG, J., HONG, T., SONG, G. & LIM, W. 2024. Relevance of the endoplasmic reticulum-mitochondria axis in cancer diagnosis and therapy. *Experimental & Molecular Medicine,* 56**,** 40-50.

ANDERSON, N. C., CHEN, P.-F., MEGANATHAN, K., AFSHAR SABER, W., PETERSEN, A. J., BHATTACHARYYA, A., KROLL, K. L. & SAHIN, M. 2021. Balancing serendipity and reproducibility: Pluripotent stem cells as experimental systems for intellectual and developmental disorders. *Stem Cell Reports,* 16**,** 1446-1457.
ANDO, M., HASHIGUCHI, A., OKAMOTO, Y., YOSHIMURA, A., HIRAMATSU, Y., YUAN, J., HIGUCHI, Y., MITSUI, J., ISHIURA, H., UMEMURA, A., MARUYAMA, K., MATSUSHIGE, T., MORISHITA, S., NAKAGAWA, M., TSUJI, S. & TAKASHIMA, H. 2017. Clinical and genetic diversities of Charcot‐Marie‐Tooth disease with MFN2 mutations in a large case study. *Journal of the Peripheral Nervous System,* 22**,** 191-199.
ANDREWS, P. W. & GOKHALE, P. J. 2024. A short history of pluripotent stem cells markers. *Stem Cell Reports,* 19**,** 1-10.
ANTONIADI, T., BUXTON, C., DENNIS, G., FORRESTER, N., SMITH, D., LUNT, P. & BURTON-JONES, S. 2015. Application of targeted multi-gene panel testing for the diagnosis of inherited peripheral neuropathy provides a high diagnostic yield with unexpected phenotype-genotype variability. *BMC Medical Genetics,* 16.
ATTARIAN, S., YOUNG, P., BRANNAGAN, T. H., ADAMS, D., VAN DAMME, P., THOMAS, F. P., CASANOVAS, C., KAFAIE, J., TARD, C., WALTER, M. C., PÉRÉON, Y., WALK, D., STINO, A., DE VISSER, M., VERHAMME, C., AMATO, A., CARTER, G., MAGY, L., STATLAND, J. M. & FELICE, K. 2021. A double-blind, placebo-controlled, randomized trial of PXT3003 for the treatment of Charcot–Marie–Tooth type 1A. *Orphanet Journal of Rare Diseases,* 16.
BAAS, P. W., RAO, A. N., MATAMOROS, A. J. & LEO, L. 2016. Stability properties of neuronal microtubules. *Cytoskeleton,* 73**,** 442-460.
BADCOCK, G., PIGOTT, C., GOEPEL, J. & ANDREWS, P. W. 1999. The human embryonal carcinoma marker antigen TRA-1-60 is a sialylated keratan sulfate proteoglycan. *Cancer Res,* 59**,** 4715-9.
BAKER, D., HIRST, A. J., GOKHALE, P. J., JUAREZ, M. A., WILLIAMS, S., WHEELER, M., BEAN, K., ALLISON, T. F., MOORE, H. D., ANDREWS, P. W. & BARBARIC, I. 2016. Detecting Genetic Mosaicism in Cultures of Human Pluripotent Stem Cells. *Stem Cell Reports,* 7**,** 998-1012.
BALOH, R. H., SCHMIDT, R. E., PESTRONK, A. & MILBRANDT, J. 2007. Altered Axonal Mitochondrial Transport in the Pathogenesis of Charcot-Marie-Tooth Disease from Mitofusin 2 Mutations. *The Journal of Neuroscience,* 27**,** 422-430.
BANNERMAN, P., BURNS, T., XU, J., MIERS, L. & PLEASURE, D. 2016. Mice Hemizygous for a Pathogenic Mitofusin-2 Allele Exhibit Hind Limb/Foot Gait Deficits and Phenotypic Perturbations in Nerve and Muscle. *PLOS ONE,* 11**,** e0167573.
BÄR, J., POPP, Y., BUCHER, M. & MIKHAYLOVA, M. 2022. Direct and indirect effects of tubulin post-translational modifications on microtubule stability: Insights and regulations. *Biochimica et Biophysica Acta (BBA) - Molecular Cell Research,* 1869**,** 119241.
BARBARIC, I., BIGA, V., GOKHALE, J., PAUL, JONES, M., STAVISH, D., GLEN, A., COCA, D. & ANDREWS, W., PETER 2014. Time-Lapse Analysis of Human Embryonic Stem Cells Reveals Multiple Bottlenecks Restricting Colony Formation and Their Relief upon Culture Adaptation. *Stem Cell Reports,* 3**,** 142-155.
BARON, D. M., FENTON, A. R., SAEZ-ATIENZAR, S., GIAMPETRUZZI, A., SREERAM, A., SHANKARACHARYA, KEAGLE, P. J., DOOCY, V. R., SMITH, N. J., DANIELSON, E. W., ANDRESANO, M., MCCORMACK, M. C., GARCIA, J., BERCIER, V., VAN DEN BOSCH, L., BRENT, J. R., FALLINI, C., TRAYNOR, B. J., HOLZBAUR, E. L. F. & LANDERS, J. E. 2022. ALS-associated KIF5A mutations abolish autoinhibition resulting in a toxic gain of function. *Cell Reports,* 39**,** 110598.
BECKER, S. & BOCH, J. 2021. TALE and TALEN genome editing technologies. *Gene and Genome Editing,* 2**,** 100007.

BEIGNEUX, A. P., KOSINSKI, C., GAVINO, B., HORTON, J. D., SKARNES, W. C. & YOUNG, S. G. 2004. ATP-Citrate Lyase Deficiency in the Mouse. *Journal of Biological Chemistry,* 279**,** 9557-9564.

BEKKU, Y. & SALZER, J. L. 2020. Independent anterograde transport and retrograde cotransport of domain components of myelinated axons. *Journal of Cell Biology,* 219.

BEN-SHUSHAN, E., FELDMAN, E. & REUBINOFF, B. E. 2015. Notch Signaling Regulates Motor Neuron Differentiation of Human Embryonic Stem Cells. *Stem Cells,* 33**,** 403-415.

BENEDETTI, S., PREVITALI, S. C., COVIELLO, S., SCARLATO, M., CERRI, F., DI PIERRI, E., PIANTONI, L., SPIGA, I., FAZIO, R., RIVA, N., NATALI SORA, M. G., DACCI, P., MALAGUTI, M. C., MUNERATI, E., GRIMALDI, L. M. E., MARROSU, M. G., DE PELLEGRIN, M., FERRARI, M., COMI, G., QUATTRINI, A. & BOLINO, A. 2010. Analyzing Histopathological Features of Rare Charcot-Marie-Tooth Neuropathies to Unravel Their Pathogenesis. *Archives of Neurology,* 67.

BENNETT, E. P., PETERSEN, B. L., JOHANSEN, I. E., NIU, Y., YANG, Z., CHAMBERLAIN, C. A., MET, Ö., WANDALL, H. H. & FRÖDIN, M. 2020. INDEL detection, the 'Achilles heel' of precise genome editing: a survey of methods for accurate profiling of gene editing induced indels. *Nucleic Acids Research,* 48**,** 11958-11981.

BENOY, V., VANDEN BERGHE, P., JARPE, M., VAN DAMME, P., ROBBERECHT, W. & VAN DEN BOSCH, L. 2017. Development of Improved HDAC6 Inhibitors as Pharmacological Therapy for Axonal Charcot–Marie–Tooth Disease. *Neurotherapeutics,* 14**,** 417-428.

BERGAMIN, G., BOARETTO, F., BRIANI, C., PEGORARO, E., CACCIAVILLANI, M., MARTINUZZI, A., MUGLIA, M., VETTORI, A., VAZZA, G. & MOSTACCIUOLO, M. L. 2014. Mutation Analysis of MFN2, GJB1, MPZ and PMP22 in Italian Patients with Axonal Charcot–Marie–Tooth Disease. *NeuroMolecular Medicine,* 16**,** 540-550.

BERGAMIN, G., CIERI, D., VAZZA, G., ARGENTON, F. & MOSTACCIUOLO, M. L. 2016. Zebrafish Tg(hb9:MTS-Kaede): a new in vivo tool for studying the axonal movement of mitochondria. *Biochim Biophys Acta,* 1860**,** 1247-55.

BERNARD-MARISSAL, N., VAN HAMEREN, G., JUNEJA, M., PELLEGRINO, C., LOUHIVUORI, L., BARTESAGHI, L., ROCHAT, C., EL MANSOUR, O., MÉDARD, J.-J., CROISIER, M., MACLACHLAN, C., POIROT, O., UHLÉN, P., TIMMERMAN, V., TRICAUD, N., SCHNEIDER, B. L. & CHRAST, R. 2019. Altered interplay between endoplasmic reticulum and mitochondria in Charcot–Marie–Tooth type 2A neuropathy. *Proceedings of the National Academy of Sciences,* 116**,** 2328-2337.

BHINGE, A., NAMBOORI, S. C., ZHANG, X., VANDONGEN, A. M. J. & STANTON, L. W. 2017. Genetic Correction of SOD1 Mutant iPSCs Reveals ERK and JNK Activated AP1 as a Driver of Neurodegeneration in Amyotrophic Lateral Sclerosis. *Stem Cell Reports,* 8**,** 856-869.

BOCANEGRA, J. L., FUJITA, B. M., MELTON, N. R., COWAN, J. M., SCHINSKI, E. L., TAMIR, T. Y., MAJOR, M. B. & QUINTERO, O. A. 2020. The MyMOMA domain of MYO19 encodes for distinct Miro-dependent and Miro-independent mechanisms of interaction with mitochondrial membranes. *Cytoskeleton (Hoboken),* 77**,** 149-166.

BOECKER, C. A., GOLDSMITH, J., DOU, D., CAJKA, G. G. & HOLZBAUR, E. L. F. 2021. Increased LRRK2 kinase activity alters neuronal autophagy by disrupting the axonal transport of autophagosomes. *Current Biology,* 31**,** 2140-2154.e6.

BOUTANT, M., KULKARNI, S. S., JOFFRAUD, M., RATAJCZAK, J., VALERA-ALBERNI, M., COMBE, R., ZORZANO, A. & CANTÓ, C. 2017. Mfn2 is critical for brown adipose tissue thermogenic function. *The EMBO Journal,* 36**,** 1543-1558.

BROCKMANN, K., DREHA-KULACZEWSKI, S., DECHENT, P., BÖNNEMANN, C., HELMS, G., KYLLERMAN, M., BRÜCK, W., FRAHM, J., HUEHNE, K., GÄRTNER, J. & RAUTENSTRAUSS, B. 2008. Cerebral involvement in axonal Charcot-Marie-Tooth neuropathy caused by mitofusin2 mutations. *Journal of Neurology,* 255**,** 1049-1058.

BROŽKOVÁ, D. Š., POSÁDKA, J., LAŠŠUTHOVÁ, P., MAZANEC, R., HABERLOVÁ, J., ŠIŠKOVÁ, D., SAKMARYOVÁ, I., NEUPAUEROVÁ, J. & SEEMAN, P. 2013. Spectrum and frequencies of mutations in the MFN2 gene and its phenotypical expression in Czech hereditary motor and sensory neuropathy type II patients. *Molecular Medicine Reports,* 8**,** 1779-1784.

BUTLER, L. 2021. *Investigating the molecular mechanisms in Charcot Marie Tooth disease using human pluripotent stem cells.* University of Sheffield.

BUTLER, L., ADAMSON, K. I., JOHNSON, S. L., JESTICE, L. H., PRICE, C. J., STAVISH, D., POORANACHANDRAN, N., MALICKI, J. J., TSAKIRIDIS, A., GRIERSON, A. J. & BARBARIC, I. 2022. HDAC6 inhibition partially alleviates mitochondrial trafficking defects and restores motor function in human motor neuron and zebrafish models of Charcot-Marie-Tooth Disease Type 2A. Cold Spring Harbor Laboratory.

CAI, Z., LUO, W., WANG, H., ZHU, R., YUAN, Y., ZHAN, X., XIE, M., ZHUANG, H., CHEN, H., XU, Y., LI, X., LIU, L. & XU, G. 2024. MFN2 suppresses the accumulation of lipid droplets and the progression of clear cell renal cell carcinoma. *Cancer Science,* 115**,** 1791-1807.

CANDAYAN, A., PARMAN, Y. & BATTALOĞLU, E. 2022. Clinical and Genetic Survey for Charcot-Marie-Tooth Neuropathy Based on the Findings in Turkey, a Country with a High Rate of Consanguineous Marriages. *Balkan Medical Journal,* 39**,** 3-11.

CANTY, J. T., HENSLEY, A., ASLAN, M., JACK, A. & YILDIZ, A. 2023. TRAK adaptors regulate the recruitment and activation of dynein and kinesin in mitochondrial transport. *Nature Communications,* 14.

CAO, Y.-L., MENG, S., CHEN, Y., FENG, J.-X., GU, D.-D., YU, B., LI, Y.-J., YANG, J.-Y., LIAO, S., CHAN, D. C. & GAO, S. 2017. MFN1 structures reveal nucleotide-triggered dimerization critical for mitochondrial fusion. *Nature,* 542**,** 372-376.

CARIO, A. & BERGER, C. L. 2023. Tau, microtubule dynamics, and axonal transport: New paradigms for neurodegenerative disease. *BioEssays,* 45.

CARTONI, R., ARNAUD, E., MÉDARD, J.-J., POIROT, O., COURVOISIER, D. S., CHRAST, R. & MARTINOU, J.-C. 2010. Expression of mitofusin 2R94Q in a transgenic mouse leads to Charcot–Marie–Tooth neuropathy type 2A. *Brain,* 133**,** 1460-1469.

CASELLAS-DÍAZ, S., LARRAMONA-ARCAS, R., RIQUÉ-PUJOL, G., TENA-MORRAJA, P., MÜLLER-SÁNCHEZ, C., SEGARRA-MONDEJAR, M., GAVALDÀ-NAVARRO, A., VILLARROYA, F., REINA, M., MARTÍNEZ-ESTRADA, O. M. & SORIANO, F. X. 2021. Mfn2 localization in the ER is necessary for its bioenergetic function and neuritic development. *EMBO reports,* 22.

CATELA, C., SHIN, M., MAGGIE, LEE, H., DAVID, LIU, J.-P. & DASEN, S., JEREMY 2016. Hox Proteins Coordinate Motor Neuron Differentiation and Connectivity Programs through Ret/Gfrα Genes. *Cell Reports,* 14**,** 1901-1915.

CAVISTON, J. P., ROSS, J. L., ANTONY, S. M., TOKITO, M. & HOLZBAUR, E. L. F. 2007. Huntingtin facilitates dynein/dynactin-mediated vesicle transport. *Proceedings of the National Academy of Sciences,* 104**,** 10045-10050.

CERNECKIS, J., CAI, H. & SHI, Y. 2024. Induced pluripotent stem cells (iPSCs): molecular mechanisms of induction and applications. *Signal Transduction and Targeted Therapy,* 9.

CHAMBERS, S. M., FASANO, C. A., PAPAPETROU, E. P., TOMISHIMA, M., SADELAIN, M. & STUDER, L. 2009. Highly efficient neural conversion of human ES and iPS cells by dual inhibition of SMAD signaling. *Nature Biotechnology,* 27**,** 275-280.

CHANG, C.-Y., TING, H.-C., LIU, C.-A., SU, H.-L., CHIOU, T.-W., HARN, H.-J., LIN, S.-Z. & HO, T.-J. 2021. Differentiation of Human Pluripotent Stem Cells Into Specific Neural Lineages. *Cell Transplantation,* 30**,** 096368972110178.

CHAPMAN, A. L., BENNETT, E. J., RAMESH, T. M., DE VOS, K. J. & GRIERSON, A. J. 2013. Axonal Transport Defects in a Mitofusin 2 Loss of Function Model of Charcot-Marie-Tooth Disease in Zebrafish. *PLoS ONE,* 8**,** e67276.

CHAUDHARY, A. R., LU, H., KREMENTSOVA, E. B., BOOKWALTER, C. S., TRYBUS, K. M. & HENDRICKS, A. G. 2019. MAP7 regulates organelle transport by recruiting kinesin-1 to microtubules. *J Biol Chem,* 294**,** 10160-10171.
CHAZOTTE, B. 2011. Labeling Mitochondria with MitoTracker Dyes. *Cold Spring Harbor Protocols,* 2011**,** pdb.prot5648.
CHEN, G., GULBRANSON, D. R., HOU, Z., BOLIN, J. M., RUOTTI, V., PROBASCO, M. D., SMUGA-OTTO, K., HOWDEN, S. E., DIOL, N. R., PROPSON, N. E., WAGNER, R., LEE, G. O., ANTOSIEWICZ-BOURGET, J., TENG, J. M. & THOMSON, J. A. 2011. Chemically defined conditions for human iPSC derivation and culture. *Nat Methods,* 8**,** 424-9.
CHEN, H., CHOMYN, A. & CHAN, D. C. 2005. Disruption of fusion results in mitochondrial heterogeneity and dysfunction. *J Biol Chem,* 280**,** 26185-92.
CHEN, H., DETMER, S. A., EWALD, A. J., GRIFFIN, E. E., FRASER, S. E. & CHAN, D. C. 2003. Mitofusins Mfn1 and Mfn2 coordinately regulate mitochondrial fusion and are essential for embryonic development. *The Journal of Cell Biology,* 160**,** 189-200.
CHEN, H., MCCAFFERY, J. M. & CHAN, D. C. 2007. Mitochondrial Fusion Protects against Neurodegeneration in the Cerebellum. *Cell,* 130**,** 548-562.
CHEN, J. & ROLL-MECAK, A. 2023. Glutamylation is a negative regulator of microtubule growth. *Molecular Biology of the Cell,* 34**,** ar70.
CHEN, S., OWENS, G. C., MAKARENKOVA, H. & EDELMAN, D. B. 2010. HDAC6 Regulates Mitochondrial Transport in Hippocampal Neurons. *PLoS ONE,* 5**,** e10848.
CHEN, W., ZHAO, H. & LI, Y. 2023. Mitochondrial dynamics in health and disease: mechanisms and potential targets. *Signal Transduction and Targeted Therapy,* 8.
CHEN, Y., CSORDÁS, G., JOWDY, C., SCHNEIDER, T. G., CSORDÁS, N., WANG, W., LIU, Y., KOHLHAAS, M., MEISER, M., BERGEM, S., NERBONNE, J. M., DORN, G. W. & MAACK, C. 2012. Mitofusin 2-Containing Mitochondrial-Reticular Microdomains Direct Rapid Cardiomyocyte Bioenergetic Responses Via Interorganelle Ca

²⁺

Crosstalk. *Circulation Research,* 111**,** 863-875.
CHEN, Y. & DORN, G. W. 2013. PINK1-Phosphorylated Mitofusin 2 Is a Parkin Receptor for Culling Damaged Mitochondria. *Science,* 340**,** 471-475.
CHEN, Y. & SHENG, Z. H. 2013. Kinesin-1-syntaphilin coupling mediates activity-dependent regulation of axonal mitochondrial transport. *J Cell Biol,* 202**,** 351-64.
CHIBA, K., ORI-MCKENNEY, K. M., NIWA, S. & MCKENNEY, R. J. 2022. Synergistic autoinhibition and activation mechanisms control kinesin-1 motor activity. *Cell Reports,* 39**,** 110900.
CHOI, B. O., NAKHRO, K., PARK, H. J., HYUN, Y. S., LEE, J. H., KANWAL, S., JUNG, S. C. & CHUNG, K. W. 2015. A cohort study of <scp>MFN2</scp> mutations and phenotypic spectrums in Charcot–Marie–Tooth disease <scp>2A</scp> patients. *Clinical Genetics,* 87**,** 594-598.
CHOUDHARY, C., KUMAR, C., GNAD, F., NIELSEN, M. L., REHMAN, M., WALTHER, T. C., OLSEN, J. V. & MANN, M. 2009. Lysine acetylation targets protein complexes and co-regulates major cellular functions. *Science,* 325**,** 834-40.
CHUDAKOV, D. M., LUKYANOV, S. & LUKYANOV, K. A. 2007. Tracking intracellular protein movements using photoswitchable fluorescent proteins PS-CFP2 and Dendra2. *Nat Protoc,* 2**,** 2024-32.
CHUMAKOV, I., MILET, A., CHOLET, N., PRIMAS, G., BOUCARD, A., PEREIRA, Y., GRAUDENS, E., MANDEL, J., LAFFAIRE, J., FOUCQUIER, J., GLIBERT, F., BERTRAND, V., NAVE, K.-A., SEREDA, M. W., VIAL, E., GUEDJ, M., HAJJ, R., NABIROTCHKIN, S. & COHEN, D. 2014. Polytherapy with a combination of three repurposed drugs (PXT3003) down-regulates Pmp22 over-expression and improves myelination, axonal and functional parameters in models of CMT1A neuropathy. *Orphanet Journal of Rare Diseases,* 9**,** 201.

CHUNG, K. W. 2006. Early onset severe and late-onset mild Charcot-Marie-Tooth disease with mitofusin 2 (MFN2) mutations. *Brain,* 129**,** 2103-2118.
CHUNG, K. W., SUH, B. C., CHO, S. Y., CHOI, S. K., KANG, S. H., YOO, J. H., HWANG, J. Y. & CHOI, B. O. 2010. Early-onset Charcot-Marie-Tooth patients with mitofusin 2 mutations and brain involvement. *Journal of Neurology, Neurosurgery & Psychiatry,* 81**,** 1203-1206.
COOPER, F. & TSAKIRIDIS, A. 2022. Shaping axial identity during human pluripotent stem cell differentiation to neural crest cells. *Biochemical Society Transactions,* 50**,** 499-511.
COSSON, P., MARCHETTI, A., RAVAZZOLA, M. & ORCI, L. 2012. Mitofusin-2 Independent Juxtaposition of Endoplasmic Reticulum and Mitochondria: An Ultrastructural Study. *PLoS ONE,* 7**,** e46293.
CUDDY, L. K., WANI, W. Y., MORELLA, M. L., PITCAIRN, C., TSUTSUMI, K., FREDRIKSEN, K., JUSTMAN, C. J., GRAMMATOPOULOS, T. N., BELUR, N. R., ZUNKE, F., SUBRAMANIAN, A., AFFANEH, A., LANSBURY, P. T. & MAZZULLI, J. R. 2019. Stress-Induced Cellular Clearance Is Mediated by the SNARE Protein ykt6 and Disrupted by α-Synuclein. *Neuron,* 104**,** 869-884.e11.
D'YDEWALLE, C., KRISHNAN, J., CHIHEB, D. M., VAN DAMME, P., IROBI, J., KOZIKOWSKI, A. P., BERGHE, P. V., TIMMERMAN, V., ROBBERECHT, W. & VAN DEN BOSCH, L. 2011. HDAC6 inhibitors reverse axonal loss in a mouse model of mutant HSPB1–induced Charcot-Marie-Tooth disease. *Nature Medicine,* 17**,** 968-974.
DANG, X., WALTON, E. K., ZABLOCKA, B., BALOH, R. H., SHY, M. E. & DORN, G. W. 2022. Mitochondrial Phenotypes in Genetically Diverse Neurodegenerative Diseases and Their Response to Mitofusin Activation. *Cells,* 11**,** 1053.
DAS, R., DAS, S., CHAKRABARTI, S. & CHAKRABARTI, O. 2022a. CMT2A-linked mitochondrial hyperfusion-driving mutant MFN2 perturbs ER-mitochondrial associations and Ca²⁺ homeostasis. *Biology of the Cell,* 114**,** 309-319.
DAS, R., KAMAL, I. M., DAS, S., CHAKRABARTI, S. & CHAKRABARTI, O. 2022b. MITOL-mediated DRP1 ubiquitylation and degradation promotes mitochondrial hyperfusion in a CMT2A-linked MFN2 mutant. *Journal of Cell Science,* 135.
DAS, R., MAITY, S., DAS, P., KAMAL, I. M., CHAKRABARTI, S. & CHAKRABARTI, O. 2024. CMT2A-linked MFN2 mutation, T206I promotes mitochondrial hyperfusion and predisposes cells towards mitophagy. *Mitochondrion,* 74**,** 101825.
DAVIES, V. J., HOLLINS, A. J., PIECHOTA, M. J., YIP, W., DAVIES, J. R., WHITE, K. E., NICOLS, P. P., BOULTON, M. E. & VOTRUBA, M. 2007. Opa1 deficiency in a mouse model of autosomal dominant optic atrophy impairs mitochondrial morphology, optic nerve structure and visual function. *Hum Mol Genet,* 16**,** 1307-18.
DAVIS, M. W. & JORGENSEN, E. M. 2022. ApE, A plasmid Editor: a freelyavailable DNA manipulation and visualization program. *Frontiers in Bioinformatics,* 2**,** 818619.
DAWIDENKOW, S. 1927. Über die neurotische Muskelatrophie Charcot-Marie Klinisch-genetische Studien. *Zeitschrift für die gesamte Neurologie und Psychiatrie,* 107**,** 259-320.
DE BRITO, O. M. & SCORRANO, L. 2008. Mitofusin 2 tethers endoplasmic reticulum to mitochondria. *Nature,* 456**,** 605-610.
DE GIOIA, R., CITTERIO, G., ABATI, E., NIZZARDO, M., BRESOLIN, N., COMI, G. P., CORTI, S. & RIZZO, F. 2020. Animal Models of CMT2A: State-of-art and Therapeutic Implications. *Molecular Neurobiology,* 57**,** 5121-5129.
DE VOS, K. J., MÓROTZ, G. M., STOICA, R., TUDOR, E. L., LAU, K.-F., ACKERLEY, S., WARLEY, A., SHAW, C. E. & MILLER, C. C. J. 2012. VAPB interacts with the mitochondrial protein PTPIP51 to regulate calcium homeostasis. *Human Molecular Genetics,* 21**,** 1299-1311.
DETMER, S. A. & CHAN, D. C. 2007. Functions and dysfunctions of mitochondrial dynamics. *Nature Reviews Molecular Cell Biology,* 8**,** 870-879.

DETMER, S. A., VELDE, C. V., CLEVELAND, D. W. & CHAN, D. C. 2007. Hindlimb gait defects due to motor axon loss and reduced distal muscles in a transgenic mouse model of Charcot–Marie–Tooth type 2A. *Human Molecular Genetics,* 17**,** 367-375.
DIEZ DEL CORRAL, R. & MORALES, A. V. 2017. The Multiple Roles of FGF Signaling in the Developing Spinal Cord. *Frontiers in Cell and Developmental Biology,* 5.
DOMPIERRE, J. P., GODIN, J. D., CHARRIN, B. C., CORDELIÈRES, F. P., KING, S. J., HUMBERT, S. & SAUDOU, F. 2007. Histone Deacetylase 6 Inhibition Compensates for the Transport Deficit in Huntington's Disease by Increasing Tubulin Acetylation. *The Journal of Neuroscience,* 27**,** 3571-3583.
DRAPER, J. S., SMITH, K., GOKHALE, P., MOORE, H. D., MALTBY, E., JOHNSON, J., MEISNER, L., ZWAKA, T. P., THOMSON, J. A. & ANDREWS, P. W. 2004. Recurrent gain of chromosomes 17q and 12 in cultured human embryonic stem cells. *Nature Biotechnology,* 22**,** 53-54.
DRUCKER, J., DANIEL 2016. Never Waste a Good Crisis: Confronting Reproducibility in Translational Research. *Cell Metabolism,* 24**,** 348-360.
DYCK, P. J. 1968. Lower Motor and Primary Sensory Neuron Diseases With Peroneal Muscular Atrophy. *Archives of Neurology,* 18**,** 603.
DYCK, P. J. & LAMBERT, E. H. 1968. Lower motor and primary sensory neuron diseases with peroneal muscular atrophy. I. Neurologic, genetic, and electrophysiologic findings in hereditary polyneuropathies. *Arch Neurol,* 18**,** 603-18.
EBERHARDT, E. L., LUDLAM, A. V., TAN, Z. & CIANFROCCO, M. A. 2020. Miro: A molecular switch at the center of mitochondrial regulation. *Protein Sci,* 29**,** 1269-1284.
EIBERG, H., KJER, B., KJER, P. & ROSENBERG, T. 1994. Dominant optic atrophy (OPA1) mapped to chromosome 3q region. I. Linkage analysis. *Hum Mol Genet,* 3**,** 977-80.
EL FISSI, N., ROJO, M., AOUANE, A., KARATAS, E., POLIACIKOVA, G., DAVID, C., ROYET, J. & RIVAL, T. 2018. Mitofusin gain and loss of function drive pathogenesis in Drosophila models of CMT2A neuropathy. *EMBO Rep,* 19.
ENGEL, M., DO-HA, D., MUÑOZ, S. S. & OOI, L. 2016. Common pitfalls of stem cell differentiation: a guide to improving protocols for neurodegenerative disease models and research. *Cellular and Molecular Life Sciences,* 73**,** 3693-3709.
ENGELFRIED, K., VORGERD, M., HAGEDORN, M., HAAS, G., GILLES, J., EPPLEN, J. T. & MEINS, M. 2006. Charcot-Marie-Tooth neuropathy type 2A: novel mutations in the mitofusin 2 gene (MFN2). *BMC Medical Genetics,* 7.
ESHUN-WILSON, L., ZHANG, R., PORTRAN, D., NACHURY, M. V., TOSO, D. B., LÖHR, T., VENDRUSCOLO, M., BONOMI, M., FRASER, J. S. & NOGALES, E. 2019. Effects of α-tubulin acetylation on microtubule structure and stability. *Proceedings of the National Academy of Sciences,* 116**,** 10366-10371.
ESTEVES, A. R., PALMA, A. M., GOMES, R., SANTOS, D., SILVA, D. F. & CARDOSO, S. M. 2019. Acetylation as a major determinant to microtubule-dependent autophagy: Relevance to Alzheimer's and Parkinson disease pathology. *Biochim Biophys Acta Mol Basis Dis,* 1865**,** 2008-2023.
EVANS, M. J. & KAUFMAN, M. H. 1981. Establishment in culture of pluripotential cells from mouse embryos. *Nature,* 292**,** 154-156.
FAN, R. & LAI, K. O. 2022. Understanding how kinesin motor proteins regulate postsynaptic function in neuron. *The FEBS Journal,* 289**,** 2128-2144.
FANG, D., YAN, S., YU, Q., CHEN, D. & YAN, S. S. 2016. Mfn2 is Required for Mitochondrial Development and Synapse Formation in Human Induced Pluripotent Stem Cells/hiPSC Derived Cortical Neurons. *Scientific Reports,* 6**,** 31462.
FILADI, R., GREOTTI, E., TURACCHIO, G., LUINI, A., POZZAN, T. & PIZZO, P. 2015. Mitofusin 2 ablation increases endoplasmic reticulum–mitochondria coupling. *Proceedings of the National Academy of Sciences,* 112**,** E2174-E2181.
FOREMAN, K. J., MARQUEZ, N., DOLGERT, A., FUKUTAKI, K., FULLMAN, N., MCGAUGHEY, M., PLETCHER, M. A., SMITH, A. E., TANG, K., YUAN, C.-W., BROWN, J. C., FRIEDMAN, J., HE, J., HEUTON, K. R., HOLMBERG, M., PATEL, D.

J., REIDY, P., CARTER, A., CERCY, K., CHAPIN, A., DOUWES-SCHULTZ, D., FRANK, T., GOETTSCH, F., LIU, P. Y., NANDAKUMAR, V., REITSMA, M. B., REUTER, V., SADAT, N., SORENSEN, R. J. D., SRINIVASAN, V., UPDIKE, R. L., YORK, H., LOPEZ, A. D., LOZANO, R., LIM, S. S., MOKDAD, A. H., VOLLSET, S. E. & MURRAY, C. J. L. 2018. Forecasting life expectancy, years of life lost, and all-cause and cause-specific mortality for 250 causes of death: reference and alternative scenarios for 2016–40 for 195 countries and territories. *The Lancet,* 392**,** 2052-2090.

FRANCELLE, L., OUTEIRO, T. F. & RAPPOLD, G. A. 2020. Inhibition of HDAC6 activity protects dopaminergic neurons from alpha-synuclein toxicity. *Scientific Reports,* 10.

FRANCO, A., DANG, X., WALTON, E. K., HO, J. N., ZABLOCKA, B., LY, C., MILLER, T. M., BALOH, R. H., SHY, M. E., YOO, A. S. & DORN, G. W., 2ND 2020. Burst mitofusin activation reverses neuromuscular dysfunction in murine CMT2A. *Elife,* 9.

FRANCO, A., DANG, X., ZHANG, L., MOLINOFF, P. B. & DORN, G. W., 2ND 2022. Mitochondrial Dysfunction and Pharmacodynamics of Mitofusin Activation in Murine Charcot-Marie-Tooth Disease Type 2A. *J Pharmacol Exp Ther,* 383**,** 137-148.

FRANCO, A., KITSIS, R. N., FLEISCHER, J. A., GAVATHIOTIS, E., KORNFELD, O. S., GONG, G., BIRIS, N., BENZ, A., QVIT, N., DONNELLY, S. K., CHEN, Y., MENNERICK, S., HODGSON, L., MOCHLY-ROSEN, D. & DORN, G. W. 2016. Correcting mitochondrial fusion by manipulating mitofusin conformations. *Nature,* 540**,** 74-79.

FRANCO, A., LI, J., KELLY, D. P., HERSHBERGER, R. E., MARIAN, A. J., LEWIS, R. M., SONG, M., DANG, X., SCHMIDT, A. D., MATHYER, M. E., EDWARDS, J. R., STRONG, C. G. & DORN, G. W. 2023. A human mitofusin 2 mutation can cause mitophagic cardiomyopathy. *Elife,* 12.

FRIEDMAN, J. R., LACKNER, L. L., WEST, M., DIBENEDETTO, J. R., NUNNARI, J. & VOELTZ, G. K. 2011. ER Tubules Mark Sites of Mitochondrial Division. *Science,* 334**,** 358-362.

FUMAGALLI, L., YOUNG, F. L., BOEYNAEMS, S., DE DECKER, M., MEHTA, A. R., SWIJSEN, A., FAZAL, R., GUO, W., MOISSE, M., BECKERS, J., DEDEENE, L., SELVARAJ, B. T., VANDOORNE, T., MADAN, V., VAN BLITTERSWIJK, M., RAITCHEVA, D., MCCAMPBELL, A., POESEN, K., GITLER, A. D., KOCH, P., BERGHE, P. V., THAL, D. R., VERFAILLIE, C., CHANDRAN, S., VAN DEN BOSCH, L., BULLOCK, S. L. & VAN DAMME, P. 2021. C9orf72-derived arginine-containing dipeptide repeats associate with axonal transport machinery and impede microtubule-based motility. *Science Advances,* 7**,** eabg3013.

FUMOTO, K., HOOGENRAAD, C. C. & KIKUCHI, A. 2006. GSK-3β-regulated interaction of BICD with dynein is involved in microtubule anchorage at centrosome. *The EMBO Journal,* 25**,** 5670-5682.

GAL, J., CHEN, J., BARNETT, K. R., YANG, L., BRUMLEY, E. & ZHU, H. 2013. HDAC6 Regulates Mutant SOD1 Aggregation through Two SMIR Motifs and Tubulin Acetylation. *Journal of Biological Chemistry,* 288**,** 15035-15045.

GAO, S. & HU, J. 2021. Mitochondrial Fusion: The Machineries In and Out. *Trends in Cell Biology,* 31**,** 62-74.

GAZZOLA, M., SCHAEFFER, A., BUTLER-HALLISSEY, C., FRIEDL, K., VIANAY, B., GAILLARD, J., LETERRIER, C., BLANCHOIN, L. & THÉRY, M. 2023. Microtubules self-repair in living cells. *Current Biology,* 33**,** 122-133.e4.

GEGG, M. E., COOPER, J. M., CHAU, K. Y., ROJO, M., SCHAPIRA, A. H. & TAANMAN, J. W. 2010. Mitofusin 1 and mitofusin 2 are ubiquitinated in a PINK1/parkin-dependent manner upon induction of mitophagy. *Hum Mol Genet,* 19**,** 4861-70.

GHOSH, Z., WILSON, K. D., WU, Y., HU, S., QUERTERMOUS, T. & WU, J. C. 2010. Persistent Donor Cell Gene Expression among Human Induced Pluripotent Stem Cells Contributes to Differences with Human Embryonic Stem Cells. *PLoS ONE,* 5**,** e8975.

GIACOMELLO, M., DRAGO, I., BORTOLOZZI, M., SCORZETO, M., GIANELLE, A., PIZZO, P. & POZZAN, T. 2010. Ca2+ Hot Spots on the Mitochondrial Surface Are Generated by Ca2+ Mobilization from Stores, but Not by Activation of Store-Operated Ca2+ Channels. *Molecular Cell,* 38**,** 280-290.
GIACOMELLO, M. & PELLEGRINI, L. 2016. The coming of age of the mitochondria–ER contact: a matter of thickness. *Cell Death & Differentiation,* 23**,** 1417-1427.
GILL, S. R., SCHROER, T. A., SZILAK, I., STEUER, E. R., SHEETZ, M. P. & CLEVELAND, D. W. 1991. Dynactin, a conserved, ubiquitously expressed component of an activator of vesicle motility mediated by cytoplasmic dynein. *The Journal of cell biology,* 115**,** 1639-1650.
GINSBERG, L. 2020. Acute and chronic neuropathies. *Medicine (Abingdon),* 48**,** 612-618.
GIOVENALE, A. M. G., FERRONE, I., TOMASELLI, S., MAZZONI, M., RUOTOLO, G., TURCO, E. M., TORRES, B., DE LUCA, A., ZANFARDINO, P., VULCANO, E., FERRARI, D., DAMIANI, D., SANTORELLI, F. M., PENNUTO, M., VESCOVI, A. L., PETRUZZELLA, V. & ROSATI, J. 2025. Generation and characterization of a patient-derived iPSC line, CSSi022-A (15666), with a pathogenic MFN2 mutation causing Charcot-Marie-Tooth disease type 2A. *Stem Cell Research,* 88**,** 103817.
GLASS, M. R., WAXMAN, E. A., YAMASHITA, S., LAFFERTY, M., BELTRAN, A. A., FARAH, T., PATEL, N. K., SINGLA, R., MATOBA, N., AHMED, S., SRIVASTAVA, M., DRAKE, E., DAVIS, L. T., YETURI, M., SUN, K., LOVE, M. I., HASHIMOTO-TORII, K., FRENCH, D. L. & STEIN, J. L. 2024. Cross-site reproducibility of human cortical organoids reveals consistent cell type composition and architecture. *Stem Cell Reports,* 19**,** 1351-1367.
GODENA, V. K., BROOKES-HOCKING, N., MOLLER, A., SHAW, G., OSWALD, M., SANCHO, R. M., MILLER, C. C. J., WHITWORTH, A. J. & DE VOS, K. J. 2014. Increasing microtubule acetylation rescues axonal transport and locomotor deficits caused by LRRK2 Roc-COR domain mutations. *Nature Communications,* 5**,** 5245.
GORDON-WEEKS, P. R. & FISCHER, I. 2000. MAP1B expression and microtubule stability in growing and regenerating axons. *Microscopy Research and Technique,* 48**,** 63-74.
GOUTI, M., TSAKIRIDIS, A., WYMEERSCH, F. J., HUANG, Y., KLEINJUNG, J., WILSON, V. & BRISCOE, J. 2014. In Vitro Generation of Neuromesodermal Progenitors Reveals Distinct Roles for Wnt Signalling in the Specification of Spinal Cord and Paraxial Mesoderm Identity. *PLoS Biology,* 12**,** e1001937.
GUEDES-DIAS, P. & HOLZBAUR, E. L. F. 2019. Axonal transport: Driving synaptic function. *Science,* 366**,** eaaw9997.
GUEDES-DIAS, P., NIRSCHL, J. J., ABREU, N., TOKITO, M. K., JANKE, C., MAGIERA, M. M. & HOLZBAUR, E. L. F. 2019. Kinesin-3 Responds to Local Microtubule Dynamics to Target Synaptic Cargo Delivery to the Presynapse. *Curr Biol,* 29**,** 268-282 e8.
GUENTHER, M. G., FRAMPTON, G. M., SOLDNER, F., HOCKEMEYER, D., MITALIPOVA, M., JAENISCH, R. & YOUNG, R. A. 2010. Chromatin Structure and Gene Expression Programs of Human Embryonic and Induced Pluripotent Stem Cells. *Cell Stem Cell,* 7**,** 249-257.
GUILLET, V., GUEGUEN, N., VERNY, C., FERRE, M., HOMEDAN, C., LOISEAU, D., PROCACCIO, V., AMATI-BONNEAU, P., BONNEAU, D., REYNIER, P. & CHEVROLLIER, A. 2010. Adenine nucleotide translocase is involved in a mitochondrial coupling defect in MFN2-related Charcot–Marie–Tooth type 2A disease. *neurogenetics,* 11**,** 127-133.
GUO, W., NAUJOCK, M., FUMAGALLI, L., VANDOORNE, T., BAATSEN, P., BOON, R., ORDOVÁS, L., PATEL, A., WELTERS, M., VANWELDEN, T., GEENS, N., TRICOT, T., BENOY, V., STEYAERT, J., LEFEBVRE-OMAR, C., BOESMANS, W., JARPE, M., STERNECKERT, J., WEGNER, F., PETRI, S., BOHL, D., VANDEN BERGHE, P., ROBBERECHT, W., VAN DAMME, P., VERFAILLIE, C. & VAN DEN BOSCH, L. 2017. HDAC6 inhibition reverses axonal transport defects in motor neurons derived from FUS-ALS patients. *Nature Communications,* 8.

GUO, Y., ZHANG, H., YAN, C., SHEN, B., ZHANG, Y., GUO, X., SUN, S., YU, F., YAN, J., LIU, R., ZHANG, Q., ZHANG, D., LIU, H., LIU, Y., ZHANG, Y., LI, W., QIN, J., LV, H., WANG, Z., YUAN, Y., YANG, J.-F., ZHONG, Y.-T., GAO, S., ZHOU, B., LIU, L., KONG, D., HAO, X., HU, J. & CHEN, Q. 2023. Small molecule agonist of mitochondrial fusion repairs mitochondrial dysfunction. *Nature Chemical Biology,* 19**,** 468-477.

HALEVY, T. & URBACH, A. 2014. Comparing ESC and iPSC—Based Models for Human Genetic Disorders. *Journal of Clinical Medicine,* 3**,** 1146-1162.

HAMMOND, J. W., HUANG, C.-F., KAECH, S., JACOBSON, C., BANKER, G. & VERHEY, K. J. 2009. Posttranslational Modifications of Tubulin and the Polarized Transport of Kinesin-1 in Neurons. *Molecular Biology of the Cell,* 21**,** 572-583.

HANCOCK, W. O. 2014. Bidirectional cargo transport: moving beyond tug of war. *Nature Reviews Molecular Cell Biology,* 15**,** 615-628.

HARLEY, P., KERINS, C., GATT, A., NEVES, G., RICCIO, F., MACHADO, C. B., CHEESBROUGH, A., R'BIBO, L., BURRONE, J. & LIEBERAM, I. 2023. Aberrant axon initial segment plasticity and intrinsic excitability of ALS hiPSC motor neurons. *Cell Reports,* 42**,** 113509.

HERGENREDER, E., MINOTTI, A. P., ZORINA, Y., OBERST, P., ZHAO, Z., MUNGUBA, H., CALDER, E. L., BAGGIOLINI, A., WALSH, R. M., LISTON, C., LEVITZ, J., GARIPPA, R., CHEN, S., CICERI, G. & STUDER, L. 2024. Combined small-molecule treatment accelerates maturation of human pluripotent stem cell-derived neurons. *Nature Biotechnology,* 42**,** 1515-1525.

HETZ, C., ZHANG, K. & KAUFMAN, R. J. 2020. Mechanisms, regulation and functions of the unfolded protein response. *Nature Reviews Molecular Cell Biology,* 21**,** 421-438.

HIKIAMI, R., YAMASHITA, H., KOITA, N., JINGAMI, N., SAWAMOTO, N., FURUKAWA, K., KAWAI, H., TERASHIMA, T., OKA, N., HASHIGUCHI, A., TAKASHIMA, H., URUSHITANI, M. & TAKAHASHI, R. 2017. Charcot–Marie–Tooth disease type 2A with an autosomal-recessive inheritance: the first report of an adult-onset disease. *Journal of Human Genetics,* 63**,** 89-92.

HINES, T. J., BAILEY, J., LIU, H., GUNTUR, A. R., SEBURN, K. L., PRATT, S. L., FUNKE, J. R., TARANTINO, L. M. & BURGESS, R. W. 2023. A Novel ENU-Induced Mfn2 Mutation Causes Motor Deficits in Mice without Causing Peripheral Neuropathy. *Biology,* 12**,** 953.

HINGE, A., HE, J., BARTRAM, J., JAVIER, J., XU, J., FJELLMAN, E., SESAKI, H., LI, T., YU, J., WUNDERLICH, M., MULLOY, J., KOFRON, M., SALOMONIS, N., GRIMES, H. L. & FILIPPI, M.-D. 2020. Asymmetrically Segregated Mitochondria Provide Cellular Memory of Hematopoietic Stem Cell Replicative History and Drive HSC Attrition. *Cell Stem Cell,* 26**,** 420-430.e6.

HIROKAWA, N., NODA, Y., TANAKA, Y. & NIWA, S. 2009. Kinesin superfamily motor proteins and intracellular transport. *Nat Rev Mol Cell Biol,* 10**,** 682-96.

HONG, Y. B., LEE, J. H., PARK, H. J., CHOI, Y.-R., HYUN, Y. S., PARK, J. H., KOO, H., CHUNG, K. W. & CHOI, B.-O. 2015. A family with axonal sensorimotor polyneuropathy with TUBB3 mutation. *Molecular Medicine Reports,* 11**,** 2729-2734.

HOOIKAAS, P. J., MARTIN, M., MÜHLETHALER, T., KUIJNTJES, G.-J., PEETERS, C. A. E., KATRUKHA, E. A., FERRARI, L., STUCCHI, R., VERHAGEN, D. G. F., VAN RIEL, W. E., GRIGORIEV, I., ALTELAAR, A. F. M., HOOGENRAAD, C. C., RÜDIGER, S. G. D., STEINMETZ, M. O., KAPITEIN, L. C. & AKHMANOVA, A. 2019. MAP7 family proteins regulate kinesin-1 recruitment and activation. *Journal of Cell Biology,* 218**,** 1298-1318.

HU, B.-Y., WEICK, J. P., YU, J., MA, L.-X., ZHANG, X.-Q., THOMSON, J. A. & ZHANG, S.-C. 2010. Neural differentiation of human induced pluripotent stem cells follows developmental principles but with variable potency. *Proceedings of the National Academy of Sciences,* 107**,** 4335-4340.

HU, N. W., CORBETT, G. T., MOORE, S., KLYUBIN, I., O'MALLEY, T. T., WALSH, D. M., LIVESEY, F. J. & ROWAN, M. J. 2018. Extracellular Forms of Aβ and Tau from iPSC Models of Alzheimer's Disease Disrupt Synaptic Plasticity. *Cell Rep,* 23**,** 1932-1938.
HUANG, C. Y. M. & RASBAND, M. N. 2018. Axon initial segments: structure, function, and disease. *Annals of the New York Academy of Sciences,* 1420**,** 46-61.
HUANG, X., JIANG, C., YU, L. & YANG, A. 2020. Current and Emerging Approaches for Studying Inter-Organelle Membrane Contact Sites. *Frontiers in Cell and Developmental Biology,* 8.
HUBERT, K. A. & WELLIK, D. M. 2023. Hox genes in development and beyond. *Development,* 150.
HUMAN PROTEIN ATLAS. 2025. *Tissue expression of MFN2* [Online]. proteinatlas.org. Available: https://www.proteinatlas.org/ENSG00000116688-MFN2/tissue [Accessed 05.08.2025 2025].
HUO, Y., SUN, W., SHI, T., GAO, S. & ZHUANG, M. 2022. The MFN1 and MFN2 mitofusins promote clustering between mitochondria and peroxisomes. *Communications Biology,* 5.
IAPADRE, G., MORANA, G., VARI, M. S., PINTO, F., LANTERI, P., TESSA, A., SANTORELLI, F. M., STRIANO, P. & VERROTTI, A. 2018. A novel homozygous MFN2 mutation associated with severe and atypical CMT2 phenotype. *European Journal of Paediatric Neurology,* 22**,** 563-567.
ISHIHARA, N., EURA, Y. & MIHARA, K. 2004. Mitofusin 1 and 2 play distinct roles in mitochondrial fusion reactions via GTPase activity. *Journal of Cell Science,* 117**,** 6535-6546.
ISHIHARA, N., NOMURA, M., JOFUKU, A., KATO, H., SUZUKI, S. O., MASUDA, K., OTERA, H., NAKANISHI, Y., NONAKA, I., GOTO, Y., TAGUCHI, N., MORINAGA, H., MAEDA, M., TAKAYANAGI, R., YOKOTA, S. & MIHARA, K. 2009. Mitochondrial fission factor Drp1 is essential for embryonic development and synapse formation in mice. *Nat Cell Biol,* 11**,** 958-66.
JAKOBS, M. A. H., DIMITRACOPOULOS, A. & FRANZE, K. 2019. KymoButler, a deep learning software for automated kymograph analysis. *eLife,* 8**,** e42288.
JEAN, S. & KIGER, A. A. 2012. Coordination between RAB GTPase and phosphoinositide regulation and functions. *Nature Reviews Molecular Cell Biology,* 13**,** 463-470.
JENNINGS, M. J., KAGIAVA, A., VENDREDY, L., SPAULDING, E. L., STAVROU, M., HATHAZI, D., GRÜNEBOOM, A., DE WINTER, V., GESS, B., SCHARA, U., POGORYELOVA, O., LOCHMÜLLER, H., BORCHERS, C. H., ROOS, A., BURGESS, R. W., TIMMERMAN, V., KLEOPA, K. A. & HORVATH, R. 2022. NCAM1 and GDF15 are biomarkers of Charcot-Marie-Tooth disease in patients and mice. *Brain,* 145**,** 3999-4015.
JIANG, S., NANDY, P., WANG, W., MA, X., HSIA, J., WANG, C., WANG, Z., NIU, M., SIEDLAK, S. L., TORRES, S., FUJIOKA, H., XU, Y., LEE, H.-G., PERRY, G., LIU, J. & ZHU, X. 2018. Mfn2 ablation causes an oxidative stress response and eventual neuronal death in the hippocampus and cortex. *Molecular Neurodegeneration,* 13.
JIN, Y., LI, S., YU, Q., CHEN, T. & LIU, D. 2023. Application of stem cells in regeneration medicine. *MedComm,* 4.
KALINSKI, A. L., KAR, A. N., CRAVER, J., TOSOLINI, A. P., SLEIGH, J. N., LEE, S. J., HAWTHORNE, A., BRITO-VARGAS, P., MILLER-RANDOLPH, S., PASSINO, R., SHI, L., WONG, V. S. C., PICCI, C., SMITH, D. S., WILLIS, D. E., HAVTON, L. A., SCHIAVO, G., GIGER, R. J., LANGLEY, B. & TWISS, J. L. 2019. Deacetylation of Miro1 by HDAC6 blocks mitochondrial transport and mediates axon growth inhibition. *Journal of Cell Biology,* 218**,** 1871-1890.
KALVERAM, B., SCHMIDTKE, G. & GROETTRUP, M. 2008. The ubiquitin-like modifier FAT10 interacts with HDAC6 and localizes to aggresomes under proteasome inhibition. *Journal of Cell Science,* 121**,** 4079-4088.

KANAI, Y., OKADA, Y., TANAKA, Y., HARADA, A., TERADA, S. & HIROKAWA, N. 2000. KIF5C, a Novel Neuronal Kinesin Enriched in Motor Neurons. *The Journal of Neuroscience,* 20**,** 6374-6384.
KANEMARU, K., OGAWA, G., MOCHIZUKI, H., NAKAZATO, M. & SHIOMI, K. 2019. A Sporadic Case of Charcot-Marie-Tooth Disease Type 2 with Left Vocal Fold Palsy due to Mitofusin 2 Mutation. *Internal Medicine,* 58**,** 2091 - 2093.
KAUL, N., SOPPINA, V. & VERHEY, J., KRISTEN 2014. Effects of α-Tubulin K40 Acetylation and Detyrosination on Kinesin-1 Motility in a Purified System. *Biophysical Journal,* 106**,** 2636-2643.
KC, R., LÓPEZ DE BOER, R., LIN, M., VAGNOZZI, A. N., JEANNOTTE, L. & PHILIPPIDOU, P. 2024. Multimodal Hox5 activity generates motor neuron diversity. *Communications Biology,* 7.
KIM, J.-Y., WOO, S.-Y., HONG, Y. B., CHOI, H., KIM, J., CHOI, H., MOOK-JUNG, I., HA, N., KYUNG, J., KOO, S. K., JUNG, S.-C. & CHOI, B.-O. 2016. HDAC6 Inhibitors Rescued the Defective Axonal Mitochondrial Movement in Motor Neurons Derived from the Induced Pluripotent Stem Cells of Peripheral Neuropathy Patients with HSPB1 Mutation. *Stem Cells International,* 2016**,** 1-14.
KIM, K., DOI, A., WEN, B., NG, K., ZHAO, R., CAHAN, P., KIM, J., ARYEE, M. J., JI, H., EHRLICH, L. I. R., YABUUCHI, A., TAKEUCHI, A., CUNNIFF, K. C., HONGGUANG, H., MCKINNEY-FREEMAN, S., NAVEIRAS, O., YOON, T. J., IRIZARRY, R. A., JUNG, N., SEITA, J., HANNA, J., MURAKAMI, P., JAENISCH, R., WEISSLEDER, R., ORKIN, S. H., WEISSMAN, I. L., FEINBERG, A. P. & DALEY, G. Q. 2010. Epigenetic memory in induced pluripotent stem cells. *Nature,* 467**,** 285-290.
KIM, S. E., KIM, B. K., GIL, J. E., KIM, S. K. & KIM, J. H. 2007. Comparative analysis of the developmental competence of three human embryonic stem cell lines in vitro. *Mol Cells,* 23**,** 49-56.
KOLITSIDA, P., SAHA, A., CALIRI, A., ASSALI, E., RIERA, A. M., ITSKANOV, S., MAGANA, C. S., STORK, B., SHIRIHAI, O., SEKLER, I., KOEHLER, C. M. & VAN DER BLIEK, A. M. 2024. Mfn2 induces NCLX-mediated calcium release from mitochondria. *bioRxiv*.
KONNO, T., ROSS, O. A., TEIVE, H. A. G., SŁAWEK, J., DICKSON, D. W. & WSZOLEK, Z. K. 2017. DCTN1-related neurodegeneration: Perry syndrome and beyond. *Parkinsonism & Related Disorders,* 41**,** 14-24.
KOTRUCHOW, K., KABZIŃSKA, D., HAUSMANOWA-PETRUSEWICZ, I. & KOCHAŃSKI, A. 2013. A late-onset and mild form of Charcot-Marie-Tooth disease type 2 caused by a novel splice-site mutation within the Mitofusin-2 gene. *Acta Myologica,* 32**,** 166 - 169.
KOTRUCHOW, K., KABZIŃSKA, D. & KOCHAŃSKI, A. 2015. Pathogenic mutations and sequence variants within mitofusin 2 gene in Polish patients with different hereditary motor-sensory neuropathies. *Acta Neurobiologiae Experimentalis,* 75**,** 264-278.
KUBO, S. & BUI, K. H. 2023. Regulatory mechanisms of the dynein-2 motility by post-translational modification revealed by MD simulation. *Scientific Reports,* 13**,** 1477.
KUIJPERS, M., NGUYEN, P. T. & HAUCKE, V. 2024. The Endoplasmic Reticulum and Its Contacts: Emerging Roles in Axon Development, Neurotransmission, and Degeneration. *Neuroscientist,* 30**,** 545-559.
KUMAR, A., LARREA, D., PERO, M. E., INFANTE, P., CONENNA, M., SHIN, G. J., VAN ELIAS, V., GRUEBER, W. B., DI MARCOTULLIO, L., AREA-GOMEZ, E. & BARTOLINI, F. 2024. MFN2 coordinates mitochondria motility with α-tubulin acetylation and this regulation is disrupted in CMT2A. *iScience,* 27**,** 109994.
KUMAR, D., MD ASHRAF, G., BILGRAMI, A. L. & IMTAIYAZ HASSAN, M. 2022. Emerging therapeutic developments in neurodegenerative diseases: A clinical investigation. *Drug Discovery Today,* 27**,** 103305.
KUMAR, S., PAN, C., CHRISTOPHER, SHAH, N., WHEELER, E., SARAH, HOYT, R., KARI, HEMPEL, N., MYTHREYE, K. & LEE, Y., NAM 2016. Activation of Mitofusin2 by Smad2-RIN1 Complex during Mitochondrial Fusion. *Molecular Cell,* 62**,** 520-531.

LAING, O., HALLIWELL, J. & BARBARIC, I. 2019. Rapid PCR Assay for Detecting Common Genetic Variants Arising in Human Pluripotent Stem Cell Cultures. *Curr Protoc Stem Cell Biol,* 49**,** e83.
LARREA, D., PERA, M., GONNELLI, A., QUINTANA–CABRERA, R., AKMAN, H. O., GUARDIA-LAGUARTA, C., VELASCO, K. R., AREA-GOMEZ, E., DAL BELLO, F., DE STEFANI, D., HORVATH, R., SHY, M. E., SCHON, E. A. & GIACOMELLO, M. 2019. MFN2 mutations in Charcot–Marie–Tooth disease alter mitochondria-associated ER membrane function but do not impair bioenergetics. *Human Molecular Genetics,* 28**,** 1782-1800.
LAVIE, J., SERRAT, R., BELLANCE, N., COURTAND, G., DUPUY, J.-W., TESSON, C., COUPRY, I., BRICE, A., LACOMBE, D., DURR, A., STEVANIN, G., DARIOS, F., ROSSIGNOL, R., GOIZET, C. & BÉNARD, G. 2016. Mitochondrial morphology and cellular distribution are altered in SPG31 patients and are linked to DRP1 hyperphosphorylation. *Human Molecular Genetics***,** ddw425.
LEE, A. S., TANG, C., RAO, M. S., WEISSMAN, I. L. & WU, J. C. 2013. Tumorigenicity as a clinical hurdle for pluripotent stem cell therapies. *Nature Medicine,* 19**,** 998-1004.
LEE, C. A., CHIN, L.-S. & LI, L. 2018a. Hypertonia-linked protein Trak1 functions with mitofusins to promote mitochondrial tethering and fusion. *Protein & Cell,* 9**,** 693-716.
LEE, I.-G., OLENICK, M. A., BOCZKOWSKA, M., FRANZINI-ARMSTRONG, C., HOLZBAUR, E. L. F. & DOMINGUEZ, R. 2018b. A conserved interaction of the dynein light intermediate chain with dynein-dynactin effectors necessary for processivity. *Nature Communications,* 9.
LEE, M., PARK, C.-H., CHUNG, H. K., KIM, H. J., CHOI, Y., YOO, J. H., YOON, Y. C., HONG, Y. B., CHUNG, K. W., CHOI, B. O. & LEE, H. W. 2017. Cerebral white matter abnormalities in patients with charcot‐marie‐tooth disease. *Annals of Neurology,* 81**,** 147-151.
LEE, S.-K. & PFAFF, S. L. 2003. Synchronization of Neurogenesis and Motor Neuron Specification by Direct Coupling of bHLH and Homeodomain Transcription Factors. *Neuron,* 38**,** 731-745.
LEWIS, T. L., KWON, S.-K., LEE, A., SHAW, R. & POLLEUX, F. 2018. MFF-dependent mitochondrial fission regulates presynaptic release and axon branching by limiting axonal mitochondria size. *Nature Communications,* 9.
LI, G., JIANG, H., CHANG, M., XIE, H. & HU, L. 2011. HDAC6 α-tubulin deacetylase: A potential therapeutic target in neurodegenerative diseases. *Journal of the Neurological Sciences,* 304**,** 1-8.
LI, J., DANG, X., FRANCO, A. & DORN, G. W. 2022a. Reciprocal Regulation of Mitofusin 2-Mediated Mitophagy and Mitochondrial Fusion by Different PINK1 Phosphorylation Events. *Frontiers in Cell and Developmental Biology,* 10.
LI, Y.-J., CAO, Y.-L., FENG, J.-X., QI, Y., MENG, S., YANG, J.-F., ZHONG, Y.-T., KANG, S., CHEN, X., LAN, L., LUO, L., YU, B., CHEN, S., CHAN, D. C., HU, J. & GAO, S. 2019. Structural insights of human mitofusin-2 into mitochondrial fusion and CMT2A onset. *Nature Communications,* 10.
LI, Y., GU, Z., LIN, S., CHEN, L., DZREYAN, V., EID, M., DEMYANENKO, S. & HE, B. 2022b. Histone Deacetylases as Epigenetic Targets for Treating Parkinson's Disease. *Brain Sciences,* 12**,** 672.
LI, Y., SANG, S., REN, W., PEI, Y., BIAN, Y., CHEN, Y. & SUN, H. 2021. Inhibition of Histone Deacetylase 6 (HDAC6) as a therapeutic strategy for Alzheimer's disease: A review (2010-2020). *Eur J Med Chem,* 226**,** 113874.
LIM, D., DEMATTEIS, G., TAPELLA, L., GENAZZANI, A. A., CALÌ, T., BRINI, M. & VERKHRATSKY, A. 2021. Ca2+ handling at the mitochondria-ER contact sites in neurodegeneration. *Cell Calcium,* 98**,** 102453.
LIN, K.-P., SOONG, B.-W., YANG, C.-C., HUANG, L.-W., CHANG, M.-H., LEE, I.-H., ANTONELLIS, A. & LEE, Y.-C. 2011. The Mutational Spectrum in a Cohort of

Charcot-Marie-Tooth Disease Type 2 among the Han Chinese in Taiwan. *PLoS ONE,* 6**,** e29393.
LIN, S., XU, L.-Q., XU, G.-R., GUO, L.-L., LIN, B.-J., CHEN, W.-J., WANG, N., LIN, Y. & HE, J. 2020. Whole exome sequencing reveals a broader variant spectrum of Charcot-Marie-Tooth disease type 2. *neurogenetics,* 21**,** 79-86.
LIPPMANN, S., ETHAN, WILLIAMS, E., CLAY, RUHL, A., DAVID, ESTEVEZ-SILVA, C., MARIA, CHAPMAN, R., EDWIN, COON, J., JOSHUA & ASHTON, S., RANDOLPH 2015. Deterministic HOX Patterning in Human Pluripotent Stem Cell-Derived Neuroectoderm. *Stem Cell Reports,* 4**,** 632-644.
LIU, X., WEAVER, D., SHIRIHAI, O. & HAJNÓCZKY, G. 2009. Mitochondrial 'kiss-and-run': interplay between mitochondrial motility and fusion–fission dynamics. *The EMBO Journal,* 28**,** 3074-3089.
LIU, Y. J., MCINTYRE, R. L., JANSSENS, G. E. & HOUTKOOPER, R. H. 2020. Mitochondrial fission and fusion: A dynamic role in aging and potential target for age-related disease. *Mechanisms of Ageing and Development,* 186**,** 111212.
LIVAK, K. J. & SCHMITTGEN, T. D. 2001. Analysis of relative gene expression data using real-time quantitative PCR and the 2(-Delta Delta C(T)) Method. *Methods,* 25**,** 402-8.
LOISEAU, D., CHEVROLLIER, A., VERNY, C., GUILLET, V., GUEGUEN, N., POU DE CRESCENZO, M. A., FERRÉ, M., MALINGE, M. C., GUICHET, A., NICOLAS, G., AMATI‐BONNEAU, P., MALTHIÈRY, Y., BONNEAU, D. & REYNIER, P. 2007. Mitochondrial coupling defect in Charcot–Marie–Tooth type 2A disease. *Annals of Neurology,* 61**,** 315-323.
LOPES, A. T., HAUSRAT, T. J., HEISLER, F. F., GROMOVA, K. V., LOMBINO, F. L., FISCHER, T., RUSCHKIES, L., BREIDEN, P., THIES, E., HERMANS-BORGMEYER, I., SCHWEIZER, M., SCHWARZ, J. R., LOHR, C. & KNEUSSEL, M. 2020. Spastin depletion increases tubulin polyglutamylation and impairs kinesin-mediated neuronal transport, leading to working and associative memory deficits. *PLOS Biology,* 18**,** e3000820.
LÓPEZ-DOMÉNECH, G., SERRAT, R., MIRRA, S., D'ANIELLO, S., SOMORJAI, I., ABAD, A., VITUREIRA, N., GARCÍA-ARUMÍ, E., ALONSO, M. T., RODRIGUEZ-PRADOS, M., BURGAYA, F., ANDREU, A. L., GARCÍA-SANCHO, J., TRULLAS, R., GARCIA-FERNÀNDEZ, J. & SORIANO, E. 2012. The Eutherian Armcx genes regulate mitochondrial trafficking in neurons and interact with Miro and Trak2. *Nat Commun,* 3**,** 814.
LÓPEZ‐DOMÉNECH, G., COVILL‐COOKE, C., IVANKOVIC, D., HALFF, E. F., SHEEHAN, D. F., NORKETT, R., BIRSA, N. & KITTLER, J. T. 2018. Miro proteins coordinate microtubule‐ and actin‐dependent mitochondrial transport and distribution. *The EMBO Journal,* 37**,** 321-336.
LOPRESTI, P. 2019. The Selective HDAC6 Inhibitor ACY-738 Impacts Memory and Disease Regulation in an Animal Model of Multiple Sclerosis. *Frontiers in Neurology,* 10.
LOVAS, J. R. & WANG, X. 2013. The meaning of mitochondrial movement to a neuron's life. *Biochim Biophys Acta,* 1833**,** 184-94.
LUIGETTI, M., FABRIZI, G. M., BISOGNI, G., ROMANO, A., TAIOLI, F., FERRARINI, M., BERNARDO, D., ROSSINI, P. M. & SABATELLI, M. 2016. Charcot-Marie-Tooth type 2 and distal hereditary motor neuropathy: Clinical, neurophysiological and genetic findings from a single-centre experience. *Clinical neurology and neurosurgery,* 144**,** 67-71.
LUZ, A. L., ROONEY, J. P., KUBIK, L. L., GONZALEZ, C. P., SONG, D. H. & MEYER, J. N. 2015. Mitochondrial Morphology and Fundamental Parameters of the Mitochondrial Respiratory Chain Are Altered in Caenorhabditis elegans Strains Deficient in Mitochondrial Dynamics and Homeostasis Processes. *PLOS ONE,* 10**,** e0130940.
MACASKILL, A. F., RINHOLM, J. E., TWELVETREES, A. E., ARANCIBIA-CARCAMO, I. L., MUIR, J., FRANSSON, A., ASPENSTROM, P., ATTWELL, D. & KITTLER, J. T.

2009. Miro1 Is a Calcium Sensor for Glutamate Receptor-Dependent Localization of Mitochondria at Synapses. *Neuron,* 61**,** 541-555.
MADAY, S., TWELVETREES, E., ALISON, MOUGHAMIAN, J., ARMEN & HOLZBAUR, L. F., ERIKA 2014. Axonal Transport: Cargo-Specific Mechanisms of Motility and Regulation. *Neuron,* 84**,** 292-309.
MAGRANÉ, J., CORTEZ, C., GAN, W.-B. & MANFREDI, G. 2014. Abnormal mitochondrial transport and morphology are common pathological denominators in SOD1 and TDP43 ALS mouse models. *Human Molecular Genetics,* 23**,** 1413-1424.
MAGY, L., MATHIS, S., LE MASSON, G., GOIZET, C., TAZIR, M. & VALLAT, J.-M. 2018. Updating the classification of inherited neuropathies. *Neurology,* 90**,** e870-e876.
MAJID, T., GRIFFIN, D., CRISS, Z., JARPE, M. & PAUTLER, R. G. 2015. Pharmacologic treatment with histone deacetylase 6 inhibitor (ACY‐738) recovers Alzheimer's disease phenotype in amyloid precursor protein/presenilin 1 (APP/PS1) mice. *Alzheimer's & Dementia: Translational Research & Clinical Interventions,* 1**,** 170-181.
MARTIN, G. R. 1981. Isolation of a pluripotent cell line from early mouse embryos cultured in medium conditioned by teratocarcinoma stem cells. *Proceedings of the National Academy of Sciences,* 78**,** 7634-7638.
MARTYN, C. N. & HUGHES, R. A. 1997. Epidemiology of peripheral neuropathy. *J Neurol Neurosurg Psychiatry,* 62**,** 310-8.
MARX, A., HOENGER, A. & MANDELKOW, E. 2009. Structures of kinesin motor proteins. *Cell Motility,* 66**,** 958-966.
MASINGUE, M., VATIER, C., JÉRU, I., LATOUR, P., JARDEL, C., LAFORÊT, P., EYMARD, B., VIGOUROUX, C. & STOJKOVIC, T. 2017. Homozygous p.R707W MFN2 mutation is associated with neuropathy, lipomatosis, peripheral lipoatrophy and metabolic alterations. *Neuromuscular Disorders,* 27**,** S148.
MAURY, Y., CÔME, J., PISKOROWSKI, R. A., SALAH-MOHELLIBI, N., CHEVALEYRE, V., PESCHANSKI, M., MARTINAT, C. & NEDELEC, S. 2015. Combinatorial analysis of developmental cues efficiently converts human pluripotent stem cells into multiple neuronal subtypes. *Nature Biotechnology,* 33**,** 89-96.
MCCORQUODALE, D. S., MONTENEGRO, G., PEGUERO, A., CARLSON, N., SPEZIANI, F., PRICE, J., TAYLOR, S. W., MELANSON, M., VANCE, J. M. & ZÜCHNER, S. 2011. Mutation screening of mitofusin 2 in Charcot-Marie-Tooth disease type 2. *Journal of Neurology,* 258**,** 1234-1239.
MCKENNEY, R. J., HUYNH, W., TANENBAUM, M. E., BHABHA, G. & VALE, R. D. 2014. Activation of cytoplasmic dynein motility by dynactin-cargo adapter complexes. *Science,* 345**,** 337-341.
MEIJER, M., REHBACH, K., BRUNNER, J. W., CLASSEN, J. A., LAMMERTSE, H. C. A., VAN LINGE, L. A., SCHUT, D., KRUTENKO, T., HEBISCH, M., CORNELISSE, L. N., SULLIVAN, P. F., PEITZ, M., TOONEN, R. F., BRÜSTLE, O. & VERHAGE, M. 2019. A Single-Cell Model for Synaptic Transmission and Plasticity in Human iPSC-Derived Neurons. *Cell Reports,* 27**,** 2199-2211.e6.
MENTIS, A. A., VLACHAKIS, D., PAPAKONSTANTINOU, E., ZAGANAS, I., PATRINOS, G. P., CHROUSOS, G. P. & DARDIOTIS, E. 2022. A novel variant in DYNC1H1 could contribute to human amyotrophic lateral sclerosis-frontotemporal dementia spectrum. *Cold Spring Harb Mol Case Stud,* 8.
MERDES, A., HEALD, R., SAMEJIMA, K., EARNSHAW, W. C. & CLEVELAND, D. W. 2000. Formation of Spindle Poles by Dynein/Dynactin-Dependent Transport of Numa. *The Journal of Cell Biology,* 149**,** 851-862.
MERRILL, R. A., FLIPPO, K. H. & STRACK, S. 2017. Measuring Mitochondrial Shape with ImageJ. *Neuromethods.* Springer New York.
MERTENS, J., PAQUOLA, A. C. M., KU, M., HATCH, E., BÖHNKE, L., LADJEVARDI, S., MCGRATH, S., CAMPBELL, B., LEE, H., HERDY, J. R., GONÇALVES, J. T., TODA, T., KIM, Y., WINKLER, J., YAO, J., HETZER, M. W. & GAGE, F. H. 2015. Directly

Reprogrammed Human Neurons Retain Aging-Associated Transcriptomic Signatures and Reveal Age-Related Nucleocytoplasmic Defects. *Cell Stem Cell,* 17**,** 705-718.
MERTENS, J., PAQUOLA, A. C. M., KU, M., HATCH, E., BÖHNKE, L., LADJEVARDI, S., MCGRATH, S., CAMPBELL, B., LEE, H., HERDY, J. R., GONÇALVES, J. T., TODA, T., KIM, Y., WINKLER, J., YAO, J., HETZER, M. W. & GAGE, F. H. 2021. Directly Reprogrammed Human Neurons Retain Aging-Associated Transcriptomic Signatures and Reveal Age-Related Nucleocytoplasmic Defects. *Cell Stem Cell,* 17**,** 705-718.
MIKI, H., SETOU, M., KANESHIRO, K. & HIROKAWA, N. 2001. All kinesin superfamily protein, KIF, genes in mouse and human. *Proceedings of the National Academy of Sciences,* 98**,** 7004-7011.
MILLER, K. E. & SHEETZ, M. P. 2004. Axonal mitochondrial transport and potential are correlated. *Journal of Cell Science,* 117**,** 2791-2804.
MISKO, A., JIANG, S., WEGORZEWSKA, I., MILBRANDT, J. & BALOH, R. H. 2010. Mitofusin 2 Is Necessary for Transport of Axonal Mitochondria and Interacts with the Miro/Milton Complex. *The Journal of Neuroscience,* 30**,** 4232-4240.
MISKO, A. L., SASAKI, Y., TUCK, E., MILBRANDT, J. & BALOH, R. H. 2012. Mitofusin2 Mutations Disrupt Axonal Mitochondrial Positioning and Promote Axon Degeneration. *The Journal of Neuroscience,* 32**,** 4145-4155.
MO, Z., ZHAO, X., LIU, H., HU, Q., CHEN, X.-Q., PHAM, J., WEI, N., LIU, Z., ZHOU, J., BURGESS, R. W., PFAFF, S. L., CASKEY, C. T., WU, C., BAI, G. & YANG, X.-L. 2018. Aberrant GlyRS-HDAC6 interaction linked to axonal transport deficits in Charcot-Marie-Tooth neuropathy. *Nature Communications,* 9.
MOU, Y., DEIN, J., CHEN, Z., JAGDALE, M. & LI, X.-J. 2021. MFN2 Deficiency Impairs Mitochondrial Transport and Downregulates Motor Protein Expression in Human Spinal Motor Neurons. *Frontiers in Molecular Neuroscience,* 14.
MOU, Y., MUKTE, S., CHAI, E., DEIN, J. & LI, X.-J. 2020. Analyzing Mitochondrial Transport and Morphology in Human Induced Pluripotent Stem Cell-Derived Neurons in Hereditary Spastic Paraplegia. *Journal of Visualized Experiments*.
MUÑOZ, J. P., IVANOVA, S., SÁNCHEZ-WANDELMER, J., MARTÍNEZ-CRISTÓBAL, P., NOGUERA, E., SANCHO, A., DÍAZ-RAMOS, A., HERNÁNDEZ-ALVAREZ, M. I., SEBASTIÁN, D., MAUVEZIN, C., PALACÍN, M. & ZORZANO, A. 2013. Mfn2 modulates the UPR and mitochondrial function via repression of PERK. *The EMBO Journal,* 32**,** 2348-2361.
NAIR, M. A., NIU, Z., MADIGAN, N. N., SHIN, A. Y., BRAULT, J. S., STAFF, N. P. & KLEIN, C. J. 2023. Clinical trials in Charcot-Marie-Tooth disorders: a retrospective and preclinical assessment. *Frontiers in Neurology,* 14.
NANGAKU, M., SATO-YOSHITAKE, R., OKADA, Y., NODA, Y., TAKEMURA, R., YAMAZAKI, H. & HIROKAWA, N. 1994. KIF1B, a novel microtubule plus end-directed monomeric motor protein for transport of mitochondria. *Cell,* 79**,** 1209-20.
NAÓN, D., HERNÁNDEZ-ALVAREZ, M. I., SHINJO, S., WIECZOR, M., IVANOVA, S., MARTINS DE BRITO, O., QUINTANA, A., HIDALGO, J., PALACÍN, M., APARICIO, P., CASTELLANOS, J., LORES, L., SEBASTIÁN, D., FERNÁNDEZ-VELEDO, S., VENDRELL, J., JOVEN, J., OROZCO, M., ZORZANO, A. & SCORRANO, L. 2023. Splice variants of mitofusin 2 shape the endoplasmic reticulum and tether it to mitochondria. *Science,* 380**,** eadh9351.
NARSINH, K. H., SUN, N., SANCHEZ-FREIRE, V., LEE, A. S., ALMEIDA, P., HU, S., JAN, T., WILSON, K. D., LEONG, D., ROSENBERG, J., YAO, M., ROBBINS, R. C. & WU, J. C. 2011. Single cell transcriptional profiling reveals heterogeneity of human induced pluripotent stem cells. *Journal of Clinical Investigation,* 121**,** 1217-1221.
NASRALLAH, C. M. & HORVATH, T. L. 2014. Mitochondrial dynamics in the central regulation of metabolism. *Nat Rev Endocrinol,* 10**,** 650-8.
NATURE 2013. Smoke and mirrors. *Nature,* 496**,** 269-270.
NEIKIRK, K., G. MARSHALL, A., KULA, B., SMITH, N., LEBLANC, S. & HINTON, A. 2023. MitoTracker: A useful tool in need of better alternatives. *European Journal of Cell Biology,* 102**,** 151371.

NEUMANN, B. & HILLIARD, A., MASSIMO 2014. Loss of MEC-17 Leads to Microtubule Instability and Axonal Degeneration. *Cell Reports,* 6**,** 93-103.
NEUSCH, C., SENDEREK, J., EGGERMANN, T., ELOLFF, E., BÄHR, M. & SCHNEIDER-GOLD, C. 2007. Mitofusin 2 gene mutation (R94Q) causing severe early-onset axonal polyneuropathy (CMT2A). *European Journal of Neurology,* 14**,** 575-577.
NGOH, G. A., PAPANICOLAOU, K. N. & WALSH, K. 2012. Loss of Mitofusin 2 Promotes Endoplasmic Reticulum Stress. *Journal of Biological Chemistry,* 287**,** 20321-20332.
NICOLAS, A., KENNA, K. P., RENTON, A. E., TICOZZI, N., FAGHRI, F., CHIA, R., DOMINOV, J. A., KENNA, B. J., NALLS, M. A., KEAGLE, P., RIVERA, A. M., VAN RHEENEN, W., MURPHY, N. A., VAN VUGT, J. J. F. A., GEIGER, J. T., VAN DER SPEK, R. A., PLINER, H. A., SHANKARACHARYA, SMITH, B. N., MARANGI, G., TOPP, S. D., ABRAMZON, Y., GKAZI, A. S., EICHER, J. D., KENNA, A., MORA, G., CALVO, A., MAZZINI, L., RIVA, N., MANDRIOLI, J., CAPONNETTO, C., BATTISTINI, S., VOLANTI, P., LA BELLA, V., CONFORTI, F. L., BORGHERO, G., MESSINA, S., SIMONE, I. L., TROJSI, F., SALVI, F., LOGULLO, F. O., D'ALFONSO, S., CORRADO, L., CAPASSO, M., FERRUCCI, L., MORENO, C. D. A. M., KAMALAKARAN, S., GOLDSTEIN, D. B., GITLER, A. D., HARRIS, T., MYERS, R. M., PHATNANI, H., MUSUNURI, R. L., EVANI, U. S., ABHYANKAR, A., ZODY, M. C., KAYE, J., FINKBEINER, S., WYMAN, S. K., LENAIL, A., LIMA, L., FRAENKEL, E., SVENDSEN, C. N., THOMPSON, L. M., VAN EYK, J. E., BERRY, J. D., MILLER, T. M., KOLB, S. J., CUDKOWICZ, M., BAXI, E., BENATAR, M., TAYLOR, J. P., RAMPERSAUD, E., WU, G., WUU, J., LAURIA, G., VERDE, F., FOGH, I., TILOCA, C., COMI, G. P., SORARÙ, G., CEREDA, C., CORCIA, P., LAAKSOVIRTA, H., MYLLYKANGAS, L., JANSSON, L., VALORI, M., EALING, J., HAMDALLA, H., ROLLINSON, S., PICKERING-BROWN, S., ORRELL, R. W., SIDLE, K. C., MALASPINA, A., HARDY, J., SINGLETON, A. B., JOHNSON, J. O., AREPALLI, S., SAPP, P. C., MCKENNA-YASEK, D., et al. 2018. Genome-wide Analyses Identify KIF5A as a Novel ALS Gene. *Neuron,* 97**,** 1267-1288.
NOGALES, E., DOWNING, K. H., AMOS, L. A. & L**?**WE, J. 1998a. Tubulin and FtsZ form a distinct family of GTPases. *Nature Structural Biology,* 5**,** 451-458.
NOGALES, E., WOLF, S. G. & DOWNING, K. H. 1998b. Structure of the αβ tubulin dimer by electron crystallography. *Nature,* 391**,** 199-203.
NORDSTRÖM, U., JESSELL, T. M. & EDLUND, T. 2002. Progressive induction of caudal neural character by graded Wnt signaling. *Nature Neuroscience,* 5**,** 525-532.
NORKETT, R., MODI, S., BIRSA, N., ATKIN, T. A., IVANKOVIC, D., PATHANIA, M., TROSSBACH, S. V., KORTH, C., HIRST, W. D. & KITTLER, J. T. 2016. DISC1-dependent Regulation of Mitochondrial Dynamics Controls the Morphogenesis of Complex Neuronal Dendrites. *J Biol Chem,* 291**,** 613-29.
OKAMOTO, S., AMAISHI, Y., MAKI, I., ENOKI, T. & MINENO, J. 2019. Highly efficient genome editing for single-base substitutions using optimized ssODNs with Cas9-RNPs. *Scientific Reports,* 9.
OSAFUNE, K., CARON, L., BOROWIAK, M., MARTINEZ, R. J., FITZ-GERALD, C. S., SATO, Y., COWAN, C. A., CHIEN, K. R. & MELTON, D. A. 2008. Marked differences in differentiation propensity among human embryonic stem cell lines. *Nat Biotechnol,* 26**,** 313-5.
PAPASOZOMENOS, S. C., BINDER, L. I., BENDER, P. K. & PAYNE, M. R. 1985. Microtubule-associated protein 2 within axons of spinal motor neurons: associations with microtubules and neurofilaments in normal and beta,beta'-iminodipropionitrile-treated axons. *The Journal of cell biology,* 100**,** 74-85.
PARK, S.-Y., KIM, S. Y., HONG, Y.-H., CHO, S. I., SEONG, M.-W. & PARK, S. S. 2012. A novel double mutation in cis in MFN2 causes Charcot–Marie–Tooth neuropathy type 2A. *neurogenetics,* 13**,** 275-280.
PARK, S., JUNG, N., MYUNG, S., CHOI, Y., CHUNG, K. W., CHOI, B.-O. & JUNG, S.-C. 2018. Differentiation of Human Tonsil-Derived Mesenchymal Stem Cells into

Schwann-Like Cells Improves Neuromuscular Function in a Mouse Model of Charcot-Marie-Tooth Disease Type 1A. *International Journal of Molecular Sciences,* 19**,** 2393.
PARMIGIANI, R. B., XU, W. S., VENTA-PEREZ, G., ERDJUMENT-BROMAGE, H., YANEVA, M., TEMPST, P. & MARKS, P. A. 2008. HDAC6 is a specific deacetylase of peroxiredoxins and is involved in redox regulation. *Proceedings of the National Academy of Sciences,* 105**,** 9633-9638.
PATANI, R., HOLLINS, A. J., WISHART, T. M., PUDDIFOOT, C. A., ÁLVAREZ, S., DE LERA, A. R., WYLLIE, D. J. A., COMPSTON, D. A. S., PEDERSEN, R. A., GILLINGWATER, T. H., HARDINGHAM, G. E., ALLEN, N. D. & CHANDRAN, S. 2011. Retinoid-independent motor neurogenesis from human embryonic stem cells reveals a medial columnar ground state. *Nature Communications,* 2**,** 214.
PATHAK, D., SHIELDS, L. Y., MENDELSOHN, B. A., HADDAD, D., LIN, W., GERENCSER, A. A., KIM, H., BRAND, M. D., EDWARDS, R. H. & NAKAMURA, K. 2015. The Role of Mitochondrially Derived ATP in Synaptic Vesicle Recycling. *Journal of Biological Chemistry,* 290**,** 22325-22336.
PETRUNGARO, C. & KORNMANN, B. 2019. Lipid exchange at ER-mitochondria contact sites: a puzzle falling into place with quite a few pieces missing. *Current Opinion in Cell Biology,* 57**,** 71-76.
PICARD, M., SHIRIHAI, O. S., GENTIL, B. J. & BURELLE, Y. 2013. Mitochondrial morphology transitions and functions: implications for retrograde signaling? *Am J Physiol Regul Integr Comp Physiol,* 304**,** R393-406.
PICCI, C., WONG, V. S. C., COSTA, C. J., MCKINNON, M. C., GOLDBERG, D. C., SWIFT, M., ALAM, N. M., PRUSKY, G. T., SHEN, S., KOZIKOWSKI, A. P., WILLIS, D. E. & LANGLEY, B. 2020. HDAC6 inhibition promotes α-tubulin acetylation and ameliorates CMT2A peripheral neuropathy in mice. *Experimental neurology.,* 328**,** 113281.
PICH, S., BACH, D., BRIONES, P., LIESA, M., CAMPS, M., TESTAR, X., PALACÍN, M. & ZORZANO, A. 2005. The Charcot–Marie–Tooth type 2A gene product, Mfn2, up-regulates fuel oxidation through expression of OXPHOS system. *Human Molecular Genetics,* 14**,** 1405-1415.
PIPIS, M., FEELY, S. M. E., POLKE, J. M., SKORUPINSKA, M., PEREZ, L., SHY, R. R., LAURA, M., MORROW, J. M., MORONI, I., PISCIOTTA, C., TARONI, F., VUJOVIC, D., LLOYD, T. E., ACSADI, G., YUM, S. W., LEWIS, R. A., FINKEL, R. S., HERRMANN, D. N., DAY, J. W., LI, J., SAPORTA, M., SADJADI, R., WALK, D., BURNS, J., MUNTONI, F., RAMCHANDREN, S., HORVATH, R., JOHNSON, N. E., ZÜCHNER, S., PAREYSON, D., SCHERER, S. S., ROSSOR, A. M., SHY, M. E., REILLY, M. M., BARATTA, S., BRAY, P., CALABRESE, D., CORNETT, K., DONLEVY, G., EICHINGER, K., FOSCAN, M., GENITRINI, S., GRANT, N. R., JONES, T., LEE, D., MCCRAY, B. A., MAGRI, S., MENEZES, M., MULLEN, K., NANJI, T., NUZZO, S., PAGLIANO, E., POH, R., PARK, E., SADAF, S., SAVERI, P., SISKIND, C., SOWDEN, J. E., SUMNER, C. J. & THOMAS, S. 2020. Natural history of Charcot-Marie-Tooth disease type 2A: a large international multicentre study. *Brain,* 143**,** 3589-3602.
PRICE, C. J., STAVISH, D., GOKHALE, P. J., STEVENSON, B. A., SARGEANT, S., LACEY, J., RODRIGUEZ, T. A. & BARBARIC, I. 2021. Genetically variant human pluripotent stem cells selectively eliminate wild-type counterparts through YAP-mediated cell competition. *Dev Cell,* 56**,** 2455-2470 e10.
PULS, I., JONNAKUTY, C., LAMONTE, B. H., HOLZBAUR, E. L. F., TOKITO, M., MANN, E., FLOETER, M. K., BIDUS, K., DRAYNA, D., OH, S. J., BROWN, R. H., LUDLOW, C. L. & FISCHBECK, K. H. 2003. Mutant dynactin in motor neuron disease. *Nature Genetics,* 33**,** 455-456.
QI, Y., YAN, L., YU, C., GUO, X., ZHOU, X., HU, X., HUANG, X., RAO, Z., LOU, Z. & HU, J. 2016. Structures of human mitofusin 1 provide insight into mitochondrial tethering. *Journal of Cell Biology,* 215**,** 621-629.

RECK-PETERSON, S. L., REDWINE, W. B., VALE, R. D. & CARTER, A. P. 2018. The cytoplasmic dynein transport machinery and its many cargoes. *Nature Reviews Molecular Cell Biology,* 19**,** 382-398.

REED, N. A., CAI, D., BLASIUS, T. L., JIH, G. T., MEYHOFER, E., GAERTIG, J. & VERHEY, K. J. 2006. Microtubule Acetylation Promotes Kinesin-1 Binding and Transport. *Current Biology,* 16**,** 2166-2172.

REID, E., KLOOS, M., ASHLEY-KOCH, A., HUGHES, L., BEVAN, S., SVENSON, I. K., GRAHAM, F. L., GASKELL, P. C., DEARLOVE, A., PERICAK-VANCE, M. A., RUBINSZTEIN, D. C. & MARCHUK, D. A. 2002. A kinesin heavy chain (KIF5A) mutation in hereditary spastic paraplegia (SPG10). *Am J Hum Genet,* 71**,** 1189-94.

RIZZO, F., BONO, S., RUEPP, M. D., SALANI, S., OTTOBONI, L., ABATI, E., MELZI, V., CORDIGLIERI, C., PAGLIARANI, S., DE GIOIA, R., ANASTASIA, A., TAIANA, M., GARBELLINI, M., LODATO, S., KUNDERFRANCO, P., CAZZATO, D., CARTELLI, D., LONATI, C., BRESOLIN, N., COMI, G., NIZZARDO, M. & CORTI, S. 2023. Combined RNA interference and gene replacement therapy targeting MFN2 as proof of principle for the treatment of Charcot–Marie–Tooth type 2A. *Cellular and Molecular Life Sciences,* 80.

RIZZO, F., RONCHI, D., SALANI, S., NIZZARDO, M., FORTUNATO, F., BORDONI, A., STUPPIA, G., DEL BO, R., PIGA, D., FATO, R., BRESOLIN, N., COMI, G. P. & CORTI, S. 2016. Selective mitochondrial depletion, apoptosis resistance, and increased mitophagy in human Charcot-Marie-Tooth 2A motor neurons. *Human Molecular Genetics,* 25**,** 4266-4281.

ROCHA, A. G., FRANCO, A., KREZEL, A. M., RUMSEY, J. M., ALBERTI, J. M., KNIGHT, W. C., BIRIS, N., ZACHARIOUDAKIS, E., JANETKA, J. W., BALOH, R. H., KITSIS, R. N., MOCHLY-ROSEN, D., TOWNSEND, R. R., GAVATHIOTIS, E. & DORN, G. W. 2018. MFN2 agonists reverse mitochondrial defects in preclinical models of Charcot-Marie-Tooth disease type 2A. *Science,* 360**,** 336-341.

ROELINK, H., PORTER, J. A., CHIANG, C., TANABE, Y., CHANG, D. T., BEACHY, P. A. & JESSELL, T. M. 1995. Floor plate and motor neuron induction by different concentrations of the amino-terminal cleavage product of sonic hedgehog autoproteolysis. *Cell,* 81**,** 445-55.

ROSSOR, A. M., KAPOOR, M., WELLINGTON, H., SPAULDING, E., SLEIGH, J. N., BURGESS, R. W., LAURA, M., ZETTERBERG, H., BACHA, A., WU, X., HESLEGRAVE, A., SHY, M. E. & REILLY, M. M. 2022. A longitudinal and cross-sectional study of plasma neurofilament light chain concentration in <scp>Charcot-Marie-Tooth</scp> disease. *Journal of the Peripheral Nervous System,* 27**,** 50-57.

SAINIO, M. T., RASILA, T., MOLCHANOVA, S. M., JÄRVILEHTO, J., TORREGROSA-MUÑUMER, R., HARJUHAAHTO, S., PENNONEN, J., HUBER, N., HERUKKA, S.-K., HAAPASALO, A., ZETTERBERG, H., TAIRA, T., PALMIO, J., YLIKALLIO, E. & TYYNISMAA, H. 2022. Neurofilament Light Regulates Axon Caliber, Synaptic Activity, and Organelle Trafficking in Cultured Human Motor Neurons. *Frontiers in Cell and Developmental Biology,* 9.

SAMANAS, N. B., ENGELHART, E. A. & HOPPINS, S. 2020. Defective nucleotide-dependent assembly and membrane fusion in Mfn2 CMT2A variants improved by Bax. *Life Science Alliance,* 3**,** e201900527.

SAMANTA, K., MIRAMS, G. R. & PAREKH, A. B. 2018. Sequential forward and reverse transport of the Na(+) Ca(2+) exchanger generates Ca(2+) oscillations within mitochondria. *Nat Commun,* 9**,** 156.

SANDELIUS, Å., ZETTERBERG, H., BLENNOW, K., ADIUTORI, R., MALASPINA, A., LAURA, M., REILLY, M. M. & ROSSOR, A. M. 2018. Plasma neurofilament light chain concentration in the inherited peripheral neuropathies. *Neurology.,* 90**,** e518.

SANYAL, C., PIETSCH, N., RAMIREZ RIOS, S., PERIS, L., CARRIER, L. & MOUTIN, M.-J. 2023. The detyrosination/re-tyrosination cycle of tubulin and its role and dysfunction

in neurons and cardiomyocytes. *Seminars in Cell & Developmental Biology,* 137**,** 46-62.
SAPORTA, M. A., DANG, V., VOLFSON, D., ZOU, B., XIE, X. S., ADEBOLA, A., LIEM, R. K., SHY, M. & DIMOS, J. T. 2015. Axonal Charcot–Marie–Tooth disease patient-derived motor neurons demonstrate disease-specific phenotypes including abnormal electrophysiological properties. *Experimental Neurology,* 263**,** 190-199.
SATO-YAMADA, Y., STRICKLAND, A., SASAKI, Y., BLOOM, J., DIANTONIO, A. & MILBRANDT, J. 2022. A SARM1-mitochondrial feedback loop drives neuropathogenesis in a Charcot-Marie-Tooth disease type 2A rat model. *Journal of Clinical Investigation,* 132.
SCESA, G., ADAMI, R. & BOTTAI, D. 2021. iPSC Preparation and Epigenetic Memory: Does the Tissue Origin Matter? *Cells,* 10**,** 1470.
SCHAUKOWITCH, K., JANAS, J. A. & WERNIG, M. 2023. Insights and applications of direct neuronal reprogramming. *Curr Opin Genet Dev,* 83**,** 102128.
SEBASTIÁN, D., HERNÁNDEZ-ALVAREZ, M. I., SEGALÉS, J., SORIANELLO, E., MUÑOZ, J. P., SALA, D., WAGET, A., LIESA, M., PAZ, J. C., GOPALACHARYULU, P., OREŠIČ, M., PICH, S., BURCELIN, R., PALACÍN, M. & ZORZANO, A. 2012. Mitofusin 2 (Mfn2) links mitochondrial and endoplasmic reticulum function with insulin signaling and is essential for normal glucose homeostasis. *Proceedings of the National Academy of Sciences,* 109**,** 5523-5528.
SHAHIN, S., LU, B., ZHOU, Y., XU, H., CHETSAWANG, J., BALOH, R. H. & WANG, S. 2023. MFN1 augmentation prevents retinal degeneration in a Charcot-Marie-Tooth type 2A mouse model. *iScience,* 26**,** 106270.
SHARMA, S., GOVINDARAJ, P., CHICKABASAVIAH, Y. T., SIRAM, R., SHROTI, A., SESHAGIRI, D. V., DEBNATH, M., BINDU, P. S., TALY, A. B. & NAGAPPA, M. 2022. Genetic Spectrum of Inherited Neuropathies in India. *Annals of Indian Academy of Neurology,* 25.
SHELLEY, M. J. 2016. The Dynamics of Microtubule/Motor-Protein Assemblies in Biology and Physics. *Annual Review of Fluid Mechanics,* 48**,** 487-506.
SHEN, S., PICCI, C., USTINOVA, K., BENOY, V., KUTIL, Z., ZHANG, G., TAVARES, M. T., PAVLICEK, J., ZIMPRICH, C. A., ROBERS, M. B., VAN DEN BOSCH, L., BARINKA, C., LANGLEY, B. & KOZIKOWSKI, A. P. 2021. Tetrahydroquinoline-Capped Histone Deacetylase 6 Inhibitor SW-101 Ameliorates Pathological Phenotypes in a Charcot-Marie-Tooth Type 2A Mouse Model. *J Med Chem,* 64**,** 4810-4840.
SHEVINSKY, L. H., KNOWLES, B. B., DAMJANOV, I. & SOLTER, D. 1982. Monoclonal antibody to murine embryos defines a stage-specific embryonic antigen expressed on mouse embryos and human teratocarcinoma cells. *Cell,* 30**,** 697-705.
SIMÕES-PIRES, C., ZWICK, V., NURISSO, A., SCHENKER, E., CARRUPT, P.-A. & CUENDET, M. 2013. HDAC6 as a target for neurodegenerative diseases: what makes it different from the other HDACs? *Molecular Neurodegeneration,* 8**,** 7.
SIRAJUDDIN, M., RICE, L. M. & VALE, R. D. 2014. Regulation of microtubule motors by tubulin isotypes and post-translational modifications. *Nature Cell Biology,* 16**,** 335-344.
SKARNES, W. C., PELLEGRINO, E. & MCDONOUGH, J. A. 2019. Improving homology-directed repair efficiency in human stem cells. *Methods,* 164-165**,** 18-28.
SKOV, M., RUIJS, T. Q., GRØNNEBÆK, T. S., SKALS, M., RIISAGER, A., WINTHER, J. B., DYBDAHL, K. L. T., FINDSEN, A., MORGEN, J. J., HUUS, N., BROCH-LIPS, M., NIELSEN, O. B., DE CUBA, C. M. K. E., HEUBERGER, J. A. A. C., DE KAM, M. L., TANNEMAAT, M., VERSCHUUREN, J. J. G. M., KNUTSEN, L. J. S., KELLY, N. M., JENSEN, K. G., ARNOLD, W. D., BURGHES, A. H., OLESEN, C., BOLD, J., PETERSEN, T. K., QUIROZ, J. A., HUTCHISON, J., CHIN, E. R., GROENEVELD, G. J. & PEDERSEN, T. H. 2024. The ClC-1 chloride channel inhibitor NMD670 improves skeletal muscle function in rat models and patients with myasthenia gravis. *Science Translational Medicine,* 16.

SLANZI, A., IANNOTO, G., ROSSI, B., ZENARO, E. & CONSTANTIN, G. 2020. In vitro Models of Neurodegenerative Diseases. *Frontiers in Cell and Developmental Biology,* 8.

SLEIGH, J. N., VILLARROEL-CAMPOS, D., SURANA, S., WICKENDEN, T., TONG, Y., SIMKIN, R. L., VARGAS, J. N. S., RHYMES, E. R., TOSOLINI, A. P., WEST, S. J., ZHANG, Q., YANG, X.-L. & SCHIAVO, G. 2023. Boosting peripheral BDNF rescues impaired in vivo axonal transport in CMT2D mice. *JCI Insight,* 8.

SMITH, A. S. T., KIM, J. H., CHUN, C., GHARAI, A., MOON, H. W., KIM, E. Y., NAM, S. H., HA, N., SONG, J. Y., CHUNG, K. W., DOO, H. M., HESSON, J., MATHIEU, J., BOTHWELL, M., CHOI, B. O. & KIM, D. H. 2022. HDAC6 Inhibition Corrects Electrophysiological and Axonal Transport Deficits in a Human Stem Cell‐Based Model of Charcot‐Marie‐Tooth Disease (Type 2D). *Advanced Biology,* 6**,** 2101308.

SOPPINA, V., HERBSTMAN, J. F., SKINIOTIS, G. & VERHEY, K. J. 2012. Luminal Localization of α-tubulin K40 Acetylation by Cryo-EM Analysis of Fab-Labeled Microtubules. *PLoS ONE,* 7**,** e48204.

SPRONSEN, V., MYRRHE, MIKHAYLOVA, M., LIPKA, J., SCHLAGER, A., MAX, HEUVEL, D., VAN, J., DAVE, KUIJPERS, M., WULF, S., PHEBE, KEIJZER, N., DEMMERS, J., KAPITEIN, C., LUKAS, JAARSMA, D., GERRITSEN, C., HANS, AKHMANOVA, A. & HOOGENRAAD, C., CASPER 2013. TRAK/Milton Motor-Adaptor Proteins Steer Mitochondrial Trafficking to Axons and Dendrites. *Neuron,* 77**,** 485-502.

STANSBERRY, W. M. & PIERCHALA, B. A. 2023. Neurotrophic factors in the physiology of motor neurons and their role in the pathobiology and therapeutic approach to amyotrophic lateral sclerosis. *Frontiers in Molecular Neuroscience,* 16.

STAVISH, D., PRICE, C. J., GELEZAUSKAITE, G., ALSEHLI, H., LEONHARD, K. A., TAAPKEN, S. M., MCINTIRE, E. M., LAING, O., JAMES, B. M., RILEY, J. J., ZERBIB, J., BAKER, D., HARDING, A. L., JESTICE, L. H., ELEVELD, T. F., GILLIS, A. J. M., HILLENIUS, S., LOOIJENGA, L. H. J., GOKHALE, P. J., BEN-DAVID, U., LUDWIG, T. E. & BARBARIC, I. 2024. Feeder-free culture of human pluripotent stem cells drives MDM4-mediated gain of chromosome 1q. *Stem Cell Reports,* 19**,** 1217-1232.

STAVROPOULOS, F., GEORGIOU, E., SCHIZA, N., BELL, S., BALOH, R. H., KLEOPA, K. A. & SARGIANNIDOU, I. 2023. Mitofusin 1 overexpression rescues the abnormal mitochondrial dynamics caused by the Mitofusin 2 <scp>K357T</scp> mutation in vitro. *Journal of the Peripheral Nervous System,* 28**,** 329-340.

STAVROPOULOS, F., SARGIANNIDOU, I., POTAMITI, L., KAGIAVA, A., PANAYIOTIDIS, M. I., BAE, J. H., YEOM, S. C., LEE, J. Y. & KLEOPA, K. A. 2021. Aberrant Mitochondrial Dynamics and Exacerbated Response to Neuroinflammation in a Novel Mouse Model of CMT2A. *Int J Mol Sci,* 22.

STIFANI, N. 2014. Motor neurons and the generation of spinal motor neuron diversity. *Frontiers in Cellular Neuroscience,* 8.

STOICA, R., DE VOS, K. J., PAILLUSSON, S., MUELLER, S., SANCHO, R. M., LAU, K.-F., VIZCAY-BARRENA, G., LIN, W.-L., XU, Y.-F., LEWIS, J., DICKSON, D. W., PETRUCELLI, L., MITCHELL, J. C., SHAW, C. E. & MILLER, C. C. J. 2014. ER–mitochondria associations are regulated by the VAPB–PTPIP51 interaction and are disrupted by ALS/FTD-associated TDP-43. *Nature Communications,* 5.

SUBRAMANIAN, S., BATES, S. E., WRIGHT, J. J., ESPINOZA-DELGADO, I. & PIEKARZ, R. L. 2010. Clinical Toxicities of Histone Deacetylase Inhibitors. *Pharmaceuticals,* 3**,** 2751-2767.

SUGIURA, A., NAGASHIMA, S., TOKUYAMA, T., AMO, T., MATSUKI, Y., ISHIDO, S., KUDO, Y., MCBRIDE, H. M., FUKUDA, T., MATSUSHITA, N., INATOME, R. & YANAGI, S. 2013. MITOL regulates endoplasmic reticulum-mitochondria contacts via Mitofusin2. *Mol Cell,* 51**,** 20-34.

TADENEV, A. L. D., HATTON, C. L. & BURGESS, R. W. 2024. Lack of effect from genetic deletion of Hdac6 in a humanized mouse model of CMT2D. *Journal of the Peripheral Nervous System,* 29**,** 213-220.

TAKAHASHI, K., TANABE, K., OHNUKI, M., NARITA, M., ICHISAKA, T., TOMODA, K. & YAMANAKA, S. 2007. Induction of Pluripotent Stem Cells from Adult Human Fibroblasts by Defined Factors. *Cell,* 131**,** 861-872.

TAKAHASHI, K. & YAMANAKA, S. 2006. Induction of Pluripotent Stem Cells from Mouse Embryonic and Adult Fibroblast Cultures by Defined Factors. *Cell,* 126**,** 663-676.

TANG, Y., LIU, M. L., ZANG, T. & ZHANG, C. L. 2017. Direct Reprogramming Rather than iPSC-Based Reprogramming Maintains Aging Hallmarks in Human Motor Neurons. *Front Mol Neurosci,* 10**,** 359.

THOMPSON, O., VON MEYENN, F., HEWITT, Z., ALEXANDER, J., WOOD, A., WEIGHTMAN, R., GREGORY, S., KRUEGER, F., ANDREWS, S., BARBARIC, I., GOKHALE, P. J., MOORE, H. D., REIK, W., MILO, M., NIK-ZAINAL, S., YUSA, K. & ANDREWS, P. W. 2020. Low rates of mutation in clinical grade human pluripotent stem cells under different culture conditions. *Nature Communications,* 11.

THOMSON, J. A., ITSKOVITZ-ELDOR, J., SHAPIRO, S. S., WAKNITZ, M. A., SWIERGIEL, J. J., MARSHALL, V. S. & JONES, J. M. 1998. Embryonic Stem Cell Lines Derived from Human Blastocysts. *Science,* 282**,** 1145-1147.

TISCHFIELD, M. A., BARIS, H. N., WU, C., RUDOLPH, G., VAN MALDERGEM, L., HE, W., CHAN, W.-M., ANDREWS, C., DEMER, J. L., ROBERTSON, R. L., MACKEY, D. A., RUDDLE, J. B., BIRD, T. D., GOTTLOB, I., PIEH, C., TRABOULSI, E. I., POMEROY, S. L., HUNTER, D. G., SOUL, J. S., NEWLIN, A., SABOL, L. J., DOHERTY, E. J., DE UZCÁTEGUI, C. E., DE UZCÁTEGUI, N., COLLINS, M. L. Z., SENER, E. C., WABBELS, B., HELLEBRAND, H., MEITINGER, T., DE BERARDINIS, T., MAGLI, A., SCHIAVI, C., PASTORE-TROSSELLO, M., KOC, F., WONG, A. M., LEVIN, A. V., GERAGHTY, M. T., DESCARTES, M., FLAHERTY, M., JAMIESON, R. V., MØLLER, H. U., MEUTHEN, I., CALLEN, D. F., KERWIN, J., LINDSAY, S., MEINDL, A., GUPTA, M. L., PELLMAN, D. & ENGLE, E. C. 2010. Human TUBB3 Mutations Perturb Microtubule Dynamics, Kinesin Interactions, and Axon Guidance. *Cell,* 140**,** 74-87.

TOBA, S., JIN, M., YAMADA, M., KUMAMOTO, K., MATSUMOTO, S., YASUNAGA, T., FUKUNAGA, Y., MIYAZAWA, A., FUJITA, S., ITOH, K., FUSHIKI, S., KOJIMA, H., WANIBUCHI, H., ARAI, Y., NAGAI, T. & HIROTSUNE, S. 2017. Alpha-synuclein facilitates to form short unconventional microtubules that have a unique function in the axonal transport. *Scientific Reports,* 7.

TOMASELLI, P. J., KAPOOR, M., CORTESE, A., POLKE, J. M., ROSSOR, A. M. & REILLY, M. M. 2018. Severe cognitive impairment in a patient with CMT2A. *Journal of the Peripheral Nervous System,* 23**,** 147-148.

TUFANO, M., CAPPUCCIO, G., TERRONE, G., MANGANELLI, F., PISCIOTTA, C., GEROLDI, A., CAPPONI, S. & DEL GIUDICE, E. 2015. Early onset Charcot-Marie-Tooth neuropathy type <scp>2A</scp> and severe developmental delay: expanding the clinical phenotype of <scp>MFN2</scp>-related neuropathy. *Journal of the Peripheral Nervous System,* 20**,** 415-418.

TWIG, G., ELORZA, A., MOLINA, A. J. A., MOHAMED, H., WIKSTROM, J. D., WALZER, G., STILES, L., HAIGH, S. E., KATZ, S., LAS, G., ALROY, J., WU, M., PY, B. F., YUAN, J., DEENEY, J. T., CORKEY, B. E. & SHIRIHAI, O. S. 2008. Fission and selective fusion govern mitochondrial segregation and elimination by autophagy. *The EMBO Journal,* 27**,** 433-446.

UL FATIMA, N. & ANANTHANARAYANAN, V. 2023. Mitochondrial movers and shapers: Recent insights into regulators of fission, fusion and transport. *Current Opinion in Cell Biology,* 80**,** 102150.

URNOV, F. D., REBAR, E. J., HOLMES, M. C., ZHANG, H. S. & GREGORY, P. D. 2010. Genome editing with engineered zinc finger nucleases. *Nature Reviews Genetics,* 11**,** 636-646.
VAETH, S., VAETH, M., ANDERSEN, H., CHRISTENSEN, R. & JENSEN, U. B. 2017. Charcot-Marie-Tooth disease in Denmark: a nationwide register-based study of mortality, prevalence and incidence. *BMJ Open,* 7**,** e018048.
VALLAT, J.-M., OUVRIER, R. A., POLLARD, J. D., MAGDELAINE, C., ZHU, D., NICHOLSON, G. A., GREW, S., RYAN, M. M. & FUNALOT, B. 2008. Histopathological Findings in Hereditary Motor and Sensory Neuropathy of Axonal Type With Onset in Early Childhood Associated WithMitofusin 2Mutations. *Journal of Neuropathology & Experimental Neurology,* 67**,** 1097-1102.
VAN LENT, J., PRIOR, R., PÉREZ SILES, G., CUTRUPI, A. N., KENNERSON, M. L., VANGANSEWINKEL, T., WOLFS, E., MUKHERJEE-CLAVIN, B., NEVIN, Z., JUDGE, L., CONKLIN, B., TYYNISMAA, H., CLARK, A. J., BENNETT, D. L., VAN DEN BOSCH, L., SAPORTA, M. & TIMMERMAN, V. 2024. Advances and challenges in modeling inherited peripheral neuropathies using iPSCs. *Experimental & Molecular Medicine,* 56**,** 1348-1364.
VAN LENT, J., VERSTRAELEN, P., ASSELBERGH, B., ADRIAENSSENS, E., MATEIU, L., VERBIST, C., DE WINTER, V., EGGERMONT, K., VAN DEN BOSCH, L., DE VOS, W. H. & TIMMERMAN, V. 2021. Induced pluripotent stem cell-derived motor neurons of CMT type 2 patients reveal progressive mitochondrial dysfunction. *Brain,* 144**,** 2471-2485.
VAN SPRONSEN, M., MIKHAYLOVA, M., LIPKA, J., SCHLAGER, M. A., VAN DEN HEUVEL, D. J., KUIJPERS, M., WULF, P. S., KEIJZER, N., DEMMERS, J., KAPITEIN, L. C., JAARSMA, D., GERRITSEN, H. C., AKHMANOVA, A. & HOOGENRAAD, C. C. 2013. TRAK/Milton motor-adaptor proteins steer mitochondrial trafficking to axons and dendrites. *Neuron,* 77**,** 485-502.
VAZIN, T. & FREED, W. J. 2010. Human embryonic stem cells: Derivation, culture, and differentiation: A review. *Restorative Neurology and Neuroscience,* 28**,** 589-603.
VERFAILLIE, T., RUBIO, N., GARG, A. D., BULTYNCK, G., RIZZUTO, R., DECUYPERE, J. P., PIETTE, J., LINEHAN, C., GUPTA, S., SAMALI, A. & AGOSTINIS, P. 2012. PERK is required at the ER-mitochondrial contact sites to convey apoptosis after ROS-based ER stress. *Cell Death & Differentiation,* 19**,** 1880-1891.
VERHOEVEN, K. 2006. MFN2 mutation distribution and genotype/phenotype correlation in Charcot-Marie-Tooth type 2. *Brain,* 129**,** 2093-2102.
VERMA, M., LIZAMA, B. N. & CHU, C. T. 2022. Excitotoxicity, calcium and mitochondria: a triad in synaptic neurodegeneration. *Translational Neurodegeneration,* 11.
VOELTZ, G. K., SAWYER, E. M., HAJNÓCZKY, G. & PRINZ, W. A. 2024. Making the connection: How membrane contact sites have changed our view of organelle biology. *Cell,* 187**,** 257-270.
VOLPATO, V. & WEBBER, C. 2020. Addressing variability in iPSC-derived models of human disease: guidelines to promote reproducibility. *Disease Models & Mechanisms,* 13**,** dmm042317.
WALTER, W. J., BERÁNEK, V., FISCHERMEIER, E. & DIEZ, S. 2012. Tubulin Acetylation Alone Does Not Affect Kinesin-1 Velocity and Run Length In Vitro. *PLoS ONE,* 7**,** e42218.
WANG, C., NAJM, R., XU, Q., JEONG, D.-E., WALKER, D., BALESTRA, M. E., YOON, S. Y., YUAN, H., LI, G., MILLER, Z. A., MILLER, B. L., MALLOY, M. J. & HUANG, Y. 2018. Gain of toxic apolipoprotein E4 effects in human iPSC-derived neurons is ameliorated by a small-molecule structure corrector. *Nature Medicine,* 24**,** 647-657.
WANG, J. Y. & DOUDNA, J. A. 2023. CRISPR technology: A decade of genome editing is only the beginning. *Science,* 379.
WANG, X. & SCHWARZ, T. L. 2009. The Mechanism of Ca2+-Dependent Regulation of Kinesin-Mediated Mitochondrial Motility. *Cell,* 136**,** 163-174.

WEEDON, N., MICHAEL, HASTINGS, R., CASWELL, R., XIE, W., PASZKIEWICZ, K., ANTONIADI, T., WILLIAMS, M., KING, C., GREENHALGH, L., NEWBURY-ECOB, R. & ELLARD, S. 2011. Exome Sequencing Identifies a DYNC1H1 Mutation in a Large Pedigree with Dominant Axonal Charcot-Marie-Tooth Disease. *The American Journal of Human Genetics,* 89**,** 308-312.

WEI, C., GUO, Y., CI, Z., LI, M., ZHANG, Y. & ZHOU, Y. 2024. Advances of Schwann cells in peripheral nerve regeneration: From mechanism to cell therapy. *Biomedicine & Pharmacotherapy,* 175**,** 116645.

WEIGELE, J., ZHANG, L., FRANCO, A., CARTIER, E. & DORN, G. W., 2ND 2024. Sensory-Motor Neuropathy in Mfn2 T105M Knock-in Mice and Its Reversal by a Novel Piperine-Derived Mitofusin Activator. *J Pharmacol Exp Ther,* 391**,** 361-374.

WERT, G. D. 2003. Human embryonic stem cells: research, ethics and policy. *Human Reproduction,* 18**,** 672-682.

WESTERMANN, B. 2012. Bioenergetic role of mitochondrial fusion and fission. *Biochim Biophys Acta,* 1817**,** 1833-8.

WHITE, R. J. & REYNOLDS, I. J. 1997. Mitochondria accumulate Ca2+ following intense glutamate stimulation of cultured rat forebrain neurones. *J Physiol,* 498 (Pt 1)**,** 31-47.

WHITEHOUSE, C., CORBETT, N. & BROWNLEES, J. 2023. 3D models of neurodegeneration: implementation in drug discovery. *Trends in Pharmacological Sciences,* 44**,** 208-221.

WILLIAMS, C. H. & HONG, C. C. 2011. Multi-Step Usage of in Vivo Models During Rational Drug Design and Discovery. *International Journal of Molecular Sciences,* 12**,** 2262-2274.

WLOGA, D. & GAERTIG, J. 2010. Post-translational modifications of microtubules. *Journal of Cell Science,* 123**,** 3447-3455.

WOJTYNIAK, P., BORATYNSKA-JASINSKA, A., SERWACH, K., GRUSZCZYNSKA-BIEGALA, J., ZABLOCKA, B., JAWORSKI, J. & KAWALEC, M. 2022. Mitofusin 2 Integrates Mitochondrial Network Remodelling, Mitophagy and Renewal of Respiratory Chain Proteins in Neurons after Oxygen and Glucose Deprivation. *Molecular Neurobiology,* 59**,** 6502-6518.

WU, R., LV, H., WANG, H., WANG, Z. & YUAN, Y. 2021. The Pathological Features of Common Hereditary Mitochondrial Dynamics Neuropathy. *Frontiers in Neuroscience,* 15.

WU, S. M. & HOCHEDLINGER, K. 2011. Harnessing the potential of induced pluripotent stem cells for regenerative medicine. *Nature Cell Biology,* 13**,** 497-505.

WURZ, A. I., SCHULZ, A. M., O'BRYANT, C. T., SHARP, J. F. & HUGHES, R. M. 2022. Cytoskeletal dysregulation and neurodegenerative disease: Formation, monitoring, and inhibition of cofilin-actin rods. *Frontiers in Cellular Neuroscience,* 16.

XI, J., LIU, Y., LIU, H., CHEN, H., EMBORG, M. E. & ZHANG, S. C. 2012. Specification of Midbrain Dopamine Neurons from Primate Pluripotent Stem Cells. *STEM CELLS,* 30**,** 1655-1663.

XIAO, Y. & ZHANG, X. 2020. Recent Advances in Small Molecular Modulators Targeting Histone Deacetylase 6. *Future Drug Discovery,* 2**,** FDD53.

XU, J., FU, Y., XIA, W., HE, J., ZOU, Y., RUAN, W., LOU, Q., LI, Y., PAN, J., LI, H. & CHEN, W. 2019. Generation of induced pluripotent stem cell line, ZJUCHi002-A, from Charcot-Marie-Tooth disease type 2A (CMT2A) patient with a mutation of c.752C>T in MFN2. *Stem Cell Research,* 36**,** 101411.

XU, X., KOZIKOWSKI, A. P. & POZZO-MILLER, L. 2014. A selective histone deacetylase-6 inhibitor improves BDNF trafficking in hippocampal neurons from Mecp2 knockout mice: implications for Rett syndrome. *Frontiers in Cellular Neuroscience,* 8.

YAMADA, S., KUBO, Y., YAMAZAKI, D., SEKINO, Y. & KANDA, Y. 2017. Chlorpyrifos inhibits neural induction via Mfn1-mediated mitochondrial dysfunction in human induced pluripotent stem cells. *Scientific Reports,* 7**,** 40925.

YAN, L., QI, Y., HUANG, X., YU, C., LAN, L., GUO, X., RAO, Z., HU, J. & LOU, Z. 2018. Structural basis for GTP hydrolysis and conformational change of MFN1 in mediating membrane fusion. *Nature Structural & Molecular Biology,* 25**,** 233-243.
YANG, H., REN, S., YU, S., PAN, H., LI, T., GE, S., ZHANG, J. & XIA, N. 2020. Methods Favoring Homology-Directed Repair Choice in Response to CRISPR/Cas9 Induced-Double Strand Breaks. *International Journal of Molecular Sciences,* 21**,** 6461.
YENKIN, A. L., BRAMLEY, J. C., KREMITZKI, C. L., WALIGORSKI, J. E., LIEBESKIND, M. J., XU, X. E., CHANDRASEKARAN, V. D., VAKAKI, M. A., BACHMAN, G. W., MITRA, R. D., MILBRANDT, J. D. & BUCHSER, W. J. 2022. Pooled image-base screening of mitochondria with microraft isolation distinguishes pathogenic mitofusin 2 mutations. *Communications Biology,* 5**,** 1128.
YOSHIMI, K., KUNIHIRO, Y., KANEKO, T., NAGAHORA, H., VOIGT, B. & MASHIMO, T. 2016. ssODN-mediated knock-in with CRISPR-Cas for large genomic regions in zygotes. *Nature Communications,* 7**,** 10431.
YOU, Y., WANG, X., LI, S., ZHAO, X. & ZHANG, X. 2018. Exome sequencing reveals a novel MFN2 missense mutation in a Chinese family with Charcot-Marie-Tooth type 2A. *Experimental and Therapeutic Medicine*.
YUFENG, X. & XUAN, Z. 2020. Recent Advances in Small Molecular Modulators Targeting Histone Deacetylase 6. *Future Drug Discovery,* 2**,** FDD53.
ZAHAVI, E. E., HUMMEL, J. J. A., HAN, Y., BAR, C., STUCCHI, R., ALTELAAR, M. & HOOGENRAAD, C. C. 2021. Combined kinesin-1 and kinesin-3 activity drives axonal trafficking of TrkB receptors in Rab6 carriers. *Developmental Cell,* 56**,** 494-508.e7.
ZHANG, F., SU, B., WANG, C., SIEDLAK, S. L., MONDRAGON-RODRIGUEZ, S., LEE, H.-G., WANG, X., PERRY, G. & ZHU, X. 2015. Posttranslational modifications of α-tubulin in alzheimer disease. *Translational Neurodegeneration,* 4.
ZHANG, K., FISHEL BEN KENAN, R., OSAKADA, Y., XU, W., SINIT, R. S., CHEN, L., ZHAO, X., CHEN, J. Y., CUI, B. & WU, C. 2013. Defective axonal transport of Rab7 GTPase results in dysregulated trophic signaling. *J Neurosci,* 33**,** 7451-62.
ZHANG, L., DANG, X., FRANCO, A., ZHAO, H. & DORN, G. W. 2022a. Piperine Derivatives Enhance Fusion and Axonal Transport of Mitochondria by Activating Mitofusins. *Chemistry,* 4**,** 655-668.
ZHANG, X., ZHANG, S. & WANG, T. 2022b. How the mechanical microenvironment of stem cell growth affects their differentiation: a review. *Stem Cell Research & Therapy,* 13.
ZHANG, Y., MA, L., WANG, Z., GAO, C., YANG, L., LI, M., TANG, X., YUAN, H., PANG, D. & OUYANG, H. 2024. Mfn2(R364W), Mfn2(G176S), and Mfn2(H165R) mutations drive Charcot-Marie-Tooth type 2A disease by inducing apoptosis and mitochondrial oxidative phosphorylation damage. *Int J Biol Macromol,* 278**,** 134673.
ZHANG, Z., LI, T.-E., CHEN, M., XU, D., ZHU, Y., HU, B.-Y., LIN, Z.-F., PAN, J.-J., WANG, X., WU, C., ZHENG, Y., LU, L., JIA, H.-L., GAO, S., DONG, Q.-Z. & QIN, L.-X. 2020. MFN1-dependent alteration of mitochondrial dynamics drives hepatocellular carcinoma metastasis by glucose metabolic reprogramming. *British Journal of Cancer,* 122**,** 209-220.
ZHAO, C., TAKITA, J., TANAKA, Y., SETOU, M., NAKAGAWA, T., TAKEDA, S., YANG, H. W., TERADA, S., NAKATA, T., TAKEI, Y., SAITO, M., TSUJI, S., HAYASHI, Y. & HIROKAWA, N. 2001. Charcot-Marie-Tooth Disease Type 2A Caused by Mutation in a Microtubule Motor KIF1Bβ. *Cell,* 105**,** 587-597.
ZHOU, Y., CARMONA, S., MUHAMMAD, A. K. M. G., BELL, S., LANDEROS, J., VAZQUEZ, M., HO, R., FRANCO, A., LU, B., DORN, G. W., WANG, S., LUTZ, C. M. & BALOH, R. H. 2019. Restoring mitofusin balance prevents axonal degeneration in a Charcot-Marie-Tooth type 2A model. *Journal of Clinical Investigation,* 129**,** 1756-1771.
ZHOU, Y., CARMONA, S., MUHAMMAD, A. K. M. G., BELL, S., LANDEROS, J., VAZQUEZ, M., HO, R., FRANCO, A., LU, B., DORN, G. W., WANG, S., LUTZ, C. M. & BALOH, R. H. 2021. Restoring mitofusin balance prevents axonal degeneration in a Charcot-Marie-Tooth type 2A model. *Journal of Clinical Investigation,* 131.

ZHUANG, P., SUN, A. X., AN, J., CHUA, C. K. & CHEW, S. Y. 2018. 3D neural tissue models: From spheroids to bioprinting. *Biomaterials,* 154**,** 113-133.

ZÜCHNER, S., DE JONGHE, P., JORDANOVA, A., CLAEYS, K. G., GUERGUELTCHEVA, V., CHERNINKOVA, S., HAMILTON, S. R., VAN STAVERN, G., KRAJEWSKI, K. M., STAJICH, J., TOURNEV, I., VERHOEVEN, K., LANGERHORST, C. T., DE VISSER, M., BAAS, F., BIRD, T., TIMMERMAN, V., SHY, M. & VANCE, J. M. 2006. Axonal neuropathy with optic atrophy is caused by mutations in mitofusin 2. *Annals of Neurology,* 59**,** 276-281.

ZÜCHNER, S., MERSIYANOVA, I. V., MUGLIA, M., BISSAR-TADMOURI, N., ROCHELLE, J., DADALI, E. L., ZAPPIA, M., NELIS, E., PATITUCCI, A., SENDEREK, J., PARMAN, Y., EVGRAFOV, O., JONGHE, P. D., TAKAHASHI, Y., TSUJI, S., PERICAK-VANCE, M. A., QUATTRONE, A., BATTOLOGLU, E., POLYAKOV, A. V., TIMMERMAN, V., SCHRÖDER, J. M. & VANCE, J. M. 2004. Mutations in the mitochondrial GTPase mitofusin 2 cause Charcot-Marie-Tooth neuropathy type 2A. *Nature Genetics,* 36**,** 449-451.